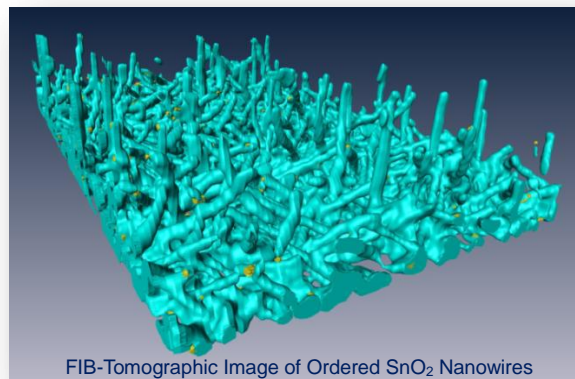


# Chemical Vapor Deposition of One Dimensional Tin Oxide Nanostructures: Structural Studies, Surface Modifications and Device Applications



## DISSERTATION

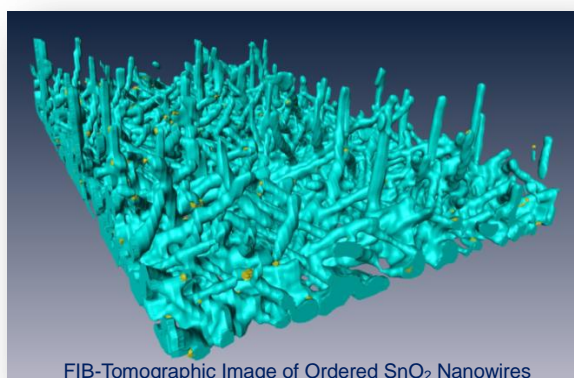
zur Erlangung des Doktorgrades  
der Mathematisch-Naturwissenschaftlichen Fakultät  
der Universität zu Köln  
vorgelegt von

**Jun Pan**



Köln, 2010

# Chemical Vapor Deposition of One Dimensional Tin Oxide Nanostructures: Structural Studies, Surface Modifications and Device Applications



FIB-Tomographic Image of Ordered SnO<sub>2</sub> Nanowires

## DISSERTATION

zur Erlangung des Doktorgrades  
der Mathematisch-Naturwissenschaftlichen Fakultät  
der Universität zu Köln  
vorgelegt von

**Jun Pan**



Köln, 2010

Tag des Kolloquiums:	22.10.2010
Dekan:	Prof. Dr. Hans-Günther Schmalz
Vorsitzender:	Prof. Dr. Annette Schmidt
Berichterstatter:	Prof. Dr. Sanjay Mathur Prof. Dr. Gerd Meyer
Beisitzer:	Dr. Hao Shen

This dissertation was carried out at the Leibniz Institute for New Materials (INM), Saarbrücken and Chair of Inorganic and Materials Chemistry, Department of Chemistry, University of Cologne, Cologne, during February 2007 and October 2010 under the supervision of Prof. Dr. Sanjay Mathur and Dr. Hao Shen.



# Acknowledgements

The work in the following pages could not have been possible completed without the assistance, guidance, and support emotionally and critically from faculty, peers, friends, and family.

First, my committee members and other mentors have made this project a possibility with their guidance and wisdom. I am grateful for the opportunity to have been influenced by your experience and advice.

I am indebted to my director and advisor Prof. Dr. Sanjay Mathur for introducing me to this exciting field and giving me the opportunity, responsibility, guidance, and freedom work in this area, also his thorough readings and insightful commentary on multiple drafts, for always challenging me to think more critically, and for his mentorship and support in the past three years.

Successful completion of this research would not have been possible without the support and cooperation of the members of staff at the Institute of Inorganic and Material Chemistry, especially thanks to Dr. N. Donia, Dr. J. Altmayer and Mr. J. Schläfer in the “MONOGAS” project, who assisted in the precursor synthesis and sample measurements. The contribution of Dr. Hao Shen, the leader of “MONOGAS” project, in the material science was invaluable and deserves special mention. I would like to express my gratitude to him for helping me always to truly understand my own project in ways I hadn't before. I have benefited from his brilliant, generous mind at every stage of this project.

Thanks to Dr. J. D. Wei, Dr. J. T. Li, Dr. X. F. Song, Mr. L. S. Xiao, Dr. K. Y. Shi, Mr. T. Fisher and Ms. R. Fiz for your invaluable input regarding AFM, XRD, SEM, simulation and surface modification and reminding me of how to maintain a balance in this potentially overwhelming process. Special recognitions are

extended to: Ms. A. Roth, Dr. W. Tyrra, Mr. T. Rügamer, Ms. N. Tosun, Mr. R. von Hagen, Ms. R. Werwig, Mr. D. Zopes, Mr. M. Hoffmann, Mr. F. Heinrich, Mr. O. Arslan, Mr. J. Pfrommer, Ms. C. Hegemann, Ms. I. Obolonskaya, Ms. I. Trinker and Ms. S. Kremer.

Completion of this project would not have been possible without cooperation from Dr. F. Hernandez in the University of Barcelona for electrical property measurement, Dr. U. Werner in the Leibniz Institute for New Material and Mr. S. M. Hühne in the University of Bonn for TEM measurement, Dr. F. Soldera in the University of Saarland for FIB-tomography measurement, Dr. N. Mathews and Mr. G. Karthik in Nanyang Technological University for FET measurement, and Dr. M. Nicoul in the University of Cologne for PL measurement.

For their ongoing support and advice, many thanks to Dr. W. D. Shi, Dr. Y. H. Sehleier and Dr. X. M. Li.

To my parents, I cannot express enough how grateful I am for your unconditional and unwavering love, for all you have given. I must express equal gratitude to my wife's parents. They have graciously welcomed me into their lives and have enthusiastically cheered me on as I took each step toward completing my degree.

And finally my dear wife Ting Ouyang listened and responded to the excitement and fear that I expressed about this undertaking with patience, thoughtfulness, and wisdom, for which I am deeply grateful. I am thankful for her meticulous proofreading skills, her assumption of day-to-day household tasks, her faith that I would indeed someday finish, and above all her partnership, love and support.

# Abstract

One-dimensional (1D) metal oxide nanostructures such as wires, rods, belts and tubes have become the focus of intensive research for investigating structure-property relationship under diminishing dimensions and probing their possible scientific and technological applications. Chemical vapor deposition (CVD), based on catalyzed vapor-liquid-solid (VLS) growth mechanism, is an efficient way to synthesize 1D metal oxide nanostructures, which can be implored by combining molecular precursors with CVD-VLS growth. This thesis contains results obtained on a molecule-based CVD approach to grow metal oxide nanowires, elaboration of experimental parameters enabling control over random and orientated growth.

(1) Controlled synthesis, growth mechanism and plasma-treatment of SnO<sub>2</sub> nanowires.

Uniform and high-density single crystalline SnO<sub>2</sub> NWs were fabricated by optimization of deposition temperature, precursor temperature, size of catalyst and angle of graphite holder, and the electrical, photoluminescence, gas sensing and field emission properties were also systematically investigated, it enabled us to have a better understanding of SnO<sub>2</sub> nanowires.

The technical highlights of this work include the successful demonstration of oriented growth of SnO<sub>2</sub> nanowires arrays on TiO<sub>2</sub>(001) substrates by MB-CVD method for the first time. A growth model for the nanowire morphology based upon crystallographic relation between the substrate and NW material is proposed. Electrical and gas sensing properties of SnO<sub>2</sub> [101] single nanowire showed that oriented nanowire arrays can be potentially used towards diameter- and orientation-dependent sensing unit for detection of gas molecules.

Surface modification of SnO<sub>2</sub> nanowires in an argon-oxygen (Ar/O<sub>2</sub>) plasma treatment caused preferential etching of the oxygen atoms from

surface and the inner volume (lattice) producing a non-stoichiometric overlayer, resulting in the higher sensitivity for ethanol gas at lower operating temperature and exhibited improved transducing response towards changing gas atmospheres.

(2) New architectures of SnO<sub>2</sub> nanowire based 1D heterostructure: Synthesis and properties.

New morphological SnO<sub>2</sub> nanowire based heterostructures (such as SnO<sub>2</sub>@TiO<sub>2</sub>, SnO<sub>2</sub>@SnO<sub>2</sub>, SnO<sub>2</sub>@VO<sub>x</sub> and SnO<sub>2</sub>@CdS) were fabricated by chemical surface modification via a two-step process.

Structural characterization of SnO<sub>2</sub>/TiO<sub>2</sub> core-shell structures revealed the formation of mixed-cation phases of composition Sn<sub>x</sub>Ti<sub>1-x</sub>O<sub>2</sub> (x = 0.857 ~ 1.0) depended on the annealing temperatures, the excellent electrical property and gas sensing performance of SnO<sub>2</sub>/TiO<sub>2</sub> core-shell structures are attributed to nanowire based sensor applications.

The SnO<sub>2</sub>@SnO<sub>2</sub> heterostructures with contact angle (CA) of 133° exhibited a superhydrophobic property in comparison with the superhydrophilic SnO<sub>2</sub> nanowires (CA = 3°). Switchable surface wettability of SiO<sub>x</sub> coated SnO<sub>2</sub>@SnO<sub>2</sub> heterostructure (CA = 155.8°) was observed by alternation of UV irradiation, dark storage and O<sub>2</sub> annealing. Geometric microstructure was the major determinant in the switchable wettability from superhydrophilic to superhydrophobic.

The SnO<sub>2</sub>@CdS QDs heterostructures were fabricated by a chemical bath deposition (CBD) method via hydroxide cluster growth mechanism, and had a remarkably enhancement in photoconductivity than non-coated SnO<sub>2</sub> nanowires when the wavelength was below 450 nm.

The work carried out in this thesis is supported by Federal Ministry of Education and Research (BMBF) in the frame of the priority program “BMBF-NanoFutur” (FKZ 03X5512).

# Zusammenfassung

Eindimensionale (1D) Metalloxid Nanostrukturen wie z. B. Drähte (wires), Stäbe (rods), Bänder (belts) und Röhren (tubes) sind Inhalt intensiver Forschung, um deren diverse Struktur-Eigenschafts Beziehungen, insbesondere in Bezug auf deren reduzierte Dimensionalität, aufzuklären, und die Möglichkeiten einer potentiellen wissenschaftlichen bzw. technologischen Anwendung auszuloten. Hierbei bietet die Methode der chemischen Gasphasenabscheidung (engl. Chemical Vapor Deposition, CVD) durch den so genannten VLS-Mechanismus (engl. Vapor-Liquid-Solid) einen guten Zugang zu 1D Metalloxid-Nanostrukturen durch die Zersetzung von molekularen Vorstufen in einem CVD-VLS Prozess. Die vorliegende Arbeit behandelt die Synthese von Metalloxid-Nanodrähten im CVD-Prozess, sowie die Optimierung der Reaktionsparameter, um ein gerichtetes Wachstum der Nanostrukturen auf Substraten zu ermöglichen, und studien von physikalischen Eigenschaften für die Anwendung im Bauteilen.

(1) Gezielte Synthese, Wachstumsmechanismus und Plasmabehandlung von  $\text{SnO}_2$  Nanodrähten.

Einheitliche einkristalline  $\text{SnO}_2$  Nanodrähte konnten nach einer Optimierung der Substrattemperatur, Precursortemperatur, Größe der Katalysatorpartikel, sowie Winkel des Substrathalters erhalten werden. Darüber hinaus lieferten elektrische Messungen, Photolumineszenz Spektroskopie, Gas-Sensor Untersuchungen Studien ein tieferes Verständnis der physikalischen Eigenschaften von  $\text{SnO}_2$  Nanodrähten.

Diese Arbeit beschreibt zum ersten Mal das gerichtete Wachstum von  $\text{SnO}_2$  Nanodrähten auf  $\text{TiO}_2(001)$  Substraten mit der molekülbasierten CVD-Methode. Darauf aufbauend konnte ein Wachstumsmodell der Nanodrähte vorgeschlagen werden, welche auf der Interaktion der verschiedenen kristallographischen Ebenen (Substrat/Nanodraht) beruht.

Sowohl elektrische, als auch Gas-Sensor-Messungen an einzelnen SnO<sub>2</sub>[101] Nanodrähten zeigten, dass ausgerichtete Nanodrähte abhängig vom jeweiligen Durchmesser und ihrer Ausrichtung unterschiedlich auf Gasmoleküle reagieren, was für zukünftige Gassensoren genutzt werden könnte.

Die Oberflächenmodifikation von SnO<sub>2</sub> Nanodrähten in einem Argon-Sauerstoff (Ar/O<sub>2</sub>) Plasma führte zu einer Verringerung der Sauerstoffkonzentration in der Oberfläche der Nanodrähte, worauf sich eine nicht-stöchiometrisch zusammengesetzte Schicht ausbildete, welche wiederum zu einer höheren Empfindlichkeit und besseren Dynamik, bei gleichzeitig geringeren Temperaturen, gegenüber Ethanol in Gas-Sensor-Messungen führte.

(2) Neuartige SnO<sub>2</sub> Heterostrukturen: Synthese und Eigenschaften Neue Heterostrukturen (wie z. B. SnO<sub>2</sub>@TiO<sub>2</sub>, SnO<sub>2</sub>@SnO<sub>2</sub>, SnO<sub>2</sub>@VO<sub>x</sub> und SnO<sub>2</sub>@CdS) wurden durch chemische Oberflächenmodifikation von SnO<sub>2</sub> Nanodrähten in einem zweistufigen CVD-Prozess hergestellt.

Eine strukturelle Charakterisierung von SnO<sub>2</sub>/TiO<sub>2</sub> Kern-Schale Strukturen zeigte, dass sich Mischphasen abhängig von der Sinter Temperatur mit der Zusammensetzung Sn<sub>x</sub>Ti<sub>1-x</sub>O<sub>2</sub> (x = 0.857 ~ 1.0) ausbilden. Die hervorragenden elektrischen Eigenschaften von SnO<sub>2</sub>/TiO<sub>2</sub> Kern-Schale-Strukturen ermöglichen den Einsatz solcher Strukturen in Nanodraht Gassensoren.

SnO<sub>2</sub>@SnO<sub>2</sub> Heterostrukturen weisen mit einem Kontaktwinkel (KW) von 133° superhydrophobe Eigenschaften auf, während einfache SnO<sub>2</sub> Nanodrähte mit einem Kontaktwinkel von 3° superhydrophile Oberflächen ausbilden. Eine schaltbare Oberflächenbenetzbarkeit von SiO<sub>x</sub> beschichteten SnO<sub>2</sub>@SnO<sub>2</sub> Heterostrukturen (KW = 155.8°) wurde bei einem Wechsel von UV-Bestrahlung zu Dunkelheit und O<sub>2</sub> Behandlung beobachtet.

Die geometrische Mikrostruktur der Nanodrähte war hierbei der Hauptgrund in der schaltbaren Benetzbarkeit von superhydrophil zu

superhydrophober Oberfläche.

SnO<sub>2</sub>@CdS Heterostrukturen wurden durch eine Infiltrationsbeschichtung (engl. chemical bath deposition, CBD) mit dem Hydroxidcluster Wachstumsmechanismus hergestellt, und zeigten eine deutliche Verbesserung der Photoleitfähigkeit im Vergleich zu nicht beschichteten SnO<sub>2</sub> Nanodrähten im Wellenlängenbereich kleiner 450 nm.

Die hier vorgestellte Arbeit wurde durch das Bundesministerium für Bildung und Forschung (BMBF) im Rahmen des Förderprogrammes "BMBF-NanoFutur" finanziert (FKZ 03X5512).

# Abbreviations and Symbols

1D	One-dimensional
AFM	Atomic force microscopy
CA	Contact angle
CB	Conduction band
CBD	Chemical bath deposition
CVD	Chemical vapor deposition
EDX	Energy dispersive X-Ray spectroscopy
FET	Field effect transistor
FFT	Fast fourier transform
FIB	Focused ion beam
HR-TEM	High resolution transmission electron microscopy
MB-CVD	Molecule-based chemical vapor deposition
NW	Nanowire
PECVD	Plasma enhanced chemical vapor deposition
PL	Photoluminescence
ppm	Parts per million
PVD	Physical vapor deposition
QDs	Quantum dots
sccm	Standard-state cubic centimeter per minute
SEM	Scanning electron microscopy
SLS	Solution-liquid-solid
UV	Ultraviolet rays
VB	Valence band
VLS	Vapor-liquid-solid
VS	Vapor-solid
XRD	X-ray diffraction
XPS	X-ray photoelectron spectroscopy



# Table of Contents

<b>Acknowledgements .....</b>	<b>I</b>
<b>Abstract .....</b>	<b>III</b>
<b>Zusammenfassung .....</b>	<b>V</b>
<b>Abbreviations and Symbols.....</b>	<b>VIII</b>
<b>Table of Contents.....</b>	<b>IX</b>
<b>1 Introduction .....</b>	<b>1</b>
1.1 Metal oxide nanowires: challenges and issues .....	1
1.2 Research objectives.....	2
1.3 Organization of thesis .....	4
<b>2 State-of-the-Art of 1D Nanosynthesis .....</b>	<b>5</b>
2.1 Synthesis of one-dimensional nanostructures .....	8
2.1.1 Top-down synthesis .....	16
2.1.1 Bottom-up synthesis.....	17
2.2 Growth mechanism of one-dimensional nanostructures .....	19
2.2.1 Vapor phase growth .....	19
2.2.1.1 Vapor-liquid-solid mechanism.....	20
2.2.1.2 Vapor-solid mechanism .....	24
2.2.2 Solution phase growth.....	25
2.2.2.1 Template-assisted growth.....	27
2.2.2.1 Template-free growth.....	29

2.3	Synthesis of one-dimensional heterostructures .....	32
2.3.1	Branched heterostructures .....	34
2.3.2	Core-shell structures .....	34
2.3.3	Nanojunction .....	35
2.4	Synthesis of one-dimensional metal oxide nanostructures by CVD .....	37
2.5	Properties and applications of one-dimensional metal oxide nanostructures.....	43
2.5.1	Electron transport properties .....	43
2.5.2	Optical properties .....	46
2.5.3	Photoconductivity switching properties.....	47
2.5.4	Field-effect transistor properties .....	48
2.5.5	Gas sensing properties .....	49
<b>3</b>	<b>Experimental Procedure .....</b>	<b>53</b>
3.1	Synthesis procedure .....	53
3.1.1	Chemical synthesis of precursors.....	53
3.1.1.1	Sn(O <sup>t</sup> Bu) <sub>4</sub> .....	53
3.1.1.2	VO(O <sup>i</sup> Pr) <sub>3</sub> .....	54
3.1.1.3	Ti(O <sup>i</sup> Pr) <sub>4</sub> .....	54
3.1.2	Synthesis of one-dimensional nanostructures by molecule-based CVD.....	54
3.1.2.1	Synthesis of nanowires.....	55
3.1.2.2	Synthesis of heterostructures .....	56
3.1.3	Synthesis of nanofilms and surface modification by PECVD...	57
3.1.4	Synthesis of SnO <sub>2</sub> @CdS QDs heterostructures.....	59

3.2	Characterization techniques .....	60
3.2.1	Structural analysis .....	60
3.2.1.1	X-ray diffraction .....	60
3.2.1.2	Scanning electron microscopy.....	61
3.2.1.3	Transmission electron microscopy .....	63
3.2.1.4	Focused ion beam tomography .....	64
3.2.1.5	Energy-dispersive X-ray spectroscopy .....	65
3.2.1.6	Atomic force microscopy .....	65
3.2.1.7	X-ray photoelectron spectroscopy .....	66
3.2.2	Fluid simulation of CVD process .....	67
3.2.3	Physical properties .....	67
3.2.3.1	Photoluminescence .....	67
3.2.3.2	Gas sensing .....	69
3.2.3.3	Electrical transport.....	70
3.2.3.4	Surface wettability .....	71
3.2.3.5	Field-effect transistor .....	71
3.2.3.6	Photoconductivity .....	72
<b>4</b>	<b>Systematic Study on Growth of SnO<sub>2</sub> Nanowires.....</b>	<b>73</b>
4.1	Introduction of tin oxide nanowires.....	73
4.2	Controlled synthesis of SnO <sub>2</sub> nanowires .....	74
4.2.1	Influence of deposition temperature .....	76
4.2.2	Influence of precursor temperature .....	77
4.2.3	Influence of size of catalyst .....	79
4.2.4	Influence of angle of graphite susceptor.....	81

4.3	Characterization of SnO <sub>2</sub> nanowires .....	85
4.4	Properties of SnO <sub>2</sub> nanowires.....	87
<b>5</b>	<b>Orientated Growth of SnO<sub>2</sub> Nanowire Arrays on TiO<sub>2</sub> Single Crystals .....</b>	<b>95</b>
5.1	Growth patterns of SnO <sub>2</sub> nanowire arrays on TiO <sub>2</sub> single crystals ..	95
5.1.1	Introduction of nanowire arrays .....	95
5.1.2	Structural study of SnO <sub>2</sub> nanowire arrays .....	96
5.1.3	Growth mechanism of SnO <sub>2</sub> nanowire arrays .....	101
5.1.4	Properties of single SnO <sub>2</sub> nanowire.....	106
5.2	FIB-Tomographic studies of SnO <sub>2</sub> nanowire arrays on TiO <sub>2</sub> single crystals .....	110
<b>6</b>	<b>Plasma-Modified SnO<sub>2</sub> Nanowires for Enhanced Gas Sensing .....</b>	<b>117</b>
6.1	Introduction of plasma-assisted modification .....	117
6.2	Characterization of plasma-treated SnO <sub>2</sub> nanowires .....	118
6.3	Gas sensing properties of plasma-treated SnO <sub>2</sub> nanowires.....	125
<b>7</b>	<b>Synthesis and Application of SnO<sub>2</sub> Nanowire Based Heterostructures.....</b>	<b>129</b>
7.1	SnO <sub>2</sub> @TiO <sub>2</sub> : Oxide-oxide anisotropic core-shell structures .....	129
7.1.1	Introduction of core-shell structures .....	129
7.1.2	Characterization of SnO <sub>2</sub> @TiO <sub>2</sub> core-shell structures .....	131
7.1.3	Properties of SnO <sub>2</sub> @TiO <sub>2</sub> core-shell structures.....	140
7.2	Switchable wettability in SnO <sub>2</sub> nanowires and SnO <sub>2</sub> @SnO <sub>2</sub> heterostructures .....	143

7.2.1	Introduction of surface wettability .....	143
7.2.2	Characterization of SnO <sub>2</sub> nanowires and SnO <sub>2</sub> @SnO <sub>2</sub> heterostructures.....	144
7.2.3	Surface wettability study of SnO <sub>2</sub> nanowires and SnO <sub>2</sub> @SnO <sub>2</sub> heterostructures .....	146
7.3	Fabrication and photoconductivity of SnO <sub>2</sub> @CdS QDs heterostructures .....	155
7.3.1	Introduction of quantum dots based photovoltaics .....	155
7.3.2	Characterization of SnO <sub>2</sub> @CdS QDs heterostructures .....	156
7.3.3	Photoconductivity property of SnO <sub>2</sub> @CdS QDs heterostructures.....	160
<b>8</b>	<b>Conclusions and Outlook.....</b>	<b>165</b>
8.1	Conclusions .....	165
8.2	Outlook .....	170
<b>9</b>	<b>References.....</b>	<b>173</b>
<b>10</b>	<b>Appendix.....</b>	<b>197</b>
10.1	List of tables.....	197
10.2	List of figures.....	198
	<b>Ehrenwörtliche Erklärung .....</b>	<b>205</b>
	<b>Curriculum Vitae .....</b>	<b>207</b>

# 1 Introduction

One-dimensional metal oxide nanostructures are emerging among the most promising family of materials to impact future electronics owing to anisotropy of functional properties and quantum confinement, which has enabled predictable variation of structure and composition on multiple length scales. Moreover, 1D metal oxide nanostructures offer probing of functional properties in individual nanostructure, due to their macroscopic features along the growth direction. In addition to new synthetic approaches to fabricate anisotropic nanostructures, currently efforts are dedicated to establish strategies for their controlled growth on pre-selected sites and the modification of the host-material to create radial (core-shell) or axial (branched) heterostructures.<sup>[1]</sup>

## 1.1 Metal oxide nanowires: challenges and issues

The overall goal of this work was to develop new design strategies and methodologies for the fabrication and characterization of novel nanostructured materials for chemical sensing and energy applications. The vast majority of literature reports, number of significant achievements in the field of 1D nanostructures and on-going research efforts by many groups across the whole world illustrate not only the technical potential of nanowires but also reveal the technical limitations and fundamental challenges associated with the science and technology of 1D nanostructures. Some of the major challenges include:

- (1) Large-scale controllable growth of 1D nanostructures with high reproducibility.
- (2) Universal understanding the growth mechanism of 1D nanostructures.

- (3) Unique functional properties of 1D nanostructures and role of reduced dimensionality.
- (4) Potential device applications of 1D nanostructures.
- (5) Synthesis - structure - functionality relationships need further investigation to improve current understanding.

## 1.2 Research objectives

The research objectives in this work were desired from the current needs of the one dimensional technology especially to demonstrate novel growth concepts, post-growth manipulation, modification of 1D nanostructures and their integration into device structures. The technical objectives included:

- (1) Demonstration of large-scale and controllable synthesis of 1D tin oxide nanostructures.

Tin oxide ( $\text{SnO}_2$ ), as a wide-band semiconductor material ( $E_g = 3.6$  eV at 300 K), was selected due to its interesting physical properties and applications in the field of electronic, optoelectronic devices as well as in conductometric nanosensors.

For the synthesis of  $\text{SnO}_2$ , a molecule-based chemical vapor deposition (MB-CVD) technique, based on catalyst-assisted decomposition of the  $\text{Sn}(\text{O}^t\text{Bu})_4$  precursor, was employed to synthesize 1D tin oxide nanostructures under controlled chemical composition, size, morphology and surface state expected from some distinctive advantages, such as: (i) synthesis of single crystal nanowires with low defect densities of molecule-based approach; (ii) area specific deposition and controlled crystal growth; (iii) textured crystal growth and (iv) low synthesis temperature.

The strategy utilized in this thesis was to understand the growth conditions of CVD process to find out the correlation between optimized growth conditions and nanowire growth.

(2) Understanding the growth mechanism of MB-CVD grown tin oxide nanowire arrays in order to achieve perpendicularly (to substrate) oriented nanowires.

The proposed concept involved hetero-epitaxy of tin oxide nanowires on crystallographically similar titanium oxide single crystals. Tin oxide nanowire arrays grown on TiO<sub>2</sub> single crystals will be characterized by various techniques (XRD, SEM, HR-TEM, FIB-Tomography, AFM and cross sectional TEM) to (i) evaluate the influence of substrate on morphology and (ii) correlate growth direction - surface energy consideration - crystallographic relationship between the substrate and NW material.

(3) Surface modification of tin oxide nanowires by post-growth treatments (e.g. plasma-assisted surface etching) and by growing a second phase on the nanowires to create heterostructures.

The surface modification (to be monitored by surface sensitive probes like X-ray photoelectron spectroscopy, photoluminescence, etc.) can change the electrical properties (e.g. band gap) of the host material and enhanced the functional behaviour (e.g. gas sensing response). Heterostructures offer exciting opportunities to achieve functionalities that are not accessible in single-phase materials, due to the combination of material classes such as metal oxides and semiconductors, which represent another approach for enhancing performance (e.g. electrical transport, gas sensing response, photoconductivity, etc.) and/or enabling new function (e.g. surface wettability).

(4) Elucidating the influence of precursor chemistry and processing method on the functional behavior of the 1D semiconductor nanomaterials.

For obtaining a deeper insight into the transformation of chemical precursors into materials, a molecule-based CVD approach was adopted in this work, which ensured high reproducibility of the material synthesis.



### 1.3 Organization of thesis

This thesis is organized in the following manner. Chapter 2 provides an introduction of research focus and an overview of the current activities by covering different methods to synthesize nanowires and current state of the research on the physical properties. Chapter 3 presents the general experimental methodology applied to synthesize and characterize 1D nanostructures. Chapter 4 contains the details of process parameters and results relevant to the fabrication of 1D nanostructures, and discuss the factors responsible to control the growth behaviors. Chapter 5 based on the results obtained on the structural and compositional of oriented SnO<sub>2</sub> NWs, describes a study of CVD-VLS growth mechanism, and introduces a novel technology. The physical and chemical surface modification studies are presented in Chapter 6 and 7 respectively. The property study of the new morphological nanostructures leads to the promising potential applications. Finally, Chapter 8 is the summary of the thesis work.

## 2 State-of-the-Art of 1D Nanosynthesis

The field of nanomaterials engineering represents an exciting and rapidly expanding research area that crosses the borders among the physical, life, and engineering sciences.<sup>[2]</sup> Most of the excitement in this area of research has arisen from the recognition that fundamentally new material properties and synthesis of multifunctional materials are possible (e.g. ceramic polymer nanocomposites) with structures designed at the nanometer-scale. The research activities represented in this domain are diverse, ranging from extensions of conventional device physics to completely new approaches based upon molecular self-assembly, from developing new materials with dimensions on the nanoscale to investigating whether we can directly control matter on the atomic scale. The interest in nanotechnology is also driven by the fact that the physical and chemical properties of synthetic materials can significantly improve or radically change as their size is reduced to the nanometer regime. More importantly, it is now becoming increasingly well realized that the emerging concepts and applications of nanotechnology are not only limited to the physical science and, indeed, can be applied to the fields of life science, medicine, nanodevices and energy production.<sup>[3-4]</sup>

Nanostructures can be defined as systems in which at least one of the dimensions is less than 100 nm; that is, reducing dimensions of a bulk material to the nanometer scale produces nanometer thick layers (2D), nanowires/nanotubes (1D), or nanoparticles/nanoclusters (0D). Nanoscaled one-dimensional (1D) structures such as nanotubes (NTs), nanowires (NWs), nanorods and nanobelts (NBs) have become interesting research objects from the standpoints of both basic scientific research and due to their unique electrical, thermal, mechanical and optical properties that vary from their

respective bulk counterparts. From a fundamental approach, nanowires allow to evaluate the role that dimensionality plays in governing the properties of the materials, for instance due to the different interaction of charge carriers in three, two- and one-dimensional structures. For example, every material has a definite conductivity, so that the conductance of a wire is inversely proportional to the length ( $L$ ) of the wire. On the other hand, as the length scale of the wire is reduced to the mean free path of electrons, the electron transport mechanism changes from diffusive to ballistic, as shown in Figure 1. When the width ( $W$ ) of the wire is further reduced to the nanometer or Fermi wavelength scale, the conductance between electrodes connected by the nanowire is quantized in steps of  $2e^2/h$ . Moreover, the conductance is no longer dependent on the length of the wire.

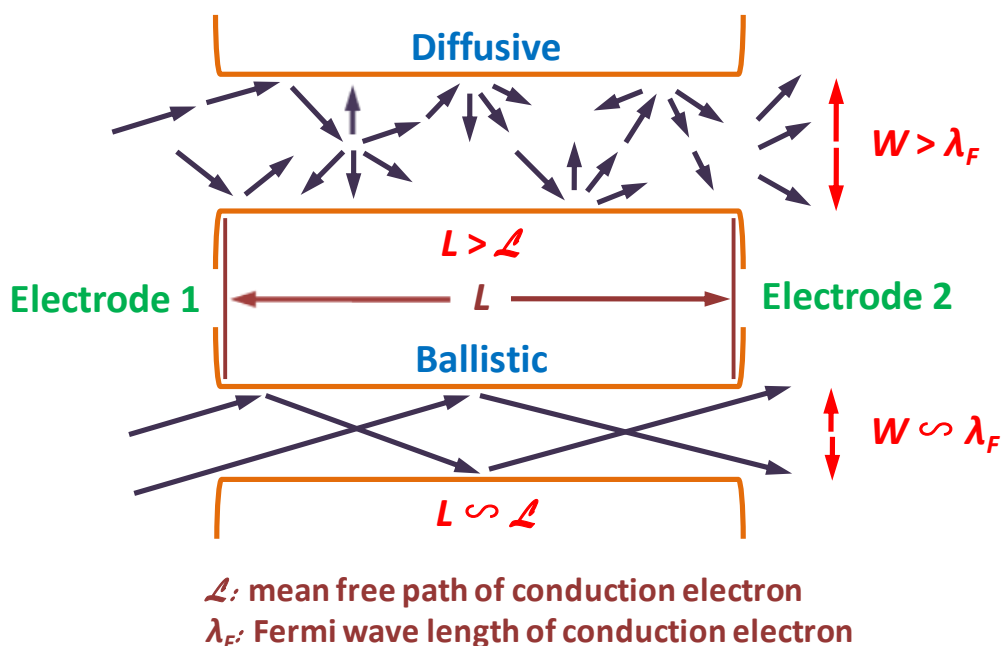


**Figure 1:** Diffusive and ballistic transport of electrons in one-dimensional wires.

The potential application of one-dimensional nanostructures has been demonstrated in various research fields such as medical sensing,<sup>[5]</sup> drug delivery,<sup>[6]</sup> microelectronics,<sup>[7]</sup> bioMEMS,<sup>[8]</sup> electrical communications,<sup>[9]</sup> energy storage<sup>[10]</sup> and computation technology.<sup>[11]</sup>

With increasing significance of nanostructure-based devices, the role of one dimensional nanomaterials is gaining importance too especially due to their potential as device components and interconnects in nano-circuitry. Nevertheless, the science and technology of 1D nanostructures suffers due to the lack of universal synthesis concepts.<sup>[12]</sup> Most of the reported procedures are either specific to a particular class of materials or they do not allow on easy scale-up in terms of the quantity of the materials. In addition, the experimental concepts for the post-synthesis modification and positional manipulation are less investigated. The later aspect being of enormous importance became for the integration of 1D nanostructures into devices, their removal from the original substrate is mandatory.

## 2.1 Synthesis of one-dimensional nanostructures

One class of nanoscale materials which has attracted tremendous attention is the one-dimensional system since the revolutionary discovery of carbon nanotubes in 1991.<sup>[3]</sup> Enormous progress has been achieved in the synthesis, characterization, and device application of the 1D nanostructures. These structures with high aspect ratio (i.e., size confinement in two coordinates) offer better crystallinity, higher integration density, and lower power consumption. Due to a large surface-to-volume ratio and a small size comparable to the Debye length, they demonstrate superior sensitivity to surface chemical processes. In addition, their size confinement renders tunable band gap, higher optical gain and faster operation speed. A variety of inorganic nanomaterials, including single element and compound semiconductors, have been successfully synthesized in last 15 years.<sup>[13]</sup> Due to their in-depth physical property characterizations, they have demonstrated to be promising candidates for future nanoscale electronic, optoelectronic and sensing device applications.

The performance or property of a material primarily depends on the efficiency and precise nature of the synthesis and fabrication methods. When developing a new synthesis and fabrication method for generating 1D nanostructures, the most important issue that one needs to address is the simultaneous control over dimensions, morphology, phase purity and chemical composition.

In the past several years, researchers have studied numerous methods to synthesize the 1D nanostructures, such as laser ablation,<sup>[14]</sup> vapor transport,<sup>[15]</sup> solvothermal,<sup>[16]</sup> Coulomb blockade (or single-electron tunneling),<sup>[17]</sup> template-assisted electrochemical synthesis<sup>[18]</sup> and chemical vapor deposition (CVD) methods,<sup>[19-20]</sup> were described in details (Table 1). These synthetic methods

for growing 1D nanostructures have made a significant progress, enabling the production of various 1D nanostructures with controlled size, morphology, chemical composition and single crystalline quality.<sup>[21-22]</sup>

**Table 1:** Summary of 1D nanostructures synthesized using different methods.

Material	Morphology	Growth Method	Applications	Ref.	
Si	Nanowires	Metal-organic CVD	Transistor	[23]	
		Chemical beam epitaxy		[24]	
Ge	Nanowires	Metal-organic CVD	Photodetector	[25]	
		Pulsed laser deposition		[14]	
Bi	Nanowires	Electrochemical deposition	FET Device	[26]	
Ag	Nanowires	Electrochemical deposition	FET Device	[27]	
Au	Nanowires	Solution phase	Nanodevice	[28]	
Co	Nanowires	Pulsed electrodeposition	Nanodevice	[29]	
Se	Nanowires	Solution phase	Resistor	[30]	
Te	Nanowires	Vapor phase growth	Resistor	[31]	
Si-SiGe	Nanowires	Laser ablation	FET Device	[32]	
Si-Ge	Nanowires	Metal-organic CVD	FET Device	[33]	
Ge-Si	Nanowires	Metal-organic CVD	Transistor	[34]	
NiSi-Si	Nanowires	Solid phase reaction	Transistor	[35]	
ZnO	Nanowires	Vapor-solid transport	FET Device	[34]	
		Vapor-liquid-solid		[36]	
		Template-assisted growth		[37]	
		Microemulsion technique		Resistor	[38]
		Template-free solution method		Nanosensor	[39]
	Nanobelts	Vapor-solid transport	Photodetector	[40]	
		Vapor-liquid-solid		[41]	
Hydrothermal		[42]			

	Nanorods	Template-free aqueous growth		[43]
		Vapor-liquid-solid		[44]
		Vapor-solid transport		[45]
		Pulsed-laser ablation		[46]
	Nanotubes	Vapor-solid transport		[47]
		Vapor-liquid-solid		[48]
Solution synthesis		[49]		
In <sub>2</sub> O <sub>3</sub>	Nanowires	Catalyst-assisted laser ablation	FET Device Nanosensor	[50]
		Vapor-solid transport		[51]
		Vapor-liquid-solid		[52]
		Templated solution		[53]
	Nanobelts	Vapor-solid transport		[54]
	Nanotubes	Thermal evaporation		[50]
Solvothermal		[55]		
MgO	Nanowires	Vapor-solid transport	FET Device	[56]
		Vapor-liquid-solid		[57]
		Catalyst-assisted laser ablation		[58]
SnO <sub>2</sub>	Nanowires	Catalyst-assisted laser ablation	Resistor Nanosensor Photonic Device	[59]
		Vapor-solid transport		[60]
		Vapor-liquid-solid		[61]
		Solution synthesis		[62]
	Nanobelts	Thermal oxidation growth		[63]
		Vapor-solid transport		[64]
		Laser ablation		[65]
	Nanorods	Microemulsion synthesis		[66]
		Hydrothermal		[67]
Solution synthesis		[68]		

		Vapor-liquid-solid		[69]	
		Nanotubes		Template hydrothermal	[70]
				Aqueous phase synthesis	[71]
				Microemulsion synthesis	[72]
Ga <sub>2</sub> O <sub>3</sub>	Nanowires	Thermal evaporation	Resistor Photonic Device	[73]	
		Catalyst-assisted arc discharge		[74]	
		Laser ablation		[75]	
		Catalyst-assisted vapor transport		[75]	
	Nanobelts	Vapor-solid transport	[76]		
		Vapor-liquid-solid	[77]		
	Nanotubes	Vapor-solid transport	[78]		
V <sub>2</sub> O <sub>5</sub>	Nanowires	Hydrothermal	Resistor	[79]	
	Nanobelts	Vapor-solid transport		[80]	
TiO <sub>2</sub>	Nanotubes	Templated solution	Photonic Device	[81]	
		Solution synthesis		[82]	
	Nanowires	Hydrothermal		[83]	
		Vapor-solid transport		[84]	
WO <sub>3</sub>	Nanowires	SBA-15 templated solution	Resistor	[85]	
		Hydrothermal		[86]	
		Thermal evaporation		[87]	
	Nanobelts	Vapor-solid transport		[88]	
ZrO <sub>2</sub>	Nanowires	Templated solution	Photonic Device	[89]	
	Nanorods	Precursor thermal decomposition		[90]	
	Nanotubes	Templated solution		[91]	
Nb <sub>2</sub> O <sub>5</sub>	Nanobelts	Precursor thermal decomposition	FET device	[92]	
	Nanowires	Vapor-liquid-solid method		[93]	
	Nanotubes	Precursor thermal decomposition		[94]	



Fe <sub>3</sub> O <sub>4</sub>	Nanotubes	templated pulsed-laser deposition	Bi-device	[95]
	Nanowires	Hydrothermal	Resistor	[96]
IrO <sub>2</sub>	Nanotubes	Metal-organic CVD	Photonic	[97]
	Nanowires	Metal-organic CVD	Device	[98]
Ta <sub>2</sub> O <sub>5</sub>	Nanotubes	Precursor thermal decomposition	FET device	[94]
MoO <sub>3</sub>	Nanotubes	Hydrothermal	FET device Nanodevice	[99]
		Template-assisted synthesis		[100]
		Vapor-solid transport		[101]
	Nanowires	Thermal evaporation		[102]
		Solution synthesis		[103]
MnO <sub>2</sub>	Nanowires	Hydrothermal	FET device	[104]
		SBA-15 templated synthesis	Nanodevice	[105]
	Nanotubes	Hydrothermal		[106]
Fe <sub>2</sub> O <sub>3</sub>	Nanowires	Thermal oxidation	Nanosensor	[107]
		Hydrothermal	Resistor	[108]
	Nanobelts	Thermal oxidation	Nanodevice	[109]
NiO	Nanowires	Wet chemical route	Resistor	[110]
		AAO-templated sol-gel	Photonic	[111]
	Nanotubes	AAO-assisted solution	Device	[112]
Co <sub>3</sub> O <sub>4</sub>	Nanowires	Thermal oxidation	Resistor Nanodevice	[113]
		Hydrothermal		[114]
	Nanotubes	Template-assisted synthesis		[115]
		Solution synthesis		[116]
Cu <sub>2</sub> O	Nanowires	Solid-state reduction	Resistor	[117]
		Surfactant-assisted synthesis		[118]
		Hydrothermal		[119]
CuO	Nanowires	Thermal oxidation	Resistor	[120]

		Templated deposition	Nanodevice	[121]
		Solution synthesis		[122]
	Nanobelts	Solution synthesis		[122]
CdO	Nanowires	AAO-assisted deposition	Nanosensor	[123]
		Chemical bath deposition	Photonic	[124]
	Nanoneedles	Vapor-liquid-solid	Device	[125]
Al <sub>2</sub> O <sub>3</sub>	Nanotubes	Pulse anodization	Resistor Nanodevice	[126]
		Thermal evaporation		[127]
		Surfactant-assisted solution		[128]
		Template-assisted synthesis		[129]
	Nanowires	Vapor-solid transport		[130]
SiO <sub>2</sub>	Nanowires	Vapor-liquid-solid	Transistor	[131]
PbO <sub>2</sub>	Nanorods	Solid-state chemical synthesis	Nanodevice	[132]
CeO <sub>2</sub>	Nanorods	Surfactant-assisted synthesis	Transistor	[133]
	Nanotube	Ultrasonic-induced synthesis	Transistor	[134]
Eu <sub>2</sub> O <sub>3</sub>	Nanorods	Ultrasound irradiation synthesis	Transistor	[135]
LiV <sub>3</sub> O <sub>8</sub>	Nanorods	Hydrothermal	Resistor	[136]
MnV <sub>2</sub> O <sub>6</sub>	Nanorods	Hydrothermal	Resistor	[137]
ZnAl <sub>2</sub> O <sub>4</sub>	Nanorods	Polycarbonate membrane template	Resistor	[138]
BaTiO <sub>3</sub>	Nanowires	Hydrothermal	Nanodevice	[139]
CoFe <sub>2</sub> O <sub>4</sub>	Nanowires	Mild chemical synthesis	Nanodevice	[140]
MnFe <sub>2</sub> O <sub>4</sub>	Nanorods	Surfactant-free hydrothermal	Nanodevice	[141]
LiFePO <sub>4</sub>	Nanowires	SBA-15 templated synthesis	Batteries	[142]
ZnFe <sub>2</sub> O <sub>4</sub>	Nanorods	AAO-assisted deposition	Resistor	[143]
GaAs	Nanowires	Pulsed laser deposition	Resistor	[144]
		Chemical beam epitaxy	Photonic	[145]
		Vapor-liquid-solid	Device	[146]

GaP	Nanowires	Pulsed laser deposition	Resistor	[147]
Bi <sub>2</sub> S <sub>3</sub>	Nanorods	Assisted Hydrothermal	Nanodevice	[148]
InP	Nanowires	Pulsed laser deposition	FET Device	[145]
InAs	Nanowires	Chemical beam epitaxy	FET Device	[149]
		Vapor-liquid-solid		[147]
In <sub>2</sub> Se <sub>3</sub>	Nanowires	Vapor-liquid-solid	Nanodevice	[150]
GaN	Nanowires	Laser-assisted catalytic growth	Photonic Device	[144]
		Magnetron sputtering		[151]
CdSe	Nanowires	Pulsed laser deposition	Nanodevice	[144]
CdS	Nanowires	Laser-assisted catalytic growth	Nanodevice	[152]
Cd <sub>3</sub> P <sub>2</sub>	Nanowires	In-situ nanorod template synthesis	Nanodevice	[153]
Cd <sub>3</sub> As <sub>2</sub>	Nanowires	Thermal evaporation	Nanodevice	[154]
SiGe	Nanowires	Pulsed laser deposition	Transistor	[144]
SiC	Nanowires	Anodization and electrodeposition	Transistor	[155]
Si <sub>3</sub> N <sub>4</sub>	Nanowires	Anodization and electrodeposition	Transistor	[156]
TiSi <sub>2</sub>	Nanowires	Chemical vapor deposition	Nanosensor	[157]
ZnS	Nanowires	Vapor-liquid-solid	FET Device	[32]
ZnSe	Nanowires	Vapor-liquid-solid	FET Device	[158]
Zn <sub>3</sub> P <sub>2</sub>	Nanowires	Electrochemical deposition	FET Device	[159]
GaP-GaAs	Nanowires	Alternating laser ablation	Nanodevice	[146]
ZnSe-CdSe	Nanowires	Atomic layer deposition	Nanodevice	[160]
ZnO-ZnMgO	Nanowires	Metal-organic vapor phase epitaxy	Nanodevice	[161]
InAs-GaAs	Nanowires	Metal-organic vapor phase epitaxy	Photonic	[162]
InAs-InP	Nanowires	Metal-organic vapor phase epitaxy	Photonic	[163]
GaN-AlGaN	Nanowires	Preferential etching synthesis	Nanodevice	[164]
Ge-SiC <sub>x</sub> N <sub>y</sub>	Nanocable	Chemical vapor deposition	Nanodevice	[165]
SnO <sub>2</sub> -M <sub>2</sub> O <sub>3</sub>	Nanowires	Thermal evaporation method	Nanosensor	[166]

$\text{SnO}_2\text{-VO}_x$	Nanowires	Chemical vapor deposition	Nanosensor	[167]
$\text{SnO}_2\text{-Fe}_3\text{O}_4$	Nanowires	Chemical vapor deposition	Nanodevice	[168]

A nomenclature for these peculiar 1D nanostructures has not been well established. As a result, in the literatures a lot of names have been used to describe the morphological features, like whiskers, fibers, fibrils, nanotubules, nanocable, etc. A few classes of these new 1D nanostructures with potential in device application are schematically summarized in Figure 2.<sup>[169-170]</sup> The typical geometrical shapes observed in various syntheses are tubes, cylindrical wires, rods, cables, belts, assembly of spheres, sheets and even more complex morphologies.

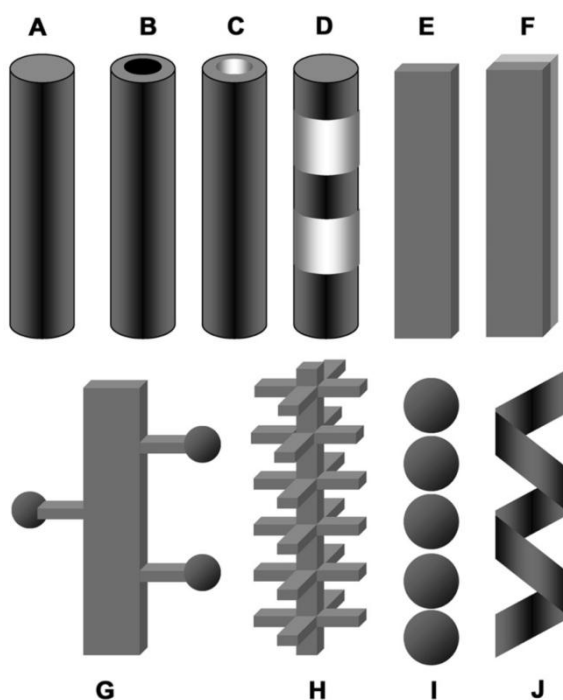
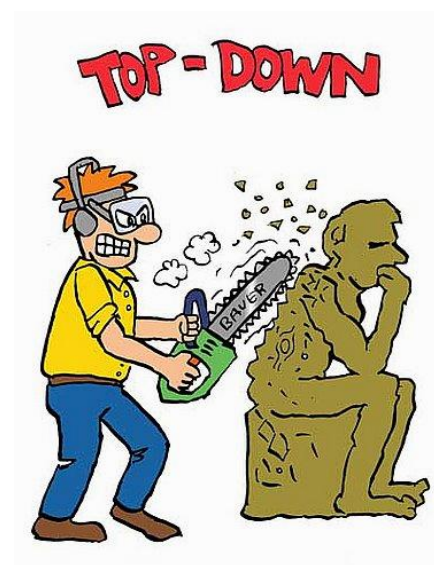


**Figure 2:** Schematic presentation of different types of one dimensional nanostructures. (A) Nanowires and nanorods; (B) core–shell structures with metallic core, semiconductor or metal-oxide shell; (C) nanotubes/nanopipes and hollow nanorods; (D) segmented heterostructures; (E) nanobelts/nanoribbons; (F) nanotapes; (G) dendrites; (H) hierarchical nanostructures; (I) nanosphere assembly; (J) nanosprings.<sup>[171]</sup>

The common materials synthesis procedures can generally be grouped in two different categories, the “**top-down**” approaches and the “**bottom-up**” approaches. In this section, these two approaches are briefly discussed with respect to the synthesis of 1D nanostructures.

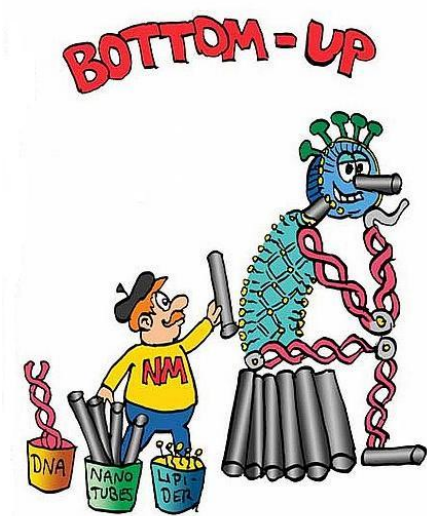
### 2.1.1 Top-down synthesis



The top-down approaches usually utilize planar, lithographic, etching, and deposition techniques to transfer a pre-designed pattern to a substrate which can form complex high density structures in well-defined positions on substrates and their integrated systems.<sup>[172-173]</sup>

The top-down approach has been exceedingly successful in extensive applications, with microelectronics being perhaps the best example today. They can produce 1D nanostructures with very uniform shapes and electronic properties. While developments continue to push the resolution limits of the top-down approach, these improvements in resolution are associated with a near-exponential increase in cost associated with each new level of manufacturing facility. However, as the microelectronic industry advances towards ever smaller devices, top-down approaches will soon reach their physical and economic limits, such as making 1D nanostructures with near-atomic perfection and incorporating materials with distinct chemical and functional properties, which motivates global efforts to search for new strategies to meet the expected demand for increased computational power as well as for integrating low-cost and flexible handling in unconventional environments in the future.<sup>[174-175]</sup>

## 2.1.2 Bottom-up synthesis



The bottom-up approach, in which functional structures are assembled from well-defined chemically and/or physically synthesized nanoscale building blocks, much like the way nature uses proteins and other macromolecules to construct complex biological systems, represents a powerful alternative approach to conventional top-down methods.<sup>[176]</sup> The bottom-up approach has the

potential to go far beyond the limits and functionality of top-down technology by defining key nanometer-scale metrics through synthesis and subsequent assembly. Moreover, it is highly likely that the bottom-up approach will enable entirely new device concepts and functional systems and thereby create technologies that we have not yet imagined. For example, it is possible to seamlessly combine chemically distinct nanoscale building blocks that could not be integrated together in top-down processing and thus obtain unique function and/or combinations of function in an integrated nanosystem.

To enable this bottom-up approach for nanotechnology requires a focus on three key areas that are at the heart of devices and integration. First, the bottom-up approach necessitates nanostructured building blocks with precisely controlled and tunable chemical composition, structure, size, and morphology, since these characteristics determine their corresponding physical properties. Meeting this goal demands methods that enable rational design and predictable synthesis of building blocks. Secondly, it is critical to develop and explore the limits of functional devices based on these building blocks. 1D nanostructures may behave in ways similar to current electronic and optoelectronic devices, although it is also expected that new and

potentially revolutionary concepts will emerge from these building blocks, for example, due to quantum properties. Third and central to the bottom-up concept will be the development of architectures that enable high-density integration with predictable function, and the development of hierarchical assembly methods that can organize building blocks into these architectures.<sup>[176]</sup>

In addition to the traditional methods discussed above, several other potentially useful approaches have also been demonstrated as alternative routes to the fabrication of 1D nanostructures, such as self-assembly of nanoparticles,<sup>[177]</sup> DNA based templating,<sup>[178]</sup> carbon nanotube and carbon nanofibre based templating,<sup>[179]</sup> and virus based templating.<sup>[180]</sup> But most of these techniques are still developmental stage, and many issues remained to be addressed before they can be used for large scale growth of 1D nanostructures.

## 2.2 Growth mechanism of one-dimensional nanostructures

In the past years the number of synthesis techniques has grown exponentially. Growth mechanisms can be divided into different categories, such as **catalyst-free** and **catalyst assisted** procedures and then are can distinguished between vapor and solution phase growth. As far as semiconductors (Si, Ge, Si-Ge, etc.) and metal oxides (ZnO, TiO<sub>2</sub>, SnO<sub>2</sub>, etc.) are concerned the most used procedure vapor phase synthesis, however solution phase growth techniques provide more flexible processing with lower production costs. There are different growth mechanisms depending on the presence of a catalyst, i.e. vapor-liquid-solid (VLS), solution-liquid-solid (SLS) or vapor-solid (VS) process.<sup>[181]</sup>

### 2.2.1 Vapor phase growth

The simplest vapor phase approach can be described as a reactive chemical transport. For instance, the reaction between metal vapor source and oxygen gas, which was used in the early 60's for the preparation of micrometer-size whiskers. These whiskers were prepared either by simple physical sublimation of the source material or through reduction of a volatile metal halide. In the last years this method had been used to prepare different materials in form of 1D metal oxide nanostructures. The growth is generally performed in a tubular furnace to obtain a proper temperature gradient. The source material once evaporated is transported by a gas carrier towards the growth site where it nucleates. The nucleation can start from particle (of the target material) or catalyst, following the vapor-solid (VS), vapor-liquid-solid (VLS) conversion mechanisms.



### 2.2.1.1 Vapor-liquid-solid mechanism

VLS mechanism was first proposed by Wagner and Ellis in 1964.<sup>[23]</sup> They found that Si whiskers could be grown by heating a Si substrate covered with Au particles in a mixture of  $\text{SiCl}_4$  and  $\text{H}_2$  and their diameters were determined by the size of Au particles. They proposed a vapor-liquid-solid (VLS) mechanism involving three phases: the vapor phase precursor, the liquid catalyst droplet, and the solid crystalline product; and three growth regimes in which: (i) a nanoscaled metallic particle forms an eutectic alloy (liquid) with the wire material (supplied as vapor); (ii) the vapor of the source material is further absorbed by the liquid catalyst till supersaturation occurs; and (iii) the vapor atoms diffuse and condense at the liquid/solid interface which will be pushed forward to form a nanowire.<sup>[182]</sup>

During this growth process, the metal nanoparticles are heated above the eutectic temperature for the metal-semiconductor system in the presence of a vapor-phase source of the semiconductor, resulting in a liquid droplet of the metal/semiconductor composite. The semiconductor source, which is delivered by the fragment of molecular precursor, feeds the liquid droplet continuously to supersaturate the eutectic through the vapor-liquid (V-L) interface. It leads to nucleation (crystallization) of the solid semiconductor NWs. The liquid-solid (L-S) interface, which forms the growth interface and acts as a sink causing the continued semiconductor incorporation into the lattice and, thereby, the growth of the nanowires with the alloy droplets is riding on the top. The crystallographic orientation of nucleated solid on the liquid/solid interface is dictated by the surface energy considerations, whereby facets with lowest surface energies show preferential growth. The formation of catalyst/nanowire interface is rather complex and depends on growth condition and nature of materials. Continuous vapor delivery provides the driving force for diffusion of the semiconductor from the liquid-catalyst particle surface to the growth

interface. In principle, vapor-liquid-solid growth technique is a simple process in which condensed or powder source material is vaporized at elevating temperature and then the resultant vapor phase condenses at certain conditions (temperature, pressure, atmosphere, substrate, etc.) to form the expected 1D product. The chemical and physical properties of sources and substrates can influence the growth behavior of 1D nanostructures via the interaction with V-L and L-S growth fronts (Figure 3). Generally, one dimensional nanostructure growth is induced by the dissolution of gaseous reactants into liquid droplets of a catalyst material, followed by nucleation and growth of single crystalline nanostructures.

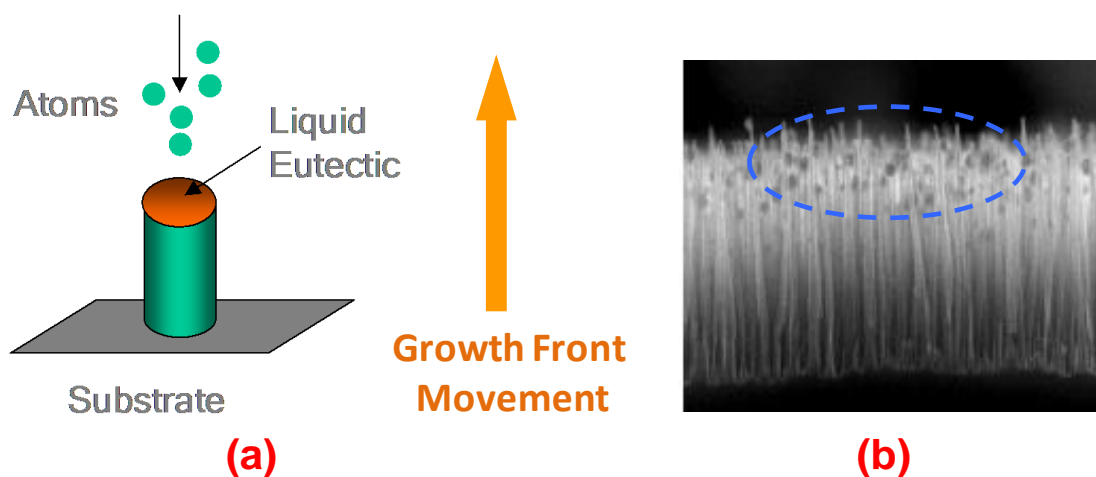


**Figure 3:** (a) Schematic presentation of VLS growth mechanism, and (b) SEM image of Si whiskers synthesized by VLS growth mechanism.

The primary steps in a typical VLS growth process (metal alloying, crystal nucleation and axial growth) are shown schematically (Figure 4(a)) for the case of nanowire growth from Au clusters. For example, high-yield synthesis of germanium nanowires is achieved by the chemical vapor deposition (CVD) of dicyclopentadienyl germanium ( $[\text{Ge}(\text{C}_5\text{H}_5)_2]$ ), as shown in Figure 4(b). The wire growth is selective and Au catalyst particles are observed at the tip of the NWs, which confirmed that the characteristic feature of a 1D growth based on

the VLS mechanism.<sup>[183]</sup>

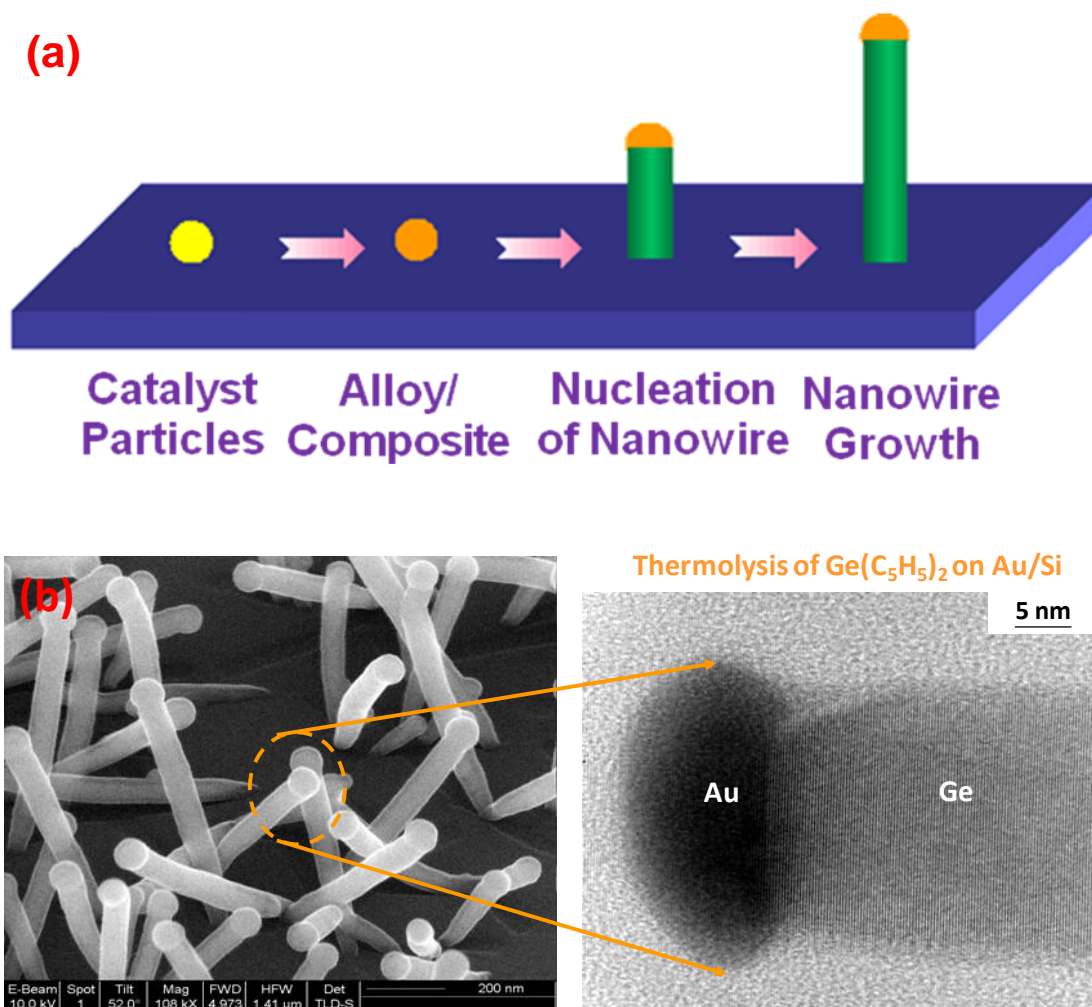


**Figure 4:** (a) The controlled growth of 1D nanostructures by VLS mechanism, and (b) SEM and TEM images of Ge nanowires grown on Si substrate.

In essence, VLS growth is a catalyst-assisted growth process which uses metal nanoclusters or nanoparticles as the nucleation seeds. These nucleation seeds determine the interfacial energy, growth direction and diameter of 1D nanostructures. Therefore, proper choice of catalyst is critical. In the case of growing 1D metal oxide nanostructures, VLS process is initiated by the formation of liquid alloy droplet which contains both catalyst and source metal. Precipitation occurs when the liquid droplet becomes supersaturated with the source metal. Normally the resulting crystal is grown along one particular

crystallographic orientation which corresponds to the minimum atomic stacking energy, leading to 1D nanostructures formation. This type of growth is epitaxial, thus it results in high crystalline quality.

In order to fabricate long and uniform-diameter nanowires, introduction of surface-active species has been suggested.<sup>[184]</sup> For instance, oxygen residues present during the growth may affect the growth of nanowires: (i) the adsorbed oxygen is sufficiently mobile on the substrate surface and thus inhibits the diffusion of Au on the surface. (ii) Au agglomeration kinetics may be modified and suppressed by oxygen. The measured growth rates for nanowires and sidewalls showed the later growth rate to be  $\sim 100$  times slower than the growth rate in axial direction.

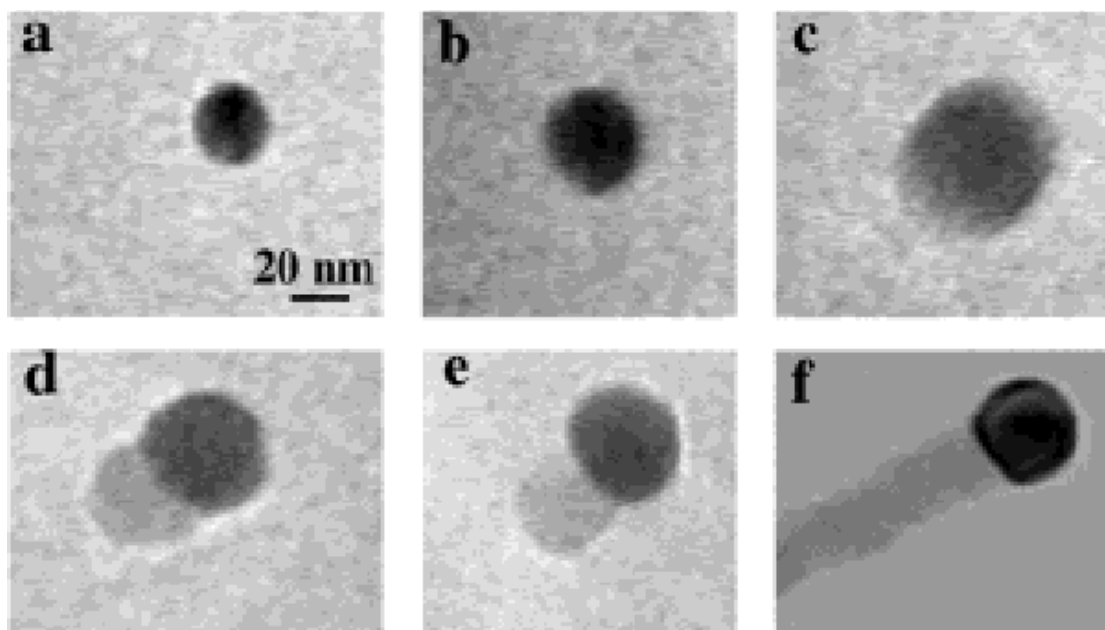


**Figure 5:** In-situ TEM images recorded during the growth process of Ge nanowire. (a) Au nanoclusters in solid state at 500 °C; (b) alloying initiates at 800 °C, at this stage Au exists in mostly solid state; (c) liquid Au/Ge alloy; (d) the nucleation of Ge nanocrystal on the alloy surface; (e) Ge nanocrystal elongates with further Ge condensation and eventually forming a nanowire.

Wu and co-workers have provided direct evidence of VLS growth by means of real time in situ transmission electron microscope observations, which unambiguously demonstrated the validity of the catalyst-assisted growth mechanism at nanometer scale. The growth stages postulated for VLS mechanism namely, metal alloying (Figure 5(b, c)), crystal nucleation (Figure 5(d, e)), and axial growth (Figure 5(f)) were evidently observed in this experiment. In-situ observation of wire nucleation/growth at nanometer scale also showed that the diameter of Ge nanowire is dependent on the size of Ge/Au alloy droplet instead of the size of Au particles used as growth seeds.<sup>[185]</sup> This work depicts a vivid dynamic insight and elucidates the understanding of such microscopic chemical process. It is important to have a greater control in the nanowires shape, diameter and for a selective growth.

VLS growth mechanism in the last decades become one of the most important methods for preparing 1D metal oxide nanostructures, it is promising as a scalable, economical and controllable growth of different materials.

#### **2.2.1.2 Vapor-solid mechanism**

Vapor-solid growth has been used extensively to produce nanostructures, including metal oxide nanowires in particular. In a typical VS process, the vapor species is generated by evaporation, reduction or other gaseous reactions. These species are then condensed onto the surface of a solid substrate in a temperature zone lower than that of the source material. 1D nanostructures growth will proceed without the need of a metal nanoparticle catalyst if the supersaturation is kept at a controlled low level.

The VS growth takes place when the 1D nanostructures crystallization originates from the direct condensation from the vapor phase without the use of a catalyst. At the beginnings the growth was attributed to the presence of lattice defects, but when defects-free 1D nanostructures were observed this

explanation cannot be any longer accepted. Another peculiar effect registered was a 1D nanostructure growth rate higher than the calculated condensation rate from the vapor phase. A possible interpretation is that all the faces of the 1D nanostructure adsorb the molecules that afterwards diffuse on the principal growth surface of the wire.

The VS transformation growth occurs in many catalyst-free growth processes.<sup>[186-187]</sup> Quite a few experimental and theoretical works have proposed that the minimization of surface free energy primarily governs the VS growth process.<sup>[188-189]</sup> Under high temperature condition, source materials are vaporized and then directly condensed on the substrate placed in the low temperature region. Once the condensation process happens, the initially condensed molecules form seed crystals serving as the nucleation sites. As a result, they facilitate directional growth to minimize the surface energy. This self-catalytic growth associated with many thermodynamic parameters is a rather complicated process that needs quantitative modelling. For example, it was reported for indium oxide,  $\text{In}_2\text{O}_3$  nanowires were synthesized through thermal evaporation of pure  $\text{In}_2\text{O}_3$  powders and the effect of substrate seeding was studied for controlling density distribution and lateral dimensions of the nanowires. The nanowires exhibit uniform section, atomically sharp lateral facets, and pyramidal termination, typical of a VS growth mechanism assisted by oxidized nanocrystalline seeds.<sup>[190]</sup>

### **2.2.2 Solution phase growth**

Growth of various 1D metal oxide nanostructures in solution phase has been successfully achieved. The primary advantage of solution based methods as opposed to the vapor phase option is the ability to perform the growth at lower ambient temperatures on a wide variety of substrates. Another advantage is the ability to control the size and shape of the nanostructure.

Hence, complexity and cost of fabrication are considerably reduced. To develop strategies that can guide and confine the growth direction to form 1D metal oxide nanostructures, researchers have used a number of approaches that may be grouped into template-assisted and template-free methods.

The solution-based catalyzed-growth mechanism is similar to the previously described VLS mechanism, in this case a nanometer-scale metallic droplet catalyze the precursors decomposition and crystalline nanostructure growth. The variants of VLS growth in solutions SLS and supercritical fluid-liquid-solid growths provide 1D nanostructure solubility control over surface ligation, and smaller diameters, however the VLS growth in general produces nanostructures of high crystalline quality.

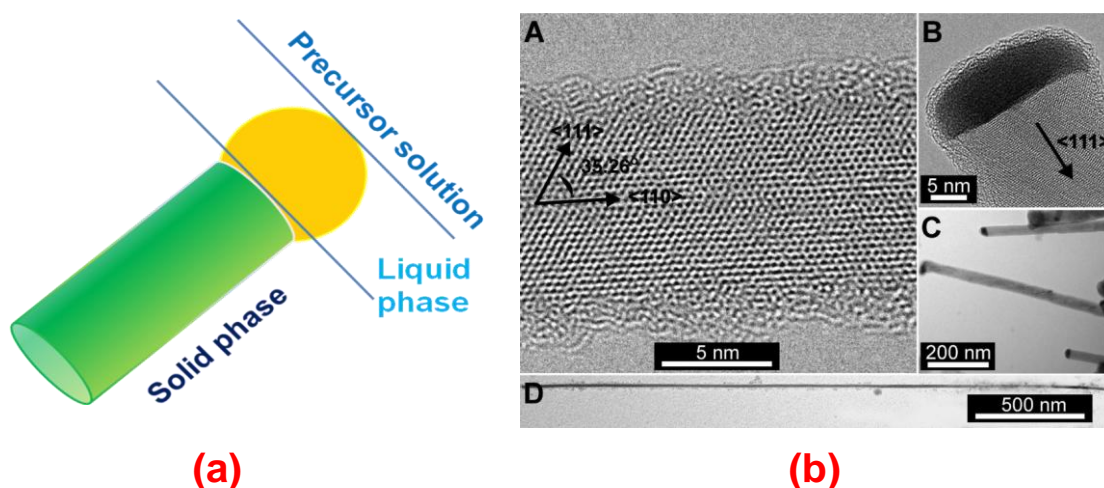


**Figure 6:** (a) Schematic presentation of SLS growth mechanism, and (b) TEM images of Si nanowires synthesized following the SLS mechanism: (A) Si nanowire synthesized at 410 °C with Au nanocrystal seeds; (B) one Si nanowire with a Au seed at the tip; (C) Si nanowires grown using Bi nanocrystals as seeds; (D) a Si nanowire (Bi seeded) longer than 3  $\mu\text{m}$ .

There exist strong indications that the metal droplets in the SLS growth, as well as in VLS growth, mechanisms play a catalytic role in precursor decomposition, in addition to catalyze the nanostructures growth (Figure 6(a)). The early VLS growth literature claimed such a role on the basis of various experimental observations, including that VLS crystal growth typically occurs at temperatures several hundreds of degrees lower than epitaxial film growth from the same precursors. Heitsch and co-workers demonstrate the first example of Si nanowire growth by the SLS mechanism at atmospheric pressure using trisilane ( $\text{Si}_3\text{H}_8$ ) as a reactant in octacosane ( $\text{C}_{28}\text{H}_{58}$ ) and either gold (Au) or bismuth (Bi) nanocrystals as seeds, as shown in Figure 6(b). EDX confirmed that the particles at the tips of the wires are composed of Au or Bi, confirming that the nanowires grow by the SLS growth mechanism.<sup>[191]</sup> Thus, the droplets perform a dual role as ideally rough surfaces for precursor adsorption and decomposition and as a crystallization solvent supporting semiconductor crystal-lattice formation and, hence, wire growth.

As well as for VLS growth mechanism, melting points, solvating abilities, and reactivities are the important criteria for selecting the potential SLS catalyst materials. Moreover, at least one of the components of the product semiconductor phase must have finite, but limited solubility in the catalyst material, so that high supersaturations can be achieved. Finally, the catalyst should not react with or form a solid solution with the target semiconductor phase, unless the catalyst material is the same as one of the constituent elements of the semiconductor.

### **2.2.2.1 Template-assisted growth**

Large-area patterning of 1D metal oxide nanostructures array assisted by template has been achieved (Figure 7).<sup>[192]</sup> By utilizing periodic structured template, such as anodic aluminum oxide (AAO), molecular sieves, and



polymer membranes, nanostructures can be formed inside the confined channels. These pores can be filled to form 1D metal oxide nanostructures using electrodeposition and sol-gel deposition methods. Because the diameter of these nanochannels and the inter-channel distance are easily controlled by the anodization voltage,<sup>[193]</sup> it provides a convenient way to manipulate the aspect ratio and the area density of 1D metal oxide nanostructures.

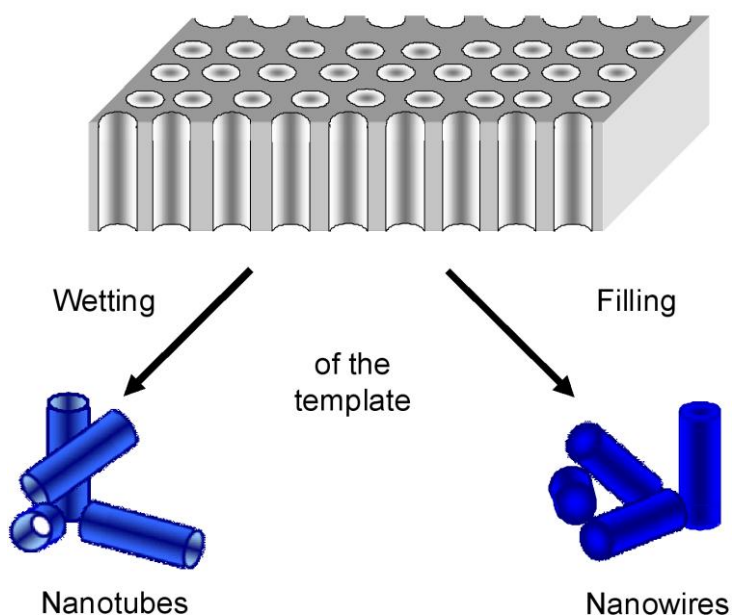


**Figure 7:** Schematic presentation of template-assisted synthesis of one-dimensional nanostructures.

Electrochemical deposition has been widely used to fabricate metallic nanowires in porous structures. It was found that it is also a convenient method to synthesize metal oxide nanostructures. In fact, there are both direct and indirect approaches to fabricate 1D metal oxides using electrodeposition.

In general, sol-gel process is associated with a gel composed of sol particles. In the latter case, as the first step, colloidal (sol) suspension of the desired particles is prepared from the solution of molecule precursor,

afterwards an AAO template is immersed into the sol suspension, so that the sol can aggregate on the AAO template surface. Deposition time must be carefully chosen in order to allow the sol particles to fill the template pores and form 1D metal oxide nanostructures. The final step consists in a thermal treatment to remove the gel. Despite its simplicity, template-based growth is characterized by the production of polycrystalline 1D metal oxide nanostructures that can limit their potential for both fundamental studies and applications.

### **2.2.2.2 Template-free growth**

Instead of plating nanomaterials inside a template, a big research effort has been reserved to develop the new template-free methods for the deposition of 1D metal oxide nanostructures in liquid environment. Several methods have been described including surfactant method, sonochemistry, hydrothermal technique, organometallic methods and electrospinning.

Surfactant-promoted anisotropic 1D crystal growth has been considered as a convenient way to synthesize oxide nanowires. The anisotropic growth is in general performed in a three-phase system, oil, surfactant and aqueous phase. In the emulsion system, these surfactants serve as microreactors to confine the crystal growth. Key points are the selection of precursor and surfactants, and parameters such as temperature, pH value, and reactants concentration. As a result, surfactant-assisted system is a trial-and-error based procedure which requires much endeavor to choose proper capping agents and reaction environment. Surfactant-assisted method is a trial-and-error procedure and requires much effort to select the appropriate capping agents and reaction environment.<sup>[194]</sup> Different surfactants have been proposed depending on the material that is being addressed, for example oleic acid (OA), hexylphosphonic acid (HPA), tetradecylphosphonic acid (TDPA),

trioctylphosphine oxide (TOPO), and trioctylphosphine (TOP).

Sonochemical method uses ultrasonic wave to acoustically agitate or alter the reaction environment, thus modifies the crystal growth. The sonication process is based on the acoustic cavitation phenomenon which involves the formation, growth, and collapse of many bubbles in the aqueous solution.<sup>[195]</sup> Extreme reaction conditions can be created at localized spots. During sonication bubbles are formed in the aqueous solution, they grow and then collapse. In such environments it is easy to reach extreme reaction conditions (temperature greater than 5000 K, pressure larger than 500 atm, and cooling rate higher than  $10^{10} \text{ K}\cdot\text{s}^{-1}$ ) that can allow the formation of 1D metal oxide nanostructures.<sup>[196]</sup>

A well-known procedure for material synthesis is the hydrothermal process, it has been carried out to produce crystalline structures since the 1970s. This process begins with aqueous mixture of soluble metal salt (metal and/or metal-organic) of the precursor materials. Usually the mixed solution is placed in an autoclave under elevated temperature and relatively high pressure conditions. Typically, the temperature ranges between 100 °C and 300 °C and the pressure exceeds 1 atm. Many works have been reported to synthesize ZnO nanorods by using wet-chemical hydrothermal approaches.<sup>[197]</sup>

Another interesting approach for the formation of 1D metal oxide nanostructures is the organometallic method.<sup>[198]</sup> It has been used for the synthesis, at room temperature, of homogeneous ZnO nanostructures of isotropic or rod shape. Organometallic complexes have been used as precursors to overcome the problem of interaction of ionic species with the particles growth process. The synthesis of metal nanoparticles takes advantage of the reactivity of metal-organic precursors to CO, H<sub>2</sub>, UV irradiation or heat treatment. The method uses both the exothermic reaction of

the organometallic precursor with water to produce crystalline zinc oxide and a kinetic control of the decomposition by long-alkylchain amine ligands in the presence or absence of additional solvents to control size and morphology. Quantitative yields of ZnO nanostructures are reported. The mechanism of particle growth involves mass transport of zinc atoms, the amine ligand playing a fundamental role in the process and remaining coordinated to the particles throughout the synthesis. The metal oxide products were dissolved in common organic solvents forming clean and clear luminescent solutions that could easily be deposited on various surfaces as monolayers or thick layers.

Finally another template-free synthesis process is electrospinning. Electrospinning uses an electrical charge to form a mat of fine fibers. It may be considered as an electrospray process. A high voltage induces the formation of a liquid jet. In electrospinning, a solid fiber is generated as the electrified jet is continuously stretched due to the electrostatic repulsions between the surface charges and the evaporation of solvent. Whipping due to a bending instability in the electrified jet and concomitant evaporation of solvent (and, in some cases reaction of the materials in the jet with the environment) allow this jet to be stretched to nanometer-scale diameters. The elongation by bending instability results in the fabrication of uniform fibers with nanometer-scale diameters. As an example, Li and co-workers have demonstrated a simple and versatile approach to the fabrication of titania nanofibers with controllable diameters and two modes of porous structures, which seem to be achievable by carefully controlling the electrospinning parameters and the composition of the precursor solution.<sup>[199]</sup>

## 2.3 Synthesis of one-dimensional heterostructures

A natural progression from single-component materials to complex structures and compositions is the next step for the development of 1D nanostructured materials. The combination of material classes such as metals, metal oxides, semiconductors, and polymers has led to unique properties and functionalities that are not accessible in the single-component materials. As discussed before, 1D metal oxide nanostructures have been grown via various template methods. Interestingly, these 1D nanostructures themselves were used as templates to grow novel one-dimensional architectures by multiple synthetic steps, as shown schematically in Figure 8.

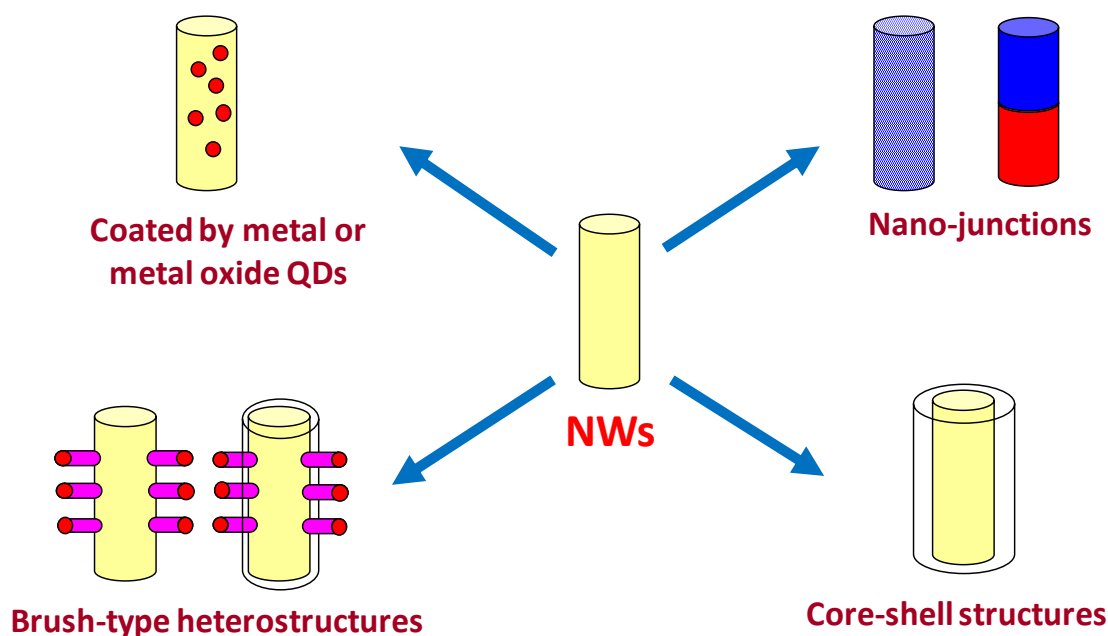


**Figure 8:** Schematic presentation of innovation to synthesize one-dimensional architectures.

The synthesis of one dimensional architecture is being strongly investigated in the last years in order to exploit the functional properties arising from the junction of different materials and/or the effect of hierarchical

organization of 1D nanostructure. In Figure 9, the typical shapes of architectures fabricated up to now are presented, such as (a) branched heterostructures, (b) superlattice in a single nanowire or nanojunction, (c) polycrystals coalescence on a single backbone, and (d) core-shell geometry structures, each shape enabling exploitation of different functional properties of these innovative structures.<sup>[200]</sup>

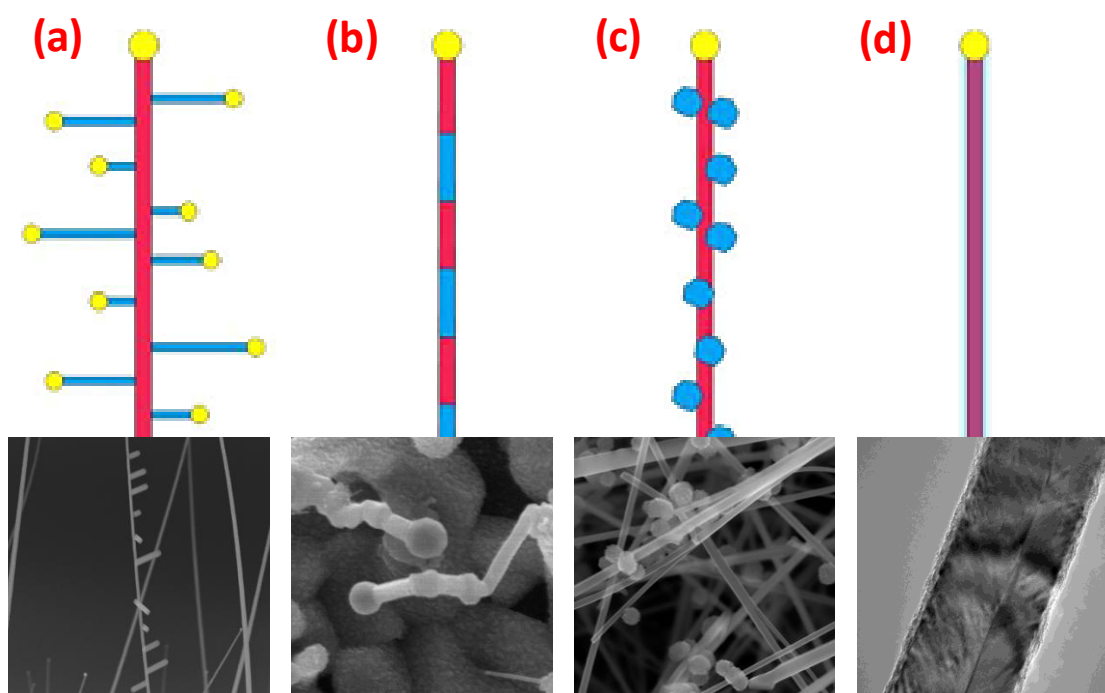


**Figure 9:** Typical shapes for architectures fabricated using various methods.

Typically VLS and VS growth mechanisms, which offer a key advantage to fabricate the architectures at the individual device level in a controlled fashion, can be combined for enabling or inhibiting predefined growth directions and modifications of the crystalline assembly. For instance, combined VLS-VLS growth under sequential seeding of the catalyst leads to formation of branched shapes; while VLS-VS process can lead to formation of core-shell structures, or decoration of nanowires with small crystals.

### 2.3.1 Branched heterostructures

Branched and tree-like nanowire heterostructures may be obtained if after the initial nanowire growth, metal catalyst nanoclusters are deposited again on the surfaces of the grown NWs (the trunks), and reactants are introduced once more to facilitate nucleation and directional growth of nanowire branches. Epitaxial growth of the branches can occur if the trunk and branches are composed of similar materials and no amorphous overcoating (e.g. oxides) is developed before the branch growth. Branched heterostructures and 'nanotrees' were independently studied by Dick and co-workers in the case of GaP using MOCVD and a sol-gel method to deposit Au catalyst nanoclusters on the nanowire trunks.<sup>[201]</sup>

### 2.3.2 Core-shell structures

Core-shell heterostructures can be achieved if dissociation of the reactants is promoted at the grown nanowire surface,<sup>[33]</sup> analogous to the layered growth of planar heterostructures. Compared with NWs in the simple homogeneous form, core-shell structure NWs offer better electrical and optical properties as they can now be tailored through band structure engineering. For example, similar to the formation of two-dimensional electron and hole gases in high electron mobility transistors, 1D electron and hole gases can be achieved in core-shell and heterostructure NWs.<sup>[202-203]</sup> Lu and co-workers observed that 1D hole gas will be formed if Si shell is epitaxially grown on top of a Ge core. The valence band offset of ca 0.5 eV between Ge and Si at the heterostructure interface then serves as a confinement potential for the quantum well,<sup>[204]</sup> and free holes will accumulate in the Ge channel when the Fermi level lies below the valence band edge of the Ge core.

Other types of core/shell nanowires have also been studied. For example, GaN based core/multi-shell nanowires have been grown using MOCVD.<sup>[205]</sup>

High-efficiency light-emitting diodes were obtained on these core/multi-shell structures using bandstructure engineering and modulation doping.<sup>[206]</sup> In a different approach, silicon-silica core/shell nanowires were produced through thermal oxidation of as-grown Si nanowires. By treating either the silica shell or the silicon core as a sacrificial material, silica nanotubes<sup>[207]</sup> or parallel array of silicon nanowires with controlled spacing<sup>[208]</sup> have been demonstrated, respectively.

### 2.3.3 Nanojunction

Unlike core-shell structures in which the shell growth does not involve reaction with the nanocluster catalyst, nanojunction can be obtained by alternative introduction of vapor phase reactants that react with the same nanocluster catalyst. A critical requirement of the nanojunction growth is then that a single nanocluster catalyst can be found which is suitable for growth of the different components under similar conditions. For a wide range of III–V and IV materials, Duan and co-worker found that Au nanoclusters can meet this requirement.<sup>[209]</sup> Using Au nanoclusters as catalysts and a laser-assisted catalytic growth, Gudiksen and co-workers have successfully obtained GaAs-GaP nanojunction (superlattices) with GaAs and GaP targets at temperatures of 700-850 °C at 100 Torr in a continuous argon flow.<sup>[146]</sup>

By repeating the modulation process, nanowire superlattices can be produced in which the number of periods and repeat spacing can be readily varied during growth. For example, Gudiksen and co-workers demonstrated a 21-layer GaAs-GaP superlattice with arbitrary repeat spacing, with the lengths of the segments controlled by the number of pulses delivered to each target.<sup>[146]</sup>

Besides various semiconductor heterostructures, metal/semiconductor nanojunction and superlattices have also been demonstrated recently. Wu and



co-workers observed that NiSi, a bulk metal, can be transformed from Si via solid phase reaction with Ni. As a result, metallic NiSi NWs were produced by first evaporating Ni on SiNWs, followed by heating the sample above the NiSi transition temperature.<sup>[210]</sup> Compared with devices using external microscale leads and interconnects, the NiSi/Si metal/semiconductor heterostructure offers an intriguing solution in which the metallic regions can be used as local contacts to the active semiconductor regions as well as interconnects, hence achieving much higher device density.

## 2.4 Synthesis of one-dimensional metal oxide nanostructures by CVD

Among several synthetic approaches demonstrated for 1D metal oxide nanostructures synthesis, CVD appears to be the most attractive candidate. As a new approach, CVD is an inherently scalable method with several advantages over competing synthetic processes.

The conventional CVD techniques,<sup>[211-212]</sup> so called thermally activated CVD (TACVD), uses thermal energy to activate the chemical reactions. However, the CVD reactions can also be initiated using different energy sources. This has given rise to other variants of CVD methods such as plasma enhanced CVD (PECVD), photo-assisted CVD (PACVD) and laser-assisted CVD (LACVD or LCVD), which use plasma, light and laser respectively, to activate the chemical reactions. Atomic Layer Epitaxy is a special mode of CVD where a 'monoatomic layer' can be grown in sequence by sequential saturating surface reactions. Such CVD variants are useful for the controlled growth of epitaxial films, and the fabrication of tailored molecular structures. Other variants of CVD include metal-organic CVD (MOCVD) which uses metal-organic as the precursor rather than the inorganic precursor used in the conventional CVD method. Other CVD variants such as pulsed injection MOCVD and aerosol assisted CVD using special precursor generation and delivery systems unlike conventional CVD. Flame assisted chemical vapor deposition (FACVD) uses a flame source to initiate the chemical reaction and/or heating the substrate. Electrochemical vapor deposition (EVD) is another variant of CVD that is tailored for the deposition of dense films onto porous substrates. Chemical vapor infiltration is a form of CVD that has been adapted for the deposition of a dense ceramic matrix during the fabrication of ceramic fiber reinforced ceramic matrix composites. All these variants have

enjoyed success in microelectronics industry. Based on their success and experience, these techniques have recently found their way into synthesis of metal oxide nanostructures.

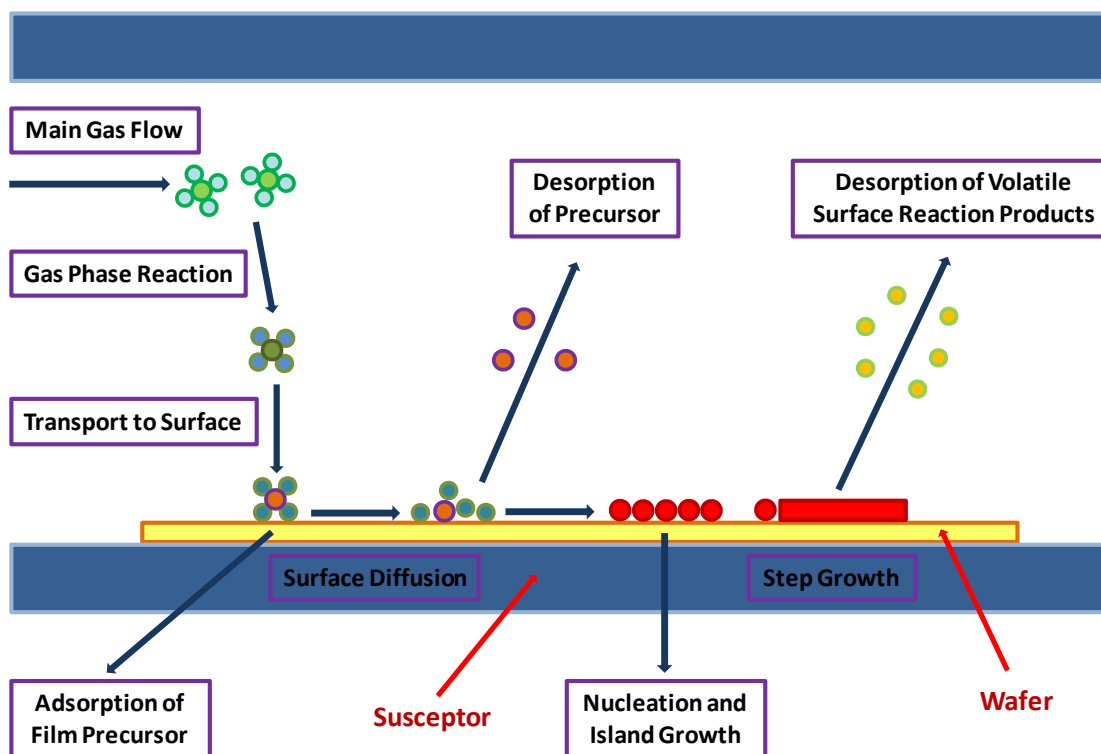


**Figure 10:** Fundamental processes active in the CVD process.

CVD techniques have the following distinctive advantages,<sup>[213]</sup> such as: (i) the capability of producing highly dense and pure materials; (ii) reproducibility of the syntheses and better adhesion of materials on substrates; (iii) high growth rate and coating of complex shaped components; (iv) the ability to control crystal structure, surface morphology and orientation of nanostructures by controlling the process parameters; (v) Reasonable processing cost; (vi) flexibility of using a wide range of chemical precursors such as halides, hydrides, organometallics which enable the deposition of a large spectrum of materials including metal, carbides, nitrides, oxides, sulphides, III-V and II-VI materials, and (vii) relatively low deposition temperatures, and the desired phases can be deposited in-situ at low energies through vapor phase reactions,

and nucleation and growth on the substrate surface.

In general, the sequence of events taking place during a CVD reaction is shown graphically in Figure 10.<sup>[214-215]</sup> This process takes place by adsorption of the gas-phase species on the substrate surface. Depending upon the interactions of the adatoms with the surface, the surface adsorption can be physical (essentially van der Waals interaction) or chemical (covalent linkage between the molecule and the surface) in nature. The adsorbed molecules may wander on the gas-solid intersurface to form the crystallization centre and growth of 1D nanostructures. The volatile by-products and the unreacted gaseous precursors released in the gas phase decomposition, collision, and the surface reactions can be removed in vacuum. In a simplified view of the surface, it is assumed that there are a fixed total number of reactive sites upon which an incoming atom (“adatom”) or molecule can adsorb. Once a site is occupied, a second molecule will not adsorb on it. This is equivalent to the assumption that the number of atoms adsorbing is equal to those desorbing, if no reaction is taking place. The number of atoms or molecules adsorbing on the surface is proportional to the concentration of the gas phase species or, in other words, equivalent to the partial pressure.

Molecule-based chemical vapor deposition (MB-CVD) technique, based on catalyst assisted vapor-liquid-solid (VLS) growth mechanism,<sup>[216]</sup> relying on the decomposition of single molecular precursors allows to synthesize different 1D metal oxide nanostructures under controlling of chemical composition, size, morphology and surface state at relatively low temperature. The main features of MB-CVD approach are that the structural properties of obtained 1D metal oxide nanostructures can be tuned by modification of molecular precursor (internal) and the regulation of process parameters (external). The gaseous semiconductor reactants are generated through decomposition of precursors in a chemical vapor deposition process. Controlled gas-phase reaction

chemistry and decomposition behaviour of molecular precursors have proved to be of great value in the chemically governed synthesis of pure thin films<sup>[217]</sup> and is equally applicable to 1D metal oxide nanostructures synthesis.<sup>[218]</sup> The choice of molecular precursor is usually based on the stability of the metal-ligand bond, convenient handling, and the possibility to use a single-source to insure a controlled and high feedstock in the gas phase. In most of the cases, metal-ligand connectivity, metal ratios and valences are conserved during the precursor-to-material conversion, which leads to chemically control of material formation (Figure 11).

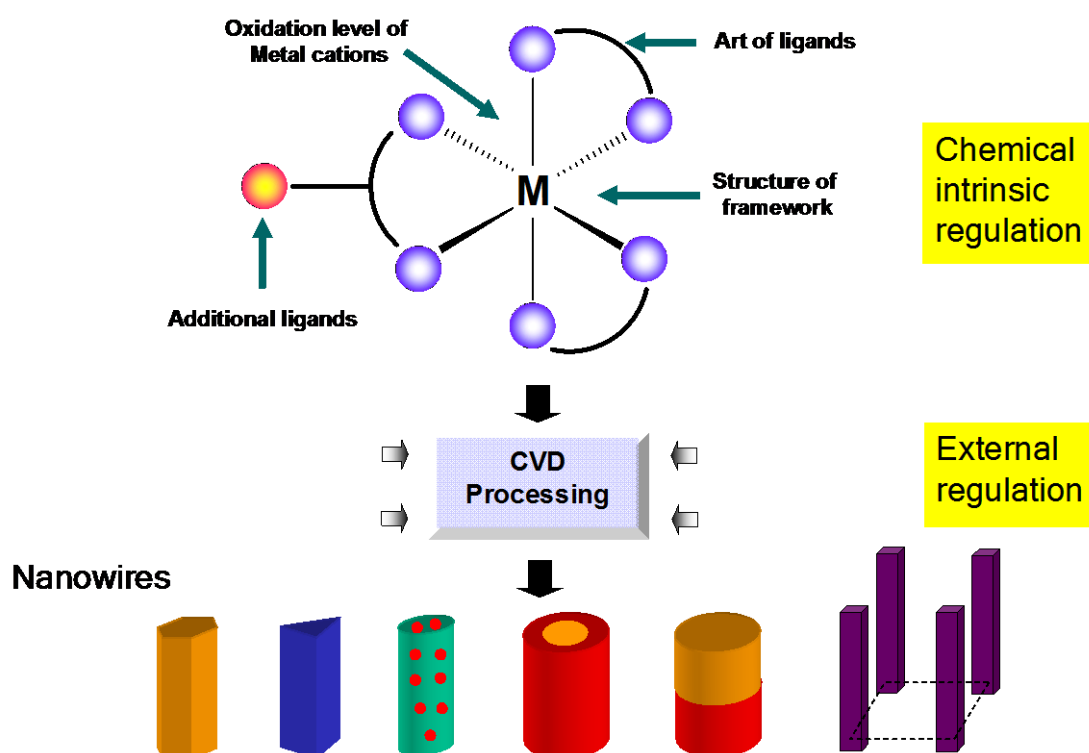


**Figure 11:** Processing of 1D metal oxide nanostructures by molecule-based CVD.

As an example, Ge/SiC<sub>x</sub>N<sub>y</sub> nanowires was achieved by MB-CVD of the molecular precursor [Ge{N(SiMe<sub>3</sub>)<sub>2</sub>}<sub>2</sub>].<sup>[165]</sup> In growth process the replacement of hexamethyldisilazane ligands in [Ge{N(SiMe<sub>3</sub>)<sub>2</sub>}<sub>2</sub>] with cyclopentadienyl groups ([Ge(C<sub>5</sub>H<sub>5</sub>)<sub>2</sub>]) produced pure Ge nanowires because the chemical

bonding of the departing  $C_xH_y$  ligands on Ge surface is energetically less favorable. SEM analysis of time dependent nanowire growth stages (Figure 12) showed 1D nanostructures morphology to be pertinent from the onset of the deposition process. SEM images of the sample deposited in 5 s showed that nanowires preferentially nucleate at defect sites, steps, and/or grain boundaries of the polycrystalline alumina substrate with unusually high growth rates ( $\sim 1 \mu\text{m}\cdot\text{min}^{-1}$ ). The growth of Ge/SiC<sub>x</sub>N<sub>y</sub> nanowires is possibly initiated by randomly formed Ge droplets, which are liquefied at the growth temperatures (700-900 °C) and used as “catalysts” to promote anisotropic growth due to the dissolution of precursor fragments followed by precipitation due to supersaturation. The axial growth is kinetically driven, which was examined by a systematic temperature variation.

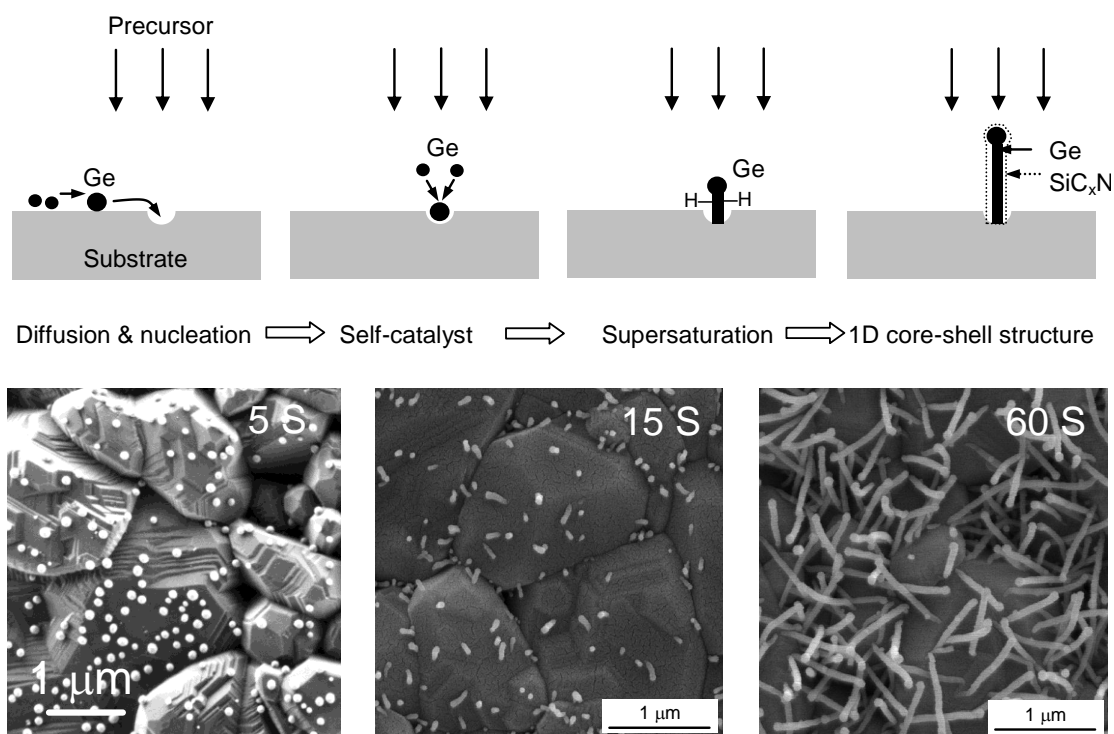


**Figure 12:** Self-catalytic growth mechanism for Ge/SiC<sub>x</sub>N<sub>y</sub> nanowires and SEM images of Ge/SiC<sub>x</sub>N<sub>y</sub> nanowires formed in 5, 15, and 60 s.

Hence, MB-CVD offers the widest range of 1D metal oxide nanostructured applications than any other CVD deposition techniques. The capability of MB-CVD processes to use any precursor sources and processing conditions have led to the development of new and advanced materials.

Although CVD-based methods generally involve complex chemistry and chemical process, the use of on-line monitoring and diagnostic tools, together with the improved understanding of the thermodynamics, kinetics and mass transport of the CVD process would help to unveil the chemistry, rate controlling steps and fluid dynamics in the CVD process. The use of single chemical precursor sources has minimised the CVD process parameters that need to be controlled. Such improvements in the fundamental understanding of CVD processes, deposition control and environmental safety, together with the versatility of variants of CVD, and the development of emerging low cost, CVD-based techniques will make CVD an important nanostructured technology for the 21st century, to improve the performance of nanostructured materials for both functional and structural applications and to develop new advanced materials to meet the industrial and social requirements.

## **2.5 Properties and applications of one-dimensional metal oxide nanostructures**

It is well known that materials behave differently at the nanoscale compared to their bulk counterparts. In many cases, low-dimensional nanoscale materials, with their large surface areas and possible quantum confinement effects, exhibit superior chemical, electrical and optical properties than those with larger dimensions. The manipulation of well-controlled precise dimensions, crystallinity and composition of 1D metal oxide nanostructures gives rise to unique properties and an array of applications that would not be possible with materials of larger dimensions.

As a group of functional materials, 1D metal oxide nanostructures have a wide range of applications, including transparent electronics, chemical sensors, piezoelectric transducers, light-emitting devices, etc. The down scaling of the material dimension not only implies a shrinkage of the active device which leads to higher packing density and lower power consumption, but also can significantly improve the device performance. In addition, when the dimension reduces to a few nanometers, quantum confinement effects start to play an important role. Doubtlessly a thorough understanding of the fundamental properties of the 1D metal oxide system is indisputably the prerequisite of research and development towards practical applications. The following sections will briefly summarize novel properties and applications that have arisen from the discovery of 1D metal oxide nanostructures.

### **2.5.1 Electron transport properties**

The characteristic electronic properties of the nanostructures are a result of tunneling currents, purely ballistic transport and the coulomb blockade effects. As the dimensions of the system become comparable with the de



Broglie wavelength of the electrons, energy bands may cease to overlap. However, owing to their wavelike nature, electrons can tunnel quantum mechanically between two closely adjacent nanostructures. If a voltage is applied between two nanostructures, which aligns the discrete energy levels, resonant tunneling occurs abruptly increasing the tunneling current. When all the scattering centers are eliminated due to extremely small size of the material and purely specular boundary reflections resulting from smooth sample boundaries, the electron transport becomes purely ballistic. This particular behavior can be used in wave guide applications. Conduction in highly confined structures is very sensitive to the presence of other charge carriers and their charge state. These coulomb blockade effects result in conduction processes involving a single electron. Requirement of a very small amount of energy for such conduction can be utilized in operating switches, transistors or memory elements.

The potential of ideal electrical properties of one dimensional nanostructures, has created a growth in research with the aim of electronic miniaturization. The implementation of the “bottom-up” approach in manufacturing electronic devices is presumed to surpass the limitations imposed by more traditional “top-down” methods. For wire diameters larger than the mean free path of carrier, nanowires exhibit transport properties similar to their respective bulk materials; however, as the critical dimension of an individual device becomes smaller and smaller, the electron transport properties of their components become diameter dependent, is an important issue to be investigated. For this reason, electron transport properties become an interesting area of study as a material is reduced from three-dimensional or two-dimensional to one-dimensional. Investigation of nanowire diameter control on electronic transport is a critical procedure in order to understand the electron carrier mobility of various one dimensional nanomaterials. Studies

from a number of groups indicated that some metal oxide nanowires might undergo a transition from semiconductor to insulator as their diameters are reduced below certain values. As a result, nanowires have recently been explored as building block to fabricate nanoscale electronic devices through self-assembly approach. The prototype devices that have been demonstrated include field-effect transistors (FETs), p-n junctions, bipolar junction transistors, complementary inverters, and resonant tunneling diodes.<sup>[219]</sup>

Although the preliminary results showed a lot of attractive application prospects, the assembly of these building blocks into various device architectures, the fabrication of cost-effective and multifunctional nano-devices still remains a challenging avenue. The charge carrier mobility “ $\mu$ ” is an important parameter for device fabrication, however the mobility is strongly influenced by the main source of carrier scattering, namely the surface states of nanowires.<sup>[220]</sup> The mobility is decreased with decreasing diameter of nanowires.<sup>[221]</sup> To circumvent this problem, surface passivation of nanowires with polymers or isolating materials such as  $\text{Si}_3\text{N}_4$  have shown to be viable solution to restrict the detrimental influence of surface states,<sup>[221]</sup> and thus to restore high mobility values essential for any possible device applications.

It is noteworthy that band-gap of semiconductor nanowires is influenced by the lateral dimensions. This size effect becomes more significant for ultrathin nanowires ( $r < 20$  nm) since the electrons are confined and separated in different band edges,<sup>[222]</sup> which offers promising possibilities to design new devices for innovative applications. However, the application of the effect in device fabrication is technically challenging due to the difficult manipulation of nanowires on nanometer scale.<sup>[223]</sup> Additionally, nanowires may find possibilities in many other applications, for example, electrons can be easily extracted out from nanowires tips by an external electric field. This effect could be used in highly efficient illumination displays by fabricating arrays of

nanowire cathodes.<sup>[224]</sup>

## 2.5.2 Optical properties

Measurement of optical properties is a facile way to understand the electronic properties of nanowires. As for the nanowires, size-confinement plays an important role in determining the energy level once its diameter has been reduced below a critical value (Bohr radius).

The ability to manipulate light pulses within submicron volumes is crucial to realize the integrated light-based devices such as optical computers. A versatile approach is to assemble photonic circuits from a collection of nanowires that assume different functions (i.e., light creation, guiding and detection). Nanowires exhibit several features including inherent one-dimensionality, low surface roughness and the power to operate above and below the diffraction limit, which make them suitable photonic building blocks.<sup>[21]</sup> Nevertheless, nanowire-based photonics still require a development of waveguides, which are able to integrate these elements in a cost-effective and flexible process. This would pave a way towards complex devices such as logic gates.<sup>[169]</sup>

Optical performances of nanowire are strongly influenced by surface effects. For instance, they act as recombination centers for minority carriers, degrading the final response of optoelectronic prototypes. Again, this problem is circumvented if nanowires are passivated with a dielectric shell which forms a high-quality optical cavity around the nanowire, namely as the gain medium. It is noteworthy that thin nanowires (radius close to the exciton Bohr radius) exhibit quantum confinement effects with strong consequences for their optical properties. Therefore, new optoelectronic devices (group of IV semiconductors) could be developed, allowing the combination of both electrical and optical functionalities on the same integrated circuit.

The potential of metal oxide nanowires to develop light detectors was demonstrated as well.<sup>[225]</sup> Nevertheless, a critical analysis of photoconduction mechanism in nanowires indicates that high performance photodetectors can be achieved with nanowires. Their high aspect ratio dramatically reduces the volume where photons are absorbed, leading to weak electrical responses.<sup>[226]</sup>

### **2.5.3 Photoconductivity switching properties**

Among all nanoscale devices, switches are critical for important applications like memory and logic. Electrical switching on the nanometer and molecular scales has been predominantly achieved through the application of a gate potential, as exemplified by nanotube and nanowire transistors.<sup>[227]</sup> Recent works from several groups demonstrated that it is also possible to create highly sensitive electrical switches by controlling the photoconductance of individual metal oxide nanowire. Yang and co-workers found that conductance of ZnO nanowire was extremely sensitive to ultraviolet light exposure. The light-induced insulator-to-conductor transition enabled them to reversibly switch a nanowire between OFF and ON states.<sup>[225]</sup> In a typical experiment, four-probe measurements on individual ZnO nanowires indicated that they were essentially insulating in the dark, with a resistivity  $> 3.5 \text{ M}\Omega \cdot \text{cm}^{-1}$ . When these nanowires were exposed to a UV-light source with wavelengths below 400 nm, their resistivity was instantly reduced 4 to 6 orders in magnitude. In addition to their high sensitivities, these photoconductive nanowires exhibited excellent wavelength selectivity.

It has been clearly established that oxygen chemisorption plays a profound role in enhancing the photosensitivity of bulk or thin film ZnO. It is believe that a similar photoresponse mechanism could be applied to the nanowire system with additional consideration of high surface area associated with nanowires, which could further enhance the sensitivity of device. These highly sensitive

photoconducting nanowires could serve as very sensitive UV-light detectors in many applications such as microanalysis and missile-plume detection, and as fast-switching devices for nanoscale optoelectronics applications where ON and OFF states can be addressed optically.

#### **2.5.4 Field-effect transistor properties**

Field-effect transistor (FET) is an electron escape process from the surface of material under the presence of sufficiently large electric field. The emitting material/electrode is called a cathode that is usually of low electron affinity. Since the discovery of excellent field-effect transistor properties of carbon nanotubes, there has been a surge of interest in studying the field-effect transistor properties of 1D nanostructures for potential FET applications due to their high aspect ratio.

It is well known that nanotubes and nanowires with sharp tips are promising candidates for the applications related to cold cathode, field emission electrons. 1D metal oxide nanostructures have been fabricated into field-effect transistors to serve as the fundamental building blocks of electronic devices such as logic gate, computing circuits and chemical sensors. Lee and co-workers have investigated the field emission characteristics of well aligned ZnO nanorods grown using a low-temperature CVD method.<sup>[228]</sup> The turn-on field was  $6 \text{ V}\cdot\mu\text{m}^{-1}$ , which corresponded to a current density of  $0.1 \mu\text{A}\cdot\text{cm}^{-2}$ . The current reached  $\text{mA}\cdot\text{cm}^{-2}$  when the applied field was increased to  $11 \text{ V}\cdot\mu\text{m}^{-1}$ . Consider their ease of preparation, these nanorods might find use as active components in fabricating FET devices.

### 2.5.5 Gas sensing properties

One-dimensional nanostructured chemical and biological sensors are an attractive, versatile application of important molecules, medical, environmental and security-checking purposes. Nanowire sensing probes possess electrical properties extremely sensitive to species to absorb on surface due to their high surface to volume ratio. Nanoscale sensors are also smaller, require less power and detect analytes faster than their microscale counterparts. Sensors based on one-dimensional nanostructures being developed for glucose oxidase (GOX) on the SWNTs indicated a clear decrease in the conductance of the tube, which can be attributed to a change in the total capacitance of the tube. A typical experiment involves the immobilisation of GOX via a linking molecule which binds through van der Waals coupling with a pyrene group on one side and on the other side covalently binds the enzyme through an amide bond. Changes of conductance of the GOX coated semiconducting SWNTs upon addition of glucose indicated that an enzyme activity sensor can be constructed at the single molecule level of an individual SWNT.

Sensing behavior is the most important and well-known property of metal oxide nanostructures. In addition to the sensitivity to light and pressure as mentioned in previous sections, metal oxides demonstrate high sensitivity to their chemical environment. With the capability of being operated in harsh environment, they surpass other chemical sensors in their sensitivity, reliability and durability. The advantage of using 1D metal oxide nanostructures for chemical sensing is manifold. With a large surface-to-volume ratio and a Debye length comparable to the nanowire radius, the electronic property of the nanowire is strongly influenced by surface processes, yielding superior sensitivity than their thin film counterpart. In order to achieve maximum sensitivity, thin film gas sensors are often operated at elevated temperature.<sup>[229-230]</sup> This indicates that a single sensing device needs to

incorporate temperature control unit, which will certainly increase the complexity of sensor design and power consumption. Fortunately, metal oxide nanowire based gas sensors have demonstrated significantly higher sensitivity at room temperature. For example, room temperature NO<sub>2</sub> sensing with ZnO nanowire shows more than 50 % conductance change under an exposure of 0.6 ppm NO<sub>2</sub>.<sup>[231]</sup> In contrast, NO<sub>2</sub> sensor made of doped ZnO thin film demonstrates less than 2 % conductance change when exposed to an even higher concentration of NO<sub>2</sub> (1.5 ppm).<sup>[229]</sup> This encouraging result manifests the potential of building room temperature operating highly sensitive gas sensors. In addition, metal oxide nanowires configured as field-effect transistors have demonstrated that a transferred electric field can effectively tune the sensing behavior of the system.

The sensing mechanism of metal oxides is mainly governed by the fact that the oxygen vacancies on the oxide surfaces are electrically and chemically active. In this case, two kinds of sensing responses have been observed. (1) Upon adsorption of charge accepting molecules, such as NO<sub>2</sub> and O<sub>2</sub>, at the vacancy sites, electrons are withdrawn and effectively depleted from the conduction band, leading to a reduction of conductivity. (2) On the other hand, in an oxygen-rich environment, gas molecules such as CO and H<sub>2</sub>, could react with the surface adsorbed oxygen and consequently release the captured electrons back to the channel, resulting in an increase in conductance.

The gas sensing mechanism is being explained by the reaction of reducing or oxidizing gases with surface oxygen. The followings are sensing mechanism of SnO<sub>2</sub> based sensor (Figure 13).

SnO<sub>2</sub> is n-type semiconductor with oxygen deficiency. The lattice oxygen is evaporated in the form of gas, which makes the doubly ionized oxygen vacancy and electrons. These electrons play the role in conduction. If tin dioxide is heated at 300-400 °C, the oxygen in the atmosphere is adsorbed at

the surface of SnO<sub>2</sub> with the negative charge. Because electron is provided from the surface of crystal, the surface of tin oxide becomes electron depletion layer. This means the formation of potential barrier near the grain boundary. The core with yellow tone shows the conducting phase and the red tone of surface layer indicates the resistive shell layer. If CO is present in the atmosphere, the CO oxidizes into CO<sub>2</sub> with the reaction of adsorbed oxygen and remaining electron returns to the SnO<sub>2</sub> crystal. This increases the electrical conductivity to a great extent. So, we can detect CO by the remarkable resistance decrease. The similar mechanism can be applied to the detection of other reducing gases. Generally speaking, the reduction in resistance occurs mainly at the surface and can be explained by the reduction of potential barrier.

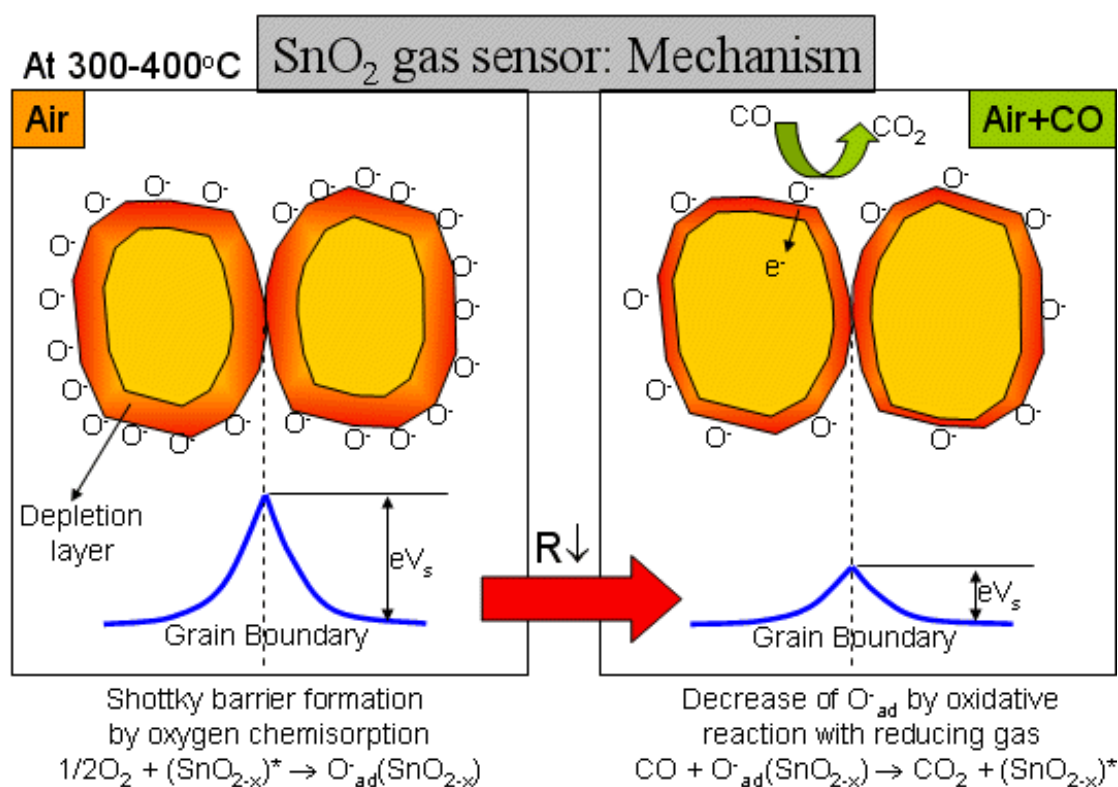


**Figure 13:** The CO sensing mechanism of SnO<sub>2</sub> gas sensor.



Selectivity has always been a major hurdle for solid state gas sensors. There have been a number of approaches developed to improve the selectivity of gas sensors, including doping metal impurities,<sup>[232]</sup> using impedance measurement,<sup>[233]</sup> modulating operating temperature,<sup>[234]</sup> surface coating,<sup>[235]</sup> etc. In the frame work of studying metal oxide nanowire field-effect sensors, it is discovered that the transverse electrical field induced by back gate can be utilized to distinguish different chemical gases.<sup>[236]</sup>

## 3 Experimental Procedure

The experimental procedure used for the synthesis and characterization of 1D metal oxide nanostructures in this work are discussed in this chapter.

### 3.1 Synthesis procedure

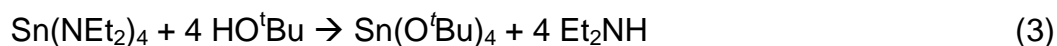
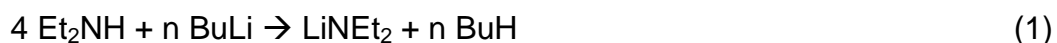
Metal-organic precursors used in the CVD of tin oxide containing nano- and hetero- structures are detailed here. Further, the experimental parameters used for the growth of tin oxide based nanostructures are also given in this section.

#### 3.1.1 Chemical synthesis of precursors

Three metal alkoxides were used as precursors to fabricate the 1D metal oxide nanostructures by MB-CVD in this work.

##### 3.1.1.1 Sn(O<sup>t</sup>Bu)<sub>4</sub>

Tin (IV) *tert*-butoxide, Sn(O<sup>t</sup>Bu)<sub>4</sub>, is monomeric in the solid state and possesses a distorted tetrahedral coordination environment about the tin atom, which was determined by single crystal X-ray diffraction (XRD) analysis by Hampden-Smith and co-workers.<sup>[237]</sup> Sn(O<sup>t</sup>Bu)<sub>4</sub> was synthesized by a reported procedure as shown in equations (1)-(3).



### 3.1.1.2 VO(O<sup>i</sup>Pr)<sub>3</sub>

Vanadium (V) tri-isopropoxy oxide, VO(O<sup>i</sup>Pr)<sub>3</sub>, was procured from ABCR chemicals (98 % purity) and used without further purification.

### 3.1.1.3 Ti(O<sup>i</sup>Pr)<sub>4</sub>

Titanium (IV) isopropoxide, Ti(O<sup>i</sup>Pr)<sub>4</sub>, a commercial product (97 %, Aldrich), was purified by distillation under vacuum (80 °C, 10<sup>-2</sup> Torr) before using in the CVD process.

## 3.1.2 Synthesis of one-dimensional nanostructures by molecule-based CVD

Molecule-based chemical vapor deposition (MB-CVD) technique relying on the decomposition of single molecular precursors, based on catalyzed vapor-liquid-solid (VLS) growth mechanism, is an efficient way to synthesize different 1D nanostructures under controlling of chemical composition, size, morphology and surface state at relatively low temperature. In this work, 1D nanostructures (nanowires and NW based heterostructures) were fabricated by the method.

The morphology of samples is strongly influenced by the main CVD process parameters, such as deposition temperature, precursor temperature, and deposition time, which needs to be well-defined controlled and monitored. The optimized experimental conditions, which were obtained by series of systematic experiments, are listed in Table 2.

**Table 2:** Experimental conditions for CVD process.

Precursor	Substrate	$T_s$ (°C)	$T_p$ (°C)	$t_d$ (min)	Morphology
Sn(O <sup>t</sup> Bu) <sub>4</sub>	Al <sub>2</sub> O <sub>3</sub> , TiO <sub>2</sub>	700-775	20-30	30-120	Nanowire
		550-650	25-30	10-30	Nanofilm
Ti(O <sup>i</sup> Pr) <sub>4</sub>	Al <sub>2</sub> O <sub>3</sub>	500-600	25-35	10-30	Nanofilm
VO(O <sup>i</sup> Pr) <sub>3</sub>	Al <sub>2</sub> O <sub>3</sub>	600-700	20-30	10-30	Nanowire
		700-800	25-35	15-45	Nanofilm

### 3.1.2.1 Synthesis of nanowires

The nanowires were grown by decomposition of molecular precursors by a CVD process (Figure 14). In this process, a cold-wall horizontal CVD reactor operating under reduced pressure was used to investigate the gas-phase decomposition of the metal-organic precursor. The Au-coated substrates were placed in the quartz reactor on a custom-made graphite susceptor and inductively heated using a 1.5 kW, 350 kHz high frequency generator for 10-90 mins. The deposition temperature was set to a suitable value and monitored using a thermocouple attached to the susceptor. The molecular precursor was introduced in the reactor through a glass flange by applying dynamic vacuum and maintaining the precursor reservoir at the desired temperatures.

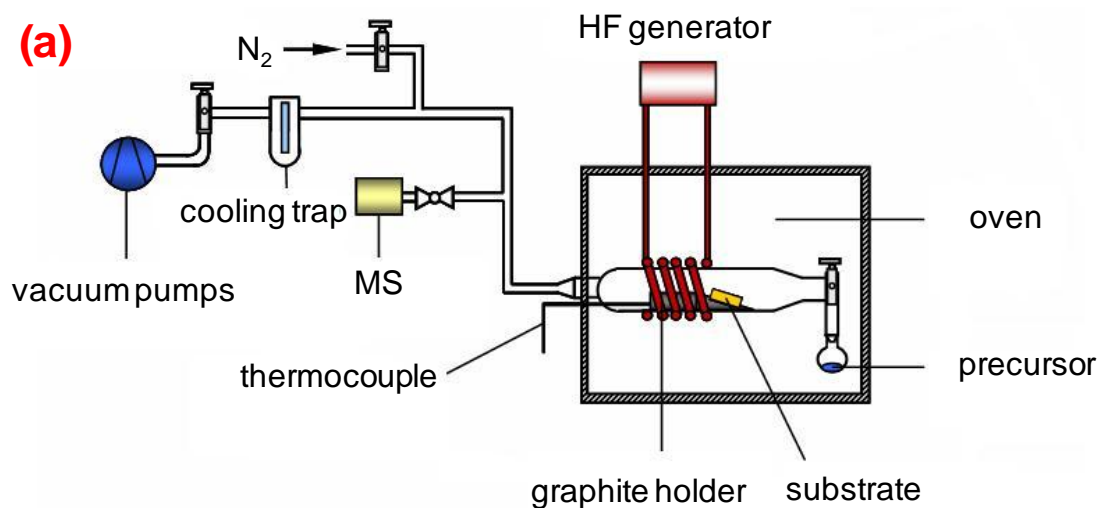


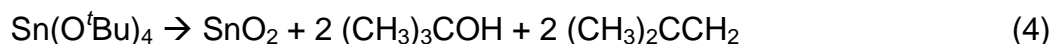
**Figure 14:** (a) Schematic presentation and (b) image of the CVD reactor.

### 3.1.2.2 Synthesis of heterostructures

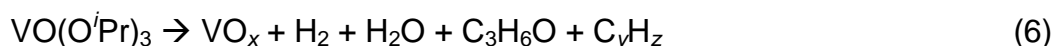
Heterostructures were synthesized by molecule-based chemical vapor deposition (MB-CVD) via a two-step growth process. The based nanowires, which were synthesized by CVD, were used as substrate to deposit architectures by second CVD process.

As-grown SnO<sub>2</sub> nanowires were used as “substrates” to deposit different materials to obtain heterostructures by sequential decomposition of Ti(O<sup>i</sup>Pr)<sub>4</sub>,

$\text{VO}(\text{O}^i\text{Pr})_3$  and  $\text{Sn}(\text{O}^i\text{Bu})_4$ , corresponding to  $\text{SnO}_2@ \text{TiO}_2$ ,  $\text{SnO}_2@ \text{VO}_x$  and  $\text{SnO}_2@ \text{SnO}_2$  heterostructures, respectively. The decomposition pattern of the molecular precursor was determined by mass spectrometry to be as followed:<sup>[238]</sup>



(where  $x/y \neq 1$ ,  $x \gg y$ ,  $z$ ,  $m$  and  $x + y + z = 4$ )



(where  $y = 1, 2, 3$ ;  $z < 2y + 2$ )

The synthesis of architectures is motivated by the expectation to create new interfaces which are precisely defined and can allow lattice-level modifications of materials both in doped and composite materials. Conceptually, heterostructures offer another approach for increasing structural complexity and enabling greater function.<sup>[239]</sup>

### 3.1.3 Synthesis of nanofilms and surface modification by PECVD

Plasma enhanced chemical vapor deposition (PECVD) is also known as glow discharge chemical vapor deposition. It uses electron energy (plasma) as the activation method to enable deposition to occur at a low temperature (0-100 °C) and at a reasonable growth rate ( $\sim 20 \text{ nm}\cdot\text{min}^{-1}$ ). Supplying electrical power at a sufficiently high voltage to a gas at reduced pressures ( $< 1.3 \text{ kPa}$ ), results in the breaking down of the gas and generates a glow discharge plasma consisting of electrons, ions and electronically excited

species. The reactants with vapor phase are ionised and dissociated by electron impact, and hence generating chemically active ions and radicals that undergo the heterogeneous chemical reaction at or near the cold substrate surface and deposit the thin film.

The main advantage of PECVD over other CVD methods is that the deposition can occur at relatively low temperatures on large areas. It also offers the flexibility for the microstructure of the film and deposition was controlled separately. The ion bombardment can be substituted for deposition temperature to obtain the required film density. Such low temperature deposition is important for applications that involve the use of temperature sensitive substrates.

In this study, the  $\text{SiO}_x$  film was deposited on heterostructures to obtain the superhydrophobic surface by decomposing hexamethyldisiloxane (HMDSO) via PECVD (Domino, Plasma Electronic). The precursor temperature was maintained at 50 °C. The thickness of  $\text{SiO}_x$  film was controlled by deposition time and precursor temperature. On the other hand, it is well known that the surface defect electronic states formed by surface oxygen vacancies has a dramatically effect on the electrical and optical properties of nanowires. Surface modification of nanowires was carried out via the PECVD method, which changes homogeneously surface chemical composition and surface defect of nanowires. Hence, the gas sensing performance of nanowires can be effectively enhanced by controlling the gas species and power for PECVD treatment.

The as-grown nanowires were treated in the PECVD chamber for desired time at different power conditions. Argon and oxygen with a flow rate of 10 and 15 sccm, respectively, were used as gas species, and then were introduced in the PECVD system through mass flow controllers.

### 3.1.4 Synthesis of SnO<sub>2</sub>@CdS QDs heterostructures

CdS quantum dots (QDs) were deposited on the surface of SnO<sub>2</sub> nanostructures via a chemical bath deposition (Figure 15). 2 mM CdS precursor solution was prepared by dissolving CdSO<sub>4</sub> and thiourea (with a molar ratio to Cd<sup>2+</sup> = 5:1) in 1 M ammonia solution.

SnO<sub>2</sub> nanostructures were cleaned with N<sub>2</sub> flow and then immersed into CdS precursor solution for several minutes to promote the precursor completely penetrating into among the nanostructures. The solution was put into oil bath at 60 °C for 30 mins. Then SnO<sub>2</sub> nanostructures were immediately took out and washed with deionized water and ethanol, getting SnO<sub>2</sub>@CdS QDs heterostructures. Finally, the heterostructure was annealed at 400 °C under vacuum for 2 h to enhance the interaction between CdS and SnO<sub>2</sub>.

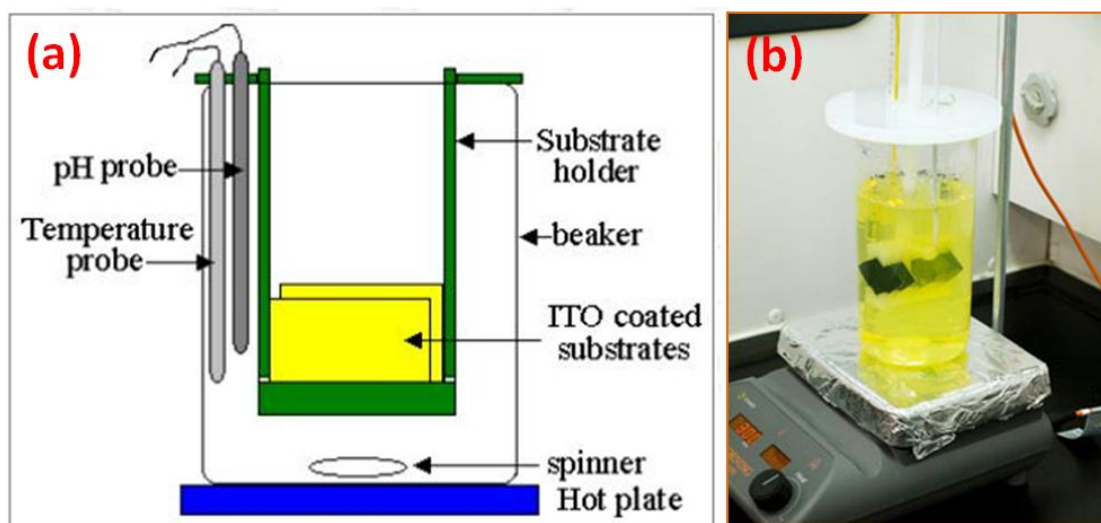


**Figure 15:** (a) Schematic presentation and (b) image of chemical bath deposition reactor.



## **3.2 Characterization techniques**

The ability to investigate nanostructures is closely linked to the advancements in the development of equipments and techniques for structural and physical characterizations. Understanding the structure of nanosized material is paramount to the determination of the relationship between structural properties and functional applications. Nanotechnology has opened a wide range of techniques for the determination of 'nanoscale' physical properties, even as compared with the same material at the micro- and microscales. This has fuelled a tremendous financial and thus academic interest in understanding nanoscale structures to better develop useful applications.

### **3.2.1 Structural analysis**

The structural properties of one-dimensional nanostructures was characterized in this work using (i) X-ray diffraction (XRD), (ii) scanning electron microscopy (SEM), (iii) transmission electron microscopy (TEM), (iv) focused ion beam tomography (FIB tomography), (v) energy dispersive X-ray spectroscopy (EDX), (vi) atomic force microscopy (AFM) and (vii) X-ray photoelectron spectroscopy (XPS) in this work.

#### **3.2.1.1 X-ray diffraction**

X-ray diffraction (XRD) is based on the fact that the wavelength of X-rays is comparable to the distances between atoms in condensed matter. When a material exhibiting a long-range (at least micrometers), periodic atomic order, such as a crystal, is irradiated with X-rays, it acts as an extended, well-defined grating and produces a diffraction pattern showing numerous sharp spots, called Bragg diffraction peaks. By measuring and analyzing the positions and

intensities of these peaks it is possible to determine the spatial characteristics of the grating - i.e. to determine the three-dimensional (3D) arrangement of atoms in the crystalline nanostructures was studied.

In this study, room-temperature powder X-ray diffraction (XRD) was performed with a STOE-STADI MP diffractometer using  $\text{CuK}\alpha$  radiation ( $\lambda = 1.540598 \text{ \AA}$ ) to analyze the structural phase and record structural information, as shown in Figure 16.

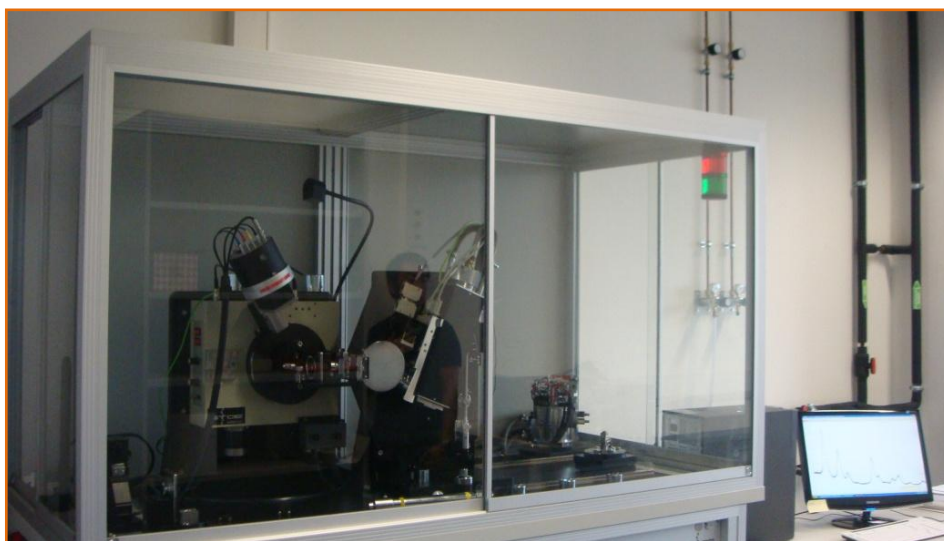


**Figure 16:** Image of XRD machine in our group.

The interplane distance ( $d$ ) of crystal was calculated by Bragg's Law, as shown in equations (7):

$$2d\sin\theta = n\lambda \quad (7)$$

Where  $\lambda$  is the wavelength of the x-ray,  $\theta$  is the angle of the diffracted wave, and  $n$  is an integer known as the order of the diffracted beam.

### 3.2.1.2 Scanning electron microscopy

The scanning electron microscope (SEM) is an excellent technique to image the sample surface by scanning it with a high-energy beam of electrons

in a raster scan pattern. The electrons interact with the atoms that make up the sample producing signals that contain information about the sample's (not just thin films or nanostructures) surface topography, composition, nature of the specimen and other properties such as electrical conductivity.

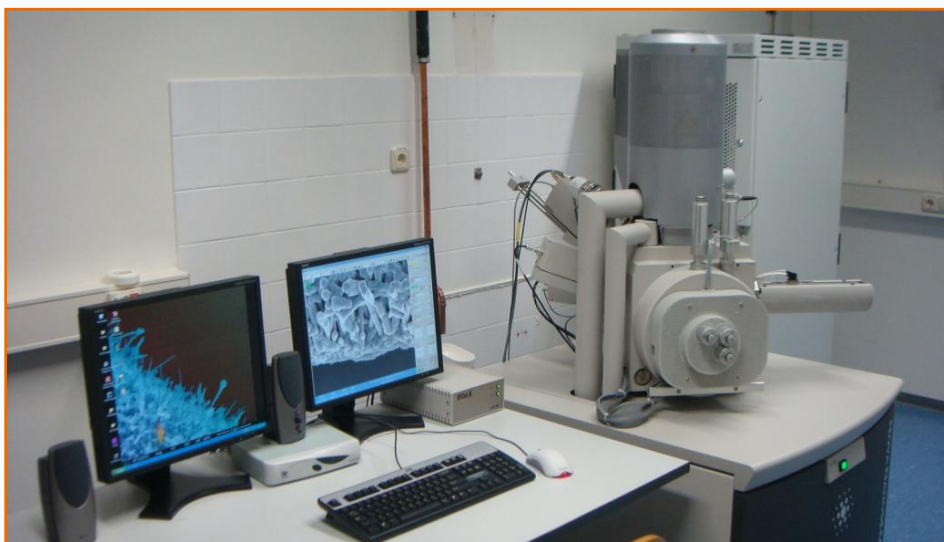


**Figure 17:** Image of SEM machine in our group.

The types of signals produced by an SEM include secondary electrons and back-scattered electrons. Secondary electron detectors are common in all SEMs, but it is rare that a single machine would have detectors for all possible signals. The signals result from interactions of the electron beam with atoms at or near the surface of the sample. In the most common or standard detection mode, secondary electron imaging or solid electrolyte interface, the SEM can produce very high-resolution images of a sample surface, revealing details about less than 1 to 5 nm in size. Due to the very narrow electron beam, SEM micrographs have a large depth of field yielding a characteristic three-dimensional appearance useful for understanding the surface structure of a sample. A wide range of magnifications is possible, from about 10 times (about equivalent to that of a powerful hand-lens) to more than 500,000 times, about 250 times the magnification limit of the best light microscopes.

Back-scattered electrons are beam electrons that are reflected from the sample by elastic scattering. Back-scattered electrons are often used in analytical SEM along with the spectra made from the characteristic X-rays. Because the intensity of the back-scattered electrons signal is strongly related to the atomic number of the specimen, back-scattered electrons images can provide information about the distribution of different elements in the sample.

The morphology of nanostructures was investigated by scanning electron microscope JSM-7000F (JEOL) and Nvision 40 (Zeiss), as shown in Figure 17.

### **3.2.1.3 Transmission electron microscopy**

Transmission electron microscopy (TEM) is a microscopy technique whereby a beam of electrons is transmitted through an ultra thin specimen, interacting with the specimen as it passes through. An image is formed from the interaction of the electrons transmitted through the specimen; the image is magnified and focused onto an imaging device, such as a fluorescent screen, on a layer of photographic film, or to be detected by a sensor such as a charge coupled device camera.

TEMs are capable of imaging at a significantly higher resolution than light microscopes, owing to the small de Broglie wavelength of electrons. This enables the instrument's user to examine fine detail, even as small as a single column of atoms, which is tens of thousands times smaller than the smallest resolvable object in a light microscope. Hence, transmission electron microscopy and high resolution transmission electron microscopy are powerful techniques to characterize atomic features found in nanostructures, and they usually provide more details than in SEM images. TEM imaging is particularly important in the study of one-dimensional nanostructures because it yields information regarding the crystal structure, grain size, crystal orientation along the axis.

The substrate-bound nanostructures were mechanically scrapped and sonicated in ethanol and deposited on carbon-coated copper grids for TEM measurements performed on a Philips CM300 FEG/UT-STEM (300 kV) transmission electron microscope. To determine the electrical response of nanostructures, the samples were connected to gold interdigital electrodes. Samples for cross sectional TEM are prepared by FIB technique (Strata 235 DB, FEI).

#### **3.2.1.4 Focused ion beam tomography**

The focused ion beam (FIB) tomography, allows for the serial slicing and imaging of a sample volume, has become an important tool in materials science for studying and modifying materials systems at the micro and nanometer levels. FIB tomography fills the gap between classical tomography methods that operate in the millimetre to micrometre range (e.g. X-ray absorption tomography) and transmission microscopy methods with nanometer resolution (TEM) but which can only be applied to very thin electron- and photon-transparent samples. This technique, due to its ability to perform precision in-situ milling by a focused beam of ions, has been extended to study three-dimensional (3D) structural and chemical relationships. With the help of computer algorithms for processing data and graphics packages for display, three-dimensional systems can easily be reconstructed and the structure interrogated to obtain both qualitative and quantitative information. It is possible to study features at spatial resolutions at the tens-of-nanometers level and volumes with dimensions of up to tens of microns. This allows the reconstruction of many systems in the size range important to nanotechnology.

The FIB tomography was performed in an area of  $3.4 \times 2.2 \mu\text{m}^2$  in order to represent the 3D structure of the ordered nanowires by a dual beam system (focused ion beam combined with SEM, FEI Strata 235DB). FIB-tomography

consists of the performing precisely serial sectioning with FIB, the imaging with SEM and afterwards reconstructing the 3D-information with a properly software. The size of the voxel was  $4.5 \times 5.6 \times 20 \text{ nm}^3$  in x, y and z direction respectively and the number of slices was 110. The serial sectioning was performed images are reconstructed in 3D by the Slice&View software and the reconstruction with the software AMIRA.

### **3.2.1.5 Energy-dispersive X-ray spectroscopy**

Energy dispersive X-ray spectroscopy (EDX) is an analytical technique used for the elemental analysis or chemical characterization of a sample. As a type of spectroscopy, it relies on the investigation of a sample through interactions between electromagnetic radiation and matter, analyzing X-rays emitted by the matter in response to being hit with charged particles. Its characterization capabilities are due in large part to the fundamental principle that each element has a unique atomic structure allowing X-rays that are characteristic of an element's atomic structure to be identified uniquely from one another.

In this study, energy dispersive X-ray spectroscopy analysis was performed with an EDS-coupled scanning electron microscope Nvision 40 (Zeiss), see Figure 17.

### **3.2.1.6 Atomic force microscopy**

Atomic force microscopy (AFM) is a very high-resolution type of scanning probe microscopy, with demonstrated resolution of fractions of a nanometer, more than 1000 times better than the optical diffraction limit. The AFM is one of the foremost tools for imaging, measuring, and manipulating matter at the nanoscale. The information is gathered by “feeling” the surface with a mechanical probe. Piezoelectric elements that facilitate tiny but accurate and

precise movements on (electronic) command enable the very precise scanning.

Atomic force microscopy (X-100, Park Systems) was used to analyze the 3D structure of the ordered nanowires in this study, as shown in 18.

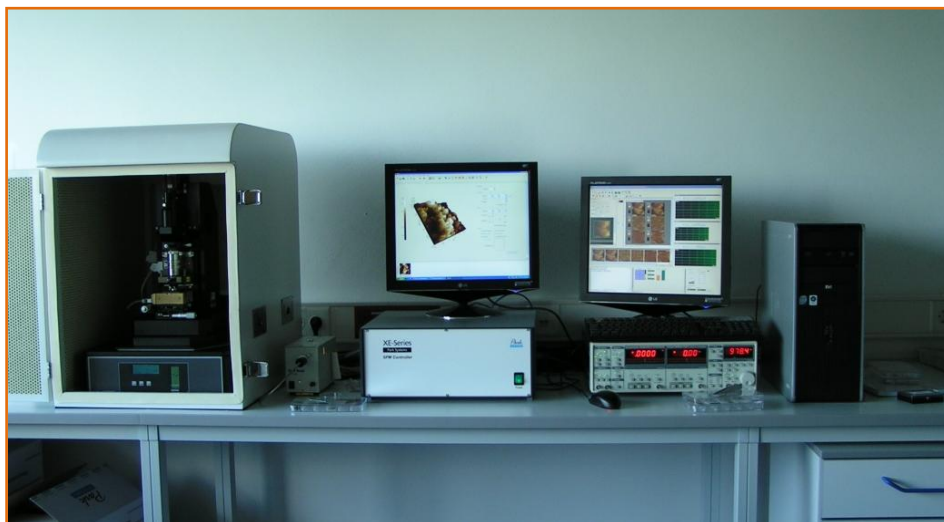


Figure 18: Image of AFM machine in our group.

#### 3.2.1.7 X-ray photoelectron spectroscopy

X-ray photoelectron spectroscopy (XPS) is a quantitative spectroscopic technique that measures the elemental composition, empirical formula, chemical state and electronic state of the elements that exist within a material. XPS spectra are obtained by irradiating a material with a beam of X-rays while simultaneously measuring the kinetic energy and number of electrons that escape from the top 1 to 10 nm of the material being analyzed. XPS requires ultra high vacuum (UHV) conditions.

In this work, X-ray photoelectron spectroscopy analysis was performed on a Surface Science Instrument, M-Probe, operating with an Al  $K_{\alpha}$  radiation and total resolution of  $\sim 0.8$  eV.

### **3.2.2 Fluid simulation of CVD process**

Computational fluid dynamics (CFD) is one of the branches of fluid mechanics that uses numerical methods and algorithms to solve and analyze problems that involve fluid flows. Computers are used to perform the millions of calculations required to simulate the interaction of liquids and gases with surfaces defined by boundary conditions. This method can reduce the need for expensive prototypes, and provide comprehensive data that is not easily obtainable from experimental tests. On the other hand, it can be used to complement physical testing. Some designers use it to analyze new systems before deciding which validation tests. When troubleshooting, problems are solved faster and more reliably because fluid dynamics analysis highlights the root cause. In addition, when optimizing new equipment designs, many what-if scenarios can be analyzed in a short time. This can result in improved performance, reliability and product consistency.

The software of FLUENT 6.3 was used to simulate the fluid dynamics of CVD process following the Dynamic Mesh Modeling. Then the FLUENT GAMBIT 2.3 was used to build the geometry model (ANSYS Inc.).

### **3.2.3 Physical properties**

The physical properties of 1D nanostructures were characterized using various methods, such as photoluminescence, gas sensing performance, electrical properties, surface wettability and field-effect transistor properties in this work.

#### **3.2.3.1 Photoluminescence**

Photoluminescence (PL), which is the spontaneous emission of light from a material under optical excitation, is a process in which a substance absorbs photons (electromagnetic radiation) and then re-emits photons. Quantum



mechanically, this can be described as an excitation to a higher energy state and then a return to a lower energy state accompanied by the emission of a photon possessing energy corresponding to the band gap. The excitation energy and intensity are chosen to probe different regions and excitation concentrations in the sample. PL investigations can be used to characterize a variety of material parameters. PL spectroscopy provides optical (as opposed to mechanical) characterization, and it is a selective and extremely sensitive probe of discrete electronic states. Features of the emission spectrum can be used to identify surface, interface, and impurity levels and to gauge alloy disorder and interface roughness. The intensity of the PL signal provides information on the quality of surfaces and interfaces. Under pulsed excitation, the transient PL intensity yields the lifetime of nonequilibrium interface and bulk states. Variation of the PL intensity under an applied bias can be used to map the electric field at the surface of a sample. In addition, thermally activated processes cause changes in PL intensity with temperature.

The laser used had 160 femtoseconds pulse duration (2.5 J per pulse, at 796 nm wavelength and 500 Hz repetition rate) on an Integra-C from Quantronix. The beam is split (70:30) and the 70 % beam is sent to an Optical Parametric Amplifier (OPA) (TOPAS-C from Light Conversion). The 240 nm laser beam is produced by generation of second harmonic from 480 nm, itself produced by sum frequency in the OPA.

The wavelengths were separated by the use of a diffraction grating. However, the 240 nm beam contains still a small scattered part of the 480 nm, since no appropriate filter could cut the 480 nm and let the 240 nm unaffected. A diaphragm limits the beam to its diameter size (approximately 5 mm) to reduce 480 nm background scattering. The beam is sent onto the sample. The scattered and emitted light from the sample surface was collected by lenses and sent onto the optic fiber of the spectrometer (USB4000 from Ocean

Optics). Each spectrum measured was the integration of the signal recorded over 10 seconds, i.e. 5000 shots.

### 3.2.3.2 Gas sensing

In this work, nanowire-based gas sensors were fabricated by contacting nanowire samples (as-prepared and plasma-treated) with gold wires and gold paste. Gas sensing performance of 1D nanostructures was characterized by a custom-built PC-automated gas sensing system with a chamber volume of 30 cm<sup>3</sup> (Figure 19). Measurement vapor with 1000 ppm concentration were mixed with synthetic air (flow rate: 200 sccm) and passed into the chamber maintained at accurate gas pressure using mass flow controllers, and a fixed heating temperature of the sensor platform.

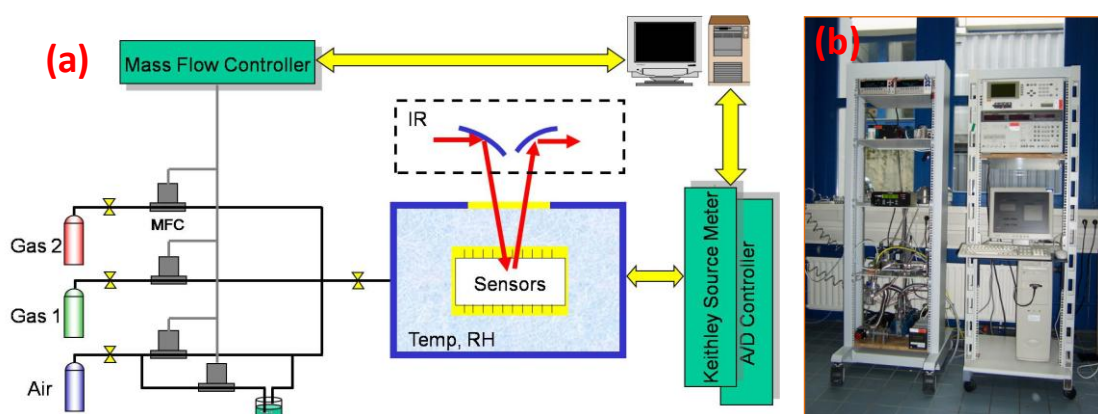


**Figure 19:** (a) Schematic presentation and (b) image of the PC-automated gas sensing system used in this work.

During the on/off gas sensing measurement, the response time and recovery time (defined as the time required to reach 90 % of the final equilibrium value) were 30 s and 270 s, respectively. The sensitivity ( $S$ ) of a sensor is defined as  $S = R_{\text{air}} / R_{\text{gas}}$ , where  $R_{\text{air}}$  is the sensor resistance in air (relative humidity is about 40 %) and  $R_{\text{gas}}$  is the resistance of the sensor when exposed to the target vapor (C<sub>2</sub>H<sub>5</sub>OH, CO).

### 3.2.3.3 Electrical transport

Individual SnO<sub>2</sub> nanowires were transferred onto suspended silicon membranes equipped with integrated microheaters and platinum interdigitated microelectrodes. Nanowires were electrically contacted to platinum microelectrodes by a lithography process using a FEI Dual-Beam Strata 235 FIB instrument combined with a trimethyl-methylcyclopentadienylplatinum [(CH<sub>3</sub>)<sub>3</sub>CH<sub>3</sub>C<sub>5</sub>H<sub>4</sub>Pt] injector to deposit platinum.<sup>[240]</sup> Four-probe DC electrical measurements were performed to avoid the parasitic contribution of the metal-semiconductor interfaces at the contacts<sup>[241]</sup> using an electronic circuit designed to guarantee and control low current levels ( $I_m \leq 0.1$  nA) minimizing undesired self-heating effects,<sup>[242]</sup> as shown in Figure 20.

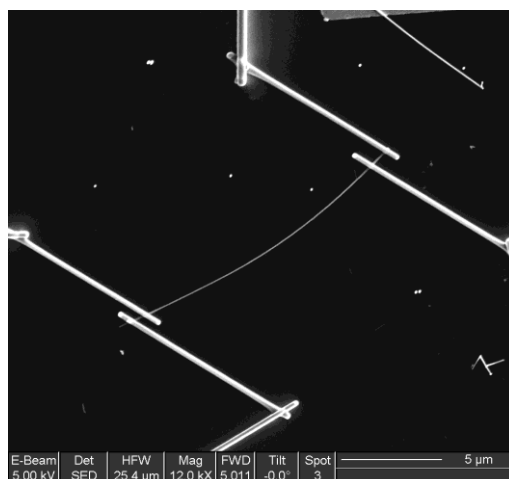


**Figure 20:** SEM image of one of the nanowires contacted in a 4-probes configuration.

$I$ - $V$  curves were acquired by using a Keithley 2400 source meter. The gas sensing experiments were carried out inside a home-made test chamber, in which accurate gaseous environments were maintained with mass-flow controllers mixing synthetic air (SA) and CO (1000 ppm  $\pm$  1 % in SA). These lab-class gases contained less than 5 ppm / V of C<sub>n</sub>H<sub>m</sub> and H<sub>2</sub>O. An electronic circuit designed to apply low current levels  $I_m$  (from 0.1 to 300 nA) and to avoid undesired fluctuations was used to record the changes of nanowire

resistance.<sup>[243]</sup>

All measurements were carried out in a ProboStat cell placed inside a furnace to control the working temperature, which was monitored by a thermocouple located next to the sample. The experimental setup (cell and furnace) was found to act as a Faraday cup which avoids electrical measurements from being affected by external electromagnetic noise. Devices were fabricated using SnO<sub>2</sub> nanowires with lengths between 5 and 15 μm, and radii between 35 and 45 nm, which showed reproducible electrical responses in experiments repeated during 4 weeks.

At last 2 individual devices were tested for each result, which showed consistent results apart from a small number (10 %) in which the performance was influenced by slight material modification, contact instabilities (FIB preparation), or twinning in NWs.

#### **3.2.3.4 Surface wettability**

Surface wettability of one-dimensional nanostructures was investigated by measuring the water contact angle (CA). The contact angles were measured on a DSA100 Krüss instrument at 25 °C using the sessile drop fitting method for the static contact angle and deionized water (5 μL) as test solution. Contact angles were determined using the tangent method. For each drop on a substrate, approximately 10 images were recorded and averaged to obtain a mean contact angle. At least five spots per substrate were averaged. Contact angles were recorded after stabilization and were checked on several surfaces.

#### **3.2.3.5 Field-effect transistor**

The SnO<sub>2</sub> nanowires were harvested from the Al<sub>2</sub>O<sub>3</sub> substrate by ultra-sonicating in ethanol. In order to prevent agglomeration the harvested

nanowires were redispersed in dichlorobenzene. They were then dropcasted on a Si/SiN substrate with a SiN thickness of 300 nm. Heavily n-doped silicon (Si) wafers with a 300 nm thick top SiN layer were patterned using photoresist AZ7220 (from Clariant). The silicon wafer and its surface SiN layer served as the gate electrode and gate dielectric, respectively. Finally, aluminium electrodes were defined on the substrate by photolithography and lift off process. The patterned Au electrodes were additionally immersed in a 3 mM solution of alkanethiol in ethanol at room temperature for 24 h, rinsed with hexane and ethanol, and dried with nitrogen gas. The devices were characterized using an Agilent 4157B semiconductor parameter analyzer system. The structures of the bottom-contact SnO<sub>2</sub> nanowires based network transistor were illustrated in Figure 21.

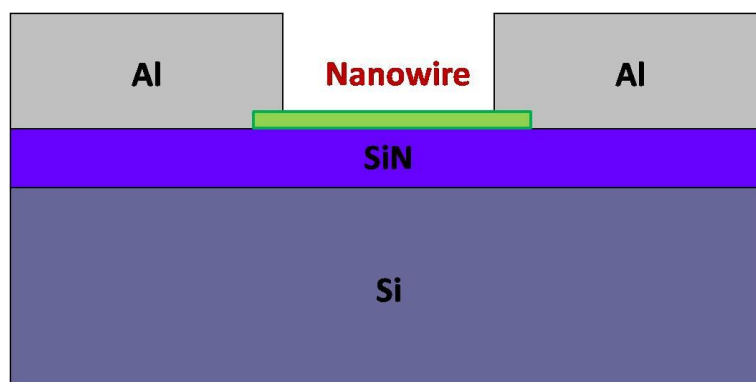


**Figure 21:** Structural illustration of the bottom-contact SnO<sub>2</sub> nanowires based network transistor.

### 3.2.3.6 Photoconductivity

Photoconductivity performance was characterized by a modified UV-VIS machine chamber. The sample was fixed on the focus of irradiation light, and contacted on two electrodes with gold wires and gold paste. A Keithley 4200 source meter was used to record the current of nanowires under the light scanning in a wavelength range of 200-800 nm.

## 4 Systematic Study on Growth of SnO<sub>2</sub> Nanowires

A molecule-based chemical vapor deposition (MB-CVD) process with Sn(O<sup>t</sup>Bu)<sub>4</sub> precursor was used at growth temperatures (~ 700 °C). Nanowires grown by vapor-liquid-solid (VLS) mechanism, whereby gold nanoparticles were used as catalysts. The influences of the growth parameters (deposition temperature, precursor temperature, size of catalyst and the angle of graphite susceptor) on the size, morphology, and dimensionality of high-density single crystalline SnO<sub>2</sub> nanowires were systematically elaborated in this work, followed by the characterization of the electrical, photoluminescence, gas sensing and field-effect transistor properties of SnO<sub>2</sub> nanowires.

### 4.1 Introduction of tin oxide nanowires

As an n-type direct wide band semiconductor ( $E_g = 3.6$  eV at 300 K), SnO<sub>2</sub> is a key functional material that has been used extensively for gas sensor,<sup>[244]</sup> optoelectronic devices,<sup>[245]</sup> catalysts,<sup>[246]</sup> transparent conducting electrodes and antireflective coatings, while responding to the test gas, which effectuates the differential sheath conductivity as a function of the analyte gas concentration.<sup>[247]</sup> 1D tin oxide nanostructures have been synthesized by a variety of techniques, including vapor transport,<sup>[248]</sup> carbothermal reduction,<sup>[249]</sup> molecule-based chemical vapor deposition (MB-CVD),<sup>[218]</sup> laser ablation of pure tin in an oxidizing Ar/O<sub>2</sub> atmosphere,<sup>[250]</sup> oxidation of electrodeposited tin wires,<sup>[251]</sup> oxidation of tin vapors at elevated temperatures,<sup>[252]</sup> solvothermal synthesis,<sup>[253]</sup> and electrospinning.<sup>[254]</sup> To date, many studies have focused on controlled synthesis of metal oxide NWs using the VLS mechanism,<sup>[255]</sup> as well

as thermodynamic and kinetic size limit of NWs growth. However, few studies exist on the growth kinetics of metal oxide NWs, especially theoretical studies related to growth mechanism.<sup>[256]</sup>

Randomly grown nanowires usually show broad distribution in growth direction and surface facets, due to the distribution in the size of catalysts and differential mobilities of the precursor species adsorbed on the substrate.<sup>[257]</sup> The widely used VLS mechanism for growing nanowires provides the control over axial and radial dimensions through gas phase supersaturation and catalyst size, respectively. The synergy of MB-CVD and VLS growth mechanism was used in this work to achieve controlled synthesis of nanowires at lower temperatures.

## 4.2 Controlled synthesis of SnO<sub>2</sub> nanowires

The CVD process is extremely sensitive to processing parameters, such as substrate temperature ( $T_s$ ), precursor temperature ( $T_p$ ), size of catalyst and angle of graphite susceptor, which play an influential role on the size, morphology, composition and dimensionality of nanostructures. To obtain the reproducible results, it is crucial to operate the nanostructures growth under optimal setting of processing parameters. However, the long time (~ 120 min) required for finding executing individual CVD experiment, optimal processing parameters through *trial and error* can be challenging. Hence identifying the optimal processing parameters for nanostructures growth is an important goal. Since even slightest temperature gradient can influence the morphological features and lead to inhomogeneous CVD deposits. To establish reproducible synthetic procedures, the development of a simulation based methodology for predicting the optimal processing parameters for CVD system is highly desirable.

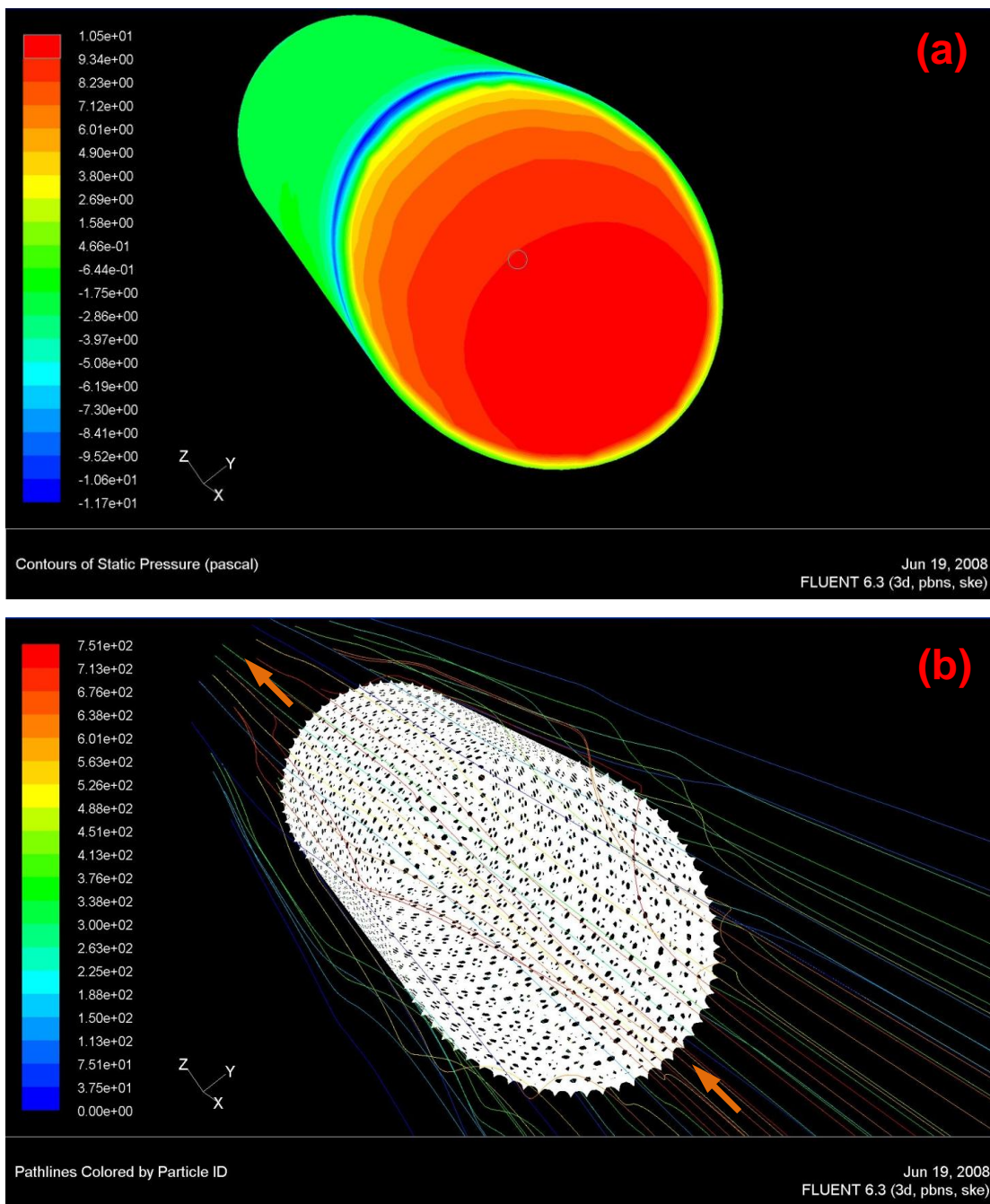


**Figure 22:** Simulation contours of (a) pressure and (b) gas flux profiles on the graphite susceptor.

In order to model the pressure distribution and precursor flow, fluid simulations have been performed by the software of FLUENT 6.3. As shown in Figure 22, the contours of pressure and gas flow are symmetric with respect to the central horizontal axis of the graphite susceptor. The slight variation of pressure and gas flux profiles in the region over the graphite susceptor is



realistic and is subjected to the position of graphite susceptor in the high frequency field. In order to ensure, similar pressure and gas flux profiles during all the screening CVD experiments, the simulation results were used to fix the position of the substrate susceptor in the individual field in such a way to avoid any significant fluctuations of experimental conditions.

#### 4.2.1 Influence of deposition temperature

The temperature at which the nanostructure is deposited is critical as it controls both the thermodynamics and the kinetics of the deposition process. The substrate temperature ( $T_s$ ) is crucial chemical reaction of precursor to occur on the substrate only and not in the gas phase. The later will lead to homogeneous gas phase reactions, which lead to particle formation in the gas phase. Small changes in the temperature (e.g.  $\pm 25$  °C) may change the reaction, and/or its kinetics, inhomogeneous surface coverage and different morphological features. Figure 23 shows the SEM images of SnO<sub>2</sub> nanowires grown at different deposition temperatures (650, 700, 750 and 800 °C), which demonstrate the influence of  $T_s$  on film morphology.

Uniform, high-density SnO<sub>2</sub> NWs with diameters of 50-80 nm and lengths up to 20  $\mu$ m could be synthesized at 750 °C. The density of these SnO<sub>2</sub> NWs gradually changes when the deposition temperature is changed to higher or lower values. The increase of the deposition temperature can result in the enhancement of the diffusion and reaction rate to elongate the NWs so that the density of NWs is decreased owing to Ostwald ripening.<sup>[258]</sup> At high deposition temperatures, the deviation in chemical potential between large and small materials becomes significantly important. If the dimension (size) of the nuclei in the initial growth of NWs is larger than the minimum size, they tend to coarsen. Otherwise, they tend to disappear, resulting in a decreased density of NWs during the growth process. On the contrary, the decrease of the

deposition temperature below the eutectic temperature for the catalyst-semiconductor system can't result in a liquid droplet of the catalyst/semiconductor composite. Hence, the density of SnO<sub>2</sub> NWs also increases.

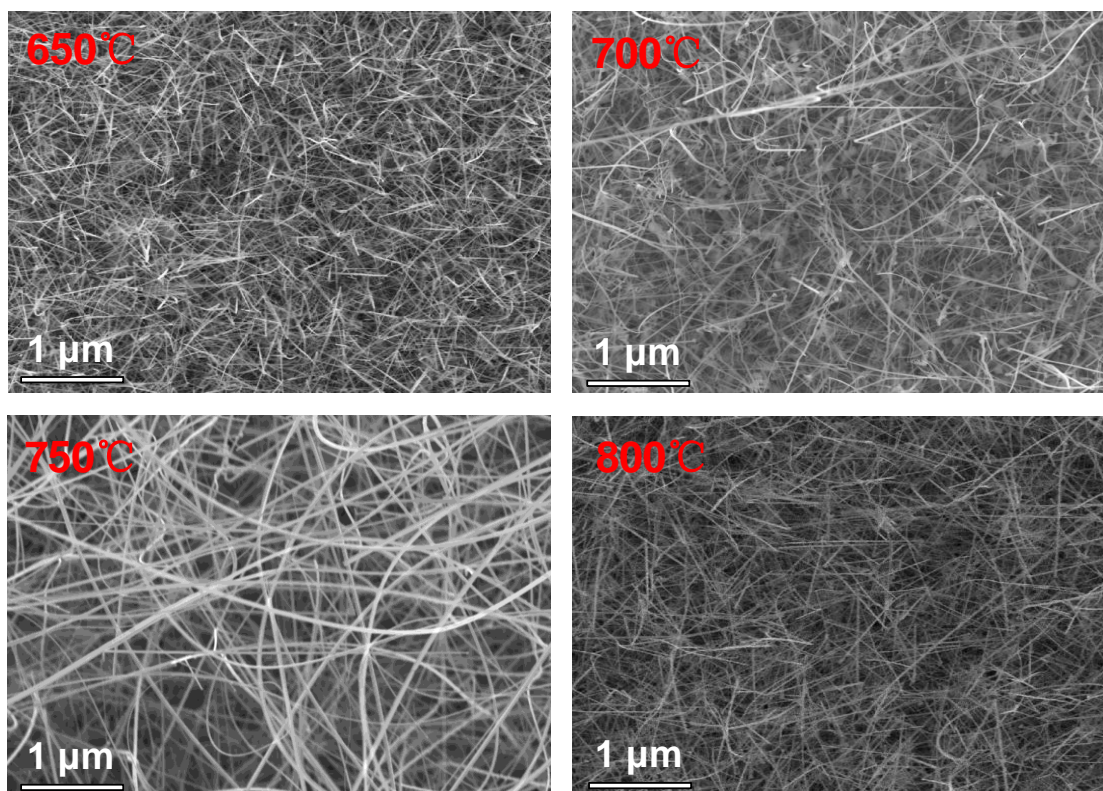


**Figure 23:** SEM images of SnO<sub>2</sub> nanowires grown at different deposition temperatures.

#### 4.2.2 Influence of precursor temperature

The next parameter important for the CVD process is the precursor temperature, which controls the precursor partial pressure in the gas phase. The ability of reactant gas to reach the substrate surface and the temperature at which the reaction is gas diffusion limited, are key factors in determining the uniformity of the nanostructures.<sup>[259]</sup> However, the transport of reactant gas to the substrate surface is directly controlled by precursor temperature, which

determines the flux under high vacuum (10<sup>-6</sup> Torr).

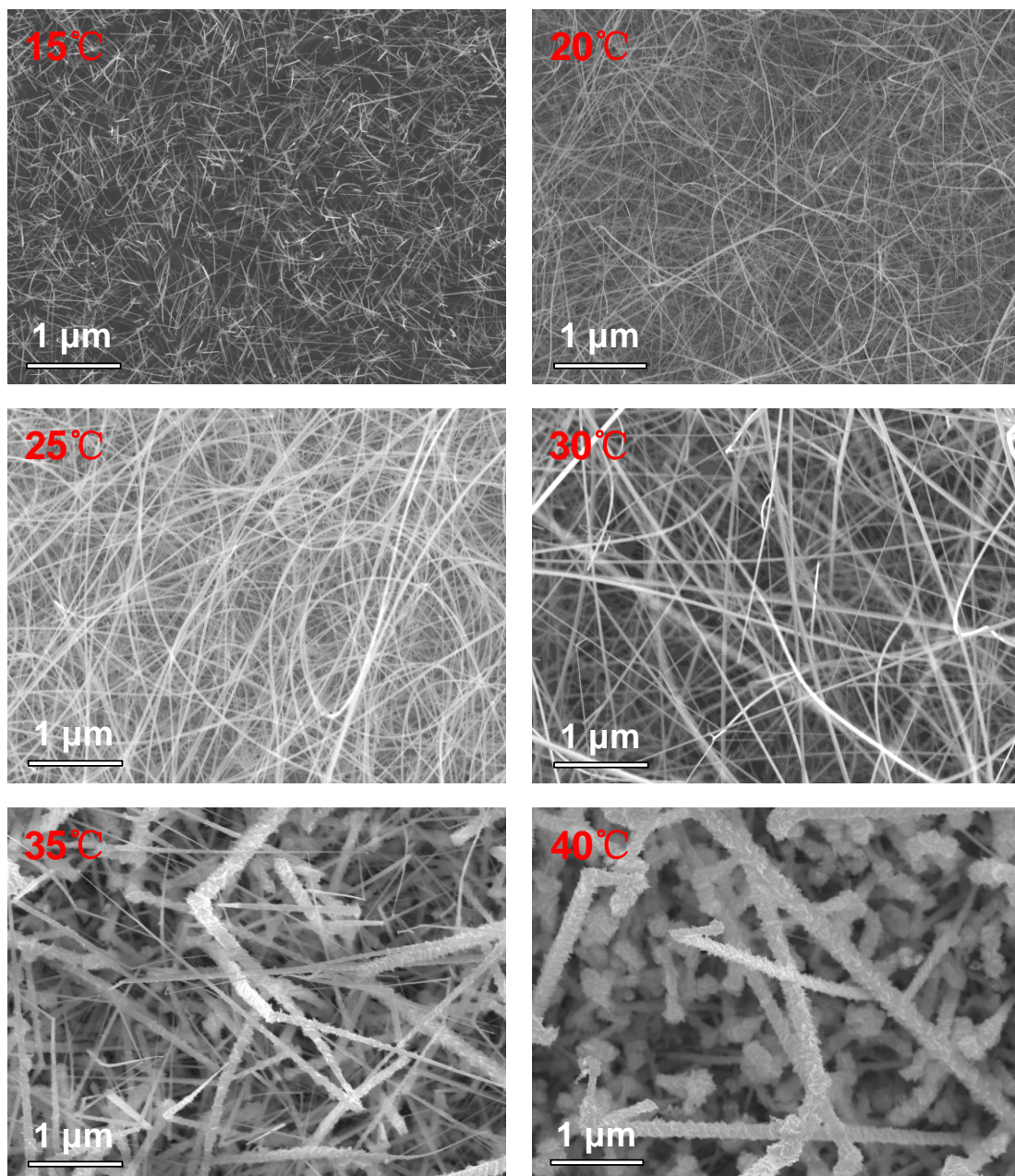


**Figure 24:** SEM images of SnO<sub>2</sub> nanowires grown at different precursor temperatures.

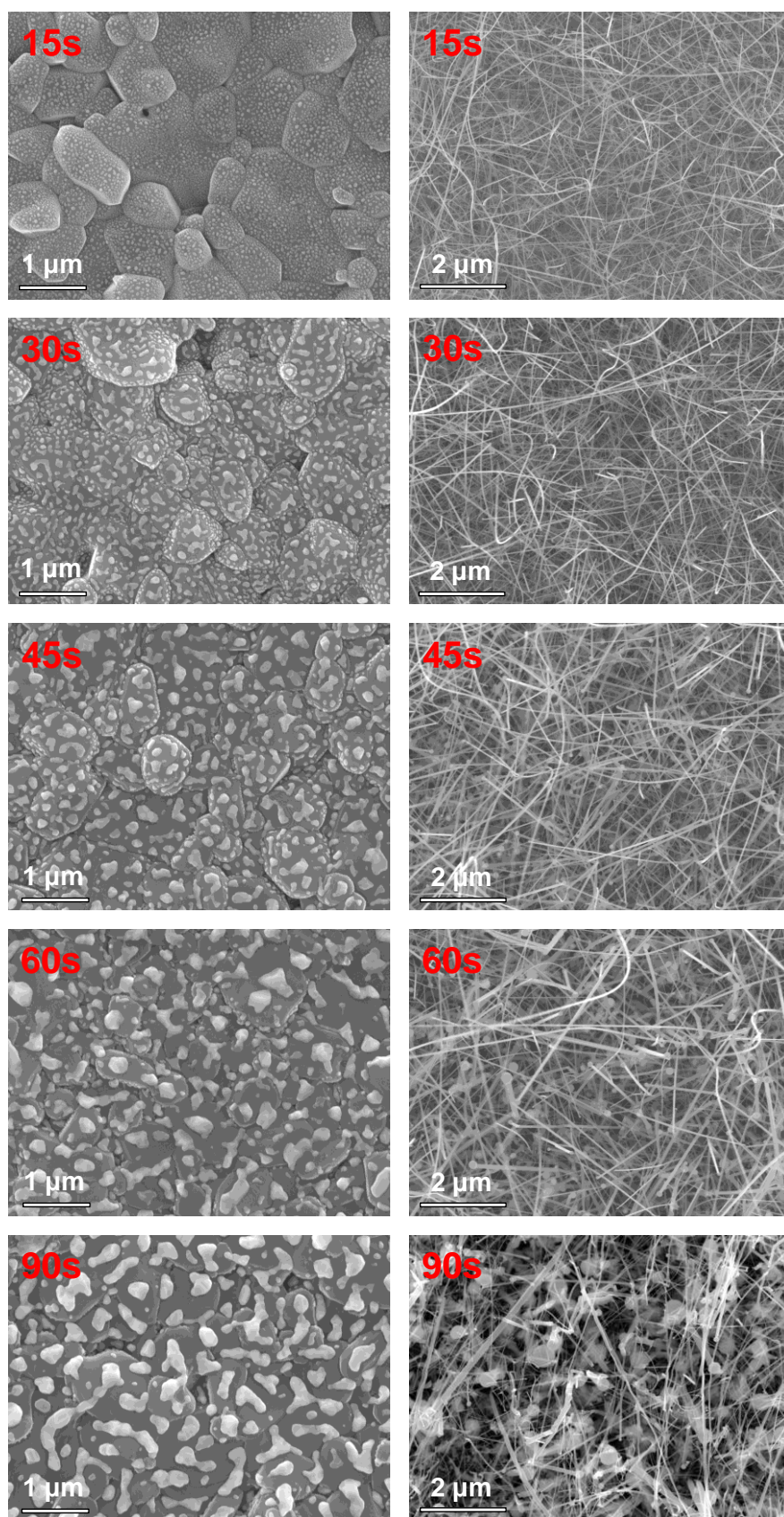
The influence of precursor temperature on the morphology of SnO<sub>2</sub> nanowires at 15, 20, 25, 30, 35 and 40 °C is shown in a series of SEM images in Figure 24. A low precursor temperature (15 °C) resulted in the low precursor

flux, leads to the possibility for NW growth via the tip-growth mechanism, due to the low supersaturation of molecular precursor in the gas phase. This is evidencing in the low lateral density of nanowires. Secondly, at a given gas flow, the low precursor temperature can result in a long resident time that can easily cause different growth rates at different reaction areas, leading to the growth of non-uniformly distributed NWs on the substrate. By reducing the resident time via increasing the flow rate, growth of uniformly distributed NWs can be enhanced. However, the density is nonuniform when the precursor temperature is more than 30 °C, because the precursor flux is oversaturated in catalyst/semiconductor composite, resulting in polycrystalline structures formed. Especially, the growth followed the multi-dimensional growth model when the precursor temperature is at 40 °C. Accordingly, the precursor temperature about 25 °C found in the present study is a moderate value to grow uniform and high density SnO<sub>2</sub> NWs. On another hand, the effect of different precursor temperatures on the morphology provides a reasonable basis that CVD process followed the VLS mechanism.

### **4.2.3 Influence of size of catalyst**

The VLS mode is a catalyst-assisted growth process which uses metal nanoparticles as the nucleation seeds that act as catalysts for controlling the growth direction and diameter of 1D nanostructures. SnO<sub>2</sub> nanowires were grown by heating Al<sub>2</sub>O<sub>3</sub> substrate covered with Au particles as catalyst, whereby their diameters was determined by the size of Au particles.<sup>[218]</sup> The Au particles were produced by annealing Au thin layer sputtered by PVD, which demands a precise control of the deposition parameters (sputtering current and time). In this study sputtering current is fixed at 20 mA, the size of Au particle was only governed by sputtering time ( $t_s$ ). That is to say, the sputtering time of Au film decided the diameter of SnO<sub>2</sub> nanowires.





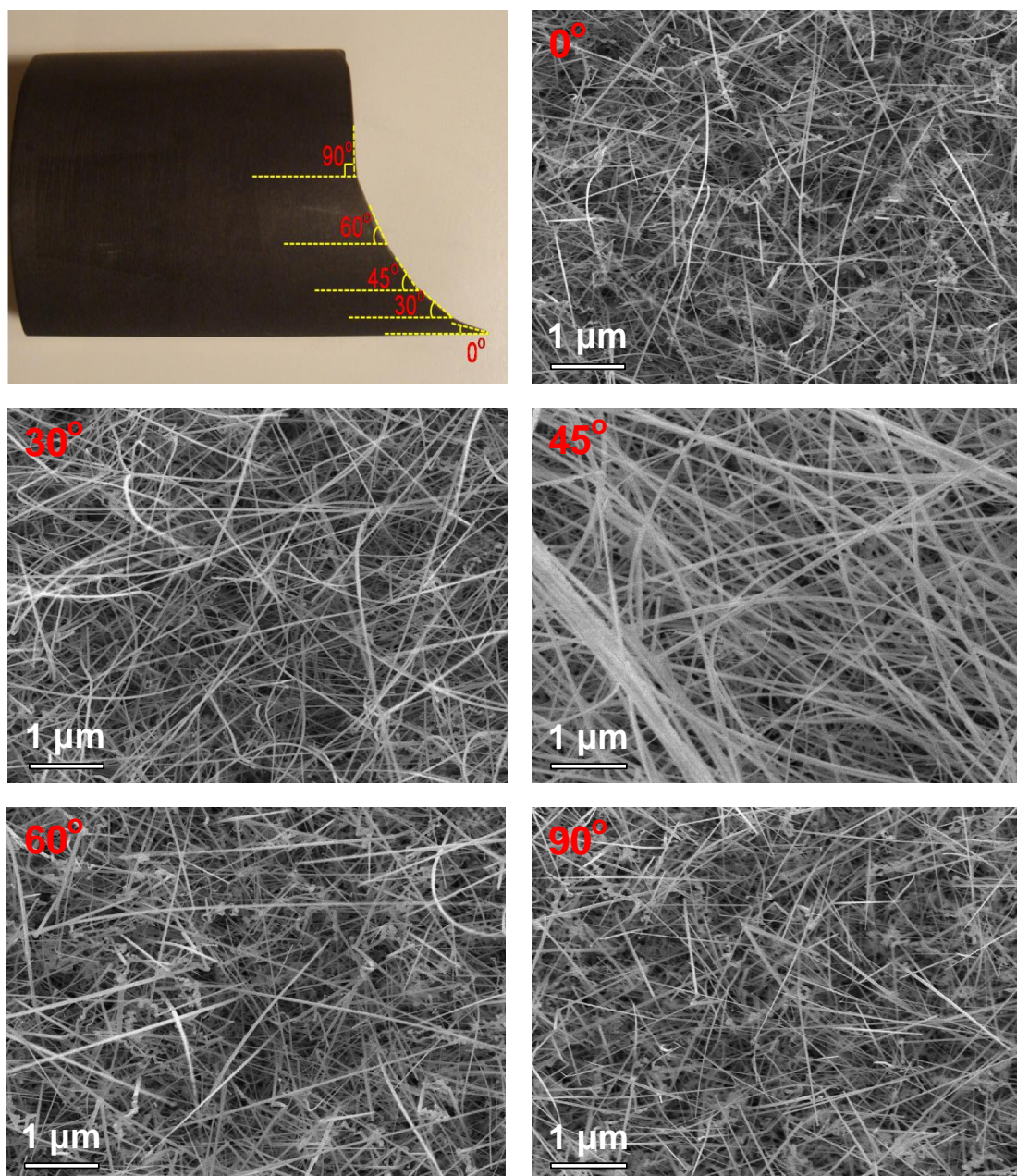
**Figure 25:** SEM images of morphology before and after CVD process at the different sputtering times.

Figure 25 shows SEM images of morphology before and after CVD process at the different sputtering times. It revealed that the observed difference in the diameters is due to the variation in the size of the initial Au particles. The size of Au particles and the diameter of SnO<sub>2</sub> NWs increased when the sputtering time was prolonged, the density of SnO<sub>2</sub> NWs decreased in contrary. When the sputtering time was 15-30 s, the high-density single crystalline SnO<sub>2</sub> NWs with the diameter 60-90 nm were observed, it was accordance with the size of Au particles. The low-density of SnO<sub>2</sub> NWs were found in 45-60 s, the diameter is about 100 nm. While the density of NWs was significantly decreased in the case of 90 s, the big flake-like Au particles can be seen on the bottom of the NWs and the nanostructures were sheetlike polycrystalline structures. It is evident that sputtering time strongly influenced the morphology and diameter of NWs. Hence, the proper sputtering time was between 15-30 s, it was fixed at 25 s in this study.

#### 4.2.4 Influence of angle of graphite susceptor

The angle of graphite susceptor is also an important factor in CVD process. The local growth environment on the substrate can critically affect the growth morphology of the nanostructures. Here, we first designed a graphite susceptor which contains different angles so that the local growth gas flow is angle-dependent and temperature across the entire substrate is same. The local growth environment, flow speed and pressure of growth could be investigated. Although the gas flow was stable and uniform in the entire substrate, the local variation of gas flow could be significant. Five different angles (0°, 30°, 45°, 60° and 90°) for the following study were chosen, and the corresponding nanostructures grown on the Al<sub>2</sub>O<sub>3</sub> substrate at 750 °C for 1 h are presented in Figure 26.





**Figure 26:** Photograph of graphite susceptor with five different angles and the corresponding SEM images of SnO<sub>2</sub> nanowires.

It is evident that different morphologies were formed in the different angles. When the angle was too small (0°), the morphology was sheetlike, and became a combination of sheetlike and NW-like at 30°. A wirelike morphology with uniform high density could be found at 45°, while the density of NWs significantly decreased at 60° and 90°, and the nanostructures converted into

could be polycrystalline structures indicating the formation of grain boundaries. A possible explanation can be attributed to the different concentrations of precursor flux in the local growth regions. The high flux provides a high concentration of precursor gas flow, resulting in an increased growth rate of the 2D structures.<sup>[260]</sup>

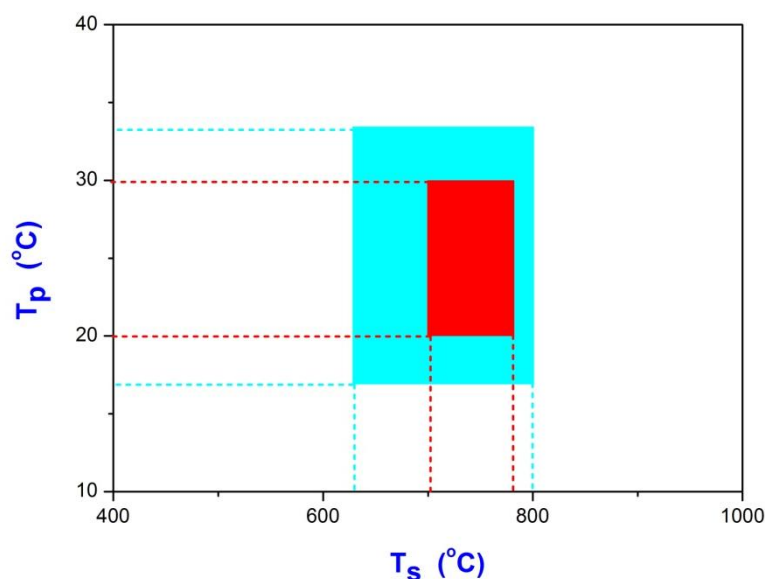


**Figure 27:** Schematic presentation of the suitable temperature area for the growth of SnO<sub>2</sub> nanowires.

Based on the systematic investigation of the main experimental conditions, such as deposition temperature, precursor temperature and angles of graphite susceptor, uniform and high-density single crystalline SnO<sub>2</sub> NWs can be fabricated by MB-CVD via VLS mechanism. The suitable temperature area was indicated, as shown schematically in Figure 27. The area with the deposition temperature range of 700-775 °C and precursor temperature range of 20-30 °C, indicated by red frame, is the most suitable area for the growth of uniform and high density single crystalline SnO<sub>2</sub> NWs. When the deposition temperature and precursor temperature were set outside the indicated (cyan colour) area, combination of uniformly multi-dimensional and low-density



wire-like nanostructures were fabricated. In other area, no nanowires were found. Hence, the growth conditions controlled in the indicated red area offer the optimized condition in order to synthesize the higher quality nanowires.

Finally, based on the systematic study of the influence of the CVD processing parameters such as substrate temperature ( $T_s$ ), precursor temperature ( $T_p$ ), size of catalyst and angle of graphite susceptor on the size, morphology, composition and dimensionality of SnO<sub>2</sub> nanowires, the best conditions ( $T_s = 750$  °C,  $T_p = 25$  °C,  $t_s = 25$  s, angle of graphite susceptor is 45°) were obtained to grow the high-density single crystalline SnO<sub>2</sub> NWs in this study.

### 4.3 Characterization of SnO<sub>2</sub> nanowires

The crystal structures of tin oxide nanowires on Al<sub>2</sub>O<sub>3</sub> polycrystalline substrate were identified by means of XRD analysis, as shown in Figure 28. The XRD data revealed that all peaks belong to the rutile crystal structure according to PDF No. 41-1445.

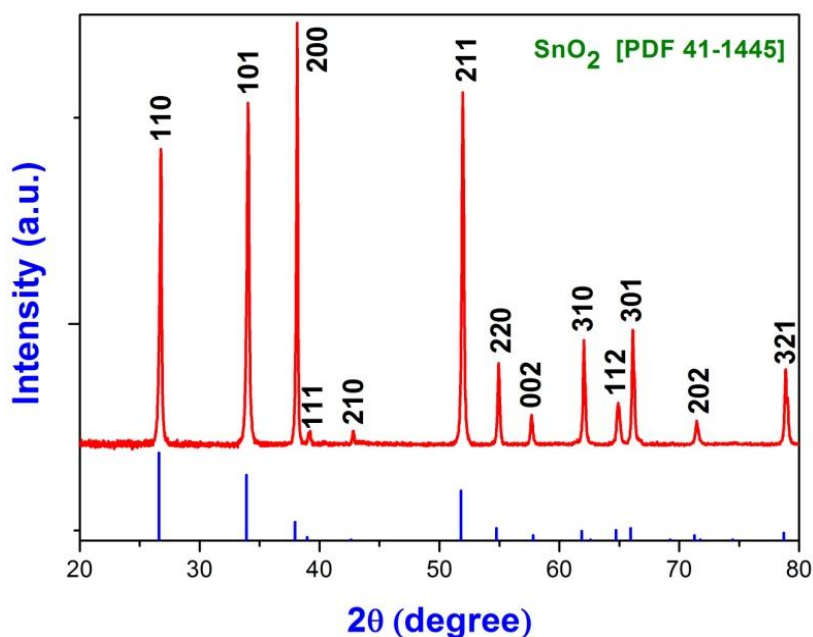


**Figure 28:** XRD patterns of tin oxide nanowires grown on Al<sub>2</sub>O<sub>3</sub> polycrystalline substrate.

The SEM (a) and TEM (b) images (Figure 29) revealed that uniform and high-density SnO<sub>2</sub> nanowires were fabricated on Al<sub>2</sub>O<sub>3</sub> polycrystalline substrate by MB-CVD. Meanwhile, it is clearly seen that multiply entangled ultra-long SnO<sub>2</sub> nanowires are about 50 μm, the diameter is about 40 nm. The polyhedral particle located on the nanowire tip was identified (EDX) to be Au, indicating a VLS growth.<sup>[218]</sup> The HR-TEM image confirmed the tin oxide nanowires to be single crystals with an interplanar spacing of 0.334 nm, which corresponds to the {110} plane of SnO<sub>2</sub> in the rutile phase. Rutile structure

SnO<sub>2</sub> has a primitive tetragonal unit cell, with unit cell parameters  $a = 4.738 \text{ \AA}$  and  $c = 3.187 \text{ \AA}$  (Figure 29 (c)). The tin cations have a co-ordination number of 6 meaning they are surrounded by an octahedron of 6 oxygen atoms. The oxygen anions have a co-ordination number of 3 resulting in a trigonal planar co-ordination.

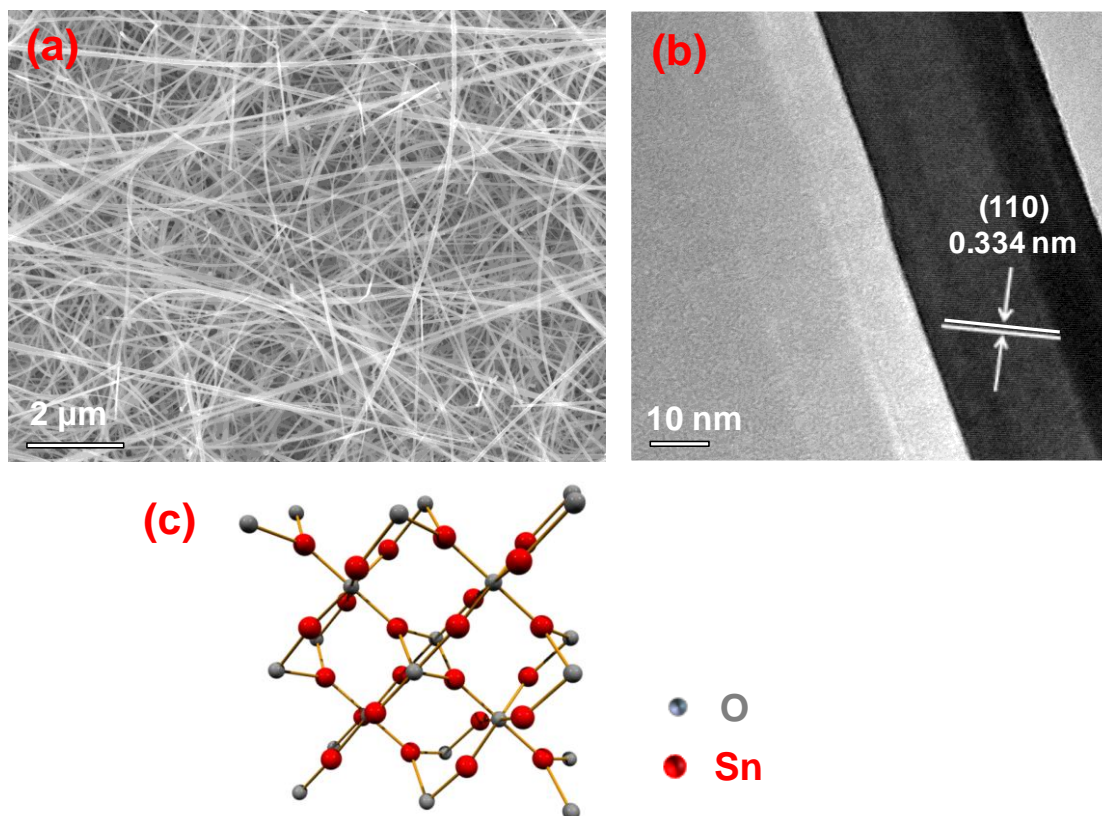


**Figure 29:** SEM (a) and TEM (b) images of SnO<sub>2</sub> nanowires grown on Al<sub>2</sub>O<sub>3</sub> polycrystalline substrate. (c) Fragment of SnO<sub>2</sub> unit cell.

## 4.4 Properties of SnO<sub>2</sub> nanowires

The SnO<sub>2</sub> NW-based sensor is based on a FET type nanodevice. In order to measure the current signals through the SnO<sub>2</sub> NW, two Au wires, used as electrodes, were connected with SnO<sub>2</sub> NW, and then fixed up by Ag and ceramic paster.

Figure 30 represents current-voltage (*I-V*) characteristics of the SnO<sub>2</sub> NW-based sensor in dry ambient condition at different temperatures. In the temperature range 20-260 °C, *I-V* curves of the device exhibit the linear behavior, which proves a good ohmic contact between the SnO<sub>2</sub> NW and Au electrodes.

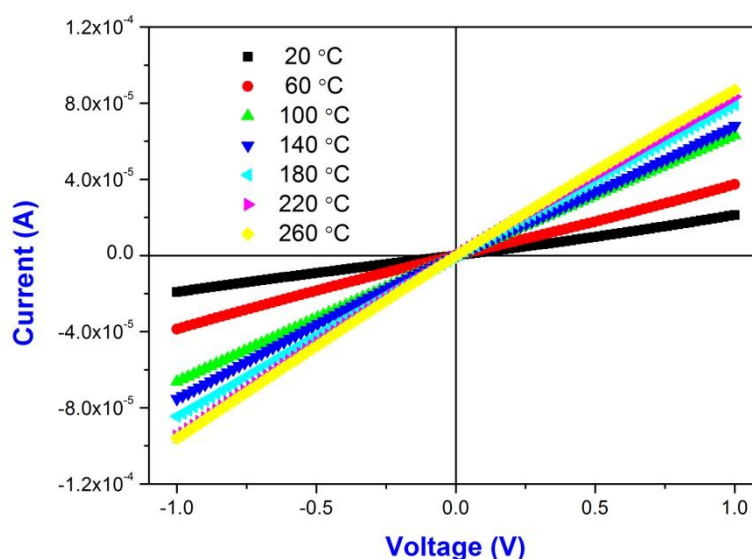


**Figure 30:** Current-voltage (*I-V*) characteristics of the SnO<sub>2</sub> NW-based sensor in dry ambient condition at different temperatures.

At the same time, the variation of the resistance of the SnO<sub>2</sub> NW-based sensor at temperatures, 20, 60, 100, 140, 180, 220 and 260 °C, respectively, is shown in Figure 31. It is clearly seen that the resistance of the SnO<sub>2</sub> NW decreases promptly with the temperature increases. The resistance of the

SnO<sub>2</sub> NW is calculated to be about  $5.5 \times 10^4 \Omega$  at room temperature (20 °C), which is 3.6 times that ( $1.5 \times 10^4 \Omega$ ) at 100 °C and about 5.5 times that ( $1.0 \times 10^4 \Omega$ ) at 260 °C, and at higher temperatures, the resistance tends towards saturation. Obviously, temperature has a strong influence on the conductivity of SnO<sub>2</sub> NWs.

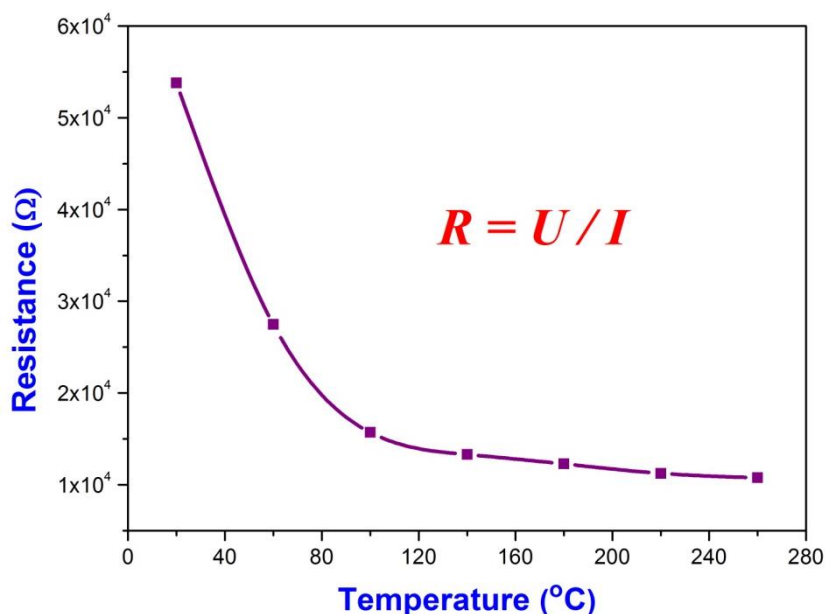


**Figure 31:** Variation of the resistance of the SnO<sub>2</sub> NW-based sensor at different temperatures.

Four-probe measurements performed on single SnO<sub>2</sub> NWs with length about 20 μm, and diameter about 80 nm, at room temperature (RT) produced slightly rectifying current-voltage (*I-V*) characteristics, as shown in Figure 32, which can be explained considering the existence of two back-to-back Schottky barriers connected in series to both extremes of the nanowires.<sup>[241]</sup> Conduction through these devices is dominated by reverse-biased junctions and, therefore, it is the major contribution to the total contact resistance. On the other hand, forward-biased junctions offer good electrical conduction and low contact resistance.

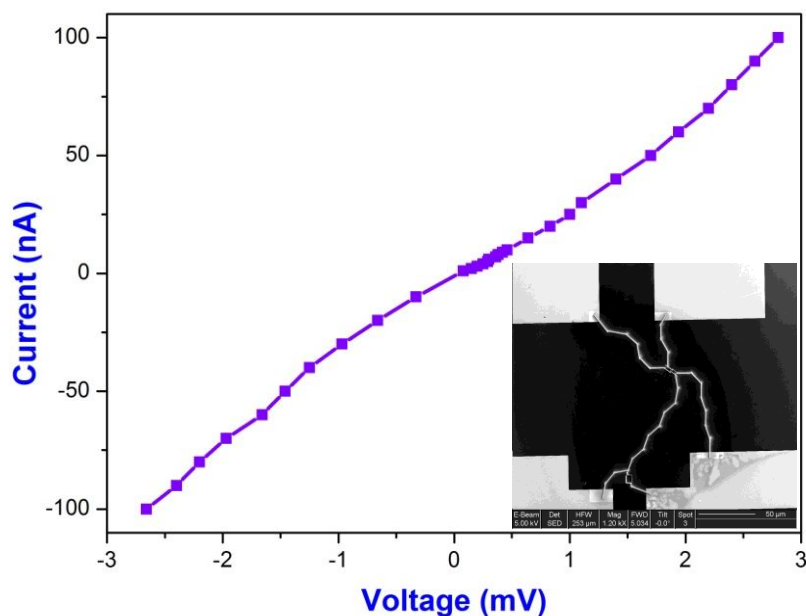


**Figure 32:** *I-V* curve of an individual SnO<sub>2</sub> nanowire at room temperature.

Photoluminescence (PL) measurement has also been carried out to evaluate the quality of the SnO<sub>2</sub> nanowires. Figure 33 shows the room-temperature PL spectrum of the SnO<sub>2</sub> nanowires. It displays a very strong visible emission band centered at about 510 nm, which is close to those in previous reports for an emission band of SnO<sub>2</sub> nanowires.<sup>[261]</sup> This emission band is associated with structural defects, probably due to high growth rate and less annealing time. (see Figure 58).

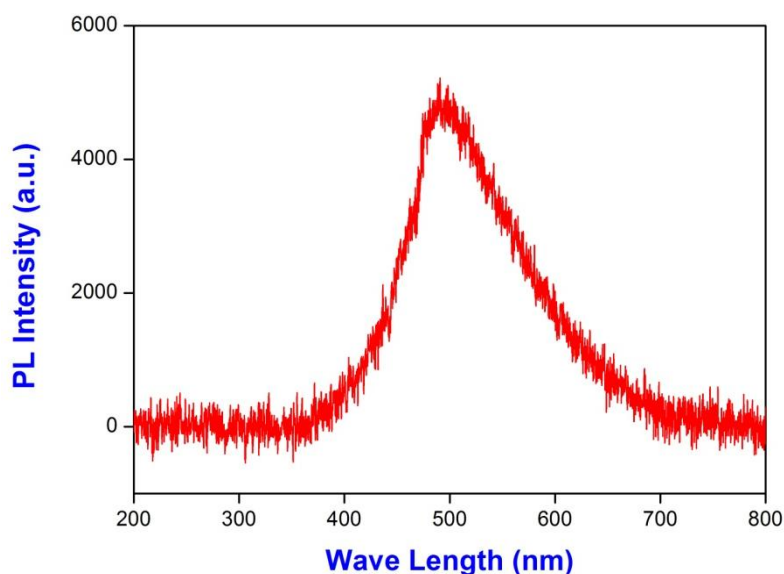


**Figure 33:** Room-temperature PL spectrum of the SnO<sub>2</sub> nanowires.

The gas sensing performance of SnO<sub>2</sub> nanowires in 1000 ppm ethanol and CO atmosphere at 250 °C is shown in Figure 34. The measurement gas was composed of 1000 ppm ethanol and CO respectively in synthetic air with a total flow rate of 200 sccm. All the samples show good reproducibility of device property with full recovery in different atmospheres during the four cycles. Furthermore, from the steep changes of the resistance in the response curves, SnO<sub>2</sub> nanowires possess short response and recovery time, and the responses also are reversible and comparable. Moreover, the sensors provide a very stable signal and reach their original baseline after each gas exposure cycle has been completed. These results are very promising for further development of SnO<sub>2</sub> nanowires based sensor devices.

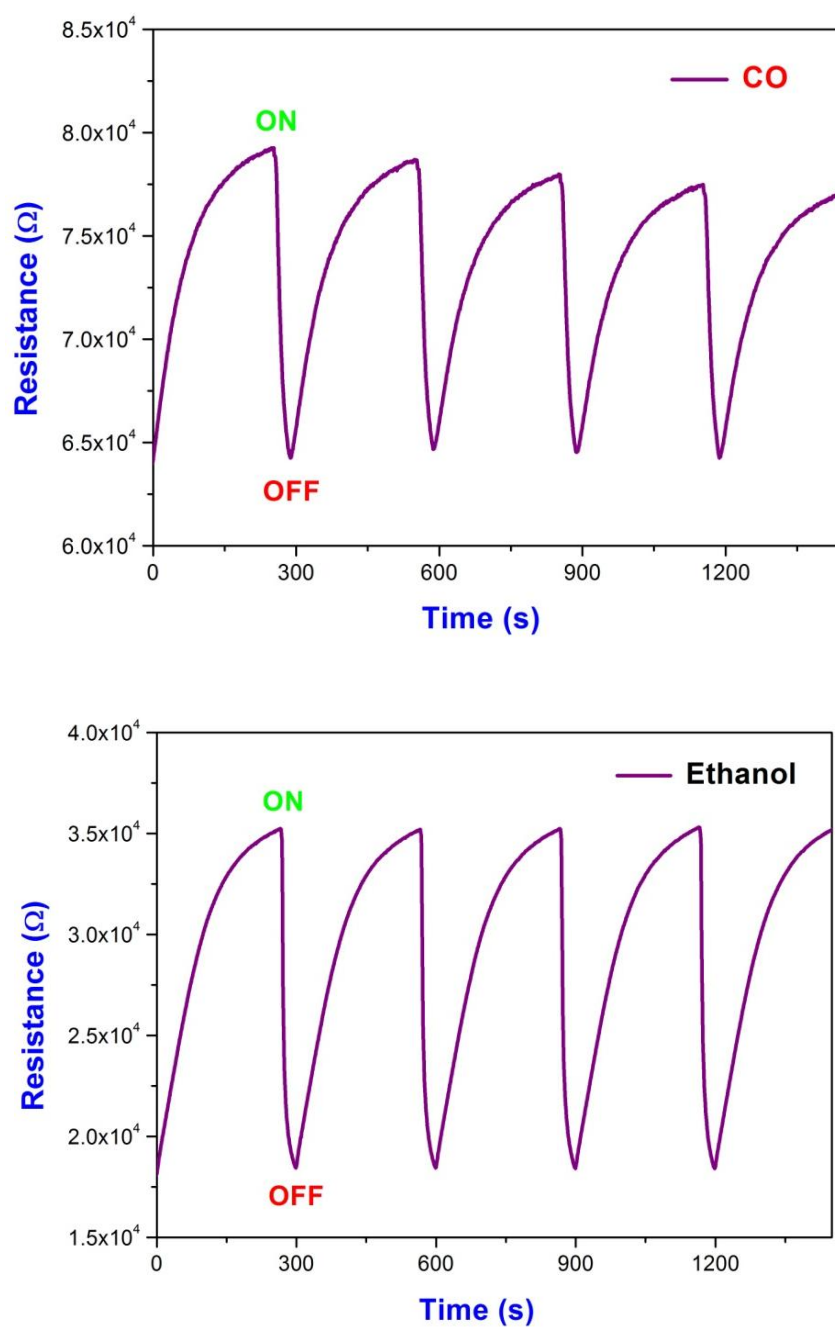


**Figure 34:** Gas sensing performance of SnO<sub>2</sub> nanowires in 1000 ppm ethanol and CO atmosphere at 250 °C.

Tests were made at different temperatures in order to find the optimum operating temperature for each analyte gas so as to get a calibration curve. The relations between working temperature and response toward different



gases are shown in Figure 35. It is evident from the curves that for all the test gases, the ethanol and CO gas sensitivity increases, while the associated operating temperature increases. The sensitivity variation is negligible in the case of the operating temperature below 100 °C. Furthermore, the response of the SnO<sub>2</sub> nanowires based sensor is greater toward ethanol atmosphere. Best response towards this gas is obtained at 260 °C, which is about 2.7.

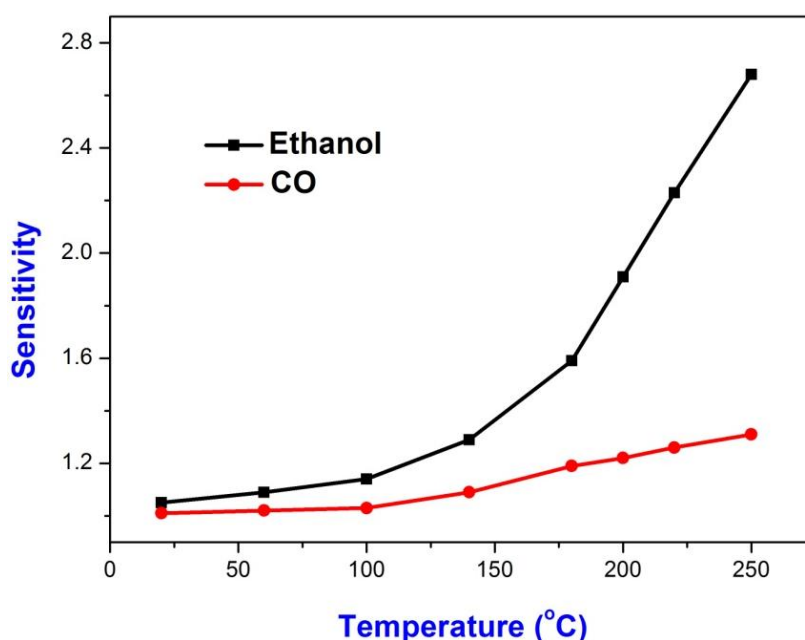


**Figure 35:** Gas sensitivity versus operating temperature of SnO<sub>2</sub> nanowires based sensor in 1000 ppm ethanol and CO atmosphere.

The FET based on SnO<sub>2</sub> nanowires was prepared and the  $I_d$ - $V_{ds}$  characteristics were measured with the different gate voltages under dark and illuminated conditions, as shown in Figure 36. It is clearly showed that the gate voltage and the lighting strongly influence the charge carrier transport properties. It is evident from the curve that for all tests, the current ( $I_d$ ) increases as the associated gate voltage ( $V_{gs}$ ) increases. The response under illuminated conditions has an enhanced performance, the maximum  $I_d$  could up to  $2.2 \times 10^{-8}$  A.  $V_{gs}$  was set from 0-50 V.

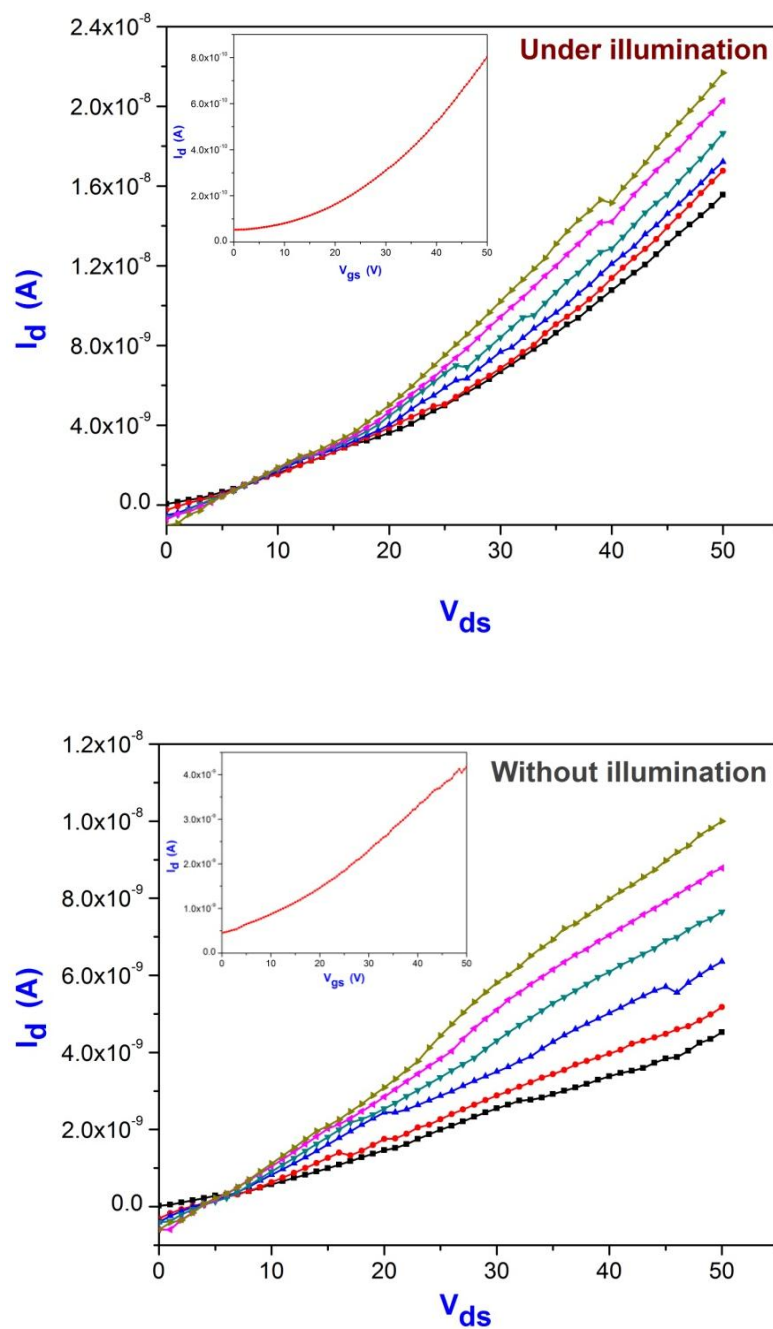


**Figure 36:**  $I_d$ - $V_{ds}$  characteristics of the SnO<sub>2</sub> nanowire based FET under dark and illuminated conditions. Inset: the variation curve of  $V_{gs}$ .

As the influences of the basic growth parameters (deposition temperature, precursor temperature, size of catalyst and angle of graphite susceptor) on the size, morphology, and dimensionality of high-density single crystalline SnO<sub>2</sub>

nanowires and the corresponding fundamental physical properties (electrical, PL, gas sensing and field-effect transistor) were systematic studied based on the simulation of CVD system. This enabled us to have a better understanding of SnO<sub>2</sub> nanowires, not only the growth process, but also the physical properties. Consequently, it paved the way to the further research (surface modification and nanowire based heterostructures), and the potential application of nanodevice fabrication.

## **5 Oriented Growth of SnO<sub>2</sub> Nanowire Arrays on TiO<sub>2</sub> Single Crystals**

In this chapter, the VLS growth mechanism of MB-CVD grown SnO<sub>2</sub> nanowire arrays on TiO<sub>2</sub> single crystals was discussed. The samples were characterized by various techniques (XRD, SEM, HR-TEM, AFM and cross sectional TEM) to understand the effect of substrate on morphology and the correlated growth directions - surface energy consideration - crystallographic relationship between the substrate and NW material. FIB-Tomography, a new approach, was exploited to reconstruct the 3D presentation of oriented SnO<sub>2</sub> nanowire arrays.

### **5.1 Growth patterns of SnO<sub>2</sub> nanowire arrays on TiO<sub>2</sub> single crystals**

#### **5.1.1 Introduction of nanowire arrays**

Controlled synthesis of ordered SnO<sub>2</sub> nanowire arrays in pre-defined orientations with respect to the substrate is meaningful for novel properties and the potential applications. The widely used VLS mechanism, for growing nanowires provides the control over axial and radial dimensions through gas phase supersaturation and catalyst size, respectively. However an oriented growth is majorly a function of the crystallographic features of substrate (polycrystalline or single crystal) and nanowire material (lattice mismatch).

To this end, only few reports exist on the fabrication of ordered SnO<sub>2</sub> nanowires.<sup>[262]</sup> In this study, molecule-based chemical vapor deposition (MB-CVD) has intrinsic advantages, such as relatively lower growth temperature (minimization of stress and mismatch due to thermal expansion in

nanomaterials), efficient feed-stock of precursor in the gas phase (precise control over supersaturation) and highly reactivity of the ionized gas phase species, whereby most of them deals with the synthesis of tin-doped indium oxide (ITO) nanowire arrays.<sup>[263-264]</sup> Ordered SnO<sub>2</sub> nanowires have been grown and aligned on the sapphire substrates ((100) or (110)), however, the growth mechanism of ordered SnO<sub>2</sub> NWs has not been investigated.<sup>[265]</sup> Given the technological importance of tin oxide, for instance in gas sensing applications,<sup>[257]</sup> fabricating of SnO<sub>2</sub> nanowire with controlled orientation and surface activity is of enormous value. Oriented growth of tin oxide nanowires on Au coated TiO<sub>2</sub> single crystal substrates, the growth mechanism and orientation-dependence of electrical properties of ordered tin oxide nanowires were reported here.

### **5.1.2 Structural study of SnO<sub>2</sub> nanowire arrays**

Tin oxide nanowires grown on single crystal (TiO<sub>2</sub>) substrates showed distinct morphological differences; whereas the different oriented growth with a meshlike network of straight NWs was observed on TiO<sub>2</sub> (001), (100), (110) and (101) substrates, respectively, as shown in Figure 37.

The polyhedral particle located on the nanowire tip was identified (EDX) to be Au, indicating a VLS kind of growth.<sup>[23]</sup> The different forms of tin oxide nanowires can be attributed to the influence of crystallographic orientation and coherent grain boundaries at the liquid-solid (L-S) growth front.

In this study, the case of SnO<sub>2</sub> nanowire arrays grown on TiO<sub>2</sub>(001) substrates was selected to illustrate the VLS growth mechanism of MB-CVD grown tin oxide nanowire arrays.

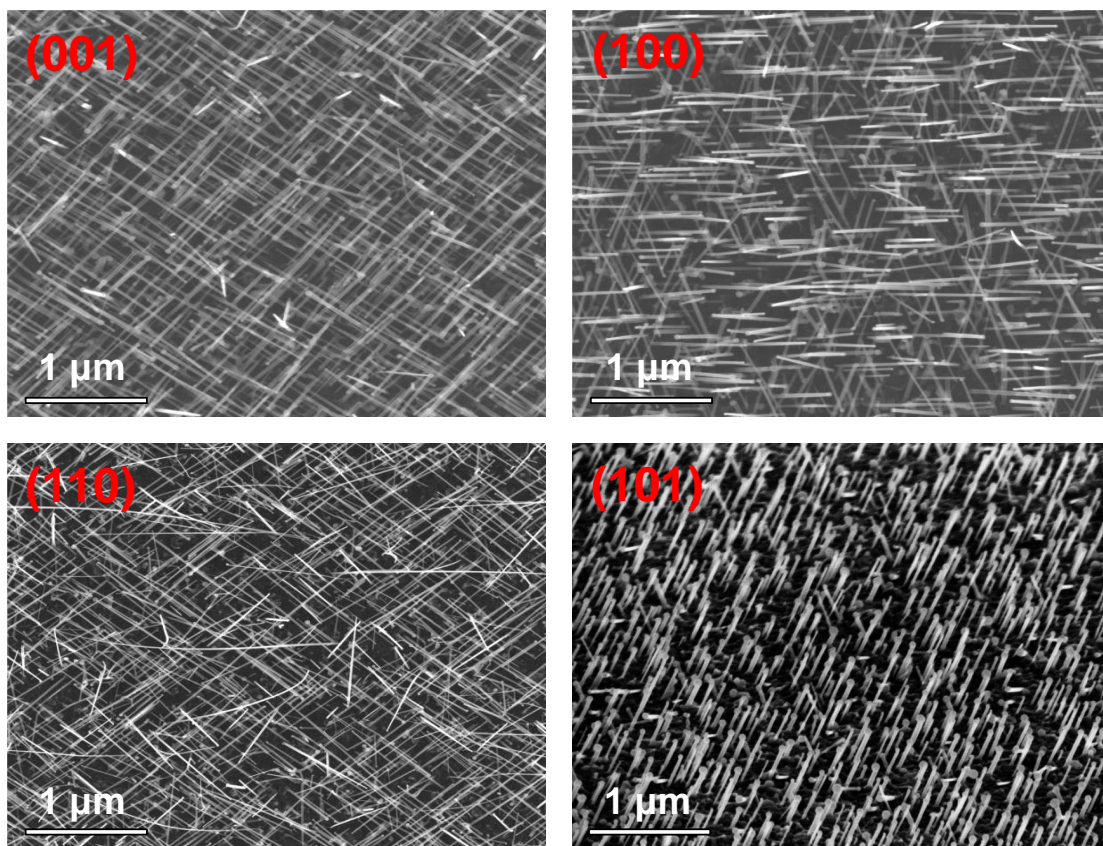


**Figure 37:** SEM images of SnO<sub>2</sub> nanowire arrays grown on TiO<sub>2</sub> (001), (100), (110) and (101) substrates, respectively.

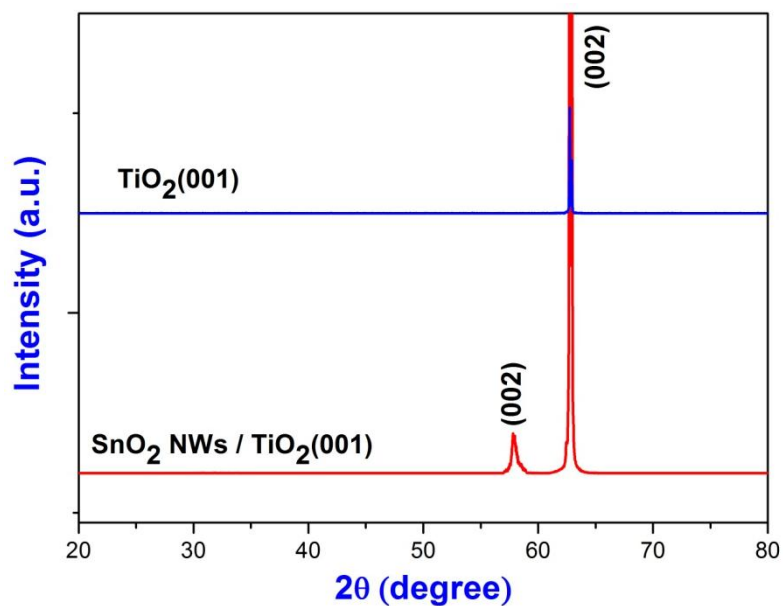


**Figure 38:** XRD patterns of tin oxide nanowires grown on TiO<sub>2</sub>(001) substrates. TiO<sub>2</sub>(001) is measured as standard.



The XRD patterns (Figure 38) of SnO<sub>2</sub> NWs grown on Al<sub>2</sub>O<sub>3</sub> and TiO<sub>2</sub>(001) substrates revealed that a major peak at 63° corresponding to (002) reflection of TiO<sub>2</sub> substrates; whereas the minor peak at 58° is attributed to (002) reflection of SnO<sub>2</sub> NWs.

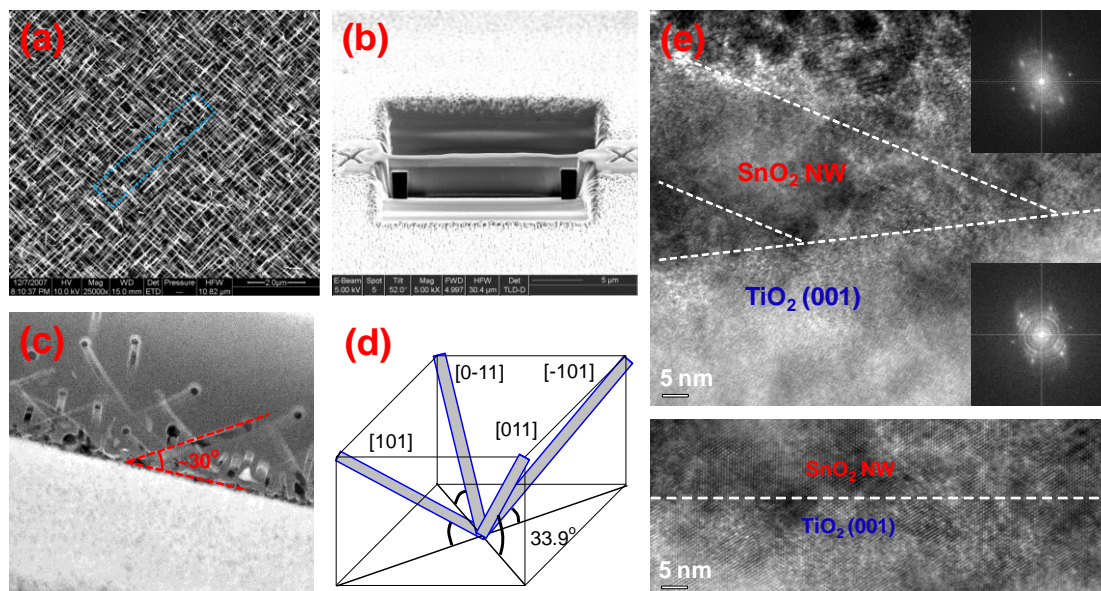


**Figure 39:** (a-c) Electron microscopic images of FIB preparation for cross sectional analysis. (d) Four growth directions of ordered SnO<sub>2</sub> nanowires. (e) The cross sectional TEM image showed the epitaxial growth of SnO<sub>2</sub> nanowires on TiO<sub>2</sub>(001) substrate.

Figure 39 shows the top and tilted views of SnO<sub>2</sub> NWs grown on TiO<sub>2</sub>(001) substrate, which confirmed the uniformity in orientation. The SEM images recorded at different incident angles of electron beam were used to measure the projected angles in order to determine the tilt angles, as shown in Figure 40. The value of tilt angles (ca.  $33 \pm 2^\circ$ ) was in agreement with the cross sectional TEM analysis (Figure 39(c)), which confirmed the characteristic angular orientation of the NWs with respect to the substrate, presumably imposed by the fourfold axis of symmetry present along the *c* axis of the TiO<sub>2</sub>(001) substrate. This led to four equivalent growth directions ([011],

[0-11], [101] and [-101]) due to mirror images of the unit cell (Figure 39(d)).

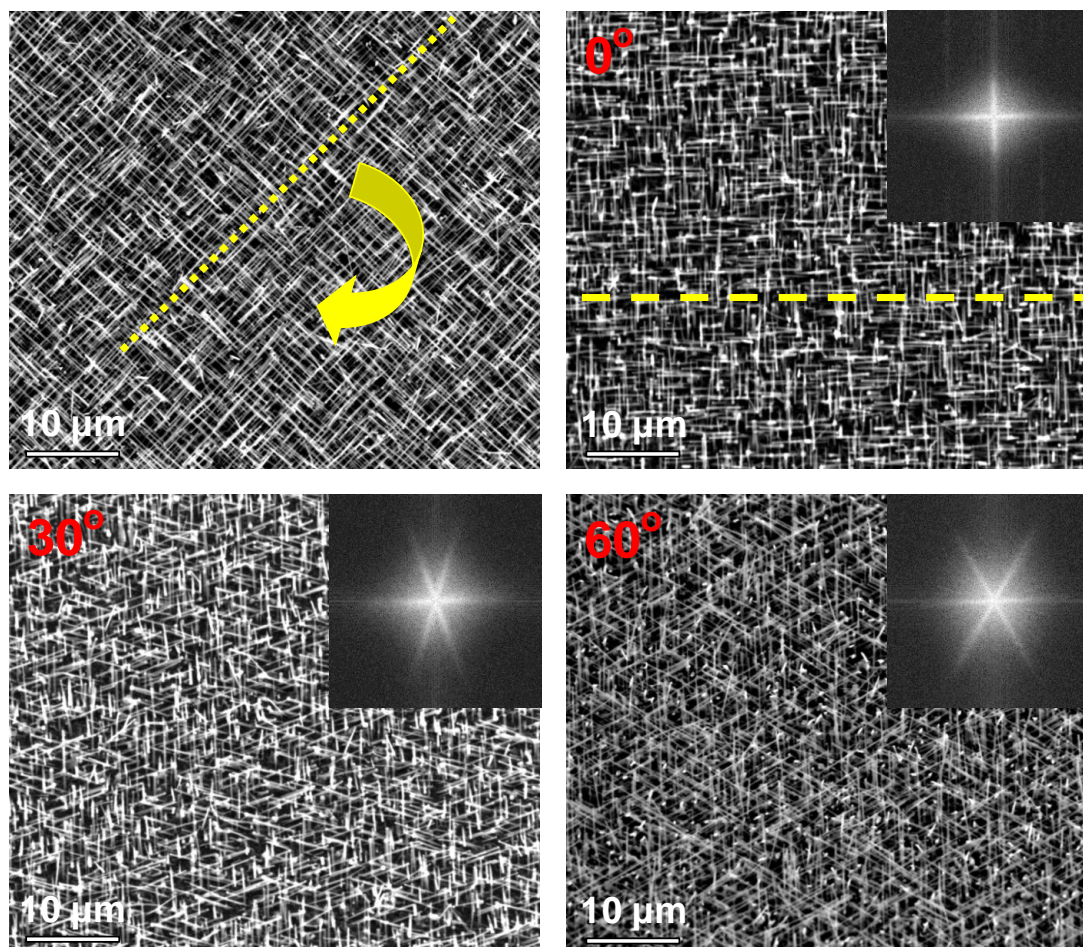


**Figure 40:** SEM images of ordered SnO<sub>2</sub> nanowires sample recorded at different incident angles of electron beams.

High-resolution TEM image of ordered tin oxide nanowires revealed an epitaxial growth of SnO<sub>2</sub> nanowires on TiO<sub>2</sub>(001) substrate (Figure 39(e)). The fast fourier transform (FFT) patterns obtained from the nanowire and substrate show identical diffraction patterns supporting the epitaxial growth and single crystalline nature of SnO<sub>2</sub> nanowires on TiO<sub>2</sub>(001) substrate. Previous works have reported that the orientations of substrate and NWs predominantly influence the degree of alignment and the control over the growth axis, the contributions of the bulk energy of tin oxide, the bulk energy of the liquid



droplet, the interfacial tension of the L-S interface and the surface tensions of the droplet and the nanowire.<sup>[266]</sup> The energetically favored growth axis of SnO<sub>2</sub> NWs was found to be along the [101] direction confirmed by HR-TEM analysis of several NWs, as shown in Figure 41.

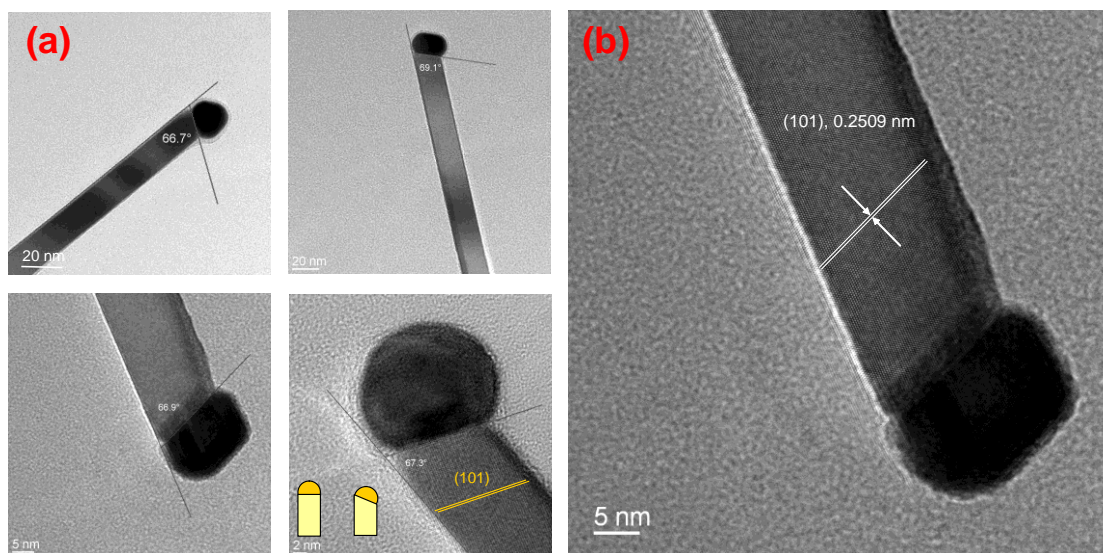


**Figure 41:** (a) TEM images of SnO<sub>2</sub> nanowire with Au catalyst tip showing the abnormal oblique interface between SnO<sub>2</sub> and the droplet. (b) HR-TEM image of ordered SnO<sub>2</sub> NW.

It is apparent that the surface energy dominates the overall growth process resulting in a preferential growth along [101] direction at the expense of [001], possibly a consequence of the growing significance of side facets, which contributes to the formation enthalpy and forces the wire to grow along the observed [101] axis.<sup>[267]</sup> Generally, the favored growth direction in a cubic crystal system is the one along the lowest surface energy. Figure 41 showed the high resolution TEM images of a SnO<sub>2</sub> NW with catalyst tip indicating the single crystalline features of nanowire and the sharp NW-catalyst growth front interface. The growth direction was found to be [101], with angular inclination to the substrate being 67-69°.

### 5.1.3 Growth mechanism of SnO<sub>2</sub> nanowire arrays

Based on the above structural analysis, crystal chemistry and surface energy consideration, a growth model can be proposed (Figure 42), which explains the oriented and tilted growth of SnO<sub>2</sub> NWs:

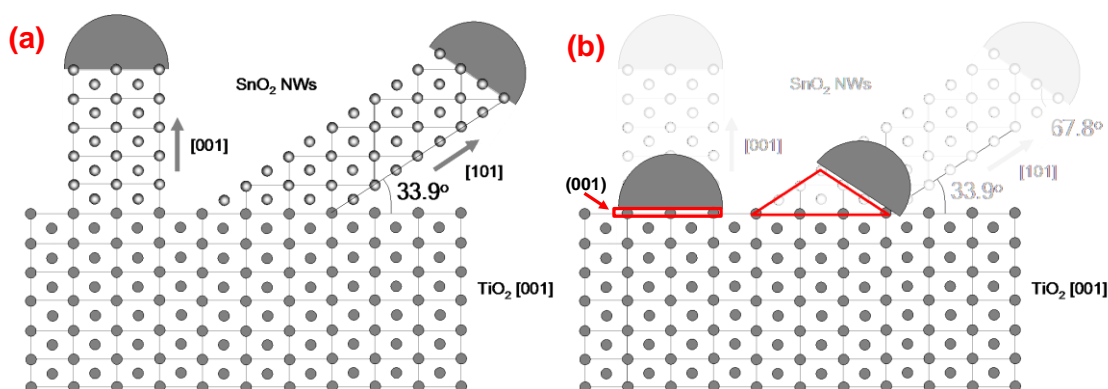


**Figure 42:** Schematic growth model of ordered tin oxide nanowires on TiO<sub>2</sub>(001) substrate. (a) [001] vs. [101] directions. (b) The “incubation” growth mode.

(i) *Lattice mismatch:* The {101} plane has a higher atomic density than {001} plane, which enforces a change in the growth direction because a higher mismatch (lattice) can accommodate the strain between the deposited material and the substrate.<sup>[268]</sup> TiO<sub>2</sub> substrate is iso-structural with the rutile phase of tetragonal tin oxide, however lattice mismatch of  $a$  value is lower ( $(a_{\text{SnO}_2} - a_{\text{TiO}_2}) / a_{\text{TiO}_2} = 2.6\%$ ) than the lattice mismatch of  $c$  value ( $(c_{\text{SnO}_2} - c_{\text{TiO}_2}) / c_{\text{TiO}_2} = 7.7\%$ ). In comparison to [001] direction, the [101] direction is similar to the gradually shifting of  $1/2a$  in each atomic layer.

Hence the minimization of strain between ordered SnO<sub>2</sub> NWs and TiO<sub>2</sub>(001) substrates is the driving force for the observed alignment and growth along [101] axis. Since the amount of surface energy between the deposited material and the substrate increases proportionally with the lattice mismatch, the lattice-induced strain in nanowires can be compensated by structural relaxation at the SnO<sub>2</sub>/TiO<sub>2</sub>(001) interface.<sup>[269]</sup> This is supported by HR-TEM

analysis of several samples (Figure 41). The microstructural analysis revealed that the interface between NW and catalyst possesses (101) alignment indicating the atomic layer-by-layer growth of nanowires. The abnormal oblique interface of Au catalyst possibly resulted from the tilting of liquefied catalyst droplets (at 33.9°) by the protruding nanowires whereby the tilt angle and surface alignment are mandatory for the anisotropic growth.<sup>[270]</sup>

(ii) *Surface energy*: Ramamoorthy and co-workers have suggested that the instability of (001) surface due to the higher surface energy results in the formation of (101) facets. For the rutile structure of SnO<sub>2</sub>, the surface energy per crystal facet can be sequenced as (110) < (100) < (101) < (001) according to the calculated data.<sup>[271]</sup> Figure 43 illustrates the incipient crystal growth, whereas in our case the (001) SnO<sub>2</sub> thin layer will be converted to (101) facets in order to minimize the surface energy of (001). There are four equal possibilities for tilt planes which results in nanowire growth in four equal directions.

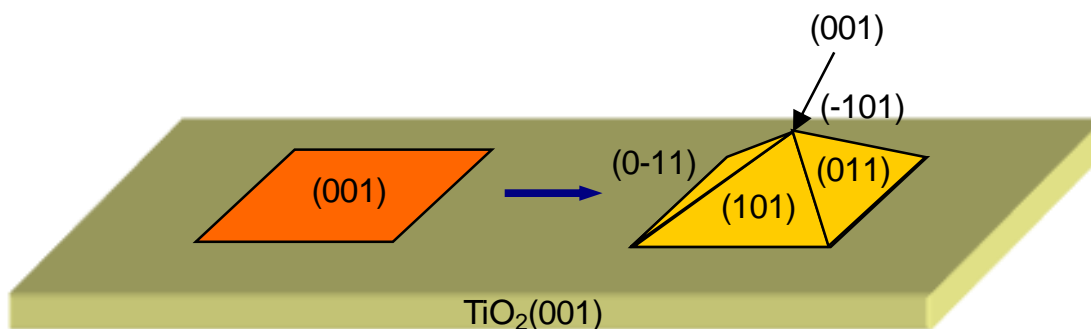


**Figure 43:** Formation of (001) to (101), (011), (0-11) and (-101) facets.

Figure 44 shows the initial growth of nanowires (process time, 5 min.) indicating the statistical distribution of the four growth probabilities. A similar phenomenon has also been observed in the controlled synthesis of size-dependent Si NWs. HR-TEM imaging of the catalyst/Si NW interface showed that a well-defined V-shaped morphology formed by the interface

consisting of two {111} planes, whereby the [111] and [11-1] directions combined to yield the [110] growth axis. These results confirmed that the liquid-solid interface (111) remained the lowest-energy interface even in very thin NWs. In addition, SnO<sub>2</sub> NWs with square-shaped cross-section have been synthesized using a template-free hydrothermal approach.<sup>[272]</sup> The TEM images showed that the growth direction of SnO<sub>2</sub> NWs is along [001] and the end facet is terminated with {101} planes.

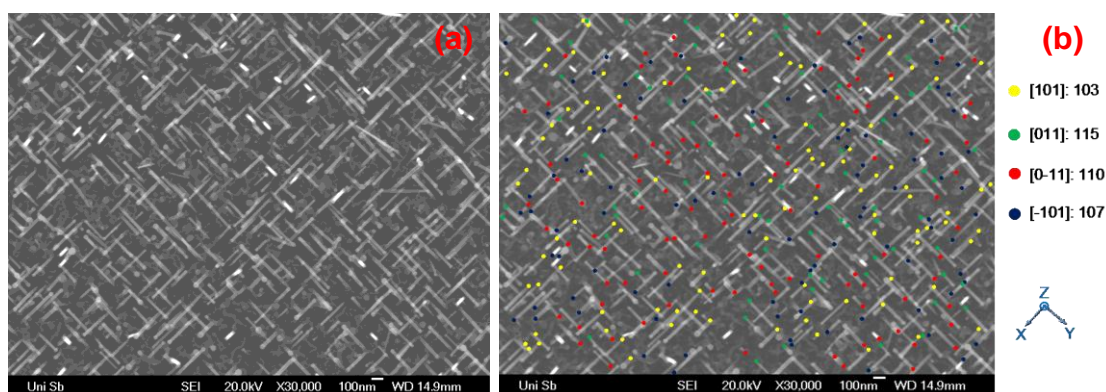


**Figure 44:** (a) SEM image of ordered SnO<sub>2</sub> NWs grown in 5 min. (b) Statistic analysis of [101], [011], [-101] and [0-11] growth directions based on Figure 43.

(iii) *Incubation growth model:* The growth process of ordered SnO<sub>2</sub> nanowires can be illustrated in Figure 42(b). Based on the VLS model, the Sn-O sources will be absorbed by liquefied Au droplets and a SnO<sub>2</sub>(001) thin layer will be formed between Au catalyst and TiO<sub>2</sub>(001) substrate. The vertical growth of SnO<sub>2</sub>(001) NWs is prohibited by the conversion of (001) to (101) facet in order to minimize the surface energy of (001). It is interesting to note that the Au catalyst needs to be rotated and aligned along one of the (011), (0-11), (101) and (-101) facets. The 1D growth will begin once the above criterion (incubation time for the rotation of SnO<sub>2</sub> islands to [101]) is fulfilled.

The proposed growth model also explains the XRD data, which exhibited {002} plane. Since the {101} nanowires have pronounced (001) planes, the

(002) reflex can be easily detected, because the observed (002) peak can be attributed to the discrete (002) islands, as a part of the epitaxial SnO<sub>2</sub> film growth.<sup>[273]</sup> As expected the intensity of (002) peak is very low due to the significantly higher nanowire growth rates, when compared to the 2D growth. This aspect was elucidated by performing CVD experiments on TiO<sub>2</sub> substrate partially coated with catalytic Au film (only the circled region, Figure 45), whereby the growth was found to be faster (enhanced diffusion at solid-liquid interface) and anisotropic (templating effect of Au seeds) on catalyst covered regions while a thin film (epitaxial) was formed in the other parts (Figure 45).

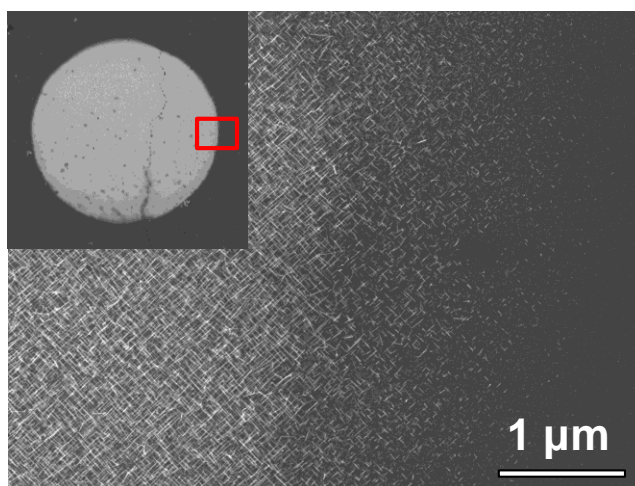


**Figure 45:** SEM images of patterned growth of tin oxide nanowires on TiO<sub>2</sub>(001) substrates.

In addition to lattice mismatch and surface energy considerations, the alignment of nanowires growth is also influenced by the orientations of the substrate. For this purpose, a focused ion beam - assisted SEM (FIB-SEM) tomographic study of ordered SnO<sub>2</sub> NWs on TiO<sub>2</sub>(001) and TiO<sub>2</sub>(101) samples was undertaken (Figure 46). Since the conventional electron microscopic analysis provides 2D projection of 3D objects,<sup>[274]</sup> the FIB-SEM tomography was applied to visualize the 3D volume of 1D nanostructures grown on the flat surface. Thin film sectioning and computer-aided combination of images are



usually used in semiconductor industry for testing of silicon-based microchips, however this techniques is founding increasing application in 3D structural analysis of materials and nanostructure based devices.<sup>[275]</sup> Figure 46 shows the 3D reconstructions of FIB-SEM tomographic images of ordered SnO<sub>2</sub> nanowires on TiO<sub>2</sub>(001) and TiO<sub>2</sub>(101) substrates, respectively.

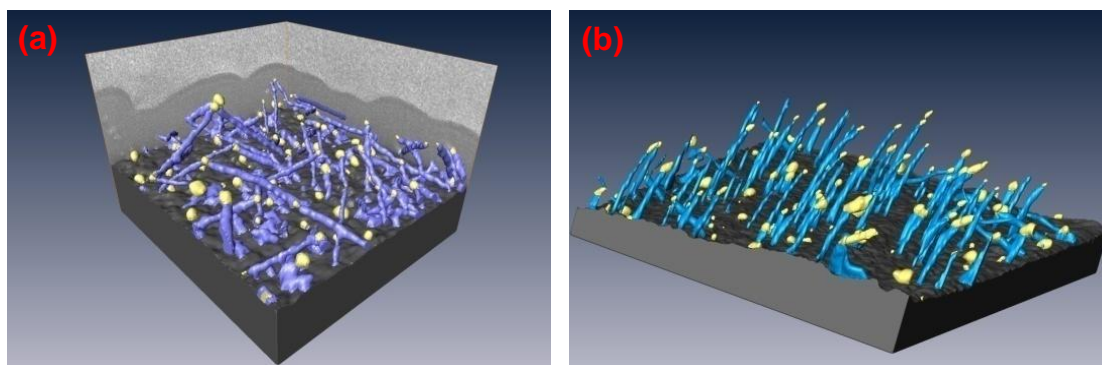


**Figure 46:** 3D SEM-FIB tomographic images of ordered SnO<sub>2</sub> NWs on (a) TiO<sub>2</sub>(001) and (b) TiO<sub>2</sub>(101) substrates.

A meshlike network of SnO<sub>2</sub> NWs has been formed on the TiO<sub>2</sub>(001) whereas ordered SnO<sub>2</sub> NWs with single orientation direction (tilt angle ~ 69°) were observed on TiO<sub>2</sub>(101) substrate. It is noted that tilting of liquefied catalyst droplets and incubation time (Figure 42(b)) in the SnO<sub>2</sub>/TiO<sub>2</sub>(001) sample was not observed in the SnO<sub>2</sub>/TiO<sub>2</sub>(101) system because the Au catalysts on TiO<sub>2</sub>[101] have met the requirement of 1D growth of SnO<sub>2</sub> system. The crystallographic relationship between ordered SnO<sub>2</sub> NWs on TiO<sub>2</sub>(001) and TiO<sub>2</sub>(101) substrates is clarified in Figure 47.

Although TiO<sub>2</sub>(001) substrates used in this study to grow vertical SnO<sub>2</sub>[001] NWs, produced a meshlike network of SnO<sub>2</sub>, our systematic investigations on the synthesis-structure relationship of ordered SnO<sub>2</sub> NWs can explain the growth mechanism of meshlike network of SnO<sub>2</sub> NWs and lack of reports on the fabrication of ordered SnO<sub>2</sub> NWs, especially those dealing with vertical NWs.



measurement. It is noted that the electrical properties of SnO<sub>2</sub> NWs depend on the model of synthesis, compositional purity and surface chemistry. It is mentioned that the growth directions of the used SnO<sub>2</sub> NW are unknown which SnO<sub>2</sub> NWs with different growth directions have different surface facets and activities. Hence, the ordered SnO<sub>2</sub> NWs in this study display only [101] growth direction, it is possible to study the resistivity and gas sensing behavior of SnO<sub>2</sub> nanowires with the defined [101] orientation. I-V curve of individual SnO<sub>2</sub>[101] nanowire (Figure 48(a)) was acquired in four-probe configuration to avoid the parasitic contributions of the contacts.<sup>[241]</sup> The nanowire radius was  $34 \pm 3$  nm and the distance between electrodes was  $3.4 \pm 0.1$   $\mu\text{m}$ . The resistance was  $5.55 \pm 0.02$  M $\Omega$ . Assuming a cylindrical geometry, the resulting resistivity  $\rho$  was  $0.59 \pm 0.08$   $\Omega\cdot\text{cm}$  at room temperature (25 °C), which was consistent with previously reported data of  $\rho$  in nanostructured SnO<sub>2</sub>.

Figure 48(b) demonstrates the potential of SnO<sub>2</sub> NWs in conductometric chemical gas sensors. The microheater integrated in the substrate was used to optimize the response to gases. At  $T = 300$  °C, individual nanowire SnO<sub>2</sub> displayed significant and monotonously growing changes in its resistance when exposed to a wide range of CO concentrations (50-1000 ppm). The lower detection limit (around 50 ppm) makes them suitable for many early gas alert applications.<sup>[276]</sup>

The long-term stability of gas sensors based on SnO<sub>2</sub> nanowires and nanoparticles indicated a higher stability in nanowires possibly due to single crystalline features, and minimum grain (crystal) growth and sintering, low alteration of the NW-NW contact nodes under long operation time. It has been shown that sintering of nanoparticles leads to aggregation and encapsulation of nanoparticles into larger agglomerates and to irreversible degradation of sensitivity of nanoparticles.<sup>[277]</sup>



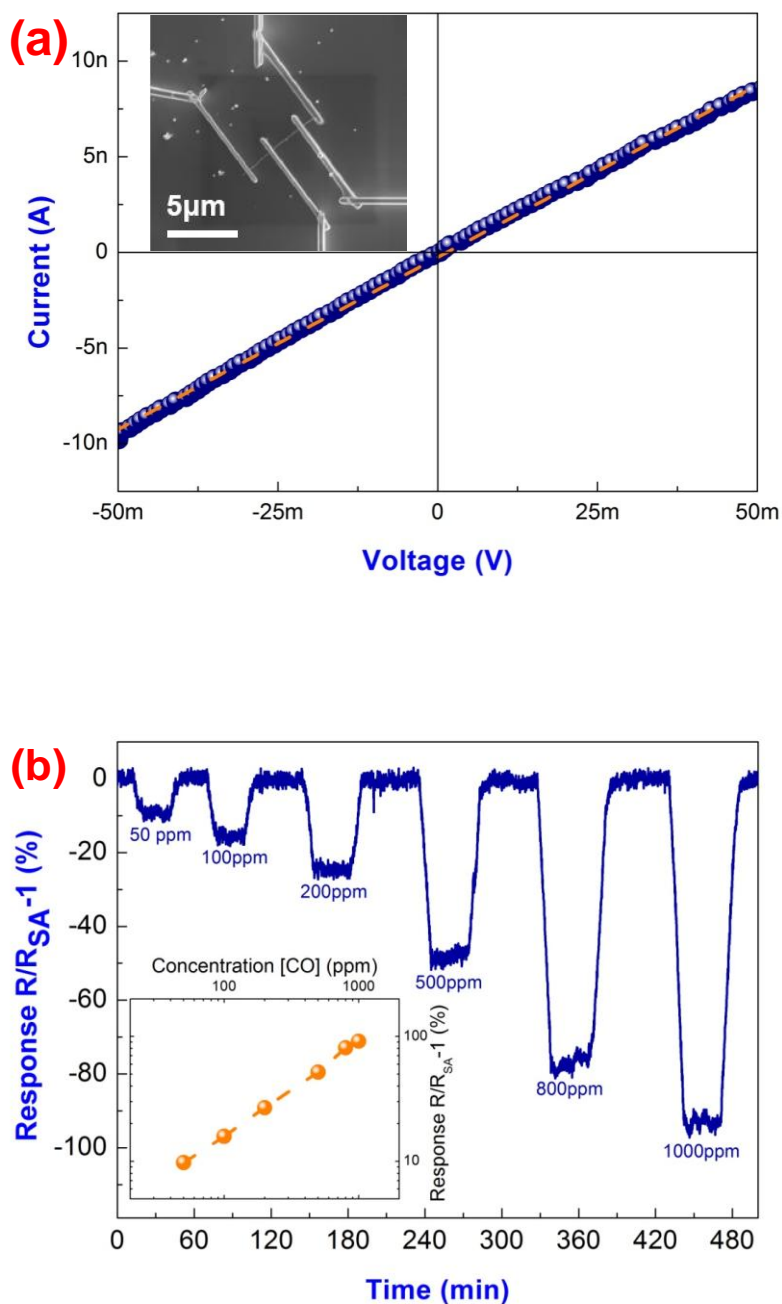


**Figure 48:** (a) Electrical  $I$ - $V$  characteristic curve of an individual SnO<sub>2</sub> [101] nanowire acquired in four-probe configuration at room temperature (25 °C). (b) Conductometric response of an individual SnO<sub>2</sub> [101] nanowire to different CO concentrations (diluted in dry synthetic air) at  $T = 300$  °C. Response vs. concentration log-log plot is shown in inset: a linear sensing characteristic behavior.

In summary, ordered SnO<sub>2</sub> NWs were grown by molecule-based CVD strategy for controlled and site-specific growth of nanoscopic crystals by combining the VLS catalytic growth mode with reactive molecular precursors. The detailed structural analyses (SEM, TEM, SEM-FIB tomography) of ordered SnO<sub>2</sub> NWs on TiO<sub>2</sub>(001) showed the growth to follow both the VLS mechanism and crystallographic epitaxial driving force. The SnO<sub>2</sub> NW arrays grow along [101] direction on TiO<sub>2</sub>(001) (~ 34°) by rotating and aligning the Au catalyst (incubation growth model) in order to minimize the total surface energy. The same growth direction [101] of SnO<sub>2</sub> NW arrays on TiO<sub>2</sub>(101) (~ 69°) indicated that the SnO<sub>2</sub> NWs preferred to grow along [101] direction and were independent of TiO<sub>2</sub> single crystal substrates with different orientations. The studies on the electrical and gas sensing properties of SnO<sub>2</sub>[101] single nanowire showed that the nanowire arrays can be potentially used for surface- and facet-sensitive detection of gas molecules.

## 5.2 FIB-Tomographic studies of SnO<sub>2</sub> nanowire arrays on TiO<sub>2</sub> single crystals

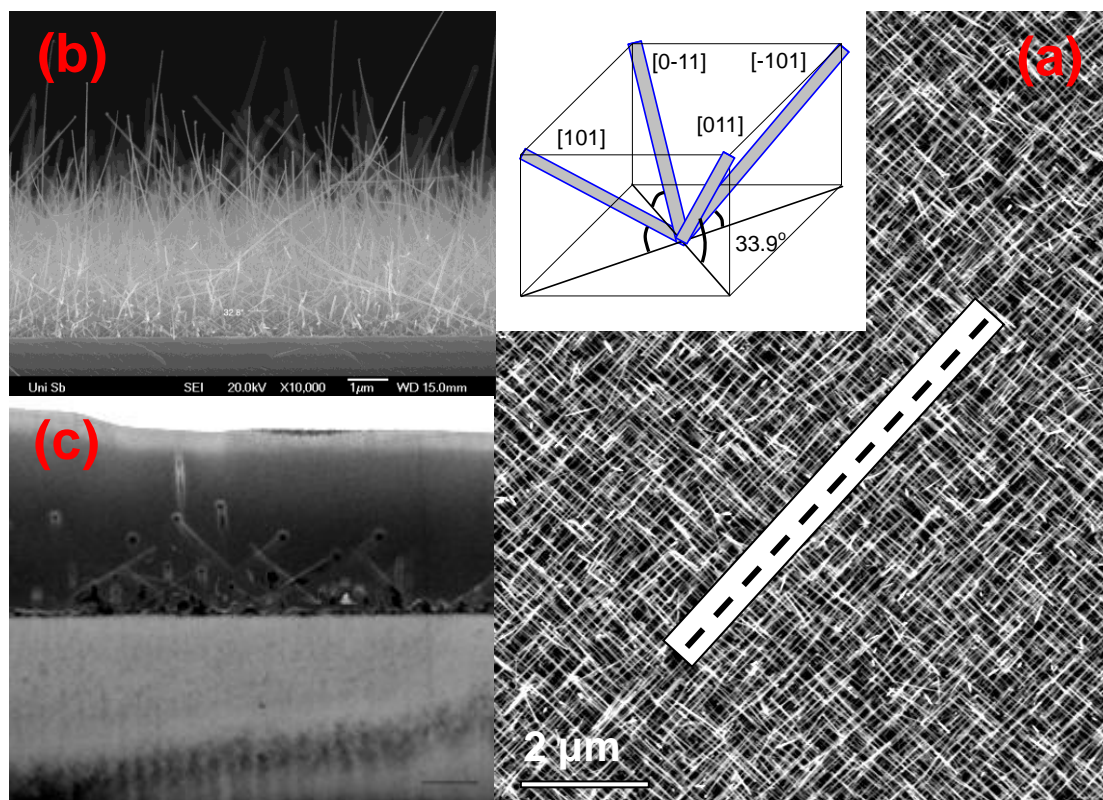
A lot of efforts in both theory and experimental investigation of growth, characterization and applications of 1D nanostructures have moved the innovation development in high level which can enable to monitor, manipulate and model the 1D building blocks in desired forms and functionality.<sup>[200]</sup> The searching of analytic methods for 3D characterization of nanostructures is required to further research and enables the continuing development of nanotechnology. One of the approaches that combines focused ion beam milling with scanning electron microscopy (FIB-SEM) can be as a useful tool for imaging 1D nanostructures in the nanometer range. Since the conventional electron microscopic analysis can only provide 2D projections of 3D objects and therefore is unable to provide the 3D spatial information.<sup>[274]</sup> Therefore, the FIB-SEM tomography can visualize the 3D volume of 1D nanostructures through the application of serial FIB sectioning, however, the method is usually used in semiconductor industry for proof of silicon-based microchips and has just begun to emerge as a demonstrate method in materials engineering and biologic applications.<sup>[275]</sup> There are few works on the FIB-SEM study of nanostructures. Kubis and co-workers have used the method to study the 3D self-organization relationship of Ge quantum dots (QDs) superlattices.<sup>[278]</sup> The analysis enabled the addressed size and position of all QDs and interaction details within the QDs. Elfallagh and co-workers have reported that the location and 3D shape of individual cracks induced by Vickers indenters can be quantitatively represented by FIB tomography.<sup>[279]</sup> 3D imaging of mammalian cells demonstrated the striking spatial relationships between the cells and membranes.<sup>[280]</sup>

The FIB-SEM tomographic analysis of ordered tin oxide nanowires on Au

coated TiO<sub>2</sub>(001) substrates will be reported here. For comparison, conventional SEM, TEM and AFM methods have been used to study the microstructures of ordered SnO<sub>2</sub> nanowires. Since the ordered nanowires have defined growth direction and surface states, they are suitable to be used in large scale device fabrication for gas sensing applications. The method has demonstrated the ability to provide volumetric data resolution down to 10 nm or less, and thus hold tremendous future potential for both materials science and biomedical applications.

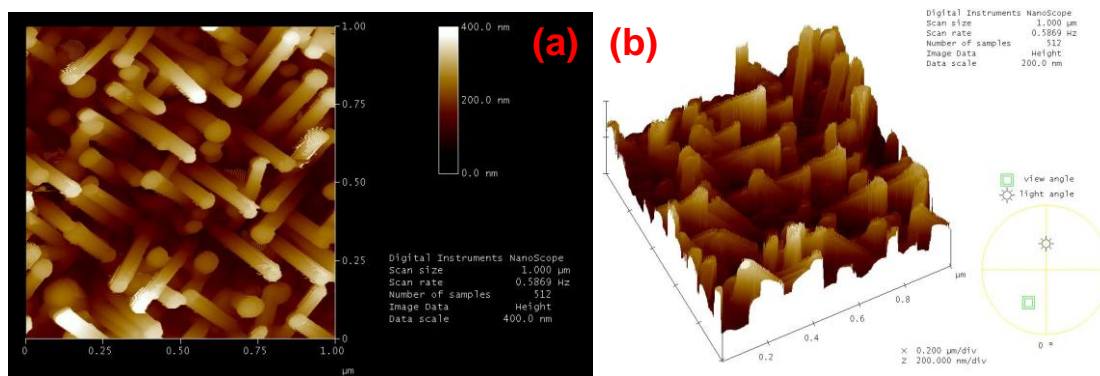
The synthesis of tin oxide nanowires in random and ordered forms by CVD has been reported.<sup>[20]</sup> However, the detailed microstructure analysis of ordered SnO<sub>2</sub> NWs is missing due to the difficulty for preparation of cross sectional samples due to the 3D morphology of ordered nanowires. In order to obtain the spatial information of ordered SnO<sub>2</sub> nanowires, cross sectional electron micrograph analysis is usually required. The cutting direction should be aligned to one of the growth directions of SnO<sub>2</sub> nanowire arrays in order to minimize the measuring error of the inclination angle.

Figure 49 shows the preparation details for cross-section and cross sectional SEM and TEM images of ordered SnO<sub>2</sub> NWs. The cross sectional TEM analysis (not shown) revealed a characteristic angular orientation of the NWs with respect to the TiO<sub>2</sub>(001) substrates. The growth directions of patterned NWs can be assigned to four equivalent [011], [0-11], [101] and [-101]. It is evident that SnO<sub>2</sub> NWs are tilted at ca. 30° to the surface of TiO<sub>2</sub>(001) substrate. However, the methods especial the cross sectional TEM are time consuming and can deliver only 2D information of a few nanowires.



**Figure 49:** (a) Overview SEM image of ordered SnO<sub>2</sub> NWs on TiO<sub>2</sub>(001) substrate. Cross sectional SEM (b) and TEM (c) micrographs showing the side-view of oriented SnO<sub>2</sub> NWs. The samples are sheared and prepared along one of the directions of SnO<sub>2</sub> nanowire arrays.

Alternative method like atomic force microscope (AFM) can provide the topographic information of the nano-objects. Figure 50 shows the AFM images of ordered SnO<sub>2</sub> NWs in 2D and 3D forms. It is indicated that SnO<sub>2</sub> NWs are grown in four directions and the tilted angles ( $\sim 30^\circ$ ) is in agreement with the values from electron microscopic analyses. Although AFM can provide the 3D information, however, the 3D image of ordered SnO<sub>2</sub> NWs is just topographic because the ordered NWs can only be resolved as triangle forms (projection) instead of real 1D forms.



**Figure 50:** AFM images of ordered SnO<sub>2</sub> NWs in 2D (a) and 3D (b) forms.

FIB-tomography was performed in an area of  $3.4 \times 2.2 \mu\text{m}^2$  in order to represent the 3D structure of the ordered nanowires. FIB-tomography consists of the performing precisely serial sectioning with FIB, the imaging with SEM and afterwards reconstructing the 3D-information with a properly software. The serial sectioning was performed with the Slice&View software and the reconstruction with the software AMIRA. The size of the voxel was  $4.5 \times 5.6 \times 20 \text{ nm}^3$  in x, y and z direction respectively and the number of slices was 110. Figure 51 shows a series of cuts. Each nanowire can be clearly seen in more than one of the slice, which means that they were cut several times allowing for a 3D-reconstruction. The Au particles can be identified in each image as very bright spots due to the material contrast.

The 3D-reconstruction showing the distribution of nanowires can be seen in Figure 52(a). Most of the nanowires have an inclination angle ca.  $30^\circ$  to the surface of TiO<sub>2</sub>(001) substrate, however some of them grow perpendicularly to the surface. The nanowires are in some cases curved, with a tendency to being perpendicular to the surface after growing with an inclination angle. In Figure 51(right) the gold particles are represented as bright spots. It can be clearly observed that the gold particles are situated at the tip of the nanowires. However, gold particles, from which there were no grow of nanowires, remain at the substrate surface. The ordered SnO<sub>2</sub> NWs can be imaged at resolutions

of ca. 20 nm in the Z-direction (milling direction) and ca. 10 nm in the X-Y plane indicating that FIB tomography can map and address the sizes and positions of individual nanowires and the catalysts. The resolution in milling direction can be increased by changing the milling parameters such as lowering the milling current and minimizing the effects of electrical, thermal or mechanical drift.<sup>[281]</sup> Although TEM tomography can offer quantitative characterization of nanoscopic 3D nanostructures,<sup>[282]</sup> the 3D information is limited to less than 100 nm thin object since the samples have to be thinned for electron transparency. In this case, the investigations of individual heterostructures such as nanoparticle and nanowires embedded in matrix or core-shell structures have been demonstrated by the method.<sup>[283-284]</sup> The study of ordered SnO<sub>2</sub> NWs has shown that FIB tomography can provide the 3D information of objects in large scale (micrometer size). It is possible to study the statistic analysis of nanowires growth direction and the distribution of catalysts. It is useful to study the nano-bio system since the location of nano-objects and the interaction of nano-objects and cells can be obtained by the method.

The 3D Au catalyst distribution of ordered SnO<sub>2</sub> NWs (Figure 52(b)) provided the insight of the growth mechanism of ordered SnO<sub>2</sub> nanowires. It is known that the anisotropic growth of nanomaterials (1D) can be easily realized by modifying the growth facets in order to reduce the energy barrier of growth (nucleation) to stimulate the high growth rate in competing to other crystallographic orientations. The growth directions of ordered SnO<sub>2</sub> nanowires prefer [101] to designed [001] possibly due to the lowest formation enthalpy. It is the fact that (101) in SnO<sub>2</sub> tetragonal system has the highest packing density of occupied atoms.



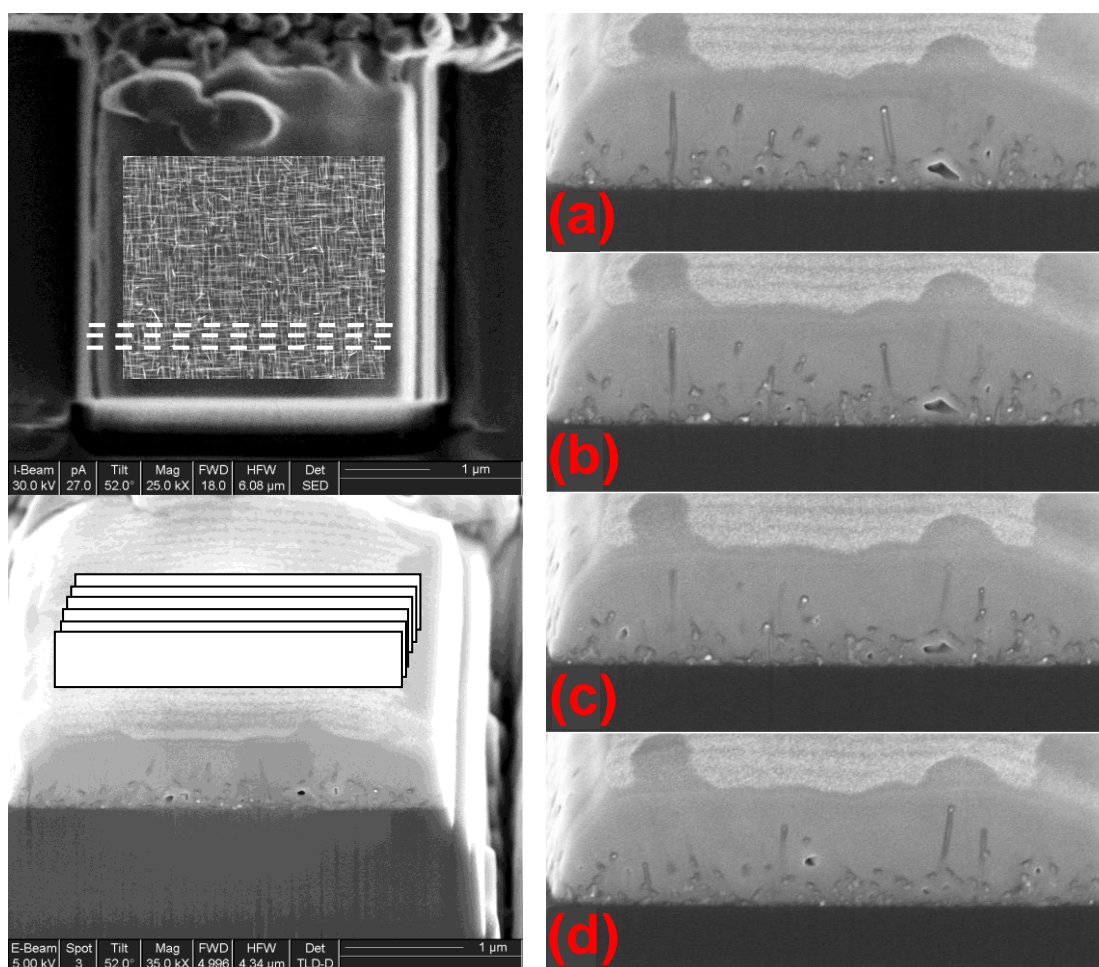


**Figure 51:** Left: Sample preparation for FIB-tomographic analysis. Right: SEM images of the serial cuts through the nanowires for the tomography. The cross section is tilted 52° with respect to the electron beam. The bright particles represent the gold catalysts.

Figure 52(b) shows at least two types of catalyst which play different role in the growth process of ordered SnO<sub>2</sub> NWs. The catalysts located on the tip of nanowires induced the VLS growth of ordered SnO<sub>2</sub> nanowires whereas the catalysts remained on the surface of TiO<sub>2</sub>(001) were inactive in 1D growth process and are buried by the SnO<sub>2</sub> thin films. The initial growth of nanowires can be described as followed: nanowires began to grow once the semi-spheric liquefied catalysts are tilted at ca. 30° to the surface of TiO<sub>2</sub>(001) substrates



and aligned to the (101) plane of SnO<sub>2</sub>. The alignment process will result in an incubation time (a characteristic time delay prior to which no nanowires are formed)<sup>[285]</sup> and the growth of nanowires will not start if the above condition is not filled. In our case the (001) SnO<sub>2</sub> thin layer determined by catalyst size was converted to (101) facets. There are four equal possibilities (pyramid form) to tilt the catalyst therefore resulting in four equal directions of nanowires growth. The catalyst-assisted chemical vapor deposition can be composed of VLS-based 1D growth and normal 2D coatings. The 1D and 2D competition resulted in the spatial separation and distribution of active and inactive catalysts. The incubation time included the formation time of (001) to (101) facets and the growth time when the tin oxide source diffused through the catalyst and segregated from the L-S catalyst/NW interface. The (001) to (101) transformation is precondition for 1D growth whereas a lot of active liquefied Au droplets are victimized and buried by the simultaneous 2D SnO<sub>2</sub> coatings due to the time delay.

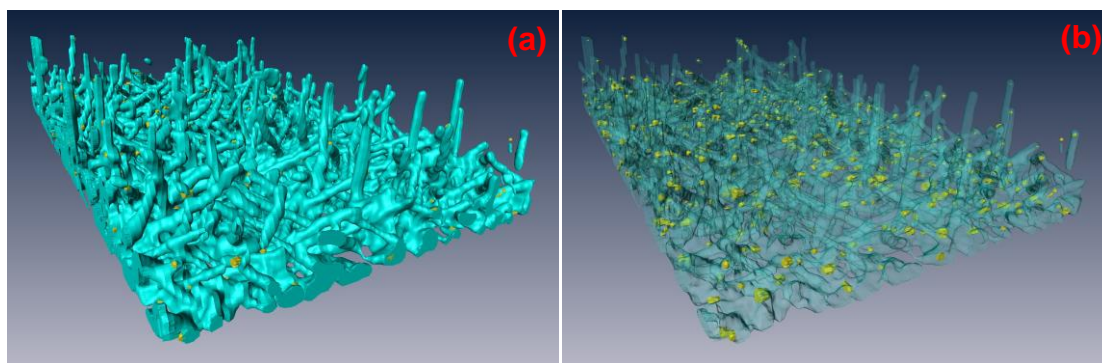


**Figure 52:** 3D-representation of (a) SnO<sub>2</sub> nanowire arrays and (b) distribution of Au catalyst as measured with FIB-tomography.

In summary, Focused Ion Beam-assisted Tomography technique can explore more insights of growth mechanism of 1D materials and the nano-bio interaction in comparison to cross sectional SEM/TEM and AFM approaches. Hence, this technique has a board application on analysis of 1D system.

## 6 Plasma-Modified SnO<sub>2</sub> Nanowires for Enhanced Gas Sensing

In this chapter, the adsorption of oxygen species on as-grown and plasma modified SnO<sub>2</sub> nanowires and the influence of surface chemistry and composition on the charge carrier transduction were analyzed. Gas sensing experiments on modified SnO<sub>2</sub> nanostructures showed higher sensitivity and improved transducing response towards changing gas atmospheres. Modulation of surface defects was also examined by PL and XPS studies.

### 6.1 Introduction of plasma-assisted modification

Tin oxide nanowires are excellent transducer elements because of the large surface sensing area and the 1D carrier transport mechanism. This offers novel and unique potential to modulate the gas sensing efficiency by making the whole nanowire as a conduction channel being able to respond to the charge-transfer reaction occurring on the nanowire surface. Stoichiometric tin oxide nanowires do not comply with the chem-resistor prerequisites evident in their marginal transducing property and high operation temperatures required for gas detection.<sup>[286]</sup> These inherent limitations can be overcome by doping the pure material with metals and/or metal oxides which leads to tunable physical and chemical properties, for instance by creating Schottky barriers at metal-semiconductor and/or metal oxide-semiconductor interfaces and modulating the crystal fields near the interfaces.<sup>[287-288]</sup> The post-growth modification of tin oxide films in capacitively coupled r.f. plasma leads to partial reduction of Sn (IV) species creating a valence dynamics (Sn<sup>2+</sup>, Sn<sup>3+</sup> and Sn<sup>4+</sup>) on the surface, which substantially enhances their ethanol sensing properties,

was discovered. The partial reduction of SnO<sub>2</sub> deposits by the preferential etching of bridging oxygen species in the lattice eventually increases the sensor performance by its higher sensitivity with lower response and recovery time, which is accompanied by the reduction in operating temperature. Plasma-assisted modification of nanowires changes homogeneously surface chemical composition without losing the characteristic high aspect ratio of nanowires. By controlling the gas species and power for plasma treatment, we can enhance the sensitivity of the SnO<sub>2</sub> nanowires based gas sensor. In addition, the surface etching is stable over several cycles and indicates that electronic fractions from an equilibrium state driven by redox reactions. To date, many studies have focused on plasma-treated SnO<sub>2</sub> film<sup>[289 - 290]</sup> and nanorods.<sup>[291-292]</sup> However, to our knowledge, there were few reports on plasma-treatment of SnO<sub>2</sub> nanowires. More importantly, plasma treatment has been used to fabricate one-dimensional nanostructures, or as a surface modification method, the mechanistic aspects of plasma treatment and their correlation to the enhanced gas sensing performance has not been reported.

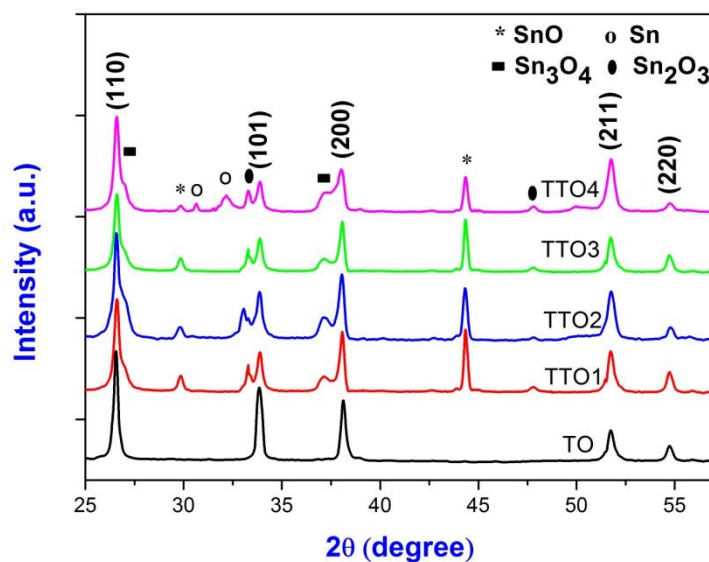
Herein, the adsorption of oxygen species (O<sub>2</sub>, O<sub>2</sub><sup>-</sup>, O<sub>2</sub><sup>2-</sup> etc.) on as-grown and plasma modified SnO<sub>2</sub> single crystalline nanowires was investigated. Then the influence of surface chemistry and composition on the charge transduction induced by adsorption of gaseous analysis was also elaborated.

## **6.2 Characterization of plasma-treated SnO<sub>2</sub> nanowires**

X-ray diffraction patterns (Figure 53) of as-deposited and plasma-treated nanowire samples confirmed nanowires to be constituted of tetragonal SnO<sub>2</sub> phase. Description of TTO series of tin oxide NWs samples is listed in Table 3.

**Table 3:** Description of TTO series of tin oxide NWs samples.

Samples	Plasma power (W)	Duration (second)
TO	0	0
TTO 1	10	240
TTO 2	20	240
TTO 3	30	240
TTO 4	40	240
TTO 5	80	240

**Figure 53:** XRD patterns of as-deposited (TO) and plasma-treated (TTO) SnO<sub>2</sub> nanowires.

The absence of any other phases confirmed the structural and chemical homogeneity of the as-deposited nanowires. The diffractograms of tin oxide nanowires exposed to plasma-treatment at 10, 20 and 40 W showed incipient evolution of SnO, Sn<sub>2</sub>O<sub>3</sub> and Sn<sub>3</sub>O<sub>4</sub> as additional phases resulting apparently from gradual reduction of tetragonal SnO<sub>2</sub> due to removal of bridging oxygen atoms from the stoichiometric SnO<sub>2</sub>. SnO<sub>2</sub> nanowires treated at 10, 20, 30 and

40 W showed a reduction in the peak intensity of (110) reflection due to the creation of amorphous overlayer on the SnO<sub>2</sub> crystalline core. The further increase in the plasma power up to 40 W (TTO4) generated more energetic ions and neutrals in plasma, which led to the formation of metallic Sn on the nanowire surface.

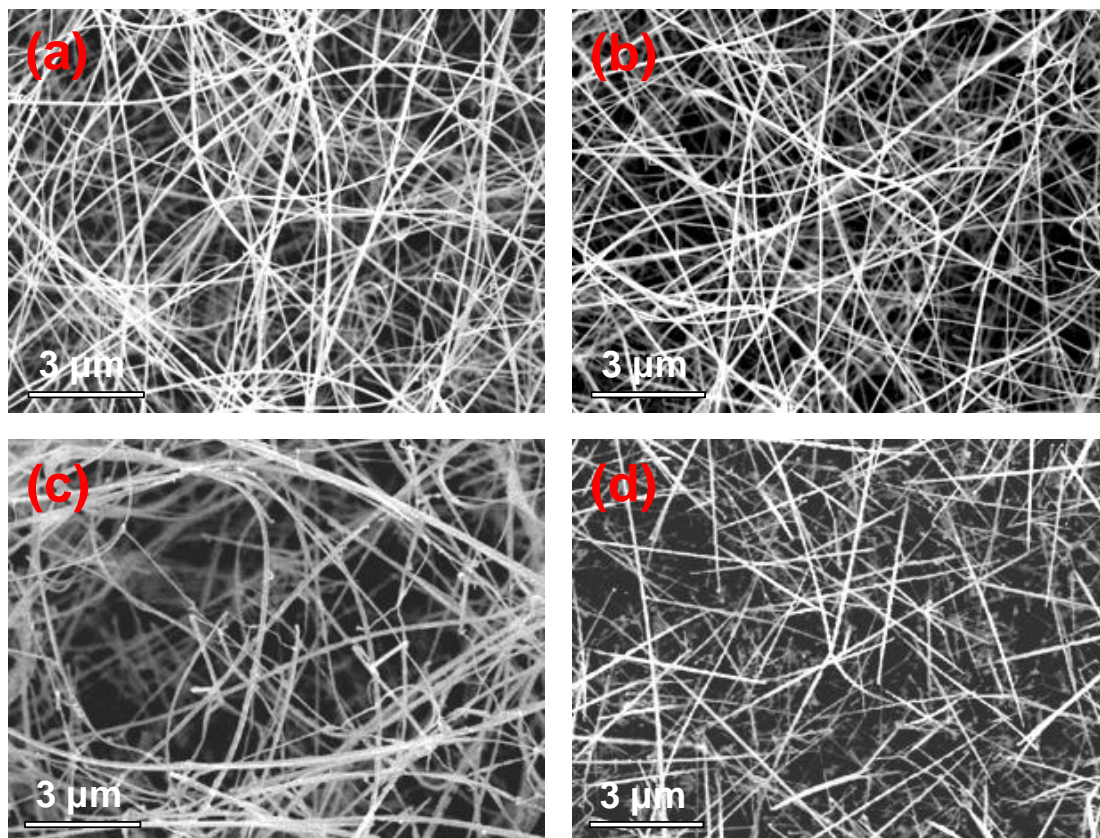


**Figure 54:** SEM micrographs of (a) as-deposited (TO) and plasma-treated (TTO) SnO<sub>2</sub> nanowire samples at (b) 10, (c) 40 and (d) 80 W, respectively.

SEM images (Figure 54) of as-deposited and plasma-treated SnO<sub>2</sub> nanowires at 10, 40 and 80 W, respectively, showed uniform one-dimensional structures with the diameters ranging from 20-80 nm. No substantial modification of the nanowire morphology was observed at lower plasma energy (10 W), whereas at higher energies (> 20 W) surface erosion accompanied by enhanced surface roughness was observed (Figure 54(c, d))

in the samples.

High-resolution TEM analysis showed uniform and well-ordered surface structure (Figure 55(a)) for untreated TO sample, whereas influence of plasma-treatment and bombardment of energetic ions was evident in TTO4 (Figure 55(b)), which showed enhanced disorder of material. TEM micrograph of TTO4 (Inset, Figure 55(b)) showed 1D heterostructures with crystalline core and amorphous overlayer and corroborated the assumed structural change by ions possessing with higher kinetic energy and impinging on the nanowire surface. The rough amorphous overlayer in plasma-treated samples increases the density of dangling bonds and free lattice sites thereby favoring surface adsorption phenomena.

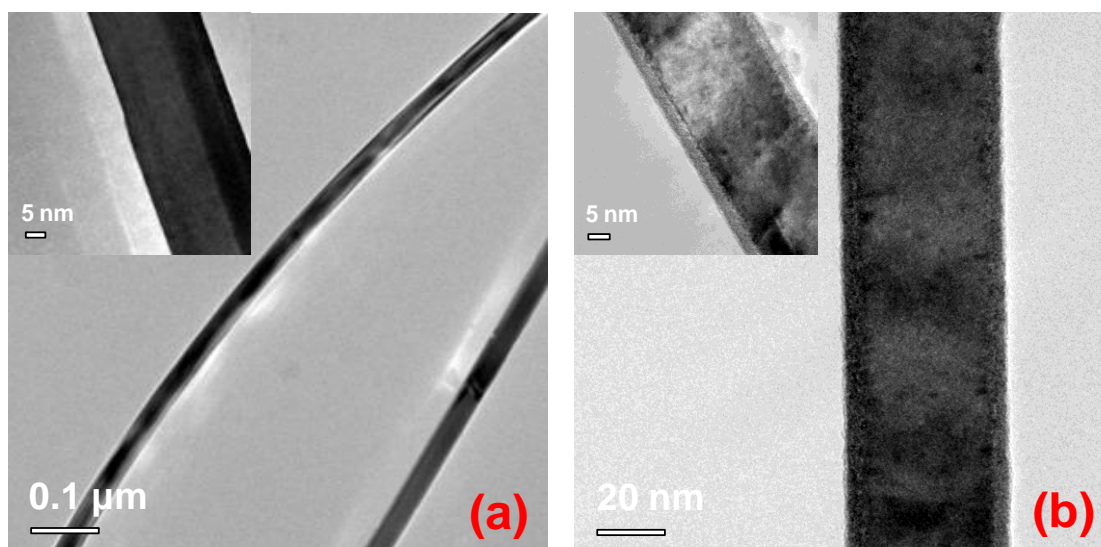


**Figure 55:** HR-TEM images of (a) as-deposited and (b) plasma treated (40 W) SnO<sub>2</sub> nanowires.

The existence of amorphous overlayer was proven by high resolution TEM (Figure 56(b)), whereby the FFT of selected overlayer showed the amorphous feature. HR-TEM images of plasma-treated SnO<sub>2</sub> NWs after short (Figure 56(a, b)) and long (Figure 56(c, d)) e-beam radiation showed that the incipient crystallization and ordering processes on the SnO<sub>2</sub> nanowire surface to form



crystalline nanoclusters.

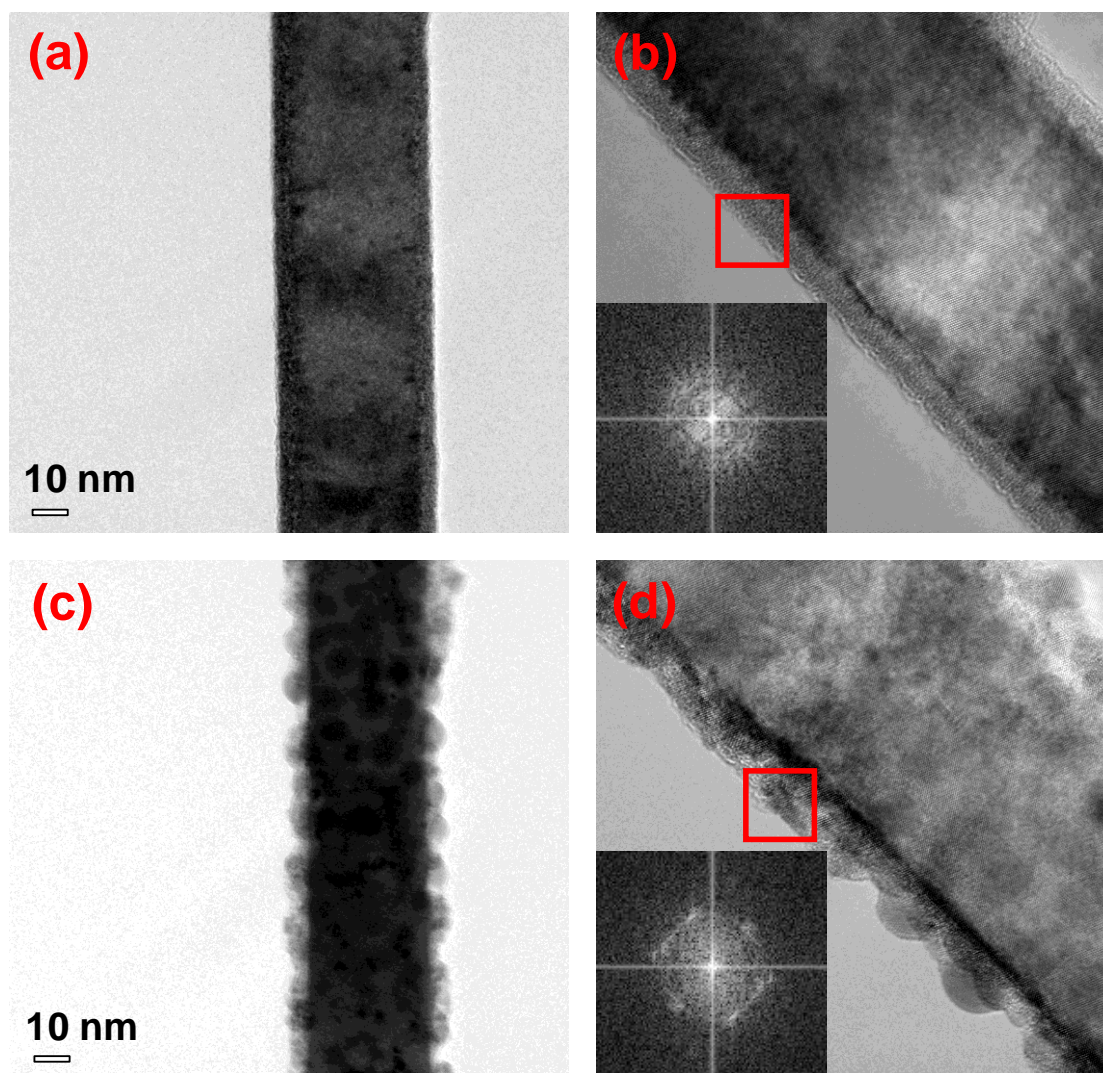


**Figure 56:** HR-TEM images of plasma-treated SnO<sub>2</sub> NWs after (a, b) short and (c, d) long e-beam radiation showing the e-beam influence on the plasma-treated SnO<sub>2</sub> nanowires.

Figure 57 shows the comparison of XPS spectra of as-deposited and plasma treated (40 W) SnO<sub>2</sub> nanowires, which confirmed the inherent phase changes of the tin oxide nanowires after exposure to r.f. plasma treatment. As-deposited SnO<sub>2</sub> sample exhibited the characteristic double peak for the Sn 3d orbital with the main peak (Sn 3d<sub>5/2</sub>) at binding energy 486.8 eV (FWHM 1.8). Upon plasma treatment at 40 W, the shifting and narrowing of Sn 3d<sub>5/2</sub>

peak (486.6 eV, FWHM 1.4) in plasma-treated samples corresponded to the conversion of dominated Sn(IV) to mixed Sn(IV)/Sn(II) phases in plasma-treated SnO<sub>2</sub> NWs.

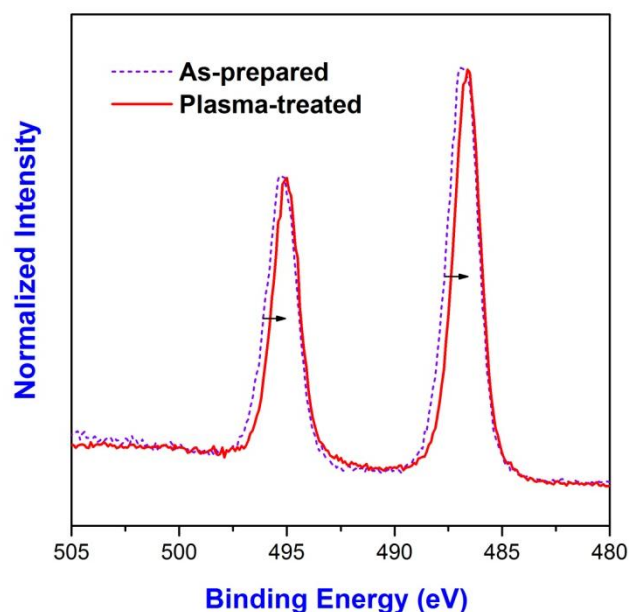


**Figure 57:** XPS spectra of as-deposited and plasma-treated (40 W) SnO<sub>2</sub> nanowires.

Influence of the surface modification on the intrinsic properties of SnO<sub>2</sub> nanowires was also supported photoluminescence (PL) data of as-prepared and plasma-treated SnO<sub>2</sub> nanowires shown in Figure 58. The comparison of the PL of the two samples indicates a red shift (500 → 550 nm) due to the possible defect states in the bandgap of surface treated SnO<sub>2</sub> nanowires. The intensity of PL signal (550 nm) of plasma treated sample was found to be four times higher when compared to the PL signal in as-prepared sample. The intensity of PL can be attributed to the increased density of oxygen vacancies (OVs) in the plasma-treated SnO<sub>2</sub> NWs which is responsible for the enhanced gas sensing performance.

It is well known that the variations in the luminescence of SnO<sub>2</sub> nanowires originate from the surface defect electronic states formed by surface oxygen



vacancies. The different types of surface oxygen deficiency result in the different locations of defect levels in the forbidden bandgap of tin oxide which are responsible for photoluminescence with different wavelengths.

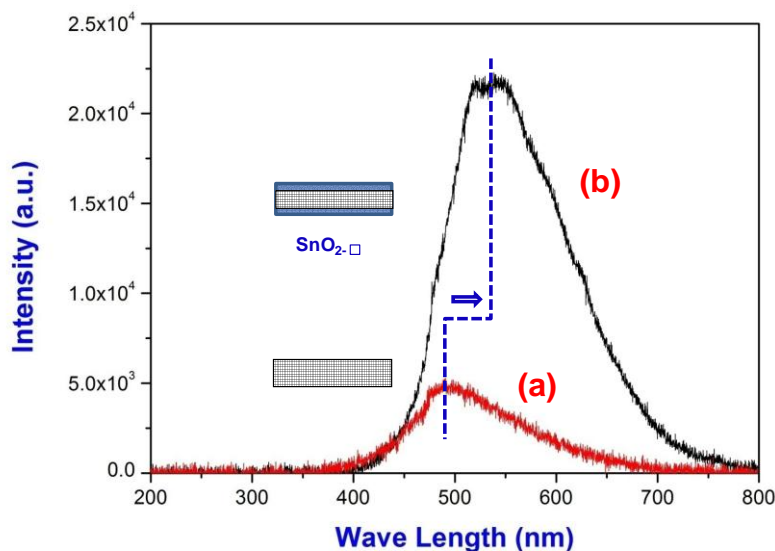


**Figure 58:** Photoluminescence spectra of as-deposited (TO) and plasma-treated (TTO4) SnO<sub>2</sub> nanowires.

Our experimental results show that the emission peak at 500 nm originates from the surface oxygen vacancies which are created in the CVD process; the emission peak at 550 nm is due to another type of oxygen vacancies induced by the plasma bombardment. The origin of temperature-dependent photoluminescence in SnO<sub>2</sub> nanowires fabricated by thermal evaporation has been reported (480 and 600 nm) to originate from defect electronic states in the bandgap formed by surface oxygen vacancies which supports our observation.<sup>[293]</sup> As-grown tin oxide nanowires have oxygen vacancies which cause the chemisorption of oxygen on the SnO<sub>2</sub> surface as well as depletion of electrons near the surface. The concentration of oxygen vacancies is increased in the plasma-treated SnO<sub>2</sub> nanowires due to preferential etching of lattice oxygen atoms which lead to higher depletion

region and larger surface electric field resulting in a larger band bending. The sensing experiments carried with both systems have confirmed the dependence of sensitivity on the concentration of oxygen vacancy. This plasma effect will be investigated in future experiments with different plasma powers, temperature- dependent and time resolved photoluminescence.

### **6.3 Gas sensing properties of plasma-treated SnO<sub>2</sub> nanowires**

Gas sensing properties of as-deposited and plasma-treated samples of TTO series showed higher conductance for plasma-treated samples, possibly due to the effect of band bending induced by the surface charges associated with the shallow donor states of high number of oxygen vacancies. Figure 59 presents sensitivity (S) against operating temperature (220-250 °C) for as-deposited (TO) and plasma-treated (TTO) SnO<sub>2</sub> nanowire samples. The sensitivity enhancement was found to commensurate with the applied plasma power, for example, the sensitivity of TTO4 (4.98) was significantly higher than the value observed for TO (1.69). The sample TTO5 treated with higher plasma power indicated that formation of significant amount of elemental tin increases the metallic behaviour which is detrimental for the sensitivity of the samples (S = 1.02; 80 W).

Stoichiometric SnO<sub>2</sub> reduced by plasma treatment leads to creation of bridging oxygen vacancies and less coordinated Sn species, which increases defect density on the surface. Neutral oxygen adsorbs weakly on the SnO<sub>2</sub> surfaces with the adsorption energy less than 0.2 eV, whereas on bridging oxygen vacancies, the adsorption energy of upto 1.8 eV was reported. These activated oxygen species passivate the SnO<sub>2</sub> nanowire surface, by withdrawing the electrons from dangling bond of surface Sn atoms. The

bridging oxygen vacancies can bind three O<sub>2</sub> molecules simultaneously with one at vacancy site and two at five fold Sn sites.<sup>[294]</sup>

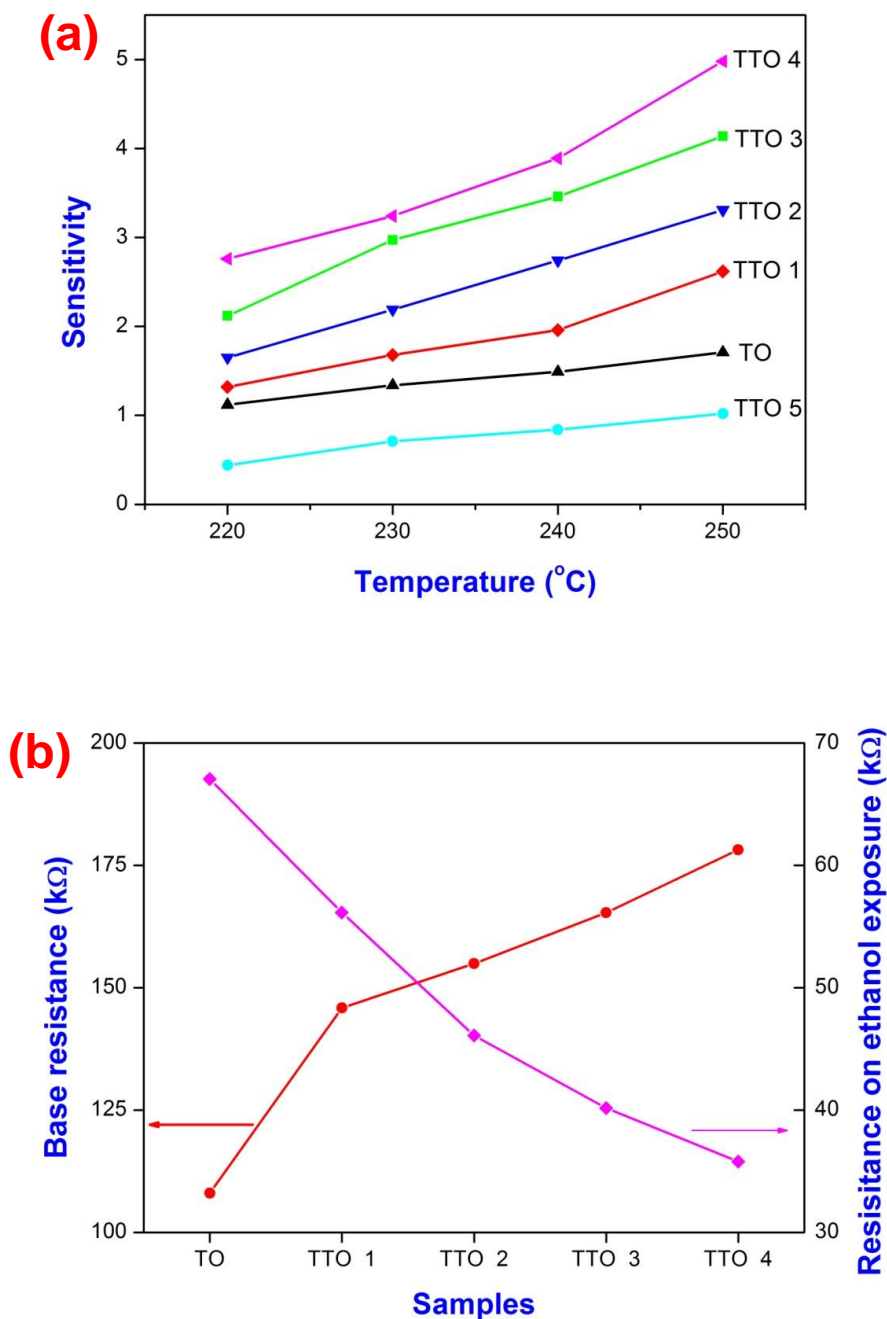


**Figure 59:** (a) Temperature-dependent sensing response curves for TTO series samples and (b) base and sensing resistances dependency to the power of plasma treatment, which reveals the increasing oxygen chemisorption over the samples.

An increased density of free sited and dangling bonds on SnO<sub>2</sub> enhanced the amount of chemisorbed oxygen as reflected in the higher base resistance of plasma treated samples. Catalytic oxidation of ethanol on tin oxide nanowire surface occurred instantaneously ( $\text{CH}_3\text{CH}_2\text{OH (g)} + \text{O}_{\text{ads}}^- \rightarrow \text{CO} + \text{CO}_2 + \text{H}_2\text{O} + \text{e}^-$ )<sup>[295]</sup> and was observed as increase in the conductance of the sample, which was found to be proportional to the applied power in the plasma-treated samples (Figure 59(b)). This confirmed that the redox reaction at the surface of plasma treated nanowires with ethanol released more charge carriers into the SnO<sub>2</sub> nanowire conduction band by increasing the cross-section of the conducting channels inside the nanowires.<sup>[296]</sup> It has been recently shown that the charge depletion sheath formed due to the combination of surface defects and underlying bulk structure leads to significant band bending and Fermi level shrinkage in the energy gap.<sup>[297]</sup> However, the electronic (oxygen vacancies) and structural defects caused by plasma treatment modulate the surface electronic structure, hereby shrinking the intrinsic bandgap, which leads to enhanced sensing properties. Since plasma treatment resulted in the formation of metallic Sn NPs on the surface of SnO<sub>2</sub> NWs, a decrease in the base resistance ( $R_{\text{Air}}$ ) can be envisaged in Sn@SnO<sub>2</sub> system. However, the nature of elemental tin leads to a dynamic surface chemistry resulting in inconsistent gas sensitivity data.

The long-term stability of plasma treated (40 W) SnO<sub>2</sub> nanowire gas sensor was studied by on/off gas sensing measurement. Figure 60 shows that the resistances of as-prepared and plasma-treated SnO<sub>2</sub> NWs (in air and in ethanol) remain relatively unchanged over the entire experiment time. Although small drifts are observed, these changes of drifts were within  $\pm 2\%$ . It should be noticed that the cycling stability of the plasma-treated SnO<sub>2</sub> NWs indicated the mixed Sn(II)/Sn(IV) phases in plasma-treated samples are stable during the gas sensing process.

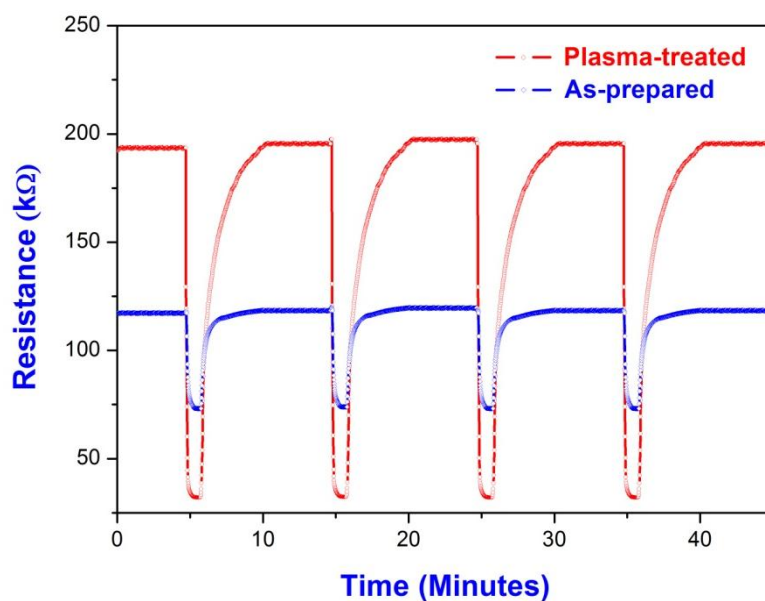


**Figure 60:** On/off gas sensing curves of as-prepared and plasma-treated (40W) SnO<sub>2</sub> nanowires in 1000 ppm ethanol at 250 °C.

In summary, surface modification of tin oxide nanowires by plasma treatment demonstrated the possibility of enhancing the sensing and catalytic properties. Plasma treatment on tin oxide nanowires generated intimate amorphous/crystalline oxide interfaces and increased concentration of oxygen vacancies responsible for efficient charge transfer (transduction) processes which consequently result in enhanced sensitivity. Moreover, the controlled reduction of tin oxide nanowires to SnO<sub>2-x</sub> / SnO<sub>2</sub> system opens up new avenues for modifying fundamental properties.

## 7 Synthesis and Application of SnO<sub>2</sub> Nanowire Based Heterostructures

Heterostructures have shown exciting unique properties and functionalities that are not accessible in the single-component materials, due to the combination of material classes such as metals, metal oxides, semiconductors, and polymers. Hence, the SnO<sub>2</sub> nanowire based heterostructures (such as SnO<sub>2</sub>@TiO<sub>2</sub>, SnO<sub>2</sub>@SnO<sub>2</sub>, SnO<sub>2</sub>@VO<sub>x</sub> and SnO<sub>2</sub>@CdS) were fabricated via a “nanowire” substrate by a two-step CVD process. The corresponding structural properties were well characterized by SEM, XRD and HR-TEM. A range of the unique properties (such as electrical, gas sensing, photoconductivity and surface wettability) of SnO<sub>2</sub> nanowire based architectures were investigated. The potential applications of SnO<sub>2</sub> nanowire based architectures in nanodevice and energy were exploring to push the development of nanotechnology forward.

### 7.1 SnO<sub>2</sub>@TiO<sub>2</sub>: Oxide-oxide anisotropic core-shell structures

#### 7.1.1 Introduction of core-shell structures

Recently, one-dimensional metal oxide semiconducting nanostructures have attracted significant research interest, due to their important application potential as building blocks of nanoscale electronic or optoelectronic devices exploiting their properties not achievable in bulk states.<sup>[298]</sup> Among all the 1D nanostructures, 1D core-shell nanostructures have shown exciting physical properties, and thus have more extensive applications in field-effect transistor devices, electronic transport, advanced coating and catalysis,<sup>[299]</sup> because

they display improved physical properties over their single-component counterparts.

The first reported 1D core-shell nanostructures were silicon carbide and silicon oxide sheathed with boron nitride and carbon respectively that were synthesized by means of reactive laser ablation in 1998.<sup>[300]</sup> Stimulated by the above interesting results, a series of 1D core-shell nanostructures successfully synthesized by various techniques,<sup>[301-302]</sup> have been recently developed for exploring their novel physical properties and fabricating new nanodevices. Kai et al. prepared GaP@GaN core-shell nanowires via vapor transport deposition, and found unusual temperature dependences of the photoluminescence intensity in the former system.<sup>[303]</sup> Hayden and co-workers synthesized p-Si/n-CdS core-shell nanowires using pulsed-laser deposition and fabricated light-emitting diodes based on this nanostructure.<sup>[304]</sup> Kuang and co-workers reported the epitaxial growth of ZnO@SnO<sub>2</sub> core-shell nanostructures, and observed the new photoluminescence properties induced by the epitaxial interfaces.<sup>[305]</sup> By a thermal evaporation method, Kim and co-workers prepared SnO<sub>2</sub>@In<sub>2</sub>O<sub>3</sub> core-shell nanostructures which could be used as Li ion battery electrodes application.<sup>[306]</sup> The reports above demonstrate that the core-shell nanostructures are promising materials for extending their applications in the future.

As wide band gap semiconductors SnO<sub>2</sub> and TiO<sub>2</sub> 1D nanostructures are more attractive because they have better performance for fabricating electronic and optoelectronic nanodevices.<sup>[307]</sup> Therefore, various SnO<sub>2</sub> and TiO<sub>2</sub> 1D nanostructure have been synthesized via different preparation methods.<sup>[308-309]</sup> However, to our knowledge, there were few reports on the preparation SnO<sub>2</sub>@TiO<sub>2</sub> core-shell structures by chemical vapor deposition, especially on the corresponding electrical and gas sensing properties.

Herein, the synthesis of SnO<sub>2</sub>@TiO<sub>2</sub> 1D core-shell nanostructures by a

two-step molecule-based chemical vapor deposition process of sequential decomposition of a molecular precursor Sn(O<sup>t</sup>Bu)<sub>4</sub> and Ti(O<sup>i</sup>Pr)<sub>4</sub>, respectively, was presented. The comparatively SnO<sub>2</sub>@TiO<sub>2</sub> core-shell structures before and after annealing treatments at different temperatures, and the diffusion processes that accompanies the chemical transformation under different temperatures were investigated. The gas sensing performance and electrical property of single SnO<sub>2</sub>@TiO<sub>2</sub> core-shell structure were also characterized.

### 7.1.2 Characterization of SnO<sub>2</sub>@TiO<sub>2</sub> core-shell structures

The crystal structures of the SnO<sub>2</sub>@TiO<sub>2</sub> core-shell structures were identified by XRD analysis, as shown in Figure 61. It revealed that all peaks come from the rutile structure of SnO<sub>2</sub> ( $a = 4.738 \text{ \AA}$  and  $c = 3.187 \text{ \AA}$ ) according to PDF No. 41-1445 and Al<sub>2</sub>O<sub>3</sub> substrates (PDF No. 01-1296). The peaks corresponding to TiO<sub>2</sub> were not observed, suggesting that the TiO<sub>2</sub> shell was X-ray amorphous.

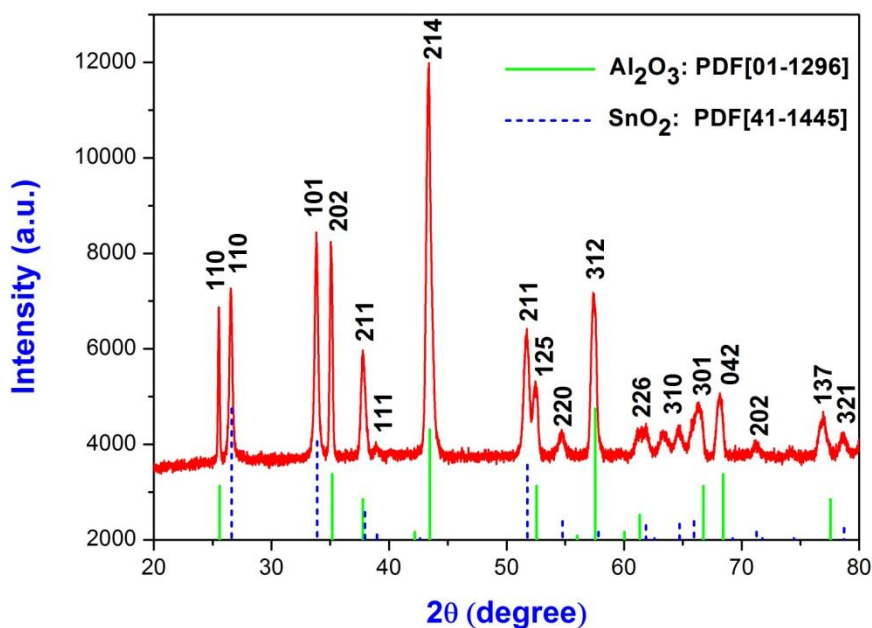


**Figure 61:** XRD patterns of SnO<sub>2</sub>@TiO<sub>2</sub> core-shell structures.



Figure 62 shows SEM and TEM images of the as-synthesized SnO<sub>2</sub> NWs and SnO<sub>2</sub>@TiO<sub>2</sub> core-shell structures, indicating that both samples consist of 1D structures. It was clearly seen that the SnO<sub>2</sub> NWs with a diameter of ~ 40 nm and length of ~10 μm was covered with a very uniform TiO<sub>2</sub> shell with a thickness of ~ 10 nm. This result revealed that the SnO<sub>2</sub>@TiO<sub>2</sub> core-shell structures were successfully fabricated by CVD in this work.

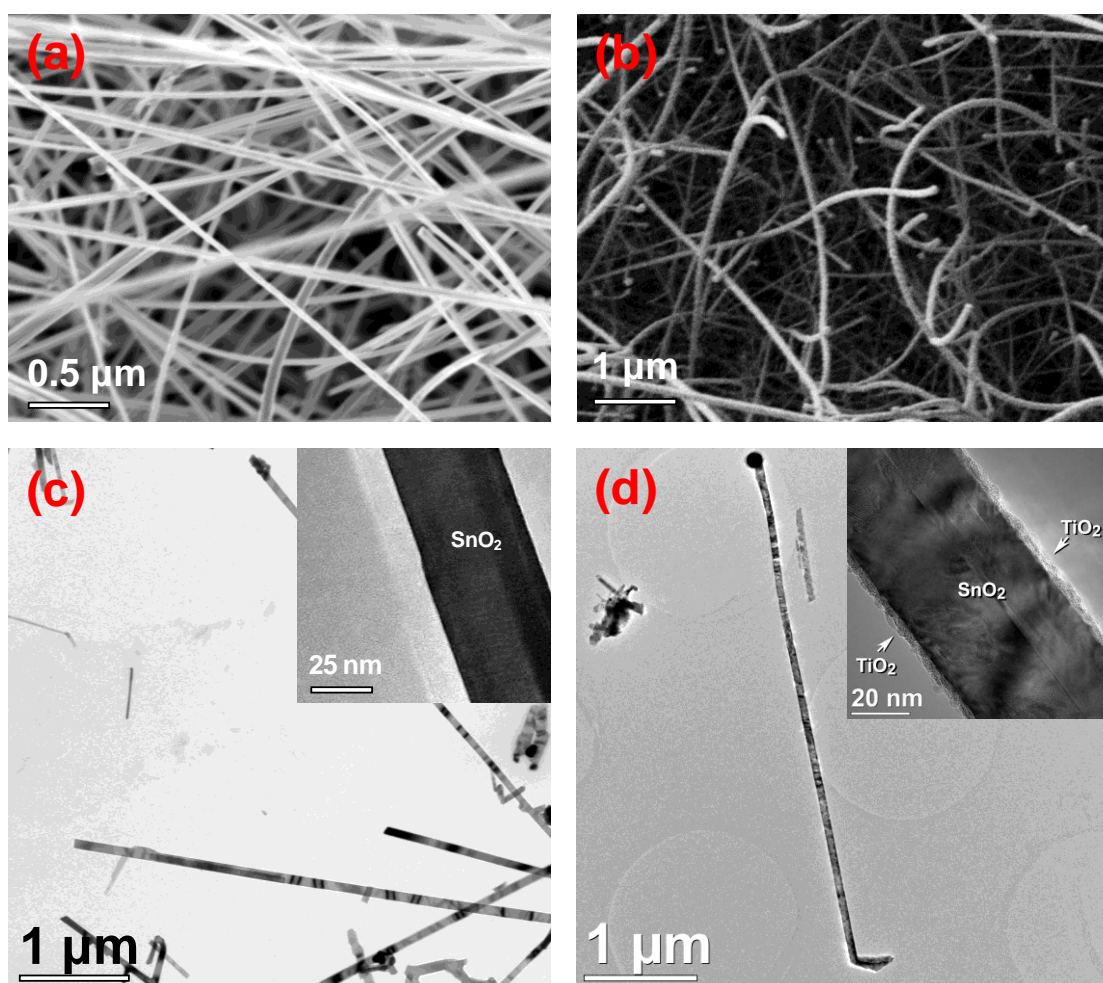


**Figure 62:** SEM (a, b) and TEM images (c, d) of the as-prepared SnO<sub>2</sub> NWs (left) and SnO<sub>2</sub>@TiO<sub>2</sub> core-shell structures (right).

TiO<sub>2</sub> shell was iso-structural with the rutile phase of SnO<sub>2</sub> NW core, however the lattice mismatch so low ( $(a_{\text{SnO}_2} - a_{\text{TiO}_2}) / a_{\text{TiO}_2} = 2.6\%$  and  $(c_{\text{SnO}_2} - c_{\text{TiO}_2}) / c_{\text{TiO}_2} = 7.7\%$ ), it might be overcome through diffusion of Sn and Ti

between SnO<sub>2</sub> NW core and TiO<sub>2</sub> shell, forming a solid solution at the interface. This solid solution might lead to a gradual change in lattice parameters, relieving strain between SnO<sub>2</sub> NW core and TiO<sub>2</sub> shell. Hence, Sn<sub>x</sub>Ti<sub>1-x</sub>O<sub>2</sub> solid solution will be formed by the interdiffusion, and was established by X-ray diffraction. To see how the annealing treatment influences the diffusion process at the interface of SnO<sub>2</sub>/TiO<sub>2</sub>, the core-shell structures were annealed at 950, 1200 and 1400 °C, respectively. Figure 63 showed the XRD patterns of the as-prepared and annealed SnO<sub>2</sub>@TiO<sub>2</sub> core-shell structures. The peaks corresponding to rutile TiO<sub>2</sub> (PDF No. 31-0180) were observed at 950 °C, suggesting that the TiO<sub>2</sub> shell was becoming crystallized structures. The peak of (110) SnO<sub>2</sub> at 27° shifted to right side obviously at 1200 °C in comparison to that of as-prepared sample whereas it disappeared when the temperature increased to 1400 °C. On the other side, the peaks of TiO<sub>2</sub> shifted to left side finely when the temperature increased to 1200 °C.

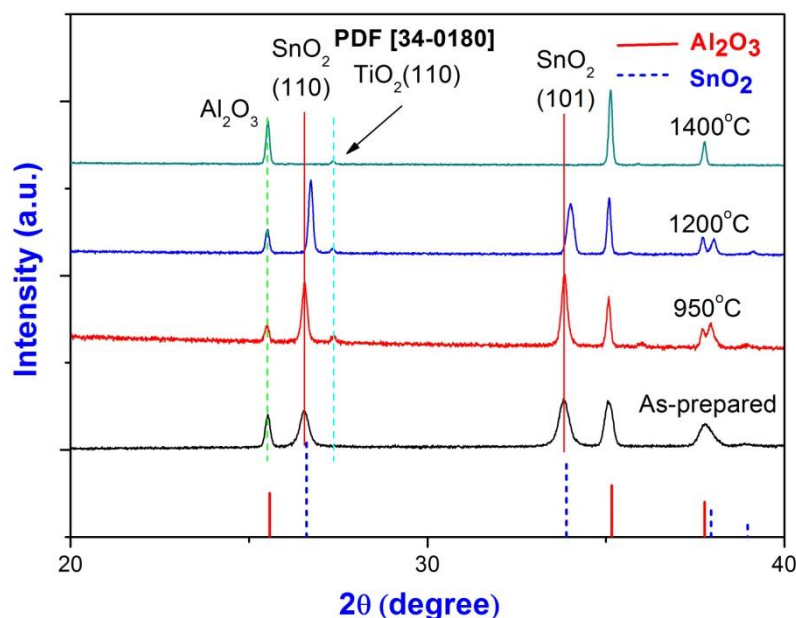


**Figure 63:** XRD patterns of the SnO<sub>2</sub>@TiO<sub>2</sub> core-shell structures: as-prepared and annealed at 950, 1200 and 1400 °C, respectively.

The deviation of SnO<sub>2</sub> (110) peaks to higher values of  $2\theta$  than for the pure SnO<sub>2</sub> phase after annealing treatment, was consistent with a contraction of the unit cell in the (110) direction. Hence, this diffraction results indicated that SnO<sub>2</sub>@TiO<sub>2</sub> core-shell structures might be best described as Sn<sub>x</sub>Ti<sub>1-x</sub>O<sub>2</sub> solid solution after annealing treatment. This deviation increased with the increase of annealing temperature; the  $2\theta$  values of the SnO<sub>2</sub> (110) peak of the as-prepared and annealed at 950 and 1200 °C samples were 26.55, 26.58 and 26.69°, respectively, a total variation of 0.14° across the samples, as shown in Figure 64.

This presence of diffraction peak at  $2\theta$  values deviation was well documented for Sn<sub>x</sub>Ti<sub>1-x</sub>O<sub>2</sub> solid solution across the composition range. On the other side, the  $2\theta$  values of the TiO<sub>2</sub> (110) were mostly invariant after annealing treatment. Hence, SnO<sub>2</sub> was identified to be the dominant diffusing species in the SnO<sub>2</sub>-TiO<sub>2</sub> system.

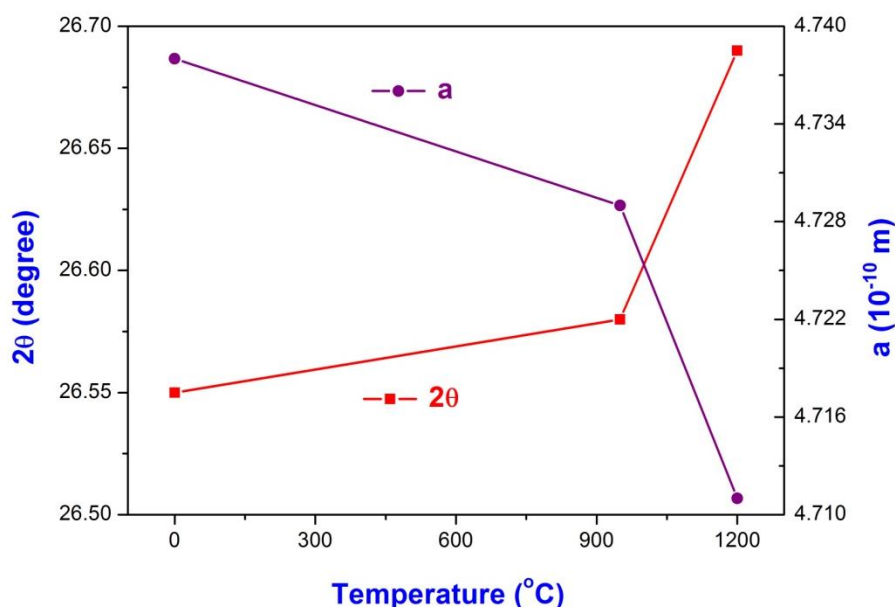


**Figure 64:** Variation curves of lattice parameter  $a$  and (110) peak of SnO<sub>2</sub> before and after annealing treatment at 950 and 1200 °C, respectively.

Although the presence of so few diffraction peaks due to the highly crystallographically orientated nature of the samples made Rietveld refinement of the patterns impossible, but the lattice parameter  $a$  of the tetragonal structure of SnO<sub>2</sub> NW can be calculated from the position of the (110) peak (4.738, 4.729 and 4.711 Å for the as-prepared and annealed at 950 and 1200 °C, respectively). Hence, assuming change in lattice parameters with changing solid solution composition (Vegard's law), the mean stoichiometry of the Sn <sub>$x$</sub> Ti<sub>1- $x$</sub> O<sub>2</sub> solid solution probed in XRD can be calculated as  $x = 1, 0.937$  and 0.857, respectively.

The equilibrium phase diagram of SnO<sub>2</sub>-TiO<sub>2</sub> system<sup>[310]</sup> (Figure 65) showed that, TiO<sub>2</sub> and SnO<sub>2</sub> form thermodynamically stable solid solution of formula Sn <sub>$x$</sub> Ti<sub>1- $x$</sub> O<sub>2</sub> across the whole composition range  $0 \leq x \leq 1$  as the temperature is above 1350 °C or the composition range Ti-rich ( $x < 0.15$ ) and Sn-rich ( $x > 0.85$ ) above 900 °C.<sup>[311]</sup> In our case, the coordinates of experimental conditions located at the “mixed oxide” area in equilibrium phase diagram. This result agreed well with the equilibrium phase diagram.

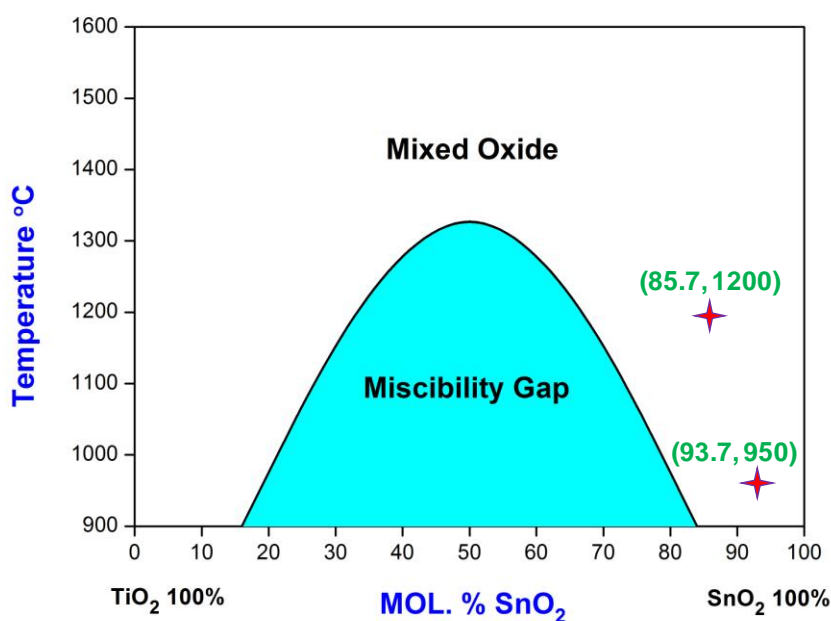


**Figure 65:** Equilibrium phase diagram of the SnO<sub>2</sub>-TiO<sub>2</sub> system.

It is well known that SnO<sub>2</sub> had a low melting point (1625 °C) and sintered by evaporation condensation mechanism,<sup>[312]</sup> while TiO<sub>2</sub> sintered by grain boundary diffusion.<sup>[313]</sup> Moreover, SnO<sub>2</sub> had a strong character of both covalent and ionic bonding, and there was a significant concentration of intrinsic Sn vacancies. Hence, quicker diffusion rate involved free surface diffusion at high temperature ( $T > 1000$  °C) whereas evaporation condensation is dominated at high-temperature ( $T > 1350$  °C).<sup>[314]</sup> On the other hand, TiO<sub>2</sub> was in fact nonstoichiometric TiO<sub>2-x</sub> with relatively low diffusion rate due to low concentration of defects such as double ionized oxygen vacancies and Ti<sup>4+</sup> interstitials.<sup>[315]</sup> Thus either the interstitial or vacancy diffusion mechanism could conceivably operate in the Sn<sub>x</sub>Ti<sub>1-x</sub>O<sub>2</sub> solid solution reaction.

From the analyses presented above, an explanation can be put forward for the thermal diffusion process at different annealing temperatures. It is known that cation diffusion occurs through motion of point defects in the cation sublattice. The diffusion rate at which Sn<sup>4+</sup> diffused into the TiO<sub>2</sub> was greater than the diffusion rate at which Ti<sup>4+</sup> diffused into the SnO<sub>2</sub>. The incident Sn<sup>4+</sup> ions diffused into the TiO<sub>2</sub> faster than Ti<sup>4+</sup> arrive, then the Sn<sub>x</sub>Ti<sub>1-x</sub>O<sub>2</sub> solid solution will be present at the interface of SnO<sub>2</sub>-TiO<sub>2</sub> and there will be no abrupt interface between SnO<sub>2</sub> and TiO<sub>2</sub>. The same conclusions were obtained by Drobeck et al.<sup>[316]</sup> and Akse et al.<sup>[317]</sup>, who inferred an interstitial diffusion mechanism involving tetravalent cation interstitial defects.

In this case, annealing at high temperature ( $T > 1000$  °C) accelerated the Sn<sup>4+</sup> ions diffused into the TiO<sub>2</sub>, meanwhile Sn<sup>4+</sup> ions were formed SnO<sub>2</sub>. When the temperature was above 1350 °C, it suspected to be the onset of an evaporation process. Then SnO<sub>2</sub> was evaporated continuously at 1400 °C. This dynamic process finished until SnO<sub>2</sub> was consumed totally, which left TiO<sub>2</sub> formed some irregularly shaped particles.



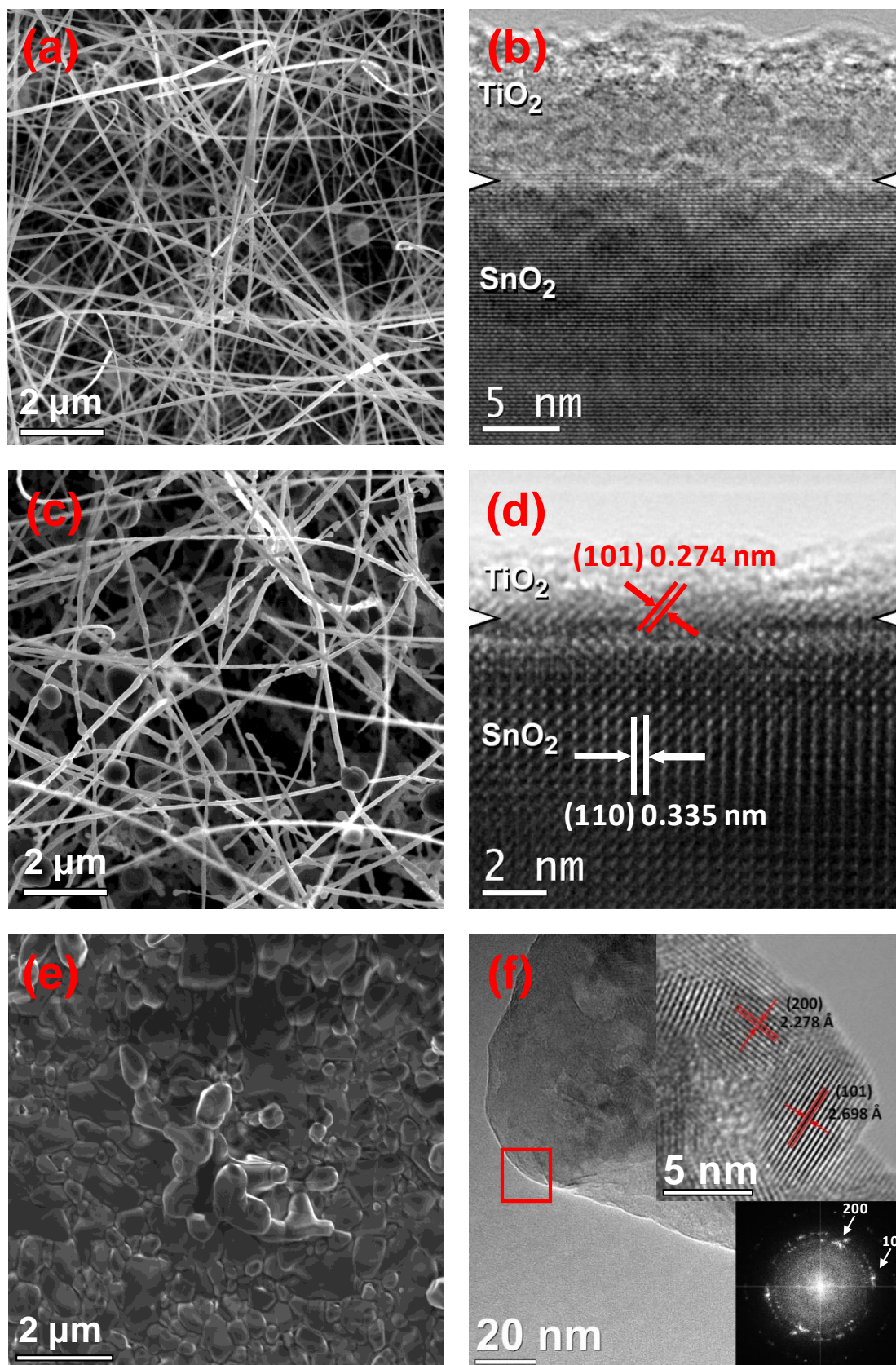


**Figure 66:** SEM and HR-TEM images of SnO<sub>2</sub>@TiO<sub>2</sub> core-shell structures after annealing treatment at 950, 1200 and 1400 °C, respectively.

It should be noted that the deviation from Vegard's law has been reported for the Sn<sub>x</sub>Ti<sub>1-x</sub>O<sub>2</sub> system, as well as distortion of the tetragonal lattice such as the lattice parameter  $a \neq b$ ,<sup>[318-319]</sup> which would introduce error into this calculation. However, these deviations were most prominent for  $0.3 < x < 0.6$ , i.e. near the middle of the solid solution composition range, within the miscibility gap, and were less-pronounced close to the end-members. Similar systematic deviations in peak position of the TiO<sub>2</sub> (110) peak were not observed, this indicated that SnO<sub>2</sub> diffusion into the voids at the interface was insufficient to alter the TiO<sub>2</sub> lattice parameter to an extent detectable by XRD.

The SEM and HR-TEM were also explored to characterize the structural properties of Sn<sub>x</sub>Ti<sub>1-x</sub>O<sub>2</sub> solid solution. Figure 66(a) showed the SEM image of SnO<sub>2</sub>@TiO<sub>2</sub> core-shell structures after annealing treatment at 950 °C. The main structural feature of the annealed core-shell structures was the encapsulation of the SnO<sub>2</sub> core in the TiO<sub>2</sub> shell. Moreover, it was clearly seen that the thickness of TiO<sub>2</sub> shell was about 10 nm from the TEM image (Figure 66(b)) of core-shell structures.

The SEM image (Figure 66(c)) showed that SnO<sub>2</sub> NW was covered with many particle-like materials along the core axis. The HR-TEM image (Figure 66(d)) revealed that the interface of SnO<sub>2</sub> and TiO<sub>2</sub> was not clear due to the crystallization of TiO<sub>2</sub> shell and the diffusion of SnO<sub>2</sub> into TiO<sub>2</sub> shell resulting in the formation of Sn<sub>x</sub>Ti<sub>1-x</sub>O<sub>2</sub> solid solution. Clear lattice fringes were observed in the image, suggesting the crystal nature of the SnO<sub>2</sub> core and TiO<sub>2</sub> shell. The spaces were 2.738 Å and 3.347 Å, corresponding to (101) plane of rutile TiO<sub>2</sub> and (110) plane of SnO<sub>2</sub> respectively.

The SEM image (Figure 66(e)) and low-magnification TEM image (Figure 66(f)) of SnO<sub>2</sub>@TiO<sub>2</sub> core-shell structures annealed at 1400 °C showed clearly irregularly shaped particles. The HR-TEM image (up inset Figure 66(f)) of the area indicated by a black frame in the Figure 66(f) revealed that a clear lattice

fringes of particles were 2.698 Å and 2.278 Å, corresponding to (101) and (200) planes of TiO<sub>2</sub>, respectively. It was also identified by the SAED pattern (down inset Figure 66(f)). Hence, the same results were observed by XRD, SEM and HR-TEM characterization to present a clear portrait of the diffusion process.

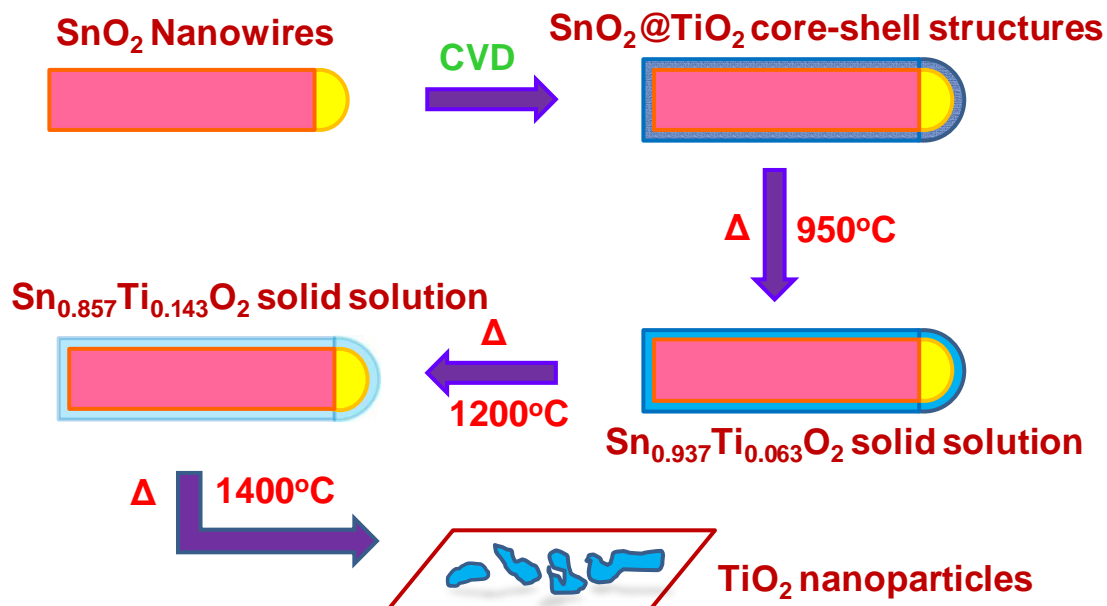


**Figure 67:** Scheme of process mechanism for the SnO<sub>2</sub>-TiO<sub>2</sub> system after annealing treatment.

Basing on the structural analysis after annealing treatment at 950, 1200 and 1400 °C, respectively, we proposed a diffusion mechanism for the SnO<sub>2</sub>-TiO<sub>2</sub> system, which was shown in Figure 67. Initially, the SnO<sub>2</sub>@TiO<sub>2</sub> core-shell nanostructures were successfully synthesized by CVD process to deposit the TiO<sub>2</sub> shell on the SnO<sub>2</sub> nanowire substrate. The as-prepared TiO<sub>2</sub> shell was amorphous, which will transform into rutile structures after annealing at 950 °C. SnO<sub>2</sub>@TiO<sub>2</sub> core-shell structures formed Sn<sub>x</sub>Ti<sub>1-x</sub>O<sub>2</sub> mixed solid solution due to the Sn<sup>4+</sup> ions diffuse into the TiO<sub>2</sub>, the mean stoichiometry of the Sn<sub>x</sub>Ti<sub>1-x</sub>O<sub>2</sub> probed by XRD can be calculated as  $x = 1, 0.927$  and  $0.857$ , respectively for the as-prepared and annealed at 950 and 1200 °C, respectively. SnO<sub>2</sub> was evaporated continuously until it was consumed totally,



then the left TiO<sub>2</sub> formed some irregularly shaped particles as the annealing temperature increased to 1400 °C.

### 7.1.3 Properties of SnO<sub>2</sub>@TiO<sub>2</sub> core-shell structures

In order to measure the current signals through the single SnO<sub>2</sub> and SnO<sub>2</sub>@TiO<sub>2</sub> nanowire, these wires were connected on the two Au electrodes by focused ion beam (FIB) technique (inset, Figure 68). Figure 68 showed that the room-temperature (25 °C) current-voltage (*I-V*) characteristics of a single SnO<sub>2</sub> nanowire and SnO<sub>2</sub>@TiO<sub>2</sub> core-shell structure in dry air condition.

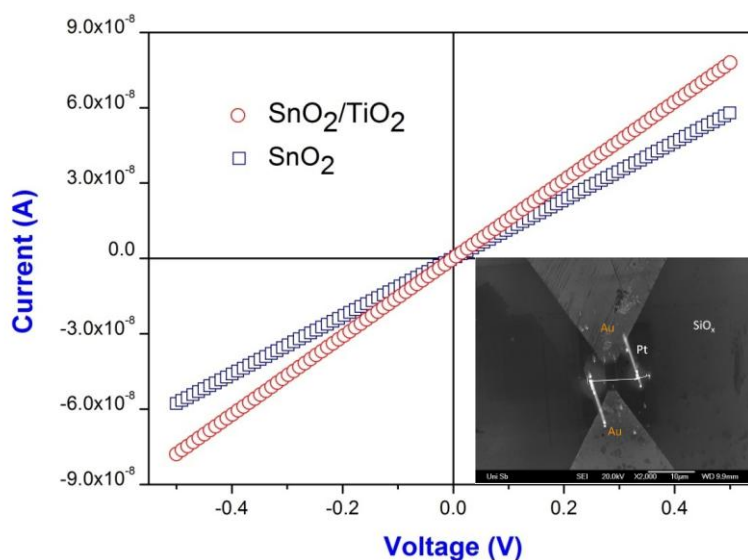


**Figure 68:** Room-temperature (25 °C) *I-V* characteristics of a single SnO<sub>2</sub> nanowire and SnO<sub>2</sub>@TiO<sub>2</sub> core-shell structure in dry air condition.

*I-V* curves exhibited good linear behavior, which proved not only a good ohmic contact between the Pt contact layers but also a good junction between Pt contact layers and 1D nanostructured structure. This ohmic behavior was very important for the sensing properties of 1D nanostructures because the sensitivity of the material can be maximized when the metal-semiconductor junction was ohmic or has a negligible junction resistance.<sup>[243]</sup> Due to the less

conductivity of amorphous TiO<sub>2</sub> overlayer, the resistivity ( $\rho$ ) of the single SnO<sub>2</sub>@TiO<sub>2</sub> core-shell structure ( $1.90 \pm 0.01 \text{ } \Omega \cdot \text{cm}$ ) was larger than single SnO<sub>2</sub> nanowire in dry air ( $0.14 \pm 0.02 \text{ } \Omega \cdot \text{cm}$ ).

The gas sensing performance of SnO<sub>2</sub> and SnO<sub>2</sub>@TiO<sub>2</sub> core-shell structures in 90 ppm ethanol atmosphere at 250 °C was shown in Figure 69. It was obviously seen that the sensitivity increased obviously from 1.6 to 3.1. It meant that the sensitivity of SnO<sub>2</sub>@TiO<sub>2</sub> core-shell structures was strongly influenced by TiO<sub>2</sub> overlayer in comparison to that of pure SnO<sub>2</sub> naowires.

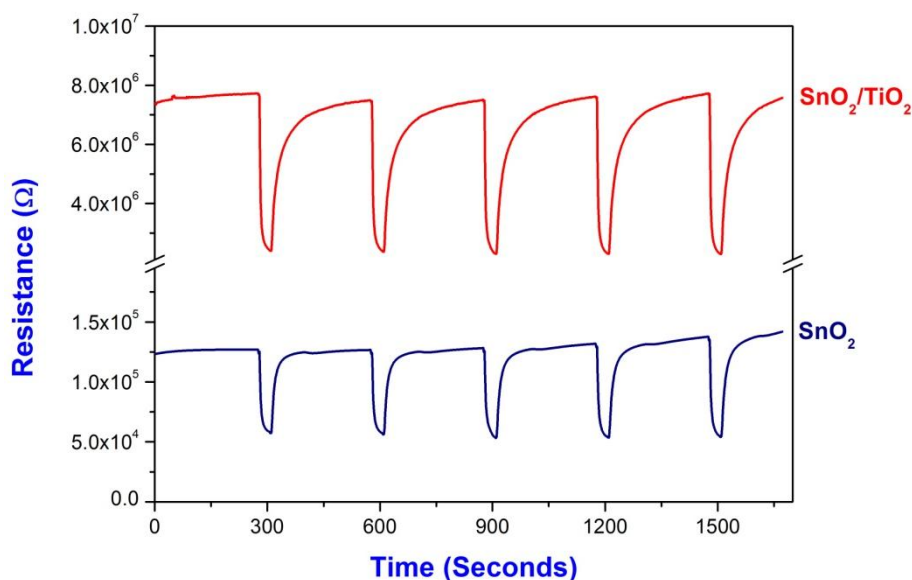


**Figure 69:** Gas sensing performance of SnO<sub>2</sub> and SnO<sub>2</sub>@TiO<sub>2</sub> core-shell structures in 90 ppm ethanol atmosphere at 250 °C.

Two types of interactions between additive and semiconducting oxide, namely chemical and electronic sensitization, have been discussed.<sup>[276]</sup> One type of promoting effect was called chemical sensitization. The gas sensitivity increased because the additive increases the rate of the chemical processes (chemical sensitization). In the case of electronic sensitization, the pure semiconducting oxide had a bare surface and surface adsorbed oxygen was utilized for the oxidation reaction. When the additive was added, the additive in

the oxidized state induces a surface space charge layer which was strongly depletive of electrons in the oxide near the interface. When the additive was reduced on contact with the reducing gas, it relaxed the space charge layer by giving electrons back to the oxide semiconductor. In this way the gas sensitivity was improved greatly. The adsorbed oxygen got trapped at the grain boundary thereby increasing the space charge region, resulting in a decrease in conductance of the material in air. It was known that TiO<sub>2</sub> has a large work function, reflecting electronic interaction takes place between SnO<sub>2</sub> and TiO<sub>2</sub>, when SnO<sub>2</sub> and TiO<sub>2</sub> were mixed together, conduction electrons of SnO<sub>2</sub> NWs were drawn toward TiO<sub>2</sub>, so the depth of the space charge region in SnO<sub>2</sub> NWs was expanded.<sup>[320]</sup> Increase of the work function of SnO<sub>2</sub> by coating of TiO<sub>2</sub> overlayer was also observed from the increase in electrical resistance. Upon exposure to ethanol, TiO<sub>2</sub> was reduced more preferentially than SnO<sub>2</sub> so that the conduction electrons were given back to SnO<sub>2</sub>, leading to larger sensor response than pure SnO<sub>2</sub>.

In summary, 1D SnO<sub>2</sub>@TiO<sub>2</sub> core-shell nanostructures were successfully synthesized by a two-step chemical vapor deposition process. SnO<sub>2</sub>@TiO<sub>2</sub> core-shell structures formed Sn<sub>x</sub>Ti<sub>1-x</sub>O<sub>2</sub> mixed solid solutions because of the Sn<sup>4+</sup> ions diffused into the TiO<sub>2</sub>, the mean stoichiometry of the Sn<sub>x</sub>Ti<sub>1-x</sub>O<sub>2</sub> solid probed in XRD can be calculated as  $x = 1, 0.927$  and  $0.857$ , for the as-prepared and annealed at 950 and 1200 °C, respectively. The single SnO<sub>2</sub>@TiO<sub>2</sub> core-shell structure had a higher resistivity ( $1.90 \pm 0.01 \text{ } \Omega \cdot \text{cm}$ ) than single SnO<sub>2</sub> nanowire ( $0.14 \pm 0.02 \text{ } \Omega \cdot \text{cm}$ ) in dry air at room temperature (25 °C) due to the less conductive amorphous TiO<sub>2</sub> shell. The SnO<sub>2</sub>@TiO<sub>2</sub> core-shell structure had a good sensing performance because the interface plays a role in the gas sensing promoter.

## 7.2 Switchable wettability in SnO<sub>2</sub> nanowires and SnO<sub>2</sub>@SnO<sub>2</sub> heterostructures

### 7.2.1 Introduction of surface wettability

Wettability is an important characteristic feature of a solid surface. It affects the interaction degree on a surface which would have with the surrounding species including water vapor and other chemicals. In addition, it is also related to surface energy which is the basic driving force for many surface reactions and interactions. Hence, the knowledge regarding wettability of a surface is more significantly. The ability to control wettability is important for various surface related technologies.

Wettability is commonly quantified by measuring the contact angle (CA) of water. A surface with a water contact angle larger than 150° is defined as a superhydrophobic surface. Superhydrophobic surface is especially beneficial for applications in nanotechnology, anticorrosion, resisting water coalescence, self-cleaning system, micro-electromechanical systems (MEMS) and solid lubrication systems that require a hydrophobic surface to decrease adhesion and friction.<sup>[321-322]</sup> In addition, the superhydrophobic surface offers much promise for the formation of high-performance nanostructured surfaces with multifunctionality that can be used in optical, photoelectric, microelectronic, and biomedical applications.<sup>[323-324]</sup> On the other hand, extremely wetting surface, or superhydrophilic surfaces with a water contact angle close to 0°, may be beneficial for applications in catalysts and surface reactant systems.<sup>[325-326]</sup>

The study of controlling surface wettability has attracted considerable attention in the past. In controlling the wettability of a surface, the chemical composition and the geometrical structure on superhydrophobicity has been

elucidated by Wenzel and Cassie models. Both the models have put emphasis on the geometrical structure of solid surfaces as an important factor in determining the wettability.<sup>[327-328]</sup>

In the past several years, nanostructured SnO<sub>2</sub> has attracted much attention due to its unique properties,<sup>[329]</sup> but these studies are mainly focused on its gas sensitivity<sup>[330]</sup> and electricity,<sup>[331]</sup> and few reports have concerned its surface wettability,<sup>[332]</sup> especially, the surface wettability switching of superhydrophobicity and superhydrophilicity on transparent and conductive SnO<sub>2</sub> films.<sup>[333]</sup> However, to our knowledge, there were few reports on the wettability of SnO<sub>2</sub> nanowire based surface.<sup>[334]</sup> More importantly, the switching from superhydrophilic to superhydrophobic surface based on SnO<sub>2</sub> nanowire by CVD growth has not been reported.

Here, an effective method to convert the SnO<sub>2</sub> nanowire based surface from superhydrophilic to superhydrophobic by a three-step CVD growth was demonstrated, and a clear portrait of the key factor in determining the surface wettability was presented. Moreover, the variation of the superhydrophobic surface by employing UV irradiation, dark storage and O<sub>2</sub> annealing were demonstrated.

### **7.2.2 Characterization of SnO<sub>2</sub> nanowires and SnO<sub>2</sub>@SnO<sub>2</sub> heterostructures**

Chemical vapor deposition (CVD) represented a cost-effective method available for the deposition of functional layers and modification of microscale and/or nanoscale structures. This technique was used in our case to prepare SnO<sub>2</sub> nanowires and SnO<sub>2</sub>@SnO<sub>2</sub> heterostructures. Figure 70 showed top-view SEM and TEM images of (a, b) SnO<sub>2</sub> NWs and (c, d) SnO<sub>2</sub>@SnO<sub>2</sub> heterostructures, indicating that both samples consist of 1D structures. It was clearly seen that the brush-type SnO<sub>2</sub>@SnO<sub>2</sub> heterostructures were fabricated

on the SnO<sub>2</sub> NWs with a diameter of ~ 60 nm and length of ~ 20 μm. The branched structures were about 300 nm in length and 20 nm in diameter.

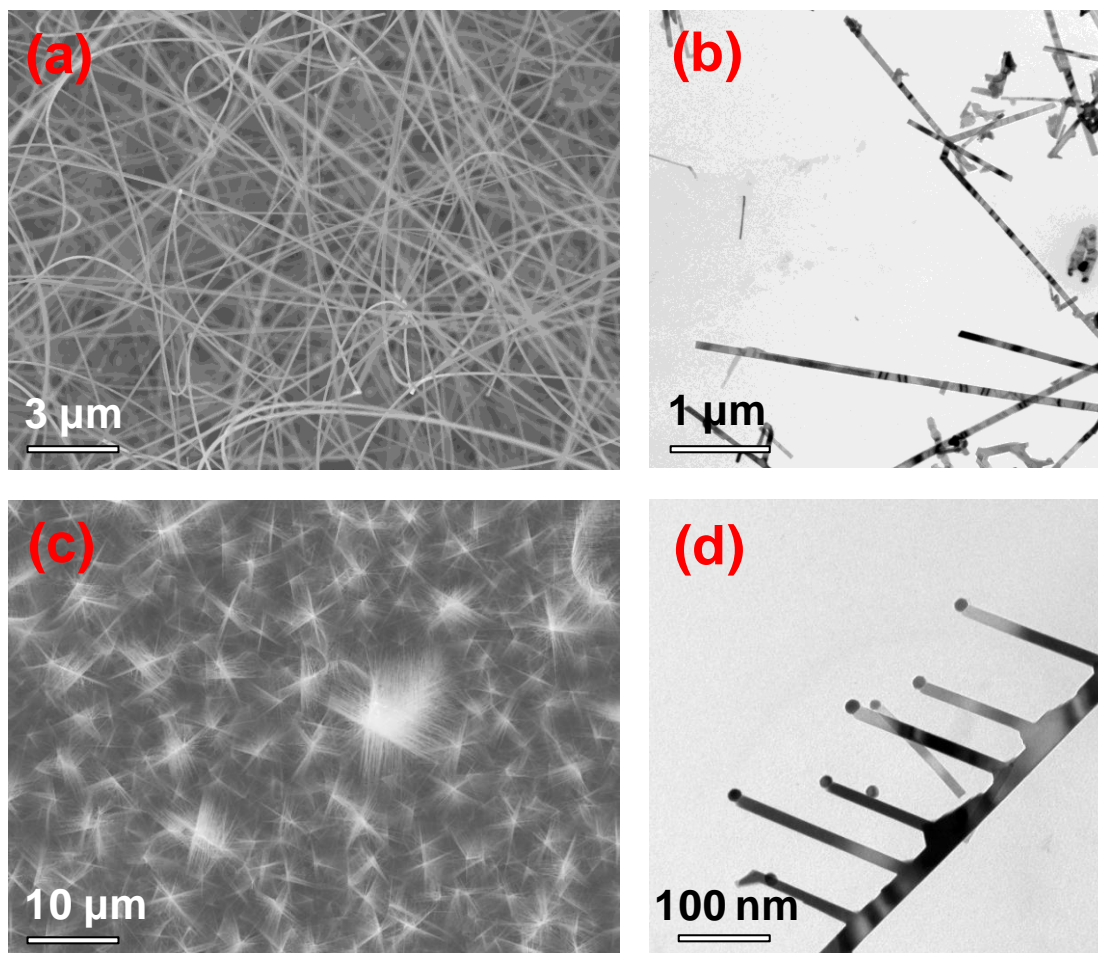


**Figure 70:** Top-view SEM and TEM images of (a, b) SnO<sub>2</sub> NWs and (c, d) SnO<sub>2</sub>@SnO<sub>2</sub> heterostructures.

The crystal structures of the SnO<sub>2</sub> nanowires and SnO<sub>2</sub>@SnO<sub>2</sub> heterostructures were identified by means of XRD analysis, as shown in Figure 71. Compared with the XRD data, all peaks can be indexed as the rutile crystal structure with lattice constants of  $a = 4.738 \text{ \AA}$  and  $c = 3.187 \text{ \AA}$  according to PDF No. 41-1445. The peaks intensity of SnO<sub>2</sub>@SnO<sub>2</sub> heterostructures was stronger than SnO<sub>2</sub> nanowires due to the better crystallization. No peaks from other phases can be detected by XRD, which revealed that the obtained

product contains of pure SnO<sub>2</sub> nanostructures.

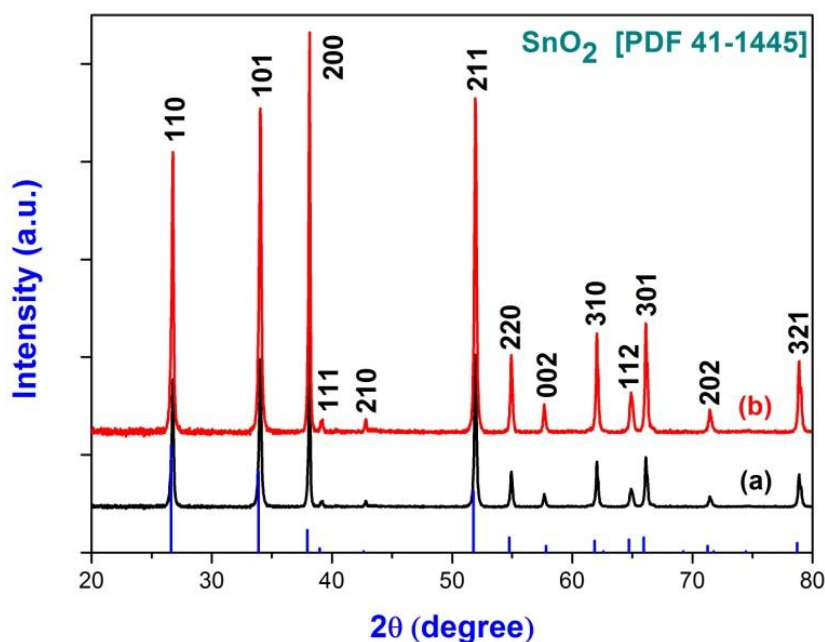


**Figure 71:** XRD patterns of (a) SnO<sub>2</sub> NWs and (b) SnO<sub>2</sub>@SnO<sub>2</sub> heterostructures.

### 7.2.3 Surface wettability study of SnO<sub>2</sub> nanowires and SnO<sub>2</sub>@SnO<sub>2</sub> heterostructures

It is generally accepted that the unusual wetting characteristics of superhydrophobic surfaces are governed by both chemical composition and geometric microstructure. Considering these factors, the wettability of SnO<sub>2</sub> nanostructures was investigated by measuring the contact angle. Figure 72 (a) and (b) showed the images of a water droplet on the surfaces of SnO<sub>2</sub> nanowires and SnO<sub>2</sub>@SnO<sub>2</sub> heterostructures, respectively.

The contact angle on SnO<sub>2</sub> nanowires was  $3.6 \pm 0.2^\circ$ . It can be considered the relatively superhydrophilic surface. In this case the distance between the nanowires was such that the radius of curvature of the liquid surface on the SnO<sub>2</sub> wires was too large to support the liquid surface. This resulted in a total wetting of the surface. The entry of water into the crevices

between the nanowires increased the effective contact area of the liquid with the nanowire surface and led to a moderately small contact angle. Hence, the CA was smaller than the corresponding value on SnO<sub>2</sub> films (~ 20°).<sup>[335]</sup>

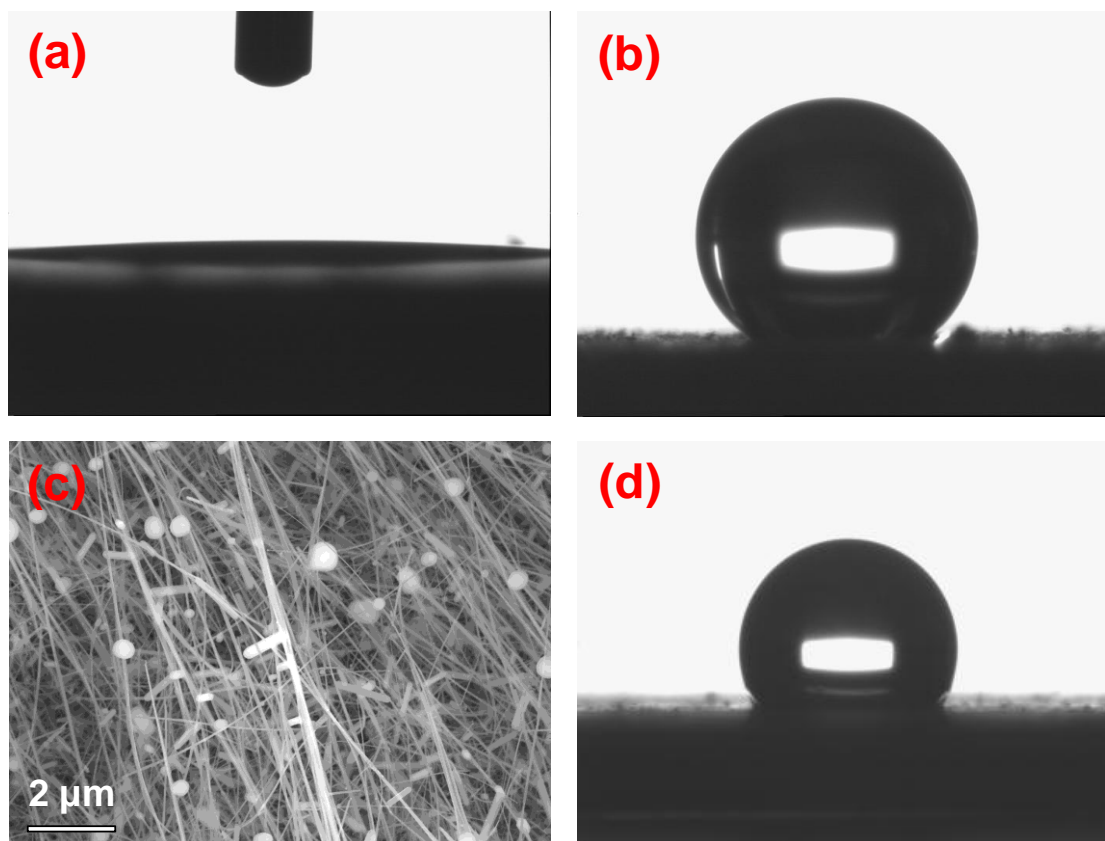


**Figure 72:** Images of water droplet on the surfaces of (a) SnO<sub>2</sub> nanowires and (b) SnO<sub>2</sub>@SnO<sub>2</sub> heterostructures. (c) SEM image of SnO<sub>2</sub>@VO<sub>x</sub> heterostructures, and (d) the corresponding sharp of water droplet.

However, the contact angle on SnO<sub>2</sub>@SnO<sub>2</sub> heterostructures increased drastically to  $133.2 \pm 0.2^\circ$ , corresponding to hydrophobicity. Heterostructures, which contain enough space to hold air in the troughs between separately heterostructures on which a water droplet sits, can efficiently increase the proportion of air/water interface, and ensure that the surface contact area available to water was very low while the branched structures prevented penetration of water into the grooves. Namely, the water did not fill the grooves



on the heterostructure surface and therefore forms nearly spherical droplets, leading to hydrophobic surface. Hence, this resulted in not only a fraction of wetting of the surface but also an increased in the effective contact angle. The SnO<sub>2</sub>@VO<sub>x</sub> heterostructure also got the similar result, the CA value was 121.1 ± 0.2° (Figure 72 (c, d)). All these results agreed well with the theory.

This result of observation can be explained by the Wenzel equation,<sup>[327]</sup> which indicated that the water contact angle of the surface increases with increasing geometric microstructure. It is generally accepted that the unusual wetting characteristics of superhydrophobic surfaces were governed by both their chemical composition and geometric microstructure based on Cassie and Baxter's equation.<sup>[328]</sup> Actually, the above results confirmed that the wettability of SnO<sub>2</sub> based surface can be controlled from superhydrophilic to hydrophobic through the increasing geometric microstructure. This indicates that different chemical modifications may provide a general route to synthesize the SnO<sub>2</sub> based heterostructure surface with superhydrophobic properties by avoiding the wetting of the surface. Hence, the SiO<sub>x</sub> film with hydrophobic property was used to modify the SnO<sub>2</sub> based heterostructure surface.<sup>[336-337]</sup>

Figure 73 showed the (a) SEM and (b) TEM images of SiO<sub>x</sub> film coated SnO<sub>2</sub>@SnO<sub>2</sub> heterostructures. The SnO<sub>2</sub>@SnO<sub>2</sub> heterostructure was covered with a uniform SiO<sub>x</sub> shell with a thickness of ~ 5 nm. The boundary between the core and the shell in the trunk was clearly displayed. The composition of this structure was verified using EDX (Figure 73(c)). The EDX pattern (a) recorded at the bottom indicated that the bottom of this structure was composed of Cu, O, Sn and Si. The EDX spectrum (b) recorded along the surface indicated that the surface of this structure was only composed of Si and O, the peak of Sn was not determined. The peak of copper was derived from Cu TEM grids. The shape of water droplet on this surface was shown in Figure 73(d), indicating a superhydrophobic behavior (CA = 155.8 ± 0.1°).

Hence, the switching from superhydrophilic to superhydrophobic surface based on SnO<sub>2</sub> nanowire by CVD growth was achieved.

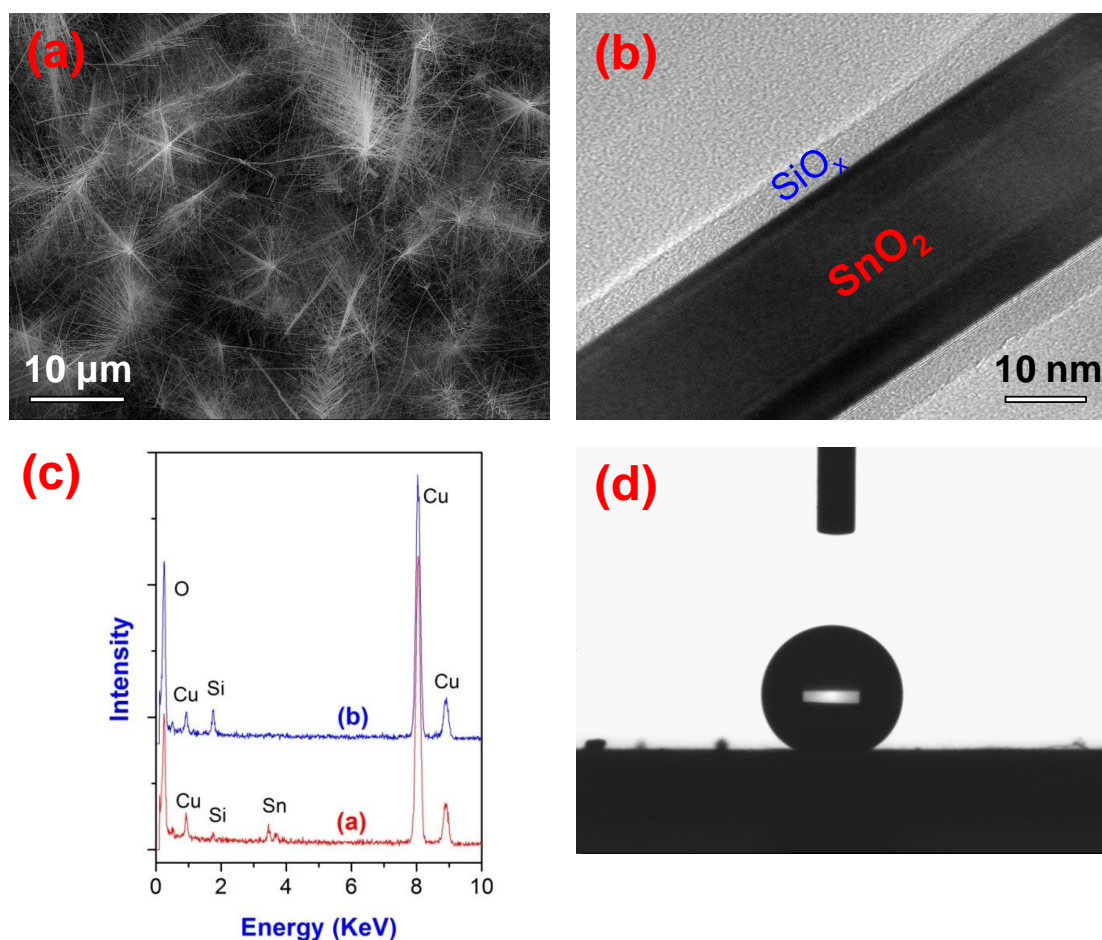


**Figure 73:** SEM (a), TEM (b) and EDX (c) images of SiO<sub>x</sub> film coated SnO<sub>2</sub>@SnO<sub>2</sub> heterostructures, and (d) the corresponding shape of water droplet.

The schematic presentation was proposed in Figure 74 to understand the results. In the case of SnO<sub>2</sub> nanowires, the liquid completely penetrated into the vacancies among individual nanowires surface without any air pockets being trapped. As a result, the water droplet is pushed to spread over the surface rapidly, and the surface shows superhydrophilic properties. Then this surface was modified to SnO<sub>2</sub>@SnO<sub>2</sub> heterostructure surface, geometric microstructure may decrease the concrete contact between the water droplet and the solid surface and the triple phase contact line (water/solid/air), and

prevent penetration of water into the grooves, leading to hydrophobic surface. For the SiO<sub>x</sub> coated SnO<sub>2</sub>@SnO<sub>2</sub> heterostructure surface, synthesized by different chemical modifications, the large fraction of air trapped within the geometric microstructure should greatly increase the air/water interface, which coated film with hydrophobic property to avoid the wetting of this surface, leading to superhydrophobicity.

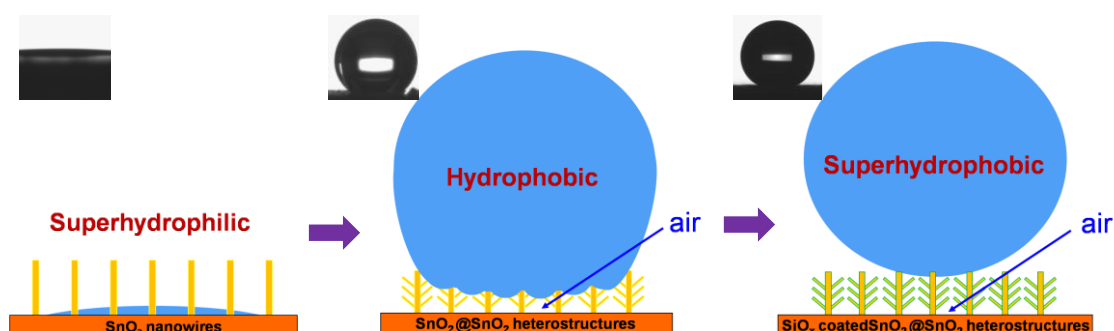


**Figure 74:** Schematic presentation of the switching of SnO<sub>2</sub> based surface.

In order to study the influence of UV irradiation on wettability of the SiO<sub>x</sub> coated SnO<sub>2</sub>@SnO<sub>2</sub> heterostructure, the contact angles as a function of UV irradiation time in ambient conditions were measured (Figure 75(a)). It revealed that the water CA was reduced abruptly at the beginning with the increase of UV irradiation time, indicating the high-speed yielding of electron-hole pairs on the initial surface. Interestingly, UV illumination time was over 10 mins and longer than 30 mins, the variation of CA was slightly, and kept closely at 133°. The water CA of SnO<sub>2</sub>@SnO<sub>2</sub> heterostructure surface was no obvious change basically, it was around 133°.

As known, UV irradiation will generate electron-hole pairs in the SiO<sub>x</sub> surface, and some of the holes react with lattice oxygen to form surface oxygen vacancies (defect sites).<sup>[338]</sup> Water molecules may easily coordinate into the oxygen vacancy sites, leading to the increase of the water adsorption. However, the surface becomes energetically unstable after the adsorption.

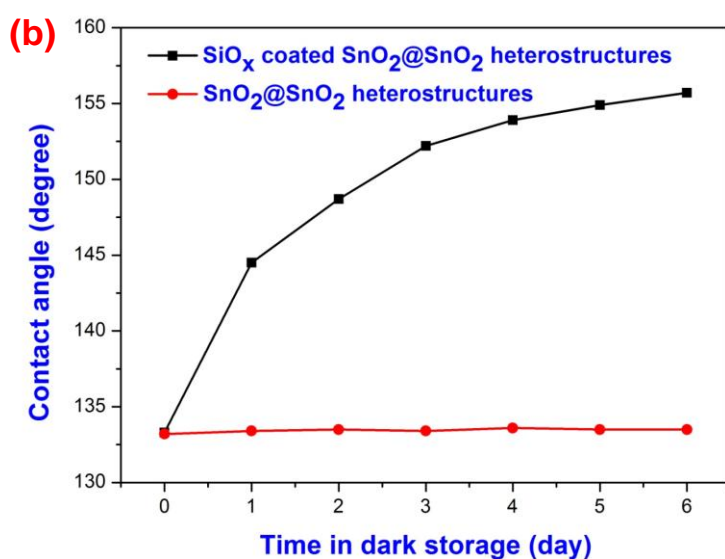
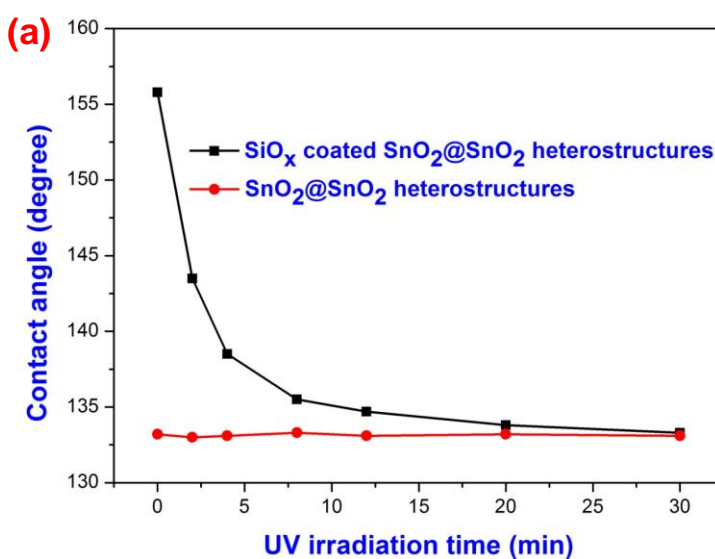
Meanwhile, the oxygen adsorption is thermodynamically favored, and it is more strongly bonded on the defect sites than the hydroxyl group. This process is similar with the case of the TiO<sub>2</sub> film.<sup>[339]</sup> Oxygen atoms can replace the hydroxyl groups adsorbed on the defective sites gradually when the UV-irradiated films are placed in the dark. Subsequently, the surface evolves back to its original state (before UV irradiation), and the wettability is reconverted to superhydrophobic.

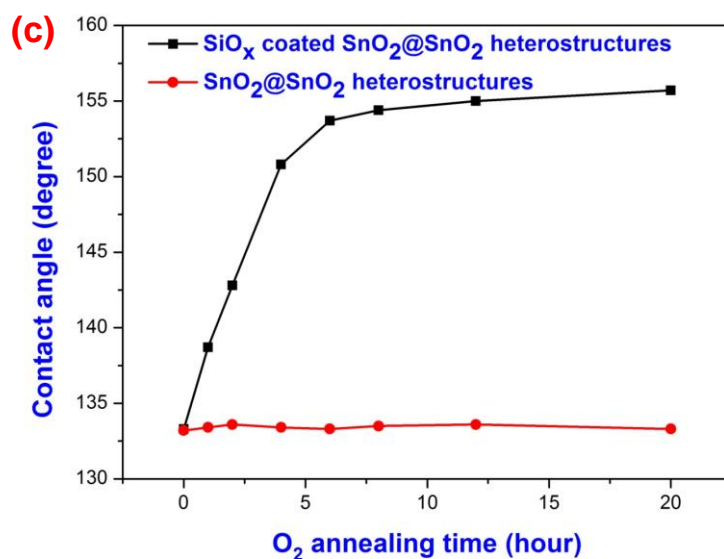
As reported, after storing the sample in dark or annealing in O<sub>2</sub> atmosphere for a certain time, defective sites will gradually disappear due to the atmospheric oxygen effect. Subsequently, the surface will recover to the original superhydrophobicity.<sup>[340]</sup>

Figure 75(b) showed the typical reversion processes of UV-irradiated SiO<sub>x</sub> coated SnO<sub>2</sub>@SnO<sub>2</sub> heterostructure surface with dark storage time. During the first three days, water CA increased remarkably, because of the high-speed bonding of oxygen atoms to the surface defect sites at the beginning. In the next several days, the water CA increased slowly, because of the gradually decrease of the defect sites. Further increase in CA was not observed after the water CA reached the values close to those at their original states (about 155°). On the other hand, there was no change for the case of SnO<sub>2</sub>@SnO<sub>2</sub> heterostructure surface.

Figure 75(c) showed the reversion processes of UV-irradiated SiO<sub>x</sub> coated SnO<sub>2</sub>@SnO<sub>2</sub> heterostructure surface with O<sub>2</sub> annealing time. The water CA increased sharply in the beginning, and fully recovered to the original states (about 155°) in less than 6 h. This result implied that the oxygen adsorption was thermodynamically favored, and it is more strongly bonded on the defect sites than the hydroxyl group. The hydroxyl groups adsorbed on the defective sites can be replaced gradually by oxygen atoms when the hydrophilic samples were annealed in oxygen atmosphere at low temperature.

Subsequently, the surface evolved back to its original state (before UV irradiation), and the wettability was reconverted to superhydrophobicity. The result for the case of SnO<sub>2</sub>@SnO<sub>2</sub> heterostructure surface was same with in dark storage. In comparison, this method in the reversion rate of SiO<sub>x</sub> coated SnO<sub>2</sub>@SnO<sub>2</sub> heterostructure surface showed significant improvement than storing the sample in dark.





**Figure 75:** Time dependence of water contact angles of SiO<sub>x</sub> coated SnO<sub>2</sub>@SnO<sub>2</sub> heterostructure surface (a) under UV irradiation, (b) in dark storage and (c) O<sub>2</sub> annealing.

It should be noted that there were any changes of the CA value of SnO<sub>2</sub>@SnO<sub>2</sub> heterostructures surface under UV irradiation, in dark storage or O<sub>2</sub> annealing. Meanwhile, the CA value of SiO<sub>x</sub> coated SnO<sub>2</sub>@SnO<sub>2</sub> heterostructure was changed from superhydrophobic to hydrophobic under UV irradiation, then the surface wettability was switched back to superhydrophobic under dark storage and O<sub>2</sub> annealing. It revealed that geometric microstructure, the factor influenced the superhydrophobic surface, was the major determinant in the switchable wettability from superhydrophilic to superhydrophobic. The different chemical compositions were the minor factor in this process.

In summary, the control of the wettability switching of SnO<sub>2</sub> nanowire based surface modified by chemical vapor deposition was demonstrated. Also, switchable surface wettability of SiO<sub>x</sub> coated SnO<sub>2</sub>@SnO<sub>2</sub> heterostructure was observed by alternation of UV irradiation, dark storage and O<sub>2</sub> annealing. These studies provided valuable information for the design of a patterned

superhydrophobic surface through a simple method, which has potential applications in chemical, biological, and microfluidic devices.

## 7.3 Fabrication and photoconductivity of SnO<sub>2</sub>@CdS QDs heterostructures

### 7.3.1 Introduction of quantum dots based photovoltaics

Due to their special physical properties, one-dimensional (1D) metal oxide nanowires with large surface-to-volume ratios and the negligible presence of grain boundaries are ideal building blocks for photovoltaics.<sup>[341-342]</sup> But the wide band gap prevents their efficient absorption of the sunlight in the visible region. A promising solution to this problem is to combine metal oxide semiconductors with lower band gaps to extend their absorption range. Comparable to other sensitizers, semiconductor quantum dots (QDs) show unique advantages.<sup>[343-344]</sup> First, the band gap of QDs can be tuned by varying the size of QDs. It is also possible to utilize electrons to generate multiple electron-hole pairs with a single high-energy photon through the impact ionization effect. Another advantage is their high absorption cross section and high extinction coefficient, which has been known to reduce the dark current and increase the overall efficiency of the solar cells.

Despite the beneficial attributes and wide studies on the synthesis and applications of QDs for light harvesting, the photophysics and photochemistry of QDs are currently poorly understood and quantum dot sensitized solar cells have not achieved efficiencies or stabilities competitive with conventional dye sensitized solar cells.<sup>[345]</sup> It is at least partially due to a lack of fundamental understanding of the surface chemistry of QD adsorption in nanocrystalline metal oxide semiconductors that leads to low QD coverage on nanoporous materials. Although the single-layer aligned molecule (SAM) technique, linking the pre-prepared QDs on the metal oxide surface using a bi-functional molecule, has the advantages of being able to control the size of QDs, the



coverage ratio of the QDs on the metal oxide surface is always low.<sup>[346]</sup> Furthermore, the structure and distribution of QDs on nanocrystalline metal oxide surface is difficult to determine because the surface is not flat and mostly inaccessible to scanning probes and electron beams.<sup>[347]</sup> It is, therefore, essential to have a systemic study on the photophysics and photochemistry of QDs sensitized metal oxides.

Here, the fabrication and photoconductivity of SnO<sub>2</sub>@CdS QDs heterostructures via a chemical bath deposition method (CBD) on CVD-grown single-crystal SnO<sub>2</sub> nanowires were investigated. Nanowires can be well partially or fully covered with CdS QDs, which provides an access to deep insight of photo-interaction between QDs and metal oxide.

### 7.3.2 Characterization of SnO<sub>2</sub>@CdS QDs heterostructures

Chemical bath deposition (CBD) of CdS has been widely studied for the various compositions of chemical solutions. One advantage of CBD method is to easily control the coverage and the thickness of QDs on the metal oxides due to direct growth of QDs on the surface of metal oxide nanowires. In this study, typical solution composites of cadmium salt (CdSO<sub>4</sub>), aqueous ammonia (complexing agent), and thiourea (NH<sub>2</sub>CSNH<sub>2</sub>, sulfur source) were used. The general reaction pathways for the CdS formation in thiourea chemical bath can be given as the following steps:



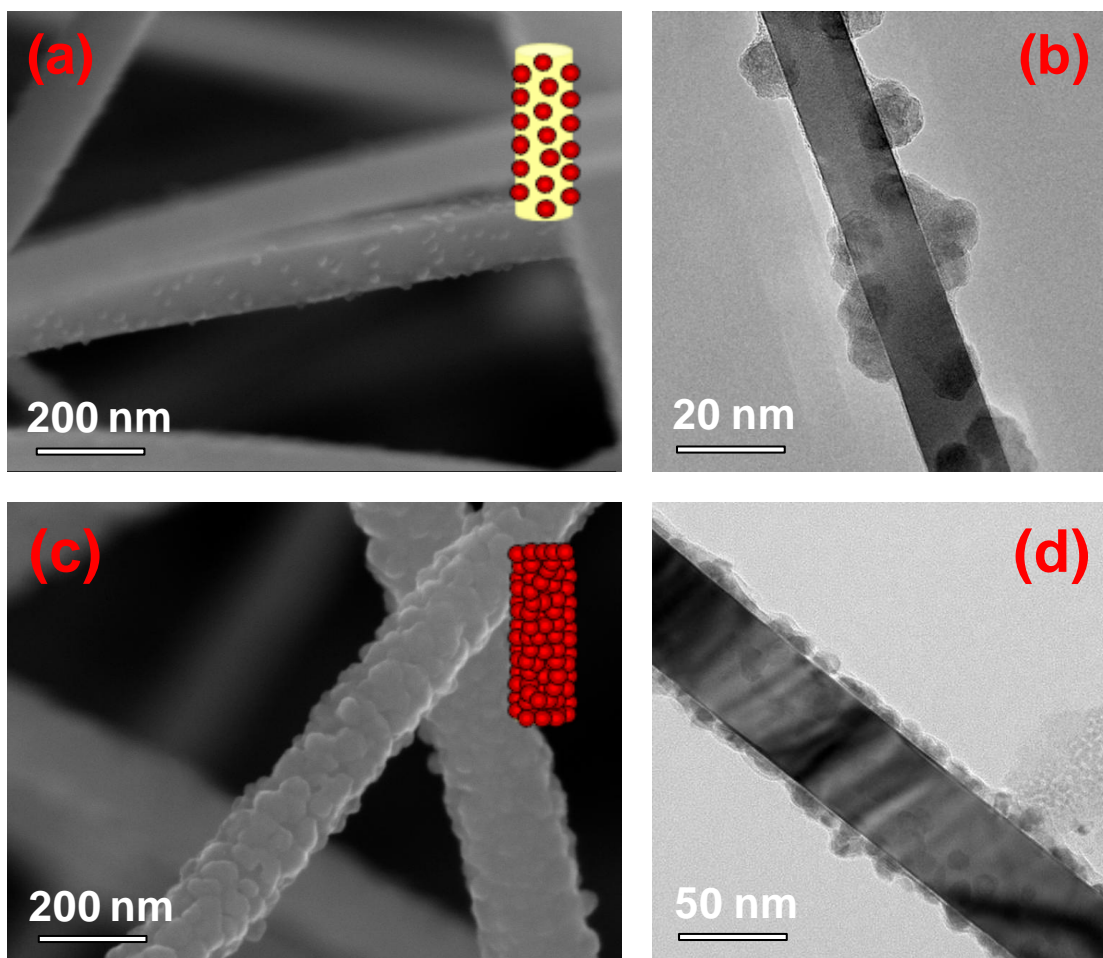


**Figure 76:** SEM and TEM images of (a, b) partially and (c, d) fully covered SnO<sub>2</sub>@CdS QDs heterostructures.

In the process, dissolved ammonia in water produced a hydroxide ion and forms a cadmium tetraamine complex by two different equilibrium reactions (8 and 9). Ammonia had roles of increasing the pH of solution and preventing

violent cadmium hydroxide formation. In an alkaline solution, thiourea decomposed and generated free sulfide ion reactions (10 and 11). CdS formed through an ion-by-ion mechanism (12), a hydroxide cluster mechanism (13 and 14), or both of them on the surface of SnO<sub>2</sub> nanowires (15).

Varying the experimental parameters, two different morphologies can be observed. Figure 76 showed typical top-view SEM and TEM images of (a, b) partially and (c, d) fully covered SnO<sub>2</sub>@CdS QDs heterostructures. It was clearly seen that CdS QDs homogeneously dispersed on the surface of SnO<sub>2</sub> nanowires with a diameter of ~35 nm in both two cases. The CdS QDs were nearly spherical in shape and had typical size in the range of 10-20 nm.

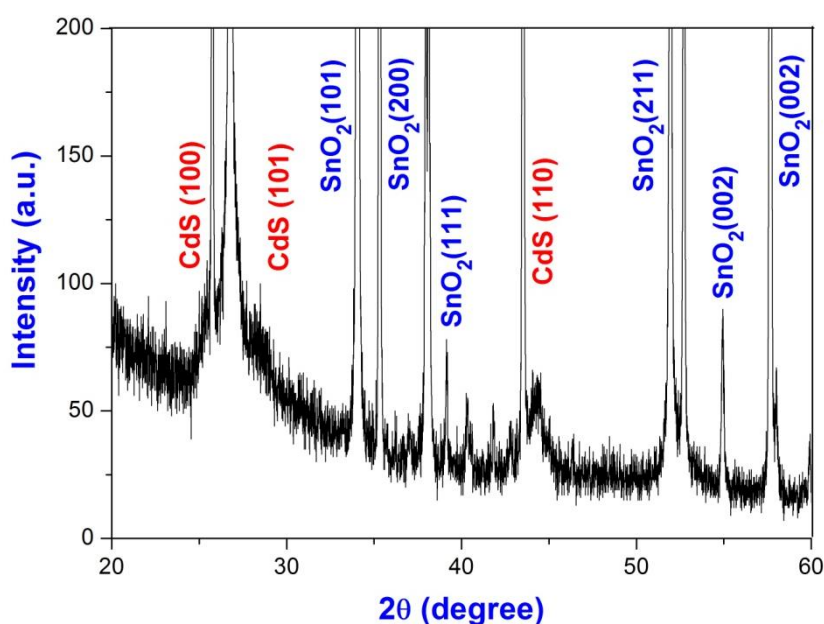


**Figure 77:** XRD patterns of SnO<sub>2</sub>@CdS QDs heterostructures.

On the basis of the SEM and TEM images, we could notice the morphology evolution of SnO<sub>2</sub>@CdS QDs heterostructures, depending on the deposition time. Under these deposition conditions, the hydroxide cluster mechanism should be the dominant pathway because we can observe that single CdS quantum dots are sparsely deposited at the initial stage and

coalesce to create big ones. It was important to note the coverage of CdS QDs on SnO<sub>2</sub> nanowires can be well controlled from partially decoration to fully covered core-shell like structure via such a CBD method.

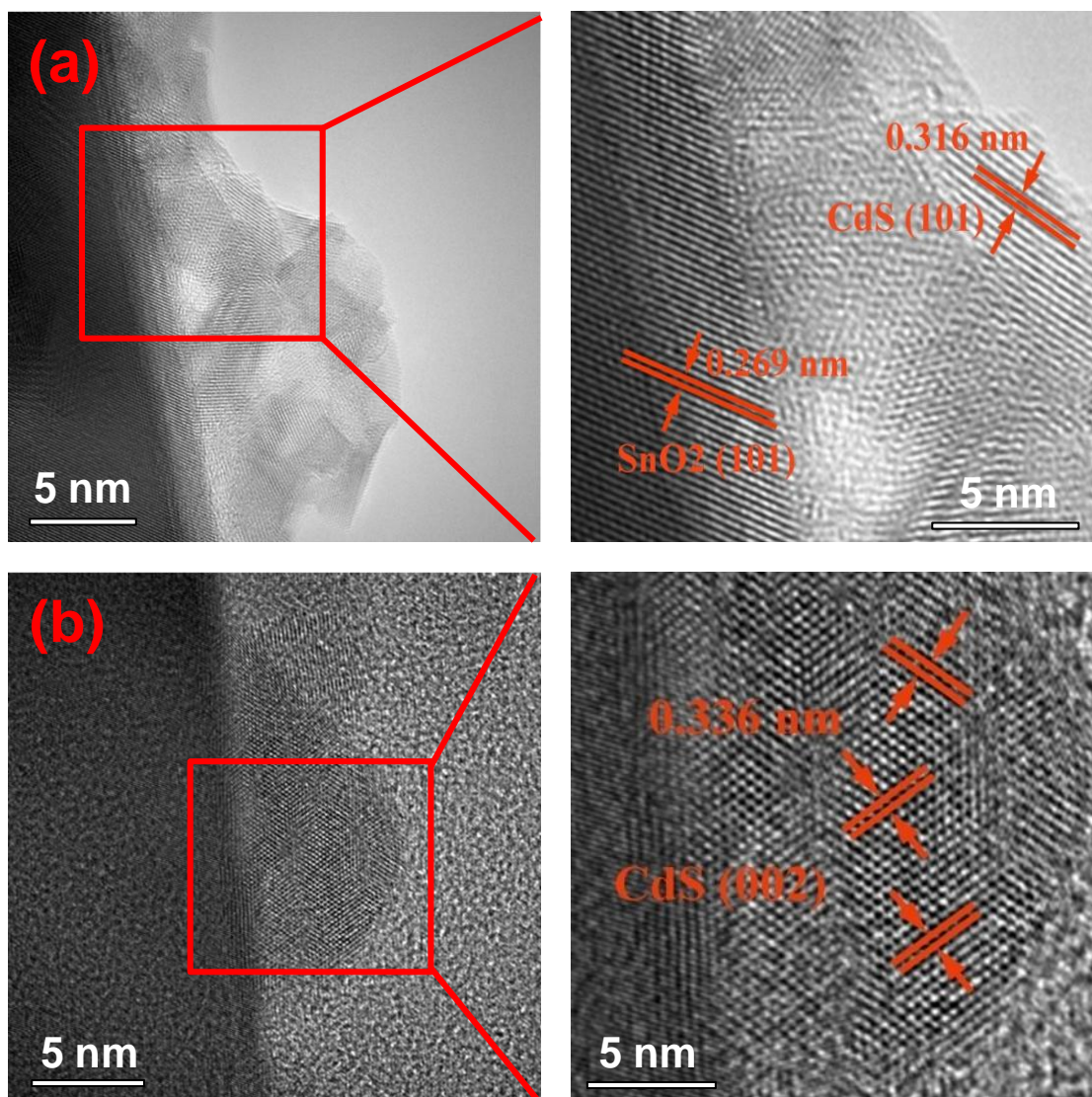


**Figure 78:** HR-TEM images of SnO<sub>2</sub>@CdS QDs heterostructures.

The crystal structures of the SnO<sub>2</sub>@CdS QDs heterostructures were identified by means of XRD analysis, as shown in Figure 77. Although the diffraction peaks of CdS were very weak due to the high-intensity of CVD-grown well-crystallized SnO<sub>2</sub> nanowires, peaks can be indexed as the hexagonal crystal structure CdS compared with the XRD data. This result

together with SEM and TEM images revealed that the SnO<sub>2</sub>@CdS QDs heterostructures are successfully achieved in this work.

High-resolution TEM analysis of SnO<sub>2</sub>@CdS QDs heterostructures revealed that SnO<sub>2</sub> nanowire and CdS QDs are crystalline structure. Clear lattice fringes were observed in the images, as shown in Figure 78. The measured spacing of the crystallographic planes was 2.69 nm, corresponding to {101} plane of the rutile structured SnO<sub>2</sub> crystal, suggesting that CVD-grown SnO<sub>2</sub> nanowires had a preferred growth orientation along (101) (Figure 73(a)). Moreover, clear lattice fringes of CdS QDs were 3.16 nm and 3.36 nm, corresponding to {101} and {002} planes of hexagonal crystal structure CdS, respectively. It was also clearly observed that CdS clusters were composed of some smaller CdS QDs, further proving the hydroxide cluster growth mechanism.

### **7.3.3 Photoconductivity property of SnO<sub>2</sub>@CdS QDs heterostructures**

The UV-Vis spectras of SnO<sub>2</sub> nanowires and SnO<sub>2</sub>@CdS QDs heterostructures were shown in Figure 79.

SnO<sub>2</sub> nanowires showed absorption edge at around 350 nm, which was close to the SnO<sub>2</sub> band gap of 3.6 eV, and the sharp absorption indicated that CVD-grown SnO<sub>2</sub> nanowires were well-crystallized. The absorption of SnO<sub>2</sub>@CdS QDs heterostructures occurred at around 540 nm. The SnO<sub>2</sub>@CdS QDs heterostructures showed an apparent increase in the absorption of the visible light to non-coated SnO<sub>2</sub> nanowires. This enhancement of the visible light absorption was possibly due to the staggered band alignment between these two different materials that allowed efficient charge separation at the junction.

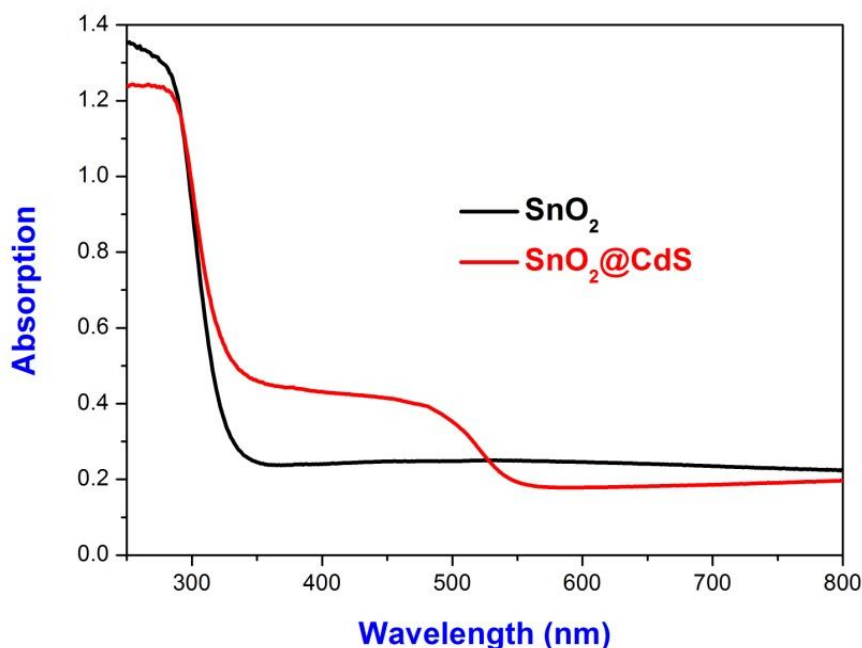


**Figure 79:** UV-visible light absorption spectras of SnO<sub>2</sub> nanowires and SnO<sub>2</sub>@CdS QDs heterostructures.

It is known that SnO<sub>2</sub> is a wide band gap ( $E_g = 3.6$  eV, at 300 K) semiconductor while CdS is a smaller one ( $E_g = 2.42$  eV, at 300 K). Due to their favorable energetics, when SnO<sub>2</sub> couples with CdS, a SnO<sub>2</sub>@CdS heterojunction with a staggered gap forms. To achieve thermal equilibrium, electrons from CdS will flow into SnO<sub>2</sub>, forming an accumulation layer of electrons in the potential well adjacent to the interface of the SnO<sub>2</sub>@CdS heterojunction. Due to the additional electron injection from CdS (also with high mobility), the conductance of the SnO<sub>2</sub>@CdS QDs heterostructures will be enhanced. It was confirmed by the current-voltage ( $I$ - $V$ ) curves of the SnO<sub>2</sub> nanowires and SnO<sub>2</sub>@CdS QDs heterostructures for comparison, as shown in Figure 80.



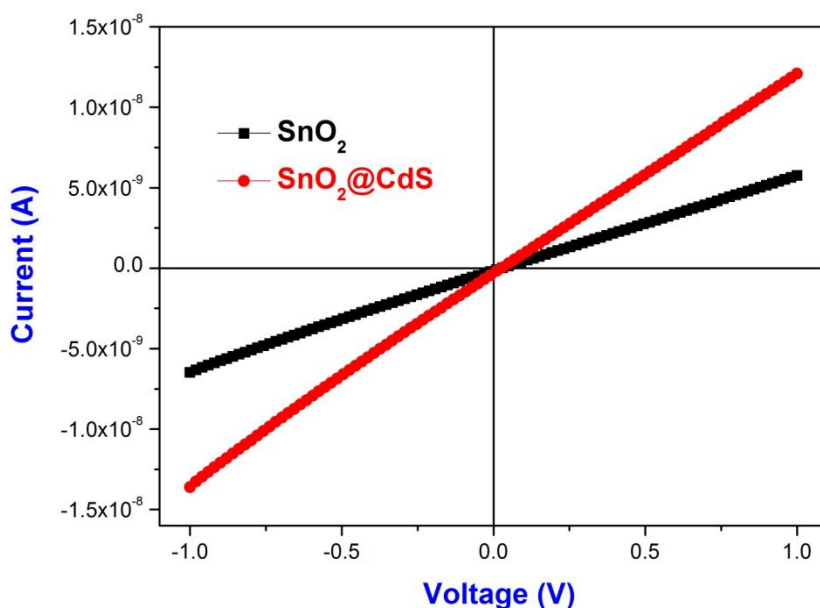


**Figure 80:** Room temperature  $I$ - $V$  curves of SnO<sub>2</sub> nanowires and SnO<sub>2</sub>@CdS QDs heterostructures in dry air condition.

The current increases linearly with the bias as the voltage is scanned from -1.0 to 1.0 V, revealing that ohmic contact between the electrodes and the materials is obtained. One can see that the SnO<sub>2</sub>@CdS QDs heterostructures have an improved conductance in comparison with that of the uncoated SnO<sub>2</sub> nanowires. The interaction between the two semiconductors of SnO<sub>2</sub> and CdS is considered as the dominant factor for such enhancement in the conductance.

Based on the fundamental measurements of absorption and conductance, the photoconductivity of SnO<sub>2</sub>@CdS QDs heterostructures was characterized, as shown in Figure 81. The current increased remarkably under the irradiation of light with the wavelength less than 350 and 450 nm for SnO<sub>2</sub> nanowires and SnO<sub>2</sub>@CdS QDs heterostructures, respectively. Conductivity of SnO<sub>2</sub> nanowires immediately increased when the wavelength was below 350 nm. When wavelength was over 350 nm, the variation of conductivity was slightly.

Conductivity of SnO<sub>2</sub>@CdS QDs heterostructures increased very slowly, when the wavelength was below 450 nm. Then conductivity maintained a specified value as the wavelength was over 450 nm.

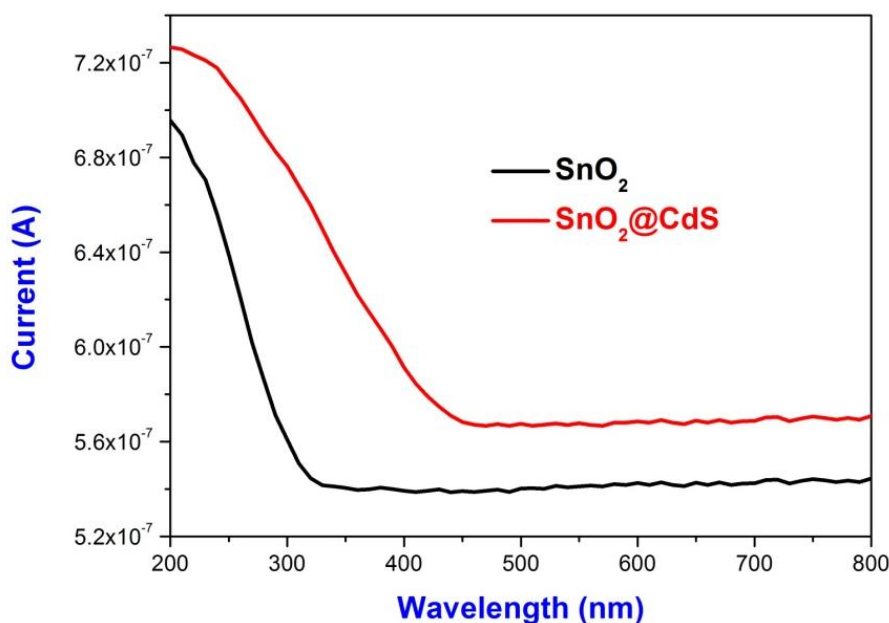


**Figure 81:** Photoconductivity curves of of SnO<sub>2</sub> nanowires and SnO<sub>2</sub>@CdS QDs heterostructures.

When the SnO<sub>2</sub> nanowires are illuminated by a UV-light whose photon energy is above the energy gap ( $E_g$ ) of the SnO<sub>2</sub> (3.6 eV), that is to say, the wavelength is below 350 nm, then light is absorbed and energy from the light excites the electrons in the SnO<sub>2</sub> from the valence band (VB) into the conduction band (CB), creating additional charge carriers and thus increasing the current through the nanowire.

In the case of SnO<sub>2</sub>@CdS QDs heterostructures, CdS is easy to be excited because of the smaller energy gap ( $E_g = 2.42$  eV, at 300 K) than SnO<sub>2</sub>. Although the absorbed light, which the wavelength is below 540 nm, excites the electrons in the CdS from the valence band (VB) into the conduction band (CB), corresponding the absorption peaks of CdS. The excited electrons do



not make contribution of the enhancement of current. Once the wavelength is below 450 nm, the transition of excited electrons from conduction band of CdS to SnO<sub>2</sub> makes a slow advancement in current because of the light energy. Continue to decrease the wavelength to 350 nm, current through the nanowire increased remarkably as the light excites the electrons in the SnO<sub>2</sub>. Hence, SnO<sub>2</sub>@CdS QDs heterostructures had a higher current than non-coated SnO<sub>2</sub> nanowires, it can be explained by a schematic diagram (Figure 82).

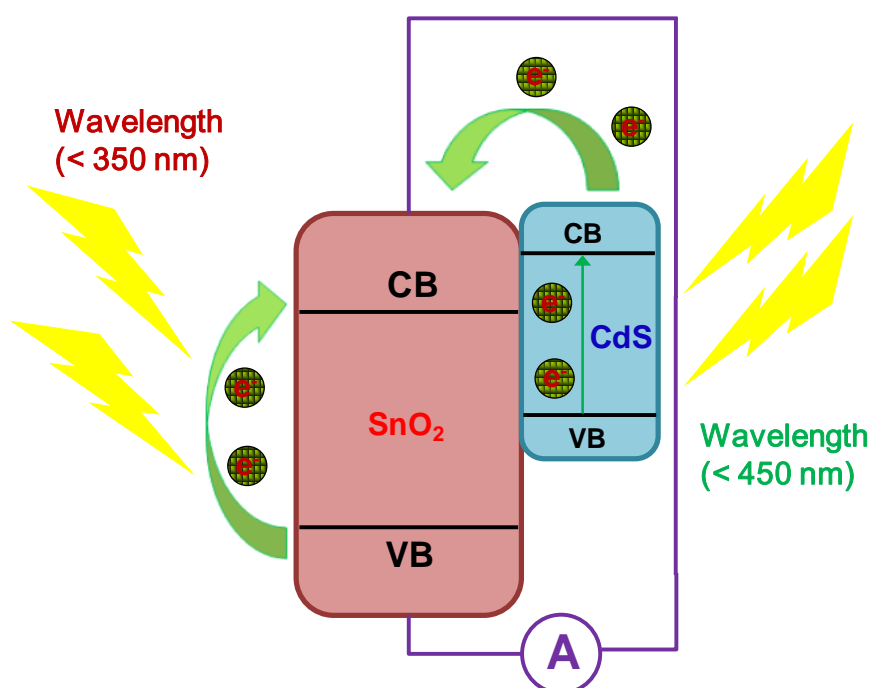


**Figure 82:** Schematic presentation of photoconductivity mechanism.

In summary, the SnO<sub>2</sub>@CdS QDs heterostructures were synthesized by a chemical bath deposition (CBD) method via hydroxide cluster growth mechanism. The UV-Vis spectras revealed that the absorption edge of SnO<sub>2</sub> nanowires and SnO<sub>2</sub>@CdS QDs heterostructures at 350 nm and 540 nm, respectively. SnO<sub>2</sub>@CdS QDs heterostructures had a remarkably enhancement in photoconductivity than non-coated SnO<sub>2</sub> nanowires when the wavelength was below 450 nm.

## 8 Conclusions and Outlook

### 8.1 Conclusions

Due to novel physical properties like high hardness, high thermal conductivity, large band gap, and chemical inertness, etc, interest in 1D nanostructures has been driven by fascinating questions and the potential to impact basic science and technology. Two questions at the heart of basic chemistry and physics research were: (i) how can 1D nanostructures be rationally synthesized in controlled dimensionality and size and (ii) what are the intrinsic and potential physics properties of 1D nanostructures?

In order to solve the questions hereinbefore, the following research can be illustrated in four stages (Figure 83), involving the synthesized process and development of the novel properties of 1D nanostructures.

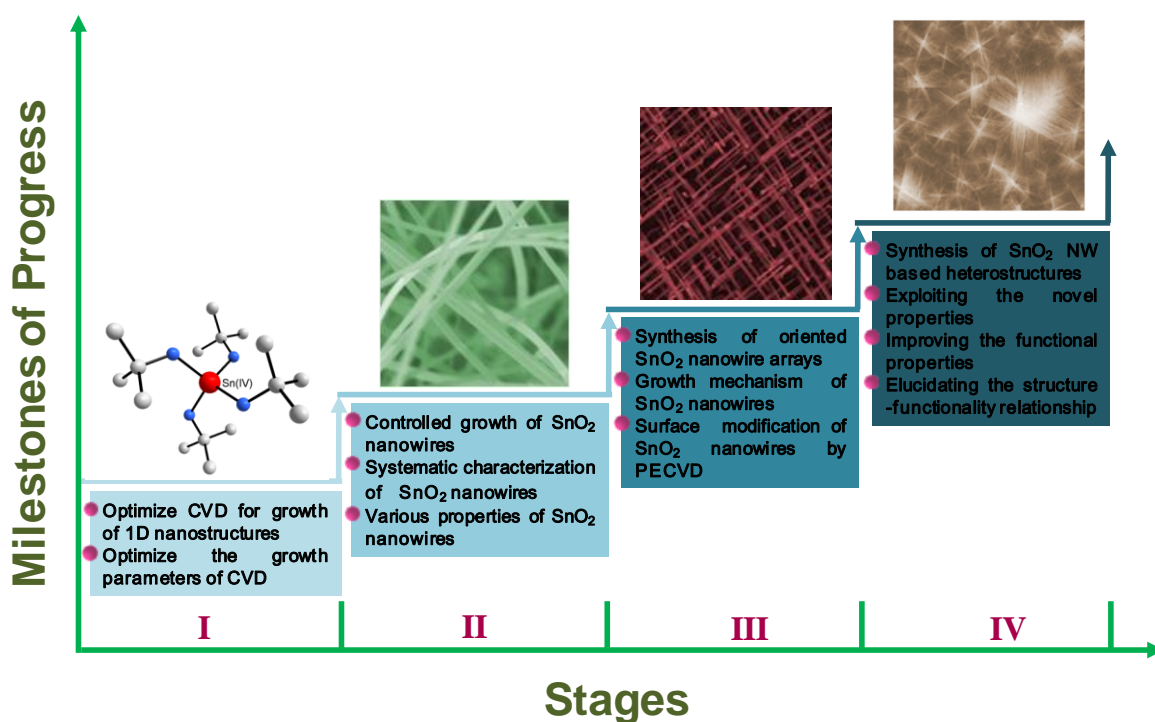


Figure 83: Roadmap of this work.

According to the above research frame, the main contributions of this work can be summarized as follows:

(1) High quality SnO<sub>2</sub> nanowires were generally grown at relatively high temperatures (~ 1000 °C), which limited the feasibility of synthetic approaches targeted to produce nanowires with controlled dimensions. Molecule-based CVD (MB-CVD) as a low-temperature approach (~ 700 °C) was described herein for controlled growth of high density single crystalline SnO<sub>2</sub> nanowires by precursor Sn(O<sup>t</sup>Bu)<sub>4</sub>. Combining the vapor-liquid-solid (VLS) catalytic growth mode, with single molecular sources allowed precise control over dimensions, site-specific growth, surface states and final transport behaviours. As the influence of the basic growth parameters (deposition temperature, precursor temperature, size of catalyst and angle of graphite susceptor) on the size, morphology, and dimensionality of high density single crystalline SnO<sub>2</sub> nanowires and corresponding fundamental physical properties (electrical, PL, gas sensing and field-effect transistor) was systematically studied based on the simulation of CVD system, it not only pave the way to the further research (surface modification and nanowire based heterostructures), but also the potential application of nanodevice fabrication.

(2) The technical highlights of this work include the successful demonstration of oriented growth of SnO<sub>2</sub> nanowires arrays on TiO<sub>2</sub>(001) substrates by MB-CVD method based on Sn(O<sup>t</sup>Bu)<sub>4</sub> as precursor for the first time. The SnO<sub>2</sub> NWs preferred growth directions ([101], [-101], [011] and [0-11]), surface energy considerations and the crystallographic relationship between the substrate and NW material were elaborated by cross sectional SEM, HR-TEM and AFM. A model for the nanowire morphology based upon crystallographic relation between the substrate and nanowire material, and preferred growth direction was proposed to explain the oriented and tilted growth of SnO<sub>2</sub> nanowire arrays.

Focused ion beam-assisted tomography technique, which can explore more insights of growth mechanism of 1D materials and the nano-bio interaction, was explored to monitor the growth of ordered nanowires with defined growth orientation and surface facets, and reconstruct the growth patterns of SnO<sub>2</sub> nanowire arrays in bulk 3D tomography.

(3) Surface modification of tin oxide nanowires by plasma treatment demonstrated the possibility of engineering the sensing and catalytic properties of metal oxide semiconductors. Plasma treatment on 1D nanostructures allowed modulating the surface (defect) electronic structure and to generate intimate amorphous/crystalline oxide interfaces and increased concentration of oxygen vacancies responsible for efficient charge transfer (transduction) processes which consequently resulted in enhanced sensitivity. Moreover, the controlled reduction of tin oxide nanowires to SnO<sub>2-x</sub>/SnO<sub>2</sub> core-shell nanowires opens up new avenues for modifying fundamental properties such as electronic conductivity, band gap and electron-hole correlation in reduced dimensionality.

(4) The various SnO<sub>2</sub> nanowire based heterostructures (such as SnO<sub>2</sub>@TiO<sub>2</sub>, SnO<sub>2</sub>@SnO<sub>2</sub>, SnO<sub>2</sub>@VO<sub>x</sub> and SnO<sub>2</sub>@CdS) were fabricated to extend the functionality by the chemical surface modification of SnO<sub>2</sub> nanowires, the detailed experimental results were obtained in the following:

(i) The 1D SnO<sub>2</sub>@TiO<sub>2</sub> core-shell nanostructures were successfully synthesized by a two-step chemical vapor deposition process of sequential decomposition of a molecular precursor Sn(O<sup>t</sup>Bu)<sub>4</sub> and Ti(O<sup>i</sup>Pr)<sub>4</sub>, respectively, in which the diameter of SnO<sub>2</sub> core and the thickness of TiO<sub>2</sub> shell are about 60 nm and 10 nm, respectively. The as-prepared TiO<sub>2</sub> shell in amorphous form will be transformed into rutile crystalline structures after annealing at 950 °C. SnO<sub>2</sub>@TiO<sub>2</sub> core-shell structures formed Sn<sub>x</sub>Ti<sub>1-x</sub>O<sub>2</sub> mixed solid solutions because the Sn<sup>4+</sup> ions diffuse into the TiO<sub>2</sub> shell, the mean stoichiometry of the

$\text{Sn}_x\text{Ti}_{1-x}\text{O}_2$  solid probed by XRD can be calculated as  $x = 1, 0.927$  and  $0.857$ , for the as-prepared and annealed at  $950$  and  $1200$  °C, respectively. As the annealing temperature increased to  $1400$  °C,  $\text{SnO}_2$  NW was evaporated continuously until it was consumed totally, then the left  $\text{TiO}_2$  formed some irregularly shaped particles. This result agreed well with the XRD, SEM and HR-TEM characterization. The single  $\text{SnO}_2@ \text{TiO}_2$  core-shell nanowires had a higher resistivity ( $1.90 \pm 0.01 \Omega \cdot \text{cm}$ ) than single  $\text{SnO}_2$  nanowire ( $0.14 \pm 0.02 \Omega \cdot \text{cm}$ ) in dry air at room temperature ( $25$  °C) due to the less conductive amorphous  $\text{TiO}_2$  shell. The  $\text{SnO}_2@ \text{TiO}_2$  core-shell structure had a good sensing performance because  $\text{TiO}_2$  shell gave the conduction electrons back to  $\text{SnO}_2$  nanowire.

(ii) The  $\text{SnO}_2@ \text{SnO}_2$  heterostructures and  $\text{SiO}_x$  coated  $\text{SnO}_2@ \text{SnO}_2$  heterostructures were obtained by multi-step CVD. The  $\text{SnO}_2$  based heterostructure surface greatly enhanced the wetting effects in comparison with the chemical composition and geometric microstructure and superhydrophobic surface was achieved. The  $\text{SnO}_2$  nanowires with CA of  $3^\circ$  exhibited a superhydrophilic property. The CA of  $\text{SnO}_2@ \text{SnO}_2$  heterostructures increased to  $133^\circ$ . The CA of  $\text{SiO}_x$  coated  $\text{SnO}_2@ \text{SnO}_2$  heterostructures was further increased to  $155.8^\circ$ . Switchable surface wettability of  $\text{SiO}_x$  coated  $\text{SnO}_2@ \text{SnO}_2$  heterostructure was observed by alternation of UV irradiation, dark storage and  $\text{O}_2$  annealing. Geometric microstructure was the major determinant role in the switchable wettability from superhydrophilic to superhydrophobic. These studies provide valuable information for the design of a patterned superhydrophobic surface through a simple method, which has potential applications in chemical, biological, and microfluidic devices.

(iii) The  $\text{SnO}_2@ \text{CdS}$  QDs heterostructures were synthesized by a chemical bath deposition (CBD) method on CVD-grown single crystalline  $\text{SnO}_2$

nanowires via hydroxide cluster growth mechanism. The morphology of CdS QDs on SnO<sub>2</sub> nanowires can be well controlled from partially decoration to fully covered core-shell structure by varying the experimental parameters. The HR-TEM indicated that the CdS QDs was grown along the (101) and (002) direction. The UV-Vis spectra revealed that the absorption edge of SnO<sub>2</sub> nanowires and SnO<sub>2</sub>@CdS QDs heterostructures were at 350 and 540 nm, corresponding to the band gaps of SnO<sub>2</sub> and CdS, respectively. The *I-V* curves showed that SnO<sub>2</sub>@CdS QDs heterostructures had a remarkably enhancement in photoconductivity than non-coated SnO<sub>2</sub> nanowires, due to the injection of electrons in the CdS from conduction band (CB) into the conduction band (CB) of SnO<sub>2</sub>, creating additional charge carriers when the wavelength was below 450 nm.

Hence, these research findings constituted the foundation for exploring in-depth understanding and broad opportunities in functional nanomaterials, helped the experiments to achieve more on-going and future investigations in nanoscience areas.

## 8.2 Outlook

The development of nanowire based materials represents breakthrough achievements with rapid expanding impact in all areas of nanotechnology. The remarkable level of synthetic control of the performance properties of NWs is leading to revolutionary technologies in electronics, optoelectronics, sensors, life sciences, and defense will continue to broadly impact the fields of physics, chemistry, biology, medicine, environmental science, and engineering.

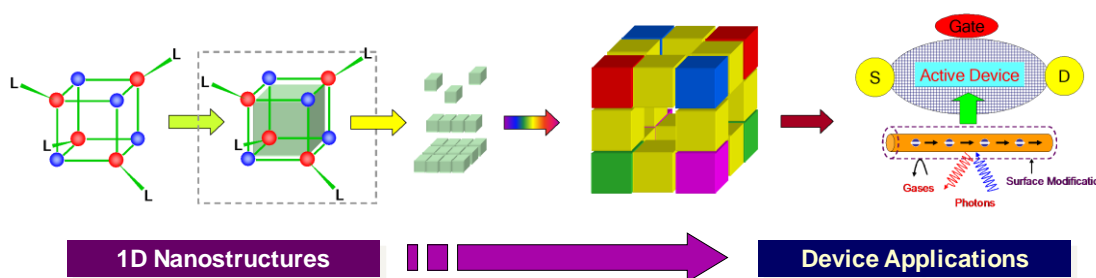


**Figure 84:** Roadmap of nanowire based devices.

These fascinating achievements of  $\text{SnO}_2$  based 1D nanostructures inspire more research effort to address the challenges that remain. One key issue is 1D nanostructures and most of the applications derived from these materials are still in early stage of posed on a carbon-coated TEM grids. For example,  $\text{SnO}_2@ \text{SnO}_2$  heterostructures broke into a number of fragments along its longitudinal axis during sample preparation, resulting in the branched structure was not enabled to preserve well. To enhance the stability of nanowires, it might be necessary to form nanoscale-type structures by coating the nanostructures with sheaths of a tougher material.

Another critical issue is the selective gas detection based on  $\text{SnO}_2$  NWs and  $\text{SnO}_2$  based nanostructures, such as  $\text{CH}_4$ ,  $\text{NO}_2$ ,  $\text{NH}_3$ ,  $\text{H}_2\text{S}$  and so on. As known, 1D system demonstrates superior sensitivity to various gases. However, selectivity has been an obstacle for practical applications. Promising

solutions lie in surface coating with chemical selective membrane, surface modification by specific functional groups, or combining multicomponent sensing modules coupled with signal processing functions, acting as an “electronic nose” to differentiate minute quantities in a complex environment.

The third issue face by chemically synthesized nanowires is their self-assembly into complex structures or device architectures. It is a key factor of process from nanostructure to device. A simply way to connect SnO<sub>2</sub> based 1D nanostructures by gold wires and gold paste was used to measure the physical property in this study. However, several promising techniques demonstrated to assemble the nanowires into pattern structures such as arrayed crossbar junctions, but increase of integration density seems to be difficult. Nanomanipulation seems to be a reasonable solution to this problem. But some new efficient approaches in this issue are also needed.

Last but not the least, there is much new science await to elucidate, especially the quantum behavior that is expected to dominate as the size of SnO<sub>2</sub> based 1D nanostructures continues to reduce. The quantum confinement will provide the means to study individual quantum states of electrons, spins and phonons. The development of devices based on the unique quantum properties will lead a great leap forward and promote a wide range of technological advancement.

Looking forward, we believe that, there are almost unlimited opportunities that are being, and will be explored by many groups around the world in this general area of 1D nanostructures. The scientific and technical potentials of 1D nanostructures are for sure great, and the future of this sub-field of nanoscience is remarkably bright. Moreover, nanowire based 1D nanosystems with likely revolutionary technologies that will impact in many ways such areas as the life sciences, healthcare, information technology, and energy science, to name just a few.





## 9 References

- [1] Z. L. Wang, *Nanomaterials for Nanoscience and Nanotechnology* (edited by Z. L. Wang), Wiley-VCH, 2000.
- [2] For an introduction, *Sci. Am.*, 2001.
- [3] (a) S. Iijima, *Nature*, 1991, **354**, 56; (b) M. A. Read, W. Kirk, *Nanostructures and Mesoscopic Systems*, Academic, San Diego, 1992; (c) A. P. Alivisatos, *Science*, 1996, **271**, 933; (d) R. C. Ashoori, *Nature*, 1996, **379**, 413.
- [4] M. H. Dvoret, D. Esteve, C. Urbina, *Nature*, 1992, **360**, 547.
- [5] P. Harrison, M. Willett, *Nature*, 1988, **332**, 337.
- [6] Y. Yin, G. Zhang, Y. N. Xia, *Adv. Funct. Mater.*, 2002, **12**, 293.
- [7] C. Tatsuyama, S. Ichimura, *Jpn. J. Appl. Phys.*, 1976, **15**, 843.
- [8] Z. Guo, F. Zhou, J. Hao, W. Liu, *J. Am. Chem. Soc.*, 2005, **127**, 15670.
- [9] M. Law, H. Kind, B. Messer, F. Kim, P. D. Yang, *Angew. Chem. Int. Ed.*, 2002, **41**, 2405.
- [10] Y. Idota, T. Kubota, A. Matsufuji, Y. Maekawa, T. Miyasaka, *Science*, 1997, **276**, 1395.
- [11] X. F. Duan, Y. Huang, Y. Cui, J. F. Wang, C. M. Lieber, *Nature*, 2001, **409**, 66.
- [12] F. Hernández-Ramírez, J. D. Prades, A. Romano-Rodríguez, S. Barth, H. Shen, S. Mathur, *Ceramic Integration and Joining Technologies: From Macro to Nanoscale*, John Wiley & Sons, 2010.
- [13] C. N. R. Rao, F. L. Deepak, G. Gundiah, A. Govindaraj, *Prog. Solid State Chem.*, 2003, **31**, 5.
- [14] A. M. Morales, C. M. Lieber, *Science*, 1998, **279**, 208.
- [15] Y. Wu, P. D. Yang, *Chem. Mater.*, 2000, **12**, 605.
- [16] J. R. Heath, F. K. Legoues, *Chem. Phys. Lett.*, 1993, **208**, 263.

- [17] K. K. Likharev, T. Claeson, *Sci. Am.*, 1992, **80**, 1.
- [18] C. Schönenberger, B. M. I. Van der Zande, L. G. J. Fokkink, M. Henny, C. Schmid, M. Krüger, A. Bachtold, R. Huber, H. Birk, U. Staufer, *J. Phys. Chem. B*, 1997, **101**, 5497.
- [19] H. Adhikari, A. F. Marshall, C. E. D. Chidsey, P. C. McIntyre, *Nano Lett.*, 2006, **6**, 318.
- [20] S. Kodambaka, J. Tersoff, M. C. Reuter, F. M. Ross, *Science*, 2007, **316**, 729.
- [21] P. D. Yang, *Mater. Res. Bull*, 2005, **30**, 85.
- [22] H. J. Fan, P. Werner, M. Zacharias, *Small*, 2006, **2**, 700.
- [23] R. S. Wagner, W. C. Ellis, *Appl. Phys. Lett.*, 1964, **4**, 89.
- [24] J. L. Liu, S. J. Cai, G. L. Jin, S. G. Thomas, K. L. Wang, *J. Cryst. Growth*, 1999, **200**, 106.
- [25] G. A. Bootsma, H. J. Gassen, *J. Cryst. Growth*, 1971, **10**, 223.
- [26] T. W. Cornelius, J. Brötz, N. Chtanko, D. Dobrev, G. Miehe, R. Neumann, M. E. T. Molares, *Nanotechn.*, 2005, **16**, 246.
- [27] Z. A. Hu, T. Xu, R. J. Liu, H. L. Li, *Mater. Sci. Eng. A*, 2004, **371**, 236.
- [28] C. Wang, S. H. Sun, *Chem. An Asian J.*, 2009, **4**, 1028.
- [29] X. H. Huang, G. H. Li, X. C. Dou, L. Li, *J. Appl. Phys.*, 2009, **105**, 084306.
- [30] B. Gates, B. Mayers, B. Cattle, Y. Xia, *Adv. Funct. Mater.*, 2002, **12**, 219.
- [31] N. Furuta, Y. Ohasi, H. Itinose, Y. Igarashi, *Jap. J. Appl. Phys.*, 1975, **14**, 929.
- [32] Y. Y. Wu, R. Fan, P. D. Yang, *Nano Lett.*, 2002, **2**, 83.
- [33] L. J. Lauhon, M. S. Gudiksen, C. L. Wang, C. M. Lieber, *Nature*, 2002, **420**, 57.
- [34] P. D. Yang, H. Q. Yan, S. Mao, R. Russo, J. Johnson, R. Saykally, N. Morris, J. Pham, R. R. He, H. J. Cho, *Adv. Funct. Mater.*, 2002, **12**, 323.
- [35] Y. Wu, Y. Cui, L. Huynh, C. J. Barrelet, D. C. Bell, C. M. Lieber, *Nano Lett.*,

- 2004, **4**, 433.
- [36] Y. W. Wang, L. D. Zhang, G. Z. Wang, X. S. Peng, Z. Q. Chu, C. H. Liang, *J. Cryst. Growth*, 2002, **234**, 171.
- [37] Y. Li, G. W. Meng, L. D. Zhang, F. Phillipp, *Appl. Phys. Lett.*, 2000, **76**, 2011.
- [38] H. Zhang, S. Boussaad, N. Ly, N. Tao, *Appl. Phys. Lett.*, 2004, **84**, 133.
- [39] H. Zhang, D. R. Yang, X. Y. Ma, D. L. Que, *J. Phys. Chem. B*, 2005, **109**, 17055.
- [40] Z. W. Pan, Z. R. Dai, Z. L. Wang, *Science*, 2001, **291**, 1947.
- [41] Y. Ding, P. X. Gao, Z. L. Wang, *J. Am. Chem. Soc.*, 2004, **126**, 2066.
- [42] H. Zhang, D. Yang, Y. J. Ji, X. Y. Ma, J. Xu, D. L. Que, *J. Phys. Chem. B*, 2004, **108**, 3955.
- [43] L. Vayssieres, *Adv. Mater.*, 2003, **15**, 464.
- [44] P. X. Gao, Z. L. Wang, *J. Phys. Chem. B*, 2004, **108**, 7534.
- [45] Z. L. Wang, *J. Nanosci. Nanotechnol.*, 2008, **8**, 27.
- [46] A. B. Hartanto, X. Ning, Y. Nakata, T. Okada, *Appl. Phys. A*, 2004, **78**, 299.
- [47] Y. J. Xing, Z. H. Xi, Z. Q. Xue, X. D. Zhang, J. H. Song, R. M. Wang, J. Xu, Y. Song, S. L. Zhang, D. P. Yu, *Appl. Phys. Lett.*, 2003, **83**, 1689.
- [48] X. Kong, X. M. Sun, X. L. Li, Y. D. Li, *Mater. Chem. Phys.*, 2003, **82**, 997.
- [49] Y. Sun, G. M. Fuge, N. A. Fox, D. J. Riley, M. N. R. Ashfold, *Adv. Mater.*, 2005, **17**, 2477.
- [50] C. Li, D. Zhang, S. Han, X. Liu, T. Tang, C. Zhou, *Adv. Mater.*, 2003, **15**, 143.
- [51] X. S. Peng, G. W. Meng, J. Zhang, X. F. Wang, Y. W. Wang, C. Z. Wang, L. D. Zhang, *J. Mater. Chem.*, 2002, **12**, 1602.
- [52] J. Zhang, X. Qing, F. H. Jiang, Z. H. Dai, *Chem. Phys. Lett.*, 2003, **371**, 311.

- [53] H. Q. Cao, X. Q. Qiu, Y. Liang, Q. Zhu, M. Zhao, *Appl. Phys. Lett.*, 2003, **83**, 761.
- [54] X. Y. Kong, Z. L. Wang, *Solid State Commun.*, 2003, **128**, 1.
- [55] C. Chen, D. Chen, X. Jiao, C. Qang, *Chem. Commun.*, 2006, 4632.
- [56] Y. Yin, G. Zhang, Y. N. Xia, *Adv. Funct. Mater.*, 2002, **12**, 293.
- [57] H. W. Kim, S. H. Shim, *Chem. Phys. Lett.*, 2006, **422**, 165.
- [58] K. Nagashima, T. Yanagida, H. Tanaka, T. Kawai, *J. Appl. Phys.*, 2007, **101**, 124304.
- [59] Z. Q. Liu, D. H. Zhang, S. Han, C. Li, T. Tang, W. Jin, X. L. Liu, B. Lei, C. W. Zhou, *Adv. Mater.*, 2003, **15**, 1754.
- [60] S. Luo, P. K. Chu, W. Liu, M. Zhang, C. L. Lin, *Appl. Phys. Lett.*, 2006, **88**, 183112.
- [61] Y. Chen, X. Cui, K. Zhang, D. Pan, S. Zhang, B. Wang, J. G. Hou, *Chem. Phys. Lett.*, 2003, **369**, 16.
- [62] Y. L. Wang, X. C. Jiang, Y. Xia, *J. Am. Chem. Soc.*, 2003, **125**, 16176.
- [63] S. Sun, G. W. Meng, G. Zhang, T. Gao, B. Geng, L. D. Zhang, L. Zuo, *Chem. Phys. Lett.*, 2003, **376**, 103.
- [64] J. Duan, S. Yang, H. Liu, J. Gong, H. Huang, X. Zhao, R. Zhang, Y. Du, *J. Am. Chem. Soc.*, 2005, **107**, 6180.
- [65] J. Hu, Y. Bando, Q. Liu, D. Golberg, *Adv. Funct. Mater.*, 2003, **13**, 493.
- [66] Y. K. Liu, C. L. Zheng, W. Z. Wang, C. R. Yin, G. H. Wang, *Adv. Mater.*, 2001, **13**, 1883.
- [67] D. F. Zhang, L. D. Sun, J. L. Yin, C. H. Yan, *Adv. Mater.*, 2003, **15**, 1022.
- [68] B. Cheng, J. M. Russell, W. S. Shi, L. Zhang, E. T. Samulski, *J. Am. Chem. Soc.*, 2004, **126**, 5972.
- [69] J. H. He, T. H. Wu, C. L. Hsin, K. M. Li, L. J. Chen, Y. L. Chueh, L. J. Chou, Z. L. Wang, *Small*, 2006, **2**, 116.
- [70] B. Liu, H. C. Zeng, *J. Phys. Chem. B*, 2004, **108**, 5867.

- [71] N. Du, H. Zhang, B. Chen, X. Ma, D. R. Yang, *Chem. Commun.*, 2008, 3028.
- [72] N. Wang, X. Cao, L. Guo, *J. Phys. Chem. C*, 2008, **112**, 12616.
- [73] H. Z. Zhang, Y. C. Kong, Y. Z. Wang, X. Du, Z. G. Bai, J. J. Wang, D. P. Yu, Y. Ding, Q. L. Hang, S. Feng, *Solid State Commun.*, 1999, **109**, 677.
- [74] Y. C. Choi, W. S. Kim, Y. S. Park, S. M. Lee, D. J. Bae, Y. H. Lee, G. S. Park, W. B. Choi, N. S. Lee, J. M. Kim, *Adv. Mater.*, 2000, **12**, 746.
- [75] J. Hu, Q. Li, X. Meng, C. S. Lee, S. T. Lee, *J. Phys. Chem. B*, 2002, **106**, 9536.
- [76] B. Geng, L. D. Zhang, G. W. Meng, T. Xie, X. Peng, Y. Lin, *J. Cryst. Growth*, 2003, **259**, 291.
- [77] J. Zhang, F. H. Jiang, Y. Yang, J. Li, *J. Phys. Chem. B*, 2005, **109**, 13143.
- [78] N. Gong, M. Lu, C. Y. Wang, Y. Chen, L. J. Chen, *Appl. Phys. Lett.*, 2008, **92**, 073101.
- [79] F. Zhou, X. Zhao, Y. Liu, C. Yuan, L. Li, *Eur. J. Inorg. Chem.*, 2008, **16**, 2506.
- [80] C. K. Chan, H. Peng, R. D. Twisten, K. Jarausch, X. F. Zhang, Y. Cui, *Nano Lett.*, 2007, **7**, 490.
- [81] H. Imai, Y. Takei, K. Shimizu, M. Matsuda, H. Hirashima, *J. Mater. Chem.*, 1999, **9**, 2971.
- [82] S. Liu, L. Gan, L. Liu, W. Zhang, H. Zeng, *Chem. Mater.*, 2002, **14**, 1391.
- [83] Y. Zhang, G. Li, Y. Jin, Y. Zhang, J. Zhang, L. D. Zhang, *Chem. Phys. Lett.*, 2002, **365**, 300.
- [84] J. M. Wu, H. C. Shih, W. T. Wu, *Chem. Phys. Lett.*, 2005, **413**, 490.
- [85] K. Zhu, H. He, S. Xie, X. Zhang, W. Zhou, S. Jin, B. Yue, *Chem. Phys. Lett.*, 2003, **377**, 317.
- [86] Y. Baek, K. Yong, *J. Phys. Chem. C*, 2007, **111**, 1213.
- [87] X. C. Song, Y. F. Zheng, E. Yang, Y. Wang, *Mater. Lett.*, 2007, **61**, 3904.

- [88] Y. Li, Y. Bando, D. Golberg, K. Kurashima, *Chem. Phys. Lett.*, 2003, **367**, 214.
- [89] H. Cao, X. Qiu, B. Luo, Y. Liang, Y. Zhang, R. Tan, M. Zhao, Q. Zhu, *Adv. Funct. Mater.*, 2004, **14**, 243.
- [90] L. Li, W. Z. Wang, *Solid State Commun.*, 2003, **127**, 639.
- [91] C. Dae, S. Kim, B. Ahn, J. Kim, M. Sung, H. Shin, *J. Mater. Chem.*, 2008, **18**, 1362.
- [92] M. Wei, Z. M. Qi, M. Ichihara, H. Zhou, *Acta Mater.*, 2008, **56**, 2488.
- [93] B. Varghese, S. C. Haur, C. T. Lim, *J. Phys. Chem. C*, 2008, **112**, 10008.
- [94] Y. Kobayashi, H. Hata, M. Salama, T. E. Mallouk, *Nano Lett.*, 2007, **7**, 2142.
- [95] Z. Q. Liu, D. H. Zhang, S. Han, C. Li, B. Lei, W. Lu, J. Fang, C. Zhou, *J. Am. Chem. Soc.*, 2005, **127**, 6.
- [96] J. Wang, Q. W. Chen, C. Zeng, B. Y. Hou, *Adv. Mater.*, 2004, **16**, 137.
- [97] R. S. Chen, Y. S. Huang, D. S. Tsai, S. Chattopadhyay, C. T. Wu, Z. H. Lan, K. H. Chen, *Chem. Mater.*, 2004, **16**, 2457.
- [98] Y. L. Chen, C. C. Hsu, Y. H. Song, Y. Chi, A. J. Carty, S. M. Peng, G. H. Lee, *Chem. Vapor. Dep.*, 2006, **12**, 442.
- [99] S. Hu, X. Wang, *J. Am. Chem. Soc.*, 2008, **130**, 8126.
- [100] B. C. Satishkumar, A. Govindaraj, E. M. Vogl, L. Basumallick, C. N. R. Rao, *J. Mater. Res.*, 1997, **12**, 604.
- [101] Y. B. Li, Y. Bando, *Chem. Phys. Lett.*, 2002, **364**, 484.
- [102] J. Zhou, S. Deng, N. S. Xu, J. Chen, J. She, *Appl. Phys. Lett.*, 2003, **83**, 2653.
- [103] B. Qi, X. Ni, D. Li, H. Zheng, *Chem. Lett.*, 2008, **37**, 336.
- [104] X. Wang, Y. D. Li, *J. Am. Chem. Soc.*, 2002, **124**, 2880.
- [105] M. Imperor-Clerc, D. Bazin, M. D. Appay, P. Beaunier, A. Davidson, *Chem. Mater.*, 2004, **16**, 1813.

- [106] D. Zheng, S. X. Sun, W. Fan, H. Yu, C. Fan, G. Cao, Z. Yin, X. Song, *J. Phys. Chem. B*, 2005, **109**, 16439.
- [107] Y. Fu, J. Chen, H. Zhang, *Chem. Phys. Lett.*, 2001, **350**, 491.
- [108] Y. Xiong, Y. Xie, Z. Li, R. Zhang, J. Yang, C. Wu, *New J. Chem.*, 2003, **27**, 588.
- [109] X. Wen, S. Wang, Y. Ding, Z. L. Wang, S. Yang, *J. Phys. Chem. B*, 2005, **109**, 215.
- [110] C. K. Xu, K. Q. Hong, S. Liu, G. H. Wang, X. N. Zhao, *J. Cryst. Growth*, 2003, **255**, 308.
- [111] Q. Yang, J. Sha, X. Y. Ma, D. R. Yang, *Mater. Lett.*, 2005, **59**, 1967.
- [112] C. S. Shi, G. Q. Wang, N. Q. Zhao, X. W. Du, J. J. Li, *Chem. Phys. Lett.*, 2008, **454**, 75.
- [113] Z. Dong, Y. Y. Fu, Q. Han, Y. Xu, H. Zhang, *J. Phys. Chem. C*, 2007, **111**, 18475.
- [114] H. Zhang, J. Wu, C. Zhai, X. Ma, N. Du, J. Tu, D. R. Yang, *Nanotechnol.*, 2008, **19**, 035711.
- [115] N. Du, H. Zhang, B. Chen, J. Wu, X. Ma, Z. Liu, Y. Zhang, D. Yang, X. Huang, J. Tu, *Adv. Mater.*, 2007, **19**, 4505.
- [116] X. W. Lou, D. Deng, J. Y. Lee, J. Feng, L. A. Archer, *Adv. Mater.*, 2008, **20**, 258.
- [117] W. Z. Wang, G. H. Wang, X. S. Wang, Y. J. Zhan, Y. K. Liu, C. L. Zheng, *Adv. Mater.*, 2002, **14**, 67.
- [118] Y. J. Xiong, Z. Q. Li, R. Zhang, Y. Xie, J. Yang, C. Z. Wu, *J. Phys. Chem. B*, 2003, **107**, 3697.
- [119] Y. W. Tan, X. Y. Xue, Q. Peng, H. Zhao, T. H. Wang, Y. D. Li, *Nano Lett.*, 2007, **7**, 3723.
- [120] X. C. Jiang, T. Herricks, Y. N. Xia, *Nano Lett.*, 2002, **2**, 1333.
- [121] E. Ko, J. Choi, K. Okamoto, Y. Tak, J. Lee, *ChemPhysChem.*, 2006, **7**,



- 1505.
- [122] G. H. Du, G. V. Tendeloo, *Chem. Phys. Lett.*, 2004, **393**, 64.
- [123] X. S. Peng, X. F. Wang, Y. W. Wang, C. Z. Wang, G. W. Meng, L. D. Zhang, *J. Phys. D*, 2002, **35**, L101.
- [124] D. S. Dhawale, A. M. More, S. S. Latthe, K. Y. Rajpure, C. D. Lokhande, *Appl. Surf. Sci.*, 2008, **254**, 3269.
- [125] X. Liu, C. Li, S. Han, J. Han, C. Zhou, *Appl. Phys. Lett.*, 2003, **82**, 1950.
- [126] W. Lee, R. Scholz, U. Gosele, *Nano Lett.*, 2008, **8**, 2155.
- [127] Y. B. Li, Y. Bando, D. Golberg, *Adv. Mater.*, 2005, **17**, 1401.
- [128] D. B. Kuang, Y. P. Fang, H. Q. Liu, C. Frommen, D. Fenske, *J. Mater. Chem.*, 2003, **13**, 660.
- [129] H. Ogihara, M. Sadakane, Y. Nodasaka, W. Ueda, *Chem. Mater.*, 2006, **18**, 4981.
- [130] X. S. Peng, L. D. Zhang, G. W. Meng, X. F. Wang, Y. W. Wang, C. Z. Wang, G. S. Wu, *J. Phys. Chem. B*, 2002, **106**, 11163.
- [131] Y. Huang, X. Zhang, M. Reiche, L. Liu, W. Lee, T. Shimizu, S. Senz, U. Gosele, *Nano Lett.*, 2008, **8**, 3046.
- [132] Y. L. Cao, D. Z. Jia, L. Liu, J. M. Luo, *Chin. J. Chem.*, 2004, **22**, 1288.
- [133] A. Vantomme, Z. Y. Yuan, G. H. Du, B. L. Su, *Langmuir*, 2005, **21**, 1132.
- [134] J. J. Miao, H. Wang, Y. R. Li, J. M. Zhu, J. J. Zhu, *J. Cryst. Growth*, 2005, **281**, 525.
- [135] V. G. Pol, O. Palchik, A. Gedanken, I. Felner, *J. Phys. Chem. B*, 2002, **106**, 9737.
- [136] H. Liu, H. Yang, T. Huang, *Mater. Sci. Eng. B*, 2007, **143**, 60.
- [137] S. Lei, K. Tang, Y. Jin, C. Chen, *Nanotechn.*, 2007, **18**, 175605.
- [138] A. Thomas, B. Premlal, M. Eswaramoorthy, *Mater. Res. Bull.*, 2006, **41**, 1008.
- [139] N. Z. Bao, L. M. Shen, A. Gupta, A. Tatarenko, G. Srinivasan, K.

- Yanagisawa, *Appl. Phys. Lett.*, 2009, **94**, 253109.
- [140] O. Ersen, S. Begin, M. Houille, J. Amadou, I. Janowska, J. M. Greneche, C. Crucifix, C. Pham-Huu, *Nano Lett.*, 2008, **8**, 1033.
- [141] L. Zhen, K. He, C. Y. Xu, W. Z. Shao, *J. Magnet. Magnet. Mater.*, 2008, **320**, 2672.
- [142] S. Y. Lim, C. S. Yoon, J. P. Cho, *Chem. Mater.*, 2008, **20**, 4560.
- [143] J. S. Jung, Y. K. Jung, E. M. Kim, S. H. Min, J. H. Jun, L. M. Malkinski, Y. Barnakov, L. Spinu, K. Stokes, *IEEE Tran. Magn.*, 2005, **41**, 3403.
- [144] B. J. Ohlsson, M. T. Björk, M. H. Magnusson, K. Deppert, L. Samuelson, L. R. Wallenberg, *Appl. Phys. Lett.*, 2001, **79**, 3335.
- [145] S. T. Lee, N. Wang, Y. F. Zhang, Y. H. Tang, *Mater. Res. Bull.*, 1999, **24**, 36.
- [146] M. S. Gudiksen, L. J. Lauhon, J. Wang, D. C. Smith, C. M. Lieber, *Nature*, 2002, **415**, 617.
- [147] X. Duan, C. M. Lieber, *J. Am. Chem. Soc.*, 2000, **122**, 188.
- [148] G. Q. Zhu, P. Liu, *Crys. Resea. Techn.*, 2009, **44**, 713.
- [149] K. A. Dick, K. Deppert, T. Martensson, B. Mandl, L. Samuelson, W. Seifert, *Nano Lett.*, 2005, **5**, 761.
- [150] X. H. Sun, B. Yu, G. Ng, T. D. Nguyen, M. Meyyappan, *Appl. Phys. Lett.*, 2006, **89**, 233121.
- [151] Y. Ai, C. Xue, C. Sun, L. Sun, H. Zhuang, F. Wang, H. Li, J. Chen, *Mater. Lett.*, 2007, **61**, 2833.
- [152] Y. Cui, Q. Q. Wei, H. K. Park, C. M. Lieber, *Science*, 2001, **293**, 1289.
- [153] G. Z. Shen, Y. Bando, C. Ye, X. Yuan, T. Sekiguchi, D. Golberg, *Angew. Chem. Int. Ed. Engl.*, 2006, **45**, 7568.
- [154] M. Omari, N. Kouklin, G. Lu, J. Chen, M. Gajdardziska-Josifovska, *Nanotechn.*, 2008, **19**, 105301.
- [155] C. J. Barrelet, Y. Wu, D. C. Bell, C. M. Lieber, *J. Am. Chem. Soc.*, 2003,

- 125**, 11498.
- [156] C. K. Chan, H. Peng, R. D. Twisten, K. Jarausch, X. F. Zhang, Y. Cui, *Nano Lett.*, 2007, **7**, 490.
- [157] S. Zhou, X. H. Liu, Y. J. Lin, D. W. Wang, *Chem. Mater.*, 2009, **21**, 1023.
- [158] H. Asoh, S. Ono, T. Hirose, M. Nakao, H. Masuda, *Electrochim. Acta*, 2003, **48**, 3171.
- [159] J. Choi, R. Wehrspohn, U. Gösele, *Adv. Mater.*, 2003, **18**, 1531.
- [160] R. Solanki, J. Huo, J. L. Freeouf, B. Miner, *Appl. Phys. Lett.*, 2002, **81**, 3864.
- [161] W. I. Park, G. C. Yi, M. Kim, S. J. Pennycook, *Adv. Mater.*, 2003, **15**, 526.
- [162] N. Panev, A. I. Persson, N. Skold, L. Samuelson, *Appl. Phys. Lett.*, 2003, **83**, 2238.
- [163] P. J. Poole, J. Lefebvre, J. Fraser, *Appl. Phys. Lett.*, 2003, **83**, 2055.
- [164] J. Goldberger, R. R. He, Y. F. Zhang, S. W. Lee, H. Q. Yan, H. J. Choi, P. D. Yang, *Nature*, 2003, **422**, 599.
- [165] S. Mathur, H. Shen, N. Donia, T. Rügamer, V. Sivakov, U. Werner, *J. Am. Chem. Soc.*, 2007, **129**, 9746.
- [166] Y. Li, G. Xu, Y. L. Zhu, X. L. Ma, H. M. Cheng, *Solid State Commun.*, 2007, **142**, 441.
- [167] S. Mathur, S. Barth, *Small*, 2007, **3**, 2070.
- [168] S. Mathur, S. Barth, U. Werner, F. Hernandez-Ramirez, A. Romano Rodriguez, *Adv. Mater.*, 2008, **20**, 1550.
- [169] J. Xiang, W. Lu, Y. Hu, Y. Wu, H. Yan, C. M. Lieber, *Nature*, 2006, **441**, 489; (b) B. Tian, X. Zheng, T. J. Kempa, Y. Fang, N. Yu, G. Yu, J. Huang, C. M. Lieber, *Nature*, 2007, **449**, 885; (c) D. Moore, J. R. Morber, R. L. Snyder, Z. L. Wang, *J. Phys. Chem. C*, 2008, **112**, 2895.
- [170] G. Liang, J. Xiang, N. Kharche, G. Klimeck, C. M. Lieber, M. Lundstrom, *Nano Lett.*, 2007, **7**, 642.

- [171] S. V. N. T. Kuchibhatla, A. S. Karaoti, D. Bera, S. Seal, *Prog. Mater. Sci.*, 2007, **52**, 699.
- [172] H. W. Ra, K. S. Choi, J. H. Kim, Y. B. Hahn, Y. H. Im, *Small*, 2008, **4**, 1105.
- [173] F. L. Zhang, T. Nyberg, O. Inganäs, *Nano Lett.*, 2002, **2**, 1373.
- [174] J. D. Meindl, Q. Chen, J. A. Davis, *Science*, 2001, **293**, 2044.
- [175] C. M. Lieber, *Sci. Am.*, 2001, **285**, 58.
- [176] J. R. Heath, P. J. Kuekes, G. S. Snider, R.S. Williams, *Science*, 1998, **280**, 1716.
- [177] (a) L. Isaacs, D. N. Chin, N. Bowden, Y. Xia, G. M. Whitesides, *Supramolecular Technology*, (Ed: D. N. Reinhoudt), John Wiley & Sons, New York, 1999, 1; (b) G. Hornyak, M. Kröll, R. Pugin, T. Sawitowski, G. Schmid, J. O. Bovin, G. Karlsson, H. Hofmeister, S. Hopfe, *Chem. Eur. J.*, 1997, **3**, 1951.
- [178] (a) E. Braun, Y. Eichen, U. Sivan, G. Ben-Yoseph, *Nature*, 1998, **391**, 775; (b) J. Richter, M. Mertig, W. Pompe, I. Monch, H. K. Schackert, *Appl. Phys. Lett.*, 2001, **78**, 536.
- [179] Y. Zhang, J. Zhu, Q. Zhang, Y. Yan, N. Wang, X. Zhang, *Chem. Phys. Lett.*, 2000, **317**, 504.
- [180] C. Mao, D. J. Solis, B. D. Reiss, S. T. Kottmann, R. Y. Sweeney, A. Hayhurst, G. Georgiou, B. Iverson, A. M. Belcher, *Science*, 2004, **303**, 213.
- [181] J. G. Lu, P. Chang, Z. Fan, *Mater. Sci. Eng. R*, 2006, **52**, 49.
- [182] K. W. Kolasinski, *Curr. Opin. Solid State Mater. Sci.*, 2006, **10**, 182.
- [183] S. Mathur, H. Shen, V. Sivakov, U. Werner, *Chem. Mater.*, 2004, **16**, 2449.
- [184] S. Kodambaka, J. B. Honnon, R. M. Tromp, F. M. Ross, *Nano Lett.*, 2006, **6**, 1292.

- [185] Y. Y. Wu, P. D. Yang, *J. Am. Chem. Soc.*, 2001, **123**, 3165.
- [186] (a) Q. Zhao, X. Xu, H. Zhang, Y. Chen, J. Xu, D. Yu, *Appl. Phys. A: Mater. Sci. Process.*, 2004, **79**, 1721; (b) A. Umar, S. H. Kim, Y. S. Lee, K. S. Nahm, Y. B. Hahn, *J. Cryst. Growth*, 2005, **282**, 131; (c) A. Sekar, S. H. Kim, A. Umar, Y. B. Hahn, *J. Cryst. Growth*, 2005, **277**, 471.
- [187] Y. Sun, G. M. Fuge, M. N. R. Ashfold, *Superlattices Microstruct.*, 2006, **39**, 33.
- [188] N. Cabrera, W. K. Burton, *Discuss. Faraday Soc.*, 1949, 40; (b) G. W. Sears, *Acta Metallurgica*, 1955, **3**, 367.
- [189] J. M. Blakely, K. A. Jackson, *J. Chem. Phys.*, 1962, **37**, 428.
- [190] A. Vomiero, S. Bianchi, E. Comini, G. Faglia, M. Ferroni, G. Sberveglieri, *Cryst. Grow. Des.*, 2007, **7**, 2500.
- [191] A. T. Heitsch, D. D. Fanfair, H. Y. Tuan, B. A. Korgel, *J. Am. Chem. Soc.*, 2008, **130**, 5436.
- [192] J. C. Hulteen, C. R. Martin, *J. Mater. Chem.*, 1997, **7**, 1075.
- [193] C. R. Martin, *Adv. Mater.*, 1991, **3**, 457.
- [194] (a) C. K. Xu, G. D. Xu, Y. K. Liu, G. H. Wang, *Solid State Commun.*, 2002, **122**, 175; (b) C. K. Xu, X. L. Zhao, S. Liu, G. H. Wang, *Solid State Commun.*, 2003, **125**, 301; (c) C. K. Xu, G. D. Xu, G. H. Wang, *J. Mater. Sci.*, 2003, **38**, 779.
- [195] L. H. Thompson, L. K. Doraiswamy, *Ind. Eng. Chem. Res.*, 1999, **38**, 1215.
- [196] T. Gao, Q. H. Li, T. H. Wang, *Chem. Mater.*, 2005, **17**, 887.
- [197] (a) B. Liu, H. C. Zeng, *J. Am. Chem. Soc.*, 2003, **125**, 4430; (b) J. M. Wang, L. Gao, *J. Mater. Chem.*, 2003, **13**, 2551; (c) M. Guo, P. Diao, S.M. Cai, *J. Solid State Chem.*, 2005, **178**, 1864.
- [198] (a) M. L. Kahn, M. Monge, E. Snoeck, A. Maisonnat, B. Chaudret, *Small*, 2005, **1**, 221; (b) M. L. Kahn, M. Monge, V. Colliere, F. Senocq, A.

- Maisonnat, B. Chaudret, *Adv. Funct. Mater.*, 2005, **15**, 458.
- [199] D. Li, Y. N. Xia, *Nano Lett.*, 2003, **3**, 555.
- [200] E. Comini, C. Baratto, G. Faglia, M. Ferroni, A. Vomiero, G. Sberveglieri, *Prog. Mater. Sci.*, 2009, **54**, 1.
- [201] K. A. Dick, K. Deppert, M. W. Larsson, T. Martensson, W. Seifert, L. R. Wallenberg, L. Samuelson, *Nat. Mater.* 2004, **3**, 380.
- [202] R. Dingle, H. L. Stormer, A. C. Gossard, W. Wiegmann, *Appl. Phys. Lett.*, 1978, **33**, 665.
- [203] F. Schäffler, *Semicond. Sci. Technol.*, 1997, **12**, 1515.
- [204] C. G. Van de Walle, R. M. Martin, *Phys. Rev. B*, 1986, **34**, 5621.
- [205] F. Qian, S. Gradecak, Y. Li, C. Y. Wen, C. M. Lieber, *Nano Lett.*, 2005, **5**, 2287.
- [206] F. Qian, Y. Li, S. Gradecak, D. Wang, C. J. Barrelet, C. M. Lieber, *Nano Lett.*, 2004, **4**, 1975.
- [207] R. Fan, Y. Y. Wu, D. Y. Li, M. Yue, A. Majumdar, P. Yang, *J. Am. Chem. Soc.*, 2003, **125**, 5254.
- [208] D. Whang, S. Jin, C. M. Lieber, *Nano Lett.*, 2003, **3**, 951.
- [209] X. Duan, C. M. Lieber, *Adv. Mater.*, 2000, **12**, 298.
- [210] Y. Wu, J. Xiang, C. Yang, W. Lu, C. M. Lieber, *Nature*, 2004, **430**, 61.
- [211] (a) J. M. Blocher, *J. Vac. Sci. Technol.*, 1974, **11**, 680; (b) W. A. Bryant, *J. Electrochem. Soc.*, 1978, **125**, 1534.
- [212] J. D. Buckley, *Am. Ceram. Soc. Bull.*, 1988, **67**, 364.
- [213] K. L. Choy, *Prog. Mater. Science*, 2003, **48**, 57.
- [214] K. L. Choy, *Handbook of Nanostructured Materials and Nanotechnology*, Vol. 1: *Synthesis and Processing*, Academic, San Diego, 2000.
- [215] K. E. Spear, *Proc. 9th. Int. Conf. on CVD: Electrochem. Soc.*, Pennington, 1984.
- [216] R. S. Wagner, *Whisker Technology*, Wiley, New York, 1970.

- [217] S. Mathur, M. Veith, T. Rügamer, E. Hemmer, H. Shen, *Chem. Mater.*, 2004, **16**, 1304.
- [218] S. Mathur, S. Barth, H. Shen, J. C. Pyun, U. Werner, *Small*, 2005, **1**, 713.
- [219] (a) X. Duan, Y. Huang, Y. Cui, J. Wang, C. M. Lieber, *Nature*, 2001, **409**, 66; (b) Y. Huang, X. Duan, Y. Cui, L. J. Lauhon, K. H. Kim, C. M. Lieber, *Science*, 2001, **294**, 1313; (c) D. H. Cobden, *Nature*, 2001, **409**, 32; (d) G. Y. Tseng, J. V. Ellenbogen, *Science*, 2001, **294**, 1293; (e) R. F. Service, *Science*, 2001, **293**, 782.
- [220] Z. Y. Fan, D. W. Wang, P. C. Chang, W. Y. Tseng, J. G. Lu, *Appl. Phys. Lett.*, 2004, **85**, 5923.
- [221] (a) P. C. Chang, Z. Y. Fan, D. W. Wang, W. Y. Tseng, W. A. Chiou, J. Hong, J. G. Lu, *Chem. Mater.*, 2004, **16**, 5133; (b) P. C. Chang, T. Fan, C. J. Chien, D. Stichtenoth, C. Ronning, J. G. Lu, *Appl. Phys. Lett.*, 2006, **89**, 133113; (c) P. C. Chang, C. J. Chien, D. Stichtenoth, C. Ronning, J. G. Lu, *Appl. Phys. Lett.*, 2007, **90**, 113101.
- [222] X. G. Zheng, Q. Li, J. P. Zhao, D. Chen, B. Zhao, Y. J. Yang, L. C. Zhang, *Appl. Surf. Sci.*, 2006, **253**, 2264.
- [223] F. Hernandez-Ramirez, A. Tarancon, O. Casals, J. Rodríguez, A. R. Rodríguez, J. R. Morante, S. Barth, S. Mathur, T. Y. Choi, D. Poulikakos, V. Callegari, P. M. Nellen, *Nanotechnol.*, 2006, **17**, 5577.
- [224] L. Gangloff, E. Minoux, K. B. K. Teo, P. Vincent, V. T. Semet, V. T. Binh, M. H. Yang, I. Y. Y. Bu, R. G. Lacerda, G. Pirio, J. P. Schnell, D. Pribat, D. G. Hasko, G. A. J. Amaratunga, W. I. Milne, P. Legagneux, *Nano Lett.*, 2004, **4**, 1575.
- [225] (a) H. Kind, H. Yan, B. Messer, M. Law, P. D. Yang, *Adv. Mater.*, 2002, **14**, 158; (b) C. Soci, A. Zhang, B. Xiang, S. A. Dayeh, D. P. R. Aplin, J. Park, X. Y. Bao, Y. H. Lo, D. Wang, *Nano Lett.*, 2007, **7**, 1003.
- [226] J. D. Prades, R. Jimenez-Diaz, F. Hernandez-Ramirez, L. Fernandez-

- Romero, T. Andreu, A. Cirera, A. Romano-Rodriguez, A. Cornet, J. R. Morante, S. Barth, S. Mathur, *J. Phys. Chem. C*, 2008, **112**, 14639.
- [227] C. Dekker, *Phys. Today*, 1999, **5**, 22.
- [228] C. J. Lee, T. J. Lee, S. C. Lyu, Y. Zhang, H. Ruh, H. J. Lee, *Appl. Phys. Lett.*, 2001, **81**, 3846.
- [229] S. T. Shishiyanu, T. S. Shishiyanu, O. I. Lupan, *Sens. Actuators B*, 2005, **107**, 379.
- [230] R. Ramamoorthy, P. K. Dutta, S. A. Akbar, *J. Mater. Sci.*, 2003, **38**, 4271.
- [231] Z. Y. Fan, J. G. Lu, *Appl. Phys. Lett.*, 2005, **86**, 123510.
- [232] H. Nanto, T. Minami, S. Takata, *J. Appl. Phys.*, 1986, **60**, 482.
- [233] G. Faglia, P. Nelli, G. Sberveglieri, *Sens. Actuators B*, 1994, **19**, 497.
- [234] A. Heilig, N. Barsan, U. Weimar, M. Schweizer-Berberich, J. W. Gardner, W. Gopel, *Sens. Actuators B*, 1997, **43**, 45.
- [235] Q. F. Pengfei, O. Vermesh, M. Grecu, *Nano Lett.*, 2003, **3**, 347.
- [236] Y. Zhang, A. Kolmakov, S. Chretien, H. Metiu, M. Moskovits, *Nano Lett.*, 2004, **4**, 403.
- [237] M. J. Hampden-Smith, T. A. Wark, A. Rheingold, J. C. Huffman, *Can. J. Chem.*, 1991, **69**, 121.
- [238] S. Mathur, V. Sivakov, H. Shen, S. Barth, A. Nilsson, P. Kuhn, *Thin Solid Films*, 2006, **502**, 88.
- [239] D. Wang, C. M. Lieber, *Nat. Mater.*, 2003, **2**, 355.
- [240] F. Hernandez-Ramirez, A. Tarancon, O. Casals, J. Rodriguez, A. Romano-Rodriguez, J. R. Morante, S. Barth, S. Mathur, T. Y. Choi, D. Poulidakos, V. Callegari, P. M. Nellen, *Nanotechn.*, 2006, **17**, 5577.
- [241] F. Hernandez-Ramirez, A. Tarancon, O. Casals, E. Pellicer, J. Rodriguez, A. Romano-Rodriguez, J. R. Morante, S. Barth, S. Mathur, *Phys. Rev. B*, 2007, **76**, 085429-1.
- [242] J. D. Prades, R. Jimenez-Diaz, F. Hernandez-Ramirez, S. Barth, A.



- Cirera, A. Romano-Rodriguez, S. Mathur, J. R. Morante, *Appl. Phys. Lett.*, 2008, **93**, 123110.
- [243] F. Hernandez-Ramirez, J. D. Prades, A. Tarancon, S. Barth, O. Casals, R. Jimenez-Diaz, E. Pellicer, J. Rodriguez, M. A. Juli, A. Romano-Rodriguez, J. R. Morante, S. Mathur, A. Helwig, J. Spannhake, G. Mueller, *Nanotechn.*, 2007, **18**, 495501.
- [244] S. Semancik, T. B. Fryberger, *Sens. Actuators B*, 1990, **1**, 97.
- [245] C. Tatsuyama, S. Ichimura, *Jpn. J. Appl. Phys.*, 1976, **15**, 843.
- [246] W. Dazhi, W. Shulin, C. Jun, Z. Suyuan, L. Fangqing, *Phys. Rev. B*, 1994, **49**, 282.
- [247] Y. S. He, J. C. Campbell, R. C. Murphy, M. F. Arendt, J. S. Swinnea, *J. Mater. Res.*, 1993, **8**, 3131.
- [248] Z. R. Dai, J. L. Gole, J. D. Stout, Z. L. Wang, *Adv. Funct. Mater.*, 2003, **13**, 9.
- [249] S. Budak, G. X. Miao, M. Ozdemir, K. B. Chetry, A. Gupta, *J. Cryst. Growth*, 2006, **291**, 405.
- [250] Z. Liu, D. Zhang, S. Han, C. Li, T. Tang, W. Jin, X. Liu, C. Zhou, *Adv. Mater.*, 2003, **15**, 1754.
- [251] A. Kolmakov, Y. Zhang, G. Cheng, M. Moskovits, *Adv. Mater.*, 2003, **15**, 997.
- [252] Y. J. Ma, F. Zhou, L. Lu, Z. Zhang, *Solid State Commun.*, 2004, **130**, 317.
- [253] X. Jiang, Y. Wang, T. Herricks, Y. Xia, *J. Mater. Chem.*, 2004, **14**, 695.
- [254] D. Li, Y. Wang, Y. Xia, *Adv. Mater.*, 2004, **16**, 361.
- [255] (a) Y. Cui, L. J. Lauhon, M. S. Gudixsen, J. Wang, C. M. Lieber, *Appl. Phys. Lett.*, 2001, **78**, 2214; (b) M. S. Gudixsen, C. M. Lieber, *J. Am. Chem. Soc.*, 2000, **122**, 8801.
- [256] (a) K. K. Lew, J. M. Redwing, *J. Cryst. Growth*, 2003, **254**, 14; (b) J. Kikkawa, Y. Ohno, S. Takeda, *Appl. Phys. Lett.*, 2005, **86**, 123109.

- [257] (a) J. T. Hu, T. W. Odom, C. M. Lieber, *Acc. Chem. Res.*, 1999, **32**, 435;  
(b) Y. N. Xia, P. D. Yang, Y. G. Sun, Y. Y. Wu, B. Mayers, B. Gates, Y. D. Yin, F. Kim, H. Q. Yan, *Adv. Mater.*, 2003, **15**, 353.
- [258] M. Ohring, *The Materials Science Of Thin Films*, Academic, San Diego, 1992.
- [259] D. C. Cranmer, *Ceram Bull*, 1989, **68**, 415.
- [260] (a) X. G. Wen, S. H. Wang, Y. Ding, Z. L. Wang, S. Yang, *J. Phys. Chem. B*, 2005, **109**, 215; (b) B. Y. Zong, Y. H. Wu, G. H. Han, B. J. Yang, P. Luo, L. Wang, J. J. Oiu, K. B. Li, *Chem. Mater.*, 2005, **17**, 1515.
- [261] D. Calestani, M. Zha, A. Zappettini, L. Lazzarini, G. Salviati, L. Zanotti, G. Sberveglieri, *Mater. Sci. Eng. C*, 2005, **25**, 625.
- [262] P. Nguyen, H. T. Ng, J. Kong, A. M. Cassell, R. Quinn, J. Li, J. Han, M. M. Neil, M. Meyyappan, *Nano Lett.*, 2003, **3**, 925.
- [263] Q. Wan, M. Wei, D. Zhi, J. L. MacManus-Driscoll, M. G. Blamire, *Adv. Mater.*, 2006, **18**, 234.
- [264] P. Nguyen, S. Vaddiraju, M. Meyyappan, *J. Electr. Mater.*, 2006, **35**, 200.
- [265] A. Leonardy, W. Z. Hung, D. S. Tsai, C. C. Chou, Y. S. Huang, *Cryst. Grow. Des.*, 2009, **9**, 3958.
- [266] S. G. Ihn, J. I. Song, T. W. Kim, D. S. Leem, T. Lee, S. G. Lee, E. K. Koh, K. Song, *Nano Lett.*, 2007, **7**, 39.
- [267] A. Beltran, J. Andres, E. Longo, E. R. Leite, *Appl. Phys. Lett.*, 2003, **83**, 635.
- [268] H. Wakabayashi, T. Suzuki, Y. Iwazaki, M. Fujimoto, *Jpn. J. Appl. Phys.*, 2001, **40**, 6081.
- [269] M. Ramamoorthy, D. Vanderbilt, R. D. King-Smith, *Phys. Rev. B*, 1994, **49**, 16721.
- [270] K. A. Dick, S. Kodambaka, M. C. Reuter, K. Deppert, L. Samuelson, W. Seifert, L. R. Wallenberg, F. M. Ross, *Nano Lett.*, 2007, **7**, 1817.

- [271] B. Slater, C. R. A. Catlow, D. H. Gay, D. E. Williams, V. Dusaatre, *J. Phys. Chem. B*, 1999, **103**, 10644.
- [272] L. P. Qin, J. Q. Xu, X. W. Dong, Q. Y. Pan, Z. X. Cheng, Q. Xiang, F. Li, *Nanotechn.*, 2008, **19**, 185705.
- [273] T. Tsuchiya, F. Kato, T. Nakajima, K. Igarashi, T. Kamagai, *Appl. Surf. Sci.*, 2009, **255**, 9808.
- [274] M. D. Uchic, L. Holzer, B. J. Inkson, E. L. Principe, P. Munroe, *MRS Bull.*, 2007, **32**, 408.
- [275] P. R. Munroe, *Mater. Characterization*, 2009, **60**, 2.
- [276] N. Yamazoe, *Sens. Actuators B*, 2005, **108**, 2.
- [277] V. V. Sysoev, T. Schneider, J. Goschnick, L. Kiselev, W. Habicht, H. Hahn, E. Strelcov, A. Kolmakov, *Sens. Actuators B*, 2009, **139**, 699.
- [278] A. J. Kubis, T. E. Vandervelde, J. C. Bean, D. N. Dunn, R. Hull, *Appl. Phys. Lett.*, 2006, **88**, 263103.
- [279] F. Elfallagh, B. J. Inkson, *J. Eur. Ceram. Soc.*, 2009, **29**, 47.
- [280] J. A. W. Heymann, D. Shi, S. Kim, D. Bliss, J. L. S. Milne, S. Subramaniam, *J. Struc. Bio.*, 2009, **166**, 1.
- [281] L. Holzer, F. Indutnyi, P. H. Gasser, B. Münch, M. Wegmann, *J. Microsc.*, 2004, **216**, 84.
- [282] G. Möbus, R. C. Doole, B. J. Inkson, *Ultramicros.*, 2003, **96**, 433.
- [283] (a) T. Inoue, T. Kita, O. Wada, M. Konno, T. Yaguchi, T. Kamino, *Appl. Phys. Lett.*, 2008, **92**, 031902; (b) M. A. Verheijen, R. E. Algra, M. T. Borgstroem, G. Immink, E. Sourty, W. J. P. van Enckevort, E. Vlieg, E. P. A. M. Bakkers, *Nano Lett.*, 2007, **7**, 3051.
- [284] (a) H. S. Kim, S. O. Hwang, Y. Myung, J. Park, S. Y. Bae, J. P. Ahn, *Nano Lett.*, 2008, **8**, 551; (b) J. Arbiol, E. Rossinyol, A. Cabot, F. Peiro, A. Cornet, J. R. Motante, *Mat. Res. Soc. Symp. Proc.*, 2004, **818**, M4.5.1.
- [285] B. Kalache, P. R. I. Cabarrocas, A. F. I. Morral, *Jpn. J. Appl. Phys.*, 2006,

- 45**, L190.
- [286] (a) S. Sharma, M. K. Sunkara, R. Miranda, G. Lian, E. C. Ickey, *Mat. Res. Soc. Symp. Proc.*, 2001, **676**, Y1.6.1; (b) Y. Zhang, A. Kolmakov, Y. Lilach, M. Maskovits, *J. Phys. Chem. B*, 2005, **109**, 1923.
- [287] V. Dobrokhotov, D. N. McIlroy, M. G. Norton, A. Abuzir, *J. Appl. Phys.*, 2006, **99**, 104302.
- [288] A. Cabot, A. Dieguez, A. Romano-Rodriguez, J. R. Morante, N. Barsan, *Sens. Actuators B*, 2001, **79**, 98.
- [289] R. Srivastava, R. Dwivedi, S. K. Srivastava, *Microelectro. J.*, 1998, **29**, 833.
- [290] A. Chaturvedi, V. N. Mishra, R. Dwivedi, S. K. Srivastava, *Microelectro. J.*, 2000, **31**, 283.
- [291] A. Forleo, L. Francioso, S. Capone, F. Casino, P. Siciliano, O. K. Tan, H. Hui, *Procedia Chem.*, 2009, **1**, 196.
- [292] H. Hui, O. K. Tan, Y. C. Lee, T. D. Tran, M. S. Tse, *Appl. Phys. Lett.*, 2005, **87**, 163123.
- [293] S. Luo, P. K. Chu, W. Liu, M. Zhang, C. Lin, *Appl. Phys. Lett.*, 2006, **88**, 183112.
- [294] M. Batzill, K. Katsiev, U. Diebold, *Appl. Phys. Lett.*, 2004, **85**, 5766.
- [295] H. Idriss, E. G. Seebauer, *J. Mol. Cataly. A: Chemical*, 2000, **152**, 201.
- [296] V. V. Sysoev, J. Goschnick, T. Schneider, E. Strelcov, A. Kolmakov, *Nano Lett.*, 2007, **7**, 3182.
- [297] S. P. Harvey, T. O. Mason, Y. Gassenbauer, R. Schafranek, A. Klein, *J. Phys. D: Appl. Phys.*, 2006, **39**, 3959.
- [298] M. H. Huang, S. Mao, H. Feick, H. Q. Yan, Y. Y. Wu, H. Kind, E. Weber, R. Russo, P. D. Yang, *Science*, 2001, **292**, 1897.
- [299] (a) C. Wang, M. Shim, P. Guyot-Sionnest, *Science*, 2001, **291**, 2390; (b) X. Michalet, F. F. Pinaud, L. A. Bentolila, J. M. Tsay, S. Doose, J. J. Li, G.

- Sundaresan, A. M. Wu, S. S. Gambhir, S. Weiss, *Science*, 2005, **307**, 538; (c) P. M. Arnal, F. Schuth, F. Kleitz, *Chem. Commun.*, 2006, 1203.
- [300] Y. Zhang, K. Suenaga, C. Colliex, S. Iijima, *Science*, 1998, **81**, 973.
- [301] (a) Y. Xie, Z. P. Qiao, M. Chen, X. M. Liu, Y. T. Qian, *Adv. Mater.*, 1999, **11**, 1512; (b) X. C. Wu, W. H. Song, B. Zhao, W. D. Huang, M. H. Pu, Y. P. Sun, J. J. Du, *Solid State Commun.*, 2000, **115**, 683; (c) Q. Li, C. R. Wang, *Appl. Phys. Lett.*, 2003, **82**, 1398; (d) J. Q. Hu, Y. Bando, Z. W. Liu, T. Sekiguchi, D. Golberg, J. H. Zhan, *J. Am. Chem. Soc.*, 2003, **125**, 11306.
- [302] (a) J. Q. Hu, X. M. Meng, Y. Jiang, C. S. Lee, S. T. Lee, *Adv. Mater.*, 2003, **15**, 70; (b) H. Z. Zhang, X. H. Luo, J. Xu, B. D. Xiang, P. Yu, *J. Phys. Chem. B*, 2004, **108**, 14866; (c) T. A. Crowley, B. Daly, M. A. Morris, D. Erts, O. Kazakova, J. J. Boland, B. Wu, J. D. Holmes, *J. Mater. Chem.*, 2005, **15**, 2408.
- [303] H. M. Lin, Y. L. Chen, J. Yang, Y. C. Liu, K. M. Yin, J. J. Kai, F. R. Chen, L. C. Chen, Y. F. Chen, C. C. Chen, *Nano Lett.*, 2003, **3**, 537.
- [304] O. Hayden, A. B. Greytak, D. C. Bell, *Adv. Mater.*, 2005, **17**, 701.
- [305] Q. Kuang, Z. Y. Jiang, Z. X. Xie, S. C. Lin, Z. W. Lin, S. Y. Xie, R. B. Huang, L. S. Zheng, *J. Am. Chem. Soc.*, 2005, **127**, 11777.
- [306] D. W. Kim, I. S. Hwang, S. J. Kwon, H. Y. Kang, K. S. Park, Y. J. Choi, K. J. Choi, J. G. Park, *Nano Lett.*, 2007, **7**, 3041.
- [307] P. Nguyen, H. T. Ng, T. Yamada, M. K. Smith, J. Li, J. Han, M. Meyyappan, *Nano Lett.*, 2004, **4**, 651.
- [308] (a) Z. R. Dai, Z. W. Pan, Z. L. Wang, *Solid State Commun.*, 2001, **118**, 351; (b) J. Q. Hu, X. L. Ma, N. G. Shang, Z. Y. Xie, N. B. Wang, C. S. Lee, S. T. Lee, *J. Phys. Chem. B*, 2002, **106**, 3823.
- [309] (a) J. Y. Lao, J. Y. Huang, D. Z. Wang, Z. F. Ren, *Adv. Mater.*, 2004, **16**, 65; (b) Y. B. Li, Y. Bando, D. Golberg, *Adv. Mater.*, 2004, **16**, 581.

- [310] N. N. Padurow, *Die Naturwissenschaften*, 1956, **43**, 395.
- [311] R. Mueller, H. K. Kammler, S. E. Pratsinis, A. Vital, G. Beaucage, P. Burtscher, *Powder Technol.*, 2004, **140**, 40.
- [312] W. Zhu, S. E. Pratsinis, *AIChE Journal.*, 1997, **43**, 2657.
- [313] C. H. Hung, J. L. Katz, *J. Mater. Res.*, 1992, **7**, 1861.
- [314] E. R. Leite, J. A. Cerri, E. Longo, J. A. Varela, C. A. Paskocima, *J. Euro. Ceram. Soc.*, 2001, **21**, 669.
- [315] A. N. Cormack, C. M. Freeman, C. R. A. Catlow, R. L. Royle, *Advances in Ceramics: Nonstoichiometric Compounds*, American Ceramic Soc., Westerville, 1987, **23**, 283.
- [316] D. L. Drobeck, A. V. Virkar, R. M. Cohen, *J. Phys. Chem. Solids*, 1990, **51**, 977.
- [317] J. R. Akse, H. B. Whitehurst, *J. Phys. Chem. Solids*, 1978, **39**, 457.
- [318] M. R. Cassia-Santos, A. G. Souza, L. E. B. Soledade, J. A. Varela, E. Longo, *J. Thermal Anal. Calorim.*, 2005, **79**, 415.
- [319] H. Uchiyama, H. Imai, *Chem. Commun.*, 2005, 6014.
- [320] S. V. Manorama, C. V. Gopal Reddy, V. Rao, *J. Appl. Surf. Sci.*, 2001, **174**, 93.
- [321] (a) D. L. Schmidt, C. E. Coburn, M. D. Benjamin, *Nature*, 1994, **368**, 39; (b) H. Shang, Y. Wang, L. S. Limmer, *Thin Solid Films*, 2005, **472**, 37.
- [322] (a) T. Onda, S. Shibuichi, N. Satoh, K. Tsujii, *Langmuir*, 1996, **12**, 2125; (b) Z. Guo, F. Zhou, J. Hao, W. Liu, *J. Am. Chem. Soc.*, 2005, **127**, 15670.
- [323] Y. Xu, D. Wu, Y. H. Sun, Z. X. Huang, X. D. Jiang, X. F. Wei, Z. H. Wei, B. Z. Dong, Z. H. Wu, *Appl. Opt.*, 2005, **44**, 527.
- [324] M. Li, J. Zhai, H. Liu, Y. L. Song, L. Jiang, D. B. Zhu, *J. Phys. Chem. B*, 2003, **107**, 9954.
- [325] (a) J. Lee, C. J. Kim, *Microelectromech. Syst.*, 2000, **9**, 171; (b) N.

- Verplanck, E. Galopin, J. C. Camart, V. Thomy, *Nano Lett.*, 2007, **7**, 813.
- [326] R. A. Hayes, B. J. Feenstra, *Nature*, 2003, **425**, 383.
- [327] R. N. Wenzel, *Ind. Eng. Chem.*, 1936, **28**, 988.
- [328] A. B. D. Cassie, S. Baxter, *Trans. Faraday. Soc.*, 1944, **40**, 546.
- [329] (a) Z. Pan, Z. Dai, Z. L. Wang, *Science*, 2001, **291**, 1947; (b) D. Zhang, L. Sun, J. Yin, C. Yan, *Adv. Mater.*, 2003, **15**, 1022; (c) Y. Liu, J. Dong, M. Liu, *Adv. Mater.*, 2004, **16**, 353; (d) L. Vayssieres, M. Graetzel, *Angew. Chem. Int. Ed.*, 2004, **43**, 3666.
- [330] Y. Wang, X. Jiang, Y. Xia, *J. Am. Chem. Soc.*, 2003, **125**, 16176.
- [331] Z. Liu, D. Zhang, S. Han, C. Li, T. Tang, W. Jin, X. Liu, B. Lei, C. Zhou, *Adv. Mater.*, 2003, **15**, 1754.
- [332] A. Chen, X. Peng, K. Koczkur, B. Miller, *Chem. Commun.*, 2004, 1964.
- [333] W. Q. Zhu, X. J. Feng, L. Feng, L. Jiang, *Chem. Commun.*, 2006, 2753.
- [334] X. Wu, J. H. Sui, W. Cai, F. Y. Qu, *Mater. Chem. Phys.*, 2008, **112**, 325.
- [335] M. Miyauchi, A. Nakajima, T. Watanabe, K. Hashimoto, *Chem. Mater.*, 2002, **14**, 2812.
- [336] D. Hegemann, U. Vohrer, C. Oehr, R. Riedel, *Surf. Coat. Technol.*, 1999, **116**, 1033.
- [337] S. C. Cho, Y. C. Hong, S. G. Cho, Y. Y. Ji, C. S. Han, H. S. Uhm, *Curr. Appl. Phys.*, 2009, **9**, 1223.
- [338] R. D. Sun, A. Nakajima, A. Fujishima, T. Watanabe, K. Hashimoto, *J. Phys. Chem. B*, 2001, **105**, 1984.
- [339] R. Wang, K. Hashimoto, A. Fujishima, M. Chikuni, E. Kojima, A. Kitamura, M. Shimohigoshi, T. Watanabe, *Nature*, 1997, **388**, 431.
- [340] X. Feng, L. Feng, M. Jin, J. Zhai, L. Jiang, D. B. Zhu, *J. Am. Chem. Soc.*, 2004, **126**, 62.
- [341] (a) G. Larramona, C. Chone, A. Jacob, D. Sakakura, B. Delatouche, D. Pere, X. Cieren, M. Nagino, R. Bayon, *Chem. Mater.*, 2006, **18**, 1688; (b)

- I. Mora-Sero, J. Bisquert, T. Dittrich, A. Belaidi, A. S. Susha, A. L. Rogach, *J. Phys. Chem. C*, 2007, **111**, 14889; (c) R. D. Schaller, M. Sykora, J. M. Pietryga, V. I. Klimov, *Nano Lett.*, 2006, **6**, 424.
- [342] (a) P. Wang, C. Klein, R. Humphry-Baker, S. M. Zakeeruddin, M. Grätzel, *J. Am. Chem. Soc.*, 2005, **127**, 808; (b) I. Robel, V. Subramanian, M. Kuno, P. V. Kamat, *J. Am. Chem. Soc.*, 2006, **128**, 2385; (c) A. Kongkanand, K. Tvrđy, K. Takechi, M. Kuno, P. V. Kamat, *J. Am. Chem. Soc.*, 2008, **130**, 4007.
- [343] (a) Z. A. Peng, X. G. Peng, *J. Am. Chem. Soc.*, 2001, **123**, 183; (b) W. W. Yu, L. H. Qu, W. Z. Guo, X. G. Peng, *Chem. Mater.*, 2003, **15**, 2854; (c) G. M. Whitesides, G. W. Crabtree, *Science*, 2007, **315**, 798.
- [344] (a) X. F. Gao, H. B. Li, W. T. Sun, Q. Chen, F. Q. Tang, L. M. Peng, *J. Phys. Chem. C*, 2009, **113**, 7531; (b) J. B. Sambur, B. A. Parkinson, *J. Am. Chem. Soc.*, 2010, **132**, 2130; (c) C. H. Chang, Y. L. Lee, *Appl. Phys. Lett.*, 2007, **91**, 053503.
- [345] Y. L. Lee, B. M. Huang, H. T. Chin, *Chem. Mater.*, 2008, **20**, 6903.
- [346] I. Robel, M. Kuno, P. V. Kamat, *J. Am. Chem. Soc.*, 2007, **129**, 4136; (b) Y. Tang, X. Hu, M. Chen, L. Luo, B. Li, L. Zhang, *Electrochimica Acta*, 2009, **54**, 2742.
- [347] (a) H. P. Liu, N. Li, S. F. Bi, D. Y. Li, *Electrochemistry Commun.*, 2009, **11**, 2265; (b) W. Lee, S. K. Min, V. Dhas, S. B. Ogale, S. H. Han, *Electrochemistry Commun.*, 2009, **11**, 103.





## 10 Appendix

### 10.1 List of tables

<b>Table 1:</b> Summary of 1D nanostructures synthesized using different methods .....	9
<b>Table 2:</b> Experimental conditions for CVD process .....	55
<b>Table 3:</b> Description of TTO series of tin oxide NWs samples .....	119

## 10.2 List of figures

- Figure 1:** Diffusive and ballistic transport of electrons in one-dimensional wires.  
.....6
- Figure 2:** Schematic presentation of different types of one dimensional nanostructures. (A) Nanowires and nanorods; (B) core–shell structures with metallic core, semiconductor or metal-oxide shell; (C) nanotubes/nanopipes and hollow nanorods; (D) segmented heterostructures; (E) nanobelts/nanoribbons; (F) nanotapes; (G) dendrites; (H) hierarchical nanostructures; (I) nanosphere assembly; (J) nanosprings.  
.....15
- Figure 3:** (a) Schematic presentation of VLS growth mechanism, and (b) SEM image of Si whiskers synthesized by VLS growth mechanism.....21
- Figure 4:** (a) The controlled growth of 1D nanostructures by VLS mechanism, and (b) SEM and TEM images of Ge nanowires grown on Si substrate. 22
- Figure 5:** In-situ TEM images recorded during the growth process of Ge nanowire. (a) Au nanoclusters in solid state at 500 °C; (b) alloying initiates at 800 °C, at this stage Au exists in mostly solid state; (c) liquid Au/Ge alloy; (d) the nucleation of Ge nanocrystal on the alloy surface; (e) Ge nanocrystal elongates with further Ge condensation and eventually forming a nanowire. ....23
- Figure 6:** (a) Schematic presentation of SLS growth mechanism, and (b) TEM images of Si nanowires synthesized following the SLS mechanism: (A) Si nanowire synthesized at 410 °C with Au nanocrystal seeds; (B) one Si nanowire with a Au seed at the tip; (C) Si nanowires grown using Bi nanocrystals as seeds; (D) a Si nanowire (Bi seeded) longer than 3 μm.  
.....26
- Figure 7:** Schematic presentation of template-assisted synthesis of

one-dimensional nanostructures.....	28
<b>Figure 8:</b> Schematic presentation of innovation to synthesize one-dimensional architectures.....	32
<b>Figure 9:</b> Typical shapes for architectures fabricated using various methods.....	33
<b>Figure 10:</b> Fundamental processes active in the CVD process. ....	38
<b>Figure 11:</b> Processing of 1D metal oxide nanostructures by molecule-based CVD.....	40
<b>Figure 12:</b> Self-catalytic growth mechanism for Ge/SiC <sub>x</sub> N <sub>y</sub> nanowires and SEM images of Ge/SiC <sub>x</sub> N <sub>y</sub> nanowires formed in 5, 15, and 60 s. ....	41
<b>Figure 13:</b> The CO sensing mechanism of SnO <sub>2</sub> gas sensor.....	51
<b>Figure 14:</b> (a) Schematic presentation and (b) image of the CVD reactor. ...	56
<b>Figure 15:</b> (a) Schematic presentation and (b) image of chemical bath deposition reactor. ....	59
<b>Figure 16:</b> Image of XRD machine in our group.....	61
<b>Figure 17:</b> Image of SEM machine in our group.....	62
<b>Figure 18:</b> Image of AFM machine in our group.....	66
<b>Figure 19:</b> (a) Schematic presentation and (b) image of the PC-automated gas sensing system used in this work. ....	69
<b>Figure 20:</b> SEM image of one of the nanowires contacted in a 4-probes configuration.....	70
<b>Figure 21:</b> Structural illustration of the bottom-contact SnO <sub>2</sub> nanowires based network transistor. ....	72
<b>Figure 22:</b> Simulation contours of (a) pressure and (b) gas flux profiles on the graphite susceptor. ....	75
<b>Figure 23:</b> SEM images of SnO <sub>2</sub> nanowires grown at different deposition temperatures. ....	77
<b>Figure 24:</b> SEM images of SnO <sub>2</sub> nanowires grown at different precursor	

temperatures.....	78
<b>Figure 25:</b> SEM images of morphology before and after CVD process at the different sputtering times.....	80
<b>Figure 26:</b> Photograph of graphite susceptor with five different angles and the corresponding SEM images of SnO <sub>2</sub> nanowires. ....	82
<b>Figure 27:</b> Schematic presentation of the suitable temperature area for the growth of SnO <sub>2</sub> nanowires. ....	83
<b>Figure 28:</b> XRD patterns of tin oxide nanowires grown on Al <sub>2</sub> O <sub>3</sub> polycrystalline substrate. ....	85
<b>Figure 29:</b> SEM (a) and TEM (b) images of SnO <sub>2</sub> nanowires grown on Al <sub>2</sub> O <sub>3</sub> polycrystalline substrate. (c) Fragment of SnO <sub>2</sub> unit cell.....	86
<b>Figure 30:</b> Current-voltage ( <i>I-V</i> ) characteristics of the SnO <sub>2</sub> NW-based sensor in dry ambient condition at different temperatures. ....	87
<b>Figure 31:</b> Variation of the resistance of the SnO <sub>2</sub> NW-based sensor at different temperatures. ....	88
<b>Figure 32:</b> <i>I-V</i> curve of an individual SnO <sub>2</sub> nanowire at room temperature....	89
<b>Figure 33:</b> Room-temperature PL spectrum of the SnO <sub>2</sub> nanowires. ....	90
<b>Figure 34:</b> Gas sensing performance of SnO <sub>2</sub> nanowires in 1000 ppm ethanol and CO atmosphere at 250 °C. ....	91
<b>Figure 35:</b> Gas sensitivity versus operating temperature of SnO <sub>2</sub> nanowires based sensor in 1000 ppm ethanol and CO atmosphere.....	92
<b>Figure 36:</b> <i>I<sub>d</sub>-V<sub>ds</sub></i> characteristics of the SnO <sub>2</sub> nanowire based FET under dark and illuminated conditions. Inset: the variation curve of <i>V<sub>gs</sub></i> . ....	93
<b>Figure 37:</b> SEM images of SnO <sub>2</sub> nanowire arrays grown on TiO <sub>2</sub> (001), (100), (110) and (101) substrates, respectively. ....	97
<b>Figure 38:</b> XRD patterns of tin oxide nanowires grown on TiO <sub>2</sub> (001) substrates. TiO <sub>2</sub> (001) is measured as standard. ....	97
<b>Figure 39:</b> (a-c) Electron microscopic images of FIB preparation for cross	

sectional analysis. (d) Four growth directions of ordered SnO <sub>2</sub> nanowires.	
(e) The cross sectional TEM image showed the epitaxial growth of SnO <sub>2</sub> nanowires on TiO <sub>2</sub> (001) substrate. ....	98
<b>Figure 40:</b> SEM images of ordered SnO <sub>2</sub> nanowires sample recorded at different incident angles of electron beams. ....	99
<b>Figure 41:</b> (a) TEM images of SnO <sub>2</sub> nanowire with Au catalyst tip showing the abnormal oblique interface between SnO <sub>2</sub> and the droplet. (b) HR-TEM image of ordered SnO <sub>2</sub> NW. ....	100
<b>Figure 42:</b> Schematic growth model of ordered tin oxide nanowires on TiO <sub>2</sub> (001) substrate. (a) [001] vs. [101] directions. (b) The “incubation” growth mode. ....	101
<b>Figure 43:</b> Formation of (001) to (101), (011), (0-11) and (-101) facets. ....	102
<b>Figure 44:</b> (a) SEM image of ordered SnO <sub>2</sub> NWs grown in 5 min. (b) Statistic analysis of [101], [011], [-101] and [0-11] growth directions based on Figure 43. ....	103
<b>Figure 45:</b> SEM images of patterned growth of tin oxide nanowires on TiO <sub>2</sub> (001) substrates. ....	104
<b>Figure 46:</b> 3D SEM-FIB tomographic images of ordered SnO <sub>2</sub> NWs on (a) TiO <sub>2</sub> (001) and (b) TiO <sub>2</sub> (101) substrates. ....	105
<b>Figure 47:</b> (a) Top-view and (b) tilt-view SEM images of tin oxide nanowires grown on TiO <sub>2</sub> (101) substrates. (c) Purposed growth models of ordered SnO <sub>2</sub> NWs on TiO <sub>2</sub> (001) and TiO <sub>2</sub> (101) substrates. ....	106
<b>Figure 48:</b> (a) Electrical <i>I-V</i> characteristic curve of an individual SnO <sub>2</sub> [101] nanowire acquired in four-probe configuration at room temperature (25 °C). (b) Conductometric response of an individual SnO <sub>2</sub> [101] nanowire to different CO concentrations (diluted in dry synthetic air) at T = 300 °C. Response vs. concentration log-log plot is shown in inset: a linear sensing characteristic behavior. ....	108

- Figure 49:** (a) Overview SEM image of ordered SnO<sub>2</sub> NWs on TiO<sub>2</sub>(001) substrate. Cross sectional SEM (b) and TEM (c) micrographs showing the side-view of oriented SnO<sub>2</sub> NWs. The samples are sheared and prepared along one of the directions of SnO<sub>2</sub> nanowire arrays. .... 112
- Figure 50:** AFM images of ordered SnO<sub>2</sub> NWs in 2D (a) and 3D (b) forms. 113
- Figure 51:** Left: Sample preparation for FIB-tomographic analysis. Right: SEM images of the serial cuts through the nanowires for the tomography. The cross section is tilted 52° with respect to the electron beam. The bright particles represent the gold catalysts. .... 115
- Figure 52:** 3D-representation of (a) SnO<sub>2</sub> nanowire arrays and (b) distribution of Au catalyst as measured with FIB-tomography. .... 116
- Figure 53:** XRD patterns of as-deposited (TO) and plasma-treated (TTO) SnO<sub>2</sub> nanowires..... 119
- Figure 54:** SEM micrographs of (a) as-deposited (TO) and plasma-treated (TTO) SnO<sub>2</sub> nanowire samples at (b) 10, (c) 40 and (d) 80 W, respectively. .... 120
- Figure 55:** HR-TEM images of (a) as-deposited and (b) plasma treated (40 W) SnO<sub>2</sub> nanowires. .... 121
- Figure 56:** HR-TEM images of plasma-treated SnO<sub>2</sub> NWs after (a, b) short and (c, d) long e-beam radiation showing the e-beam influence on the plasma-treated SnO<sub>2</sub> nanowires. .... 122
- Figure 57:** XPS spectra of as-deposited and plasma-treated (40 W) SnO<sub>2</sub> nanowires..... 123
- Figure 58:** Photoluminescence spectra of as-deposited (TO) and plasma-treated (TTO4) SnO<sub>2</sub> nanowires..... 124
- Figure 59:** (a) Temperature-dependent sensing response curves for TTO series samples and (b) base and sensing resistances dependency to the power of plasma treatment, which reveals the increasing oxygen

chemisorption over the samples. ....	126
<b>Figure 60:</b> On/off gas sensing curves of as-prepared and plasma-treated (40W) SnO <sub>2</sub> nanowires in 1000 ppm ethanol at 250 °C. ....	128
<b>Figure 61:</b> XRD patterns of SnO <sub>2</sub> @TiO <sub>2</sub> core-shell structures. ....	131
<b>Figure 62:</b> SEM (a, b) and TEM images (c, d) of the as-prepared SnO <sub>2</sub> NWs (left) and SnO <sub>2</sub> @TiO <sub>2</sub> core-shell structures (right). ....	132
<b>Figure 63:</b> XRD patterns of the SnO <sub>2</sub> @TiO <sub>2</sub> core-shell structures: as-prepared and annealed at 950, 1200 and 1400 °C, respectively. ....	133
<b>Figure 64:</b> Variation curves of lattice parameter <i>a</i> and (110) peak of SnO <sub>2</sub> before and after annealing treatment at 950 and 1200 °C, respectively. ....	134
<b>Figure 65:</b> Equilibrium phase diagram of the SnO <sub>2</sub> -TiO <sub>2</sub> system. ....	135
<b>Figure 66:</b> SEM and HR-TEM images of SnO <sub>2</sub> @TiO <sub>2</sub> core-shell structures after annealing treatment at 950, 1200 and 1400 °C, respectively. ....	137
<b>Figure 67:</b> Scheme of process mechanism for the SnO <sub>2</sub> -TiO <sub>2</sub> system after annealing treatment. ....	139
<b>Figure 68:</b> Room-temperature (25 °C) <i>I-V</i> characteristics of a single SnO <sub>2</sub> nanowire and SnO <sub>2</sub> @TiO <sub>2</sub> core-shell structure in dry air condition. ....	140
<b>Figure 69:</b> Gas sensing performance of SnO <sub>2</sub> and SnO <sub>2</sub> @TiO <sub>2</sub> core-shell structures in 90 ppm ethanol atmosphere at 250 °C. ....	141
<b>Figure 70:</b> Top-view SEM and TEM images of (a, b) SnO <sub>2</sub> NWs and (c, d) SnO <sub>2</sub> @SnO <sub>2</sub> heterostructures. ....	145
<b>Figure 71:</b> XRD patterns of (a) SnO <sub>2</sub> NWs and (b) SnO <sub>2</sub> @SnO <sub>2</sub> heterostructures. ....	146
<b>Figure 72:</b> Images of water droplet on the surfaces of (a) SnO <sub>2</sub> nanowires and (b) SnO <sub>2</sub> @SnO <sub>2</sub> heterostructures. (c) SEM image of SnO <sub>2</sub> @VO <sub>x</sub> heterostructures, and (d) the corresponding sharp of water droplet. ....	147
<b>Figure 73:</b> SEM (a), TEM (b) and EDX (c) images of SiO <sub>x</sub> film coated	



SnO <sub>2</sub> @SnO <sub>2</sub> heterostructures, and (d) the corresponding shape of water droplet.....	149
<b>Figure 74:</b> Schematic presentation of the switching of SnO <sub>2</sub> based surface. .....	150
<b>Figure 75:</b> Time dependence of water contact angles of SiO <sub>x</sub> coated SnO <sub>2</sub> @SnO <sub>2</sub> heterostructure surface (a) under UV irradiation, (b) in dark storage and (c) O <sub>2</sub> annealing. ....	153
<b>Figure 76:</b> SEM and TEM images of (a, b) partially and (c, d) fully covered SnO <sub>2</sub> @CdS QDs heterostructures.....	157
<b>Figure 77:</b> XRD patterns of SnO <sub>2</sub> @CdS QDs heterostructures.....	158
<b>Figure 78:</b> HR-TEM images of SnO <sub>2</sub> @CdS QDs heterostructures.....	159
<b>Figure 79:</b> UV-visible light absorption spectras of SnO <sub>2</sub> nanowires and SnO <sub>2</sub> @CdS QDs heterostructures.....	161
<b>Figure 80:</b> Room temperature <i>I-V</i> curves of SnO <sub>2</sub> nanowires and SnO <sub>2</sub> @CdS QDs heterostructures in dry air condition.....	162
<b>Figure 81:</b> Photoconductivity curves of of SnO <sub>2</sub> nanowires and SnO <sub>2</sub> @CdS QDs heterostructures.....	163
<b>Figure 82:</b> Schematic presentation of photoconductivity mechanism. ....	164
<b>Figure 83:</b> Roadmap of this work.....	165
<b>Figure 84:</b> Roadmap of nanowire based devices. ....	170

## **Ehrenwörtliche Erklärung**

Ich versichere, dass ich die von mir vorgelegte Dissertation selbständig angefertigt, die benutzten Quellen und Hilfsmittel vollständig angegeben und die Stellen der Arbeit – einschließlich Tabellen, Karten und Abbildungen, die anderen Werken im Wortlaut oder dem Sinn nach entnommen sind, in jedem Einzelfall als Entlehnung kenntlich gemacht habe; dass diese Dissertation noch keiner anderen Fakultät oder Universität zur Prüfung vorgelegen hat; dass sie – abgesehen von unten angegebenen Teilpublikationen – noch nicht veröffentlicht worden ist sowie, dass ich eine solche Veröffentlichung vor Abschluss des Promotionsverfahrens nicht vornehmen werde.

Die Bestimmungen der geltenden Promotionsordnung sind mir bekannt. Die von mir vorgelegte Dissertation ist von Prof. Dr. Sanjay Mathur betreut worden.

Köln, im August 2010

Jun Pan



# Curriculum Vitae

## DEMOGRAPHIC INFORMATION:

Name: Jun Pan

Birth: 16.03.1981, Gansu Province

Nationality: People's Republic of China

E-mail: jun.pan@hotmail.com

## EDUCATIONAN BACKGROUND:

Ph. D student                      2008.09 – 2010.10

Chair of Inorganic and Materials Chemistry, University of Cologne, Cologne,  
Germany

Major: Inorganic Chemistry/Material Science

Supervisor: Prof. Dr. Sanjay Mathur

Ph. D student                      2007.02 – 2008.08

Institute for New Materials, Saarland University, Saarbrücken, Germany

Major: Material Science

Supervisor: Prof. Dr. Sanjay Mathur

M. S.                                      2003.09 – 2005.12

School of Metallurgical Science and Engineering, Central South University,  
Changsha, China

Major: Nonferrous Metals Metallurgy

Supervisor: Prof. Dr. Xiaobin Li, Prof. Dr. Guihua Liu

B. S.                                      1999.09 – 2003.06

School of Metallurgical Science and Engineering, Central South University,  
Changsha, China

Major: Metallurgical Engineering

## **PUBLICATIONS:**

1. Switchable Wettability in SnO<sub>2</sub> Nanowires and SnO<sub>2</sub>@SnO<sub>2</sub> Heterostructures  
**J. Pan**, T. Rügamer, L. S. Xiao, X. F. Song, J. T. Li, H. Shen, S. Mathur, *J. Phys. Chem. C*, (Submitted).
2. FIB-Tomographic Studies on Chemical Vapor Deposition Grown SnO<sub>2</sub> Nanowire Arrays on TiO<sub>2</sub>(001)  
**J. Pan**, F. Soldera, F. Mücklich, H. Shen, S. Mathur, *Appl. Phys. Lett.*, (Submitted).
3. Structural and Electrical Properties of Anisotropic SnO<sub>2</sub>/TiO<sub>2</sub> Core-shell Structures  
**J. Pan**, J. T. Li, L. S. Xiao, S. Hühne, J. Schläfer, W. Mader, H. Shen, S. Mathur, *J. Phys. Chem. C*, (Submitted).
4. Heteroepitaxy of SnO<sub>2</sub> Nanowire Arrays on TiO<sub>2</sub> Single Crystals: Growth Patterns and Bulk Tomographic Studies  
**J. Pan**, H. Shen, U. Werner, F. Hernández-Ramírez, J. Daniel Prades, F. Soldera, F. Mücklich, S. Mathur, *Chem. Mater.*, (In Print).
5. Microwave Assisted Fast and Facile Synthesis of SnO<sub>2</sub> Quantum Dots and Their Printing Applications  
L. S. Xiao, H. Shen, R. von Hagen, **J. Pan**, L. Belkoura, S. Mathur, *Chem. Commun.*, 46, 6509-6511, 2010.
6. Plasma-Modified SnO<sub>2</sub> Nanowires for Enhanced Gas Sensing  
**J. Pan**, R. Ganesan, H. Shen, S. Mathur, *J. Phys. Chem. C*, 114(18),

8245-8250, 2010.

7. Bidimensional Versus Tridimensional Oxygen Vacancy Diffusion in SnO<sub>2-x</sub> under Different Gas Environments  
N. López, J. Daniel Prades, F. Hernández-Ramírez, J. R. Morante, **J. Pan**, S. Mathur, *Phys. Chem. Chem. Phys.*, 12, 2401-2406, 2010.
8. CVD Grown Semiconductor Nanowires: Synthesis, Properties and Challenges  
**J. Pan**, H. Shen, S. Mathur, *Ceramic Transactions*, 214, 1-10, 2010.
9. Growth Mechanism Study on Molecule-based Chemical Vapor Deposition of Tin Oxide Nanowires  
**J. Pan**, L. S. Xiao, H. Shen, S. Mathur, *Ceramic Engineering and Science Proceedings (CESP)*, 30(7), 9-16, 2009.
10. Direct Observation of the Gas-surface Interaction Kinetics in Nanowires through Pulsed Self-heating Assisted Conductometric Measurements  
J. Daniel Prades, R. Jimenez-Diaz, F. Hernández-Ramírez, **J. Pan**, S. Mathur, J. R. Morante, *Appl. Phys. Lett.*, 95, 053101, 2009.
11. An Experimental Method to Estimate the Temperature of Individual Nanowires  
J. D. Prades, R. Jimenez-Diaz, F. Hernández-Ramírez, S. Barth, **J. Pan**, S. Mathur, J. R. Morante, *Int. J. Nanotechnol.*, 9(6), 860-869, 2009.

## CONFERENCE PRESENTATIONS:

1. Growth, Surface modification, Assembly, and Their Properties of 1D SnO<sub>2</sub> Nanowires (Oral)  
**J. Pan**, J. T. Li, H. Shen, S. Mathur  
5<sup>th</sup> International Conference on Technological Advances of Thin Film &

Surface Coating (Thin Films 2010), Harbin, China, 11-14 July 2010.

2. Synthesis and Characterization of Tin Oxide Nanowire Architectures (Poster)

**J. Pan**, H. Shen, S. Mathur

34<sup>rd</sup> International Conference on Advanced Ceramics and Composites, Daytona Beach, Florida, 24-29 January 2010.

3. Synthesis and Characterizations of Tin Oxide Based One-dimensional Heterostructures (Poster)

**J. Pan**, H. Shen, S. Mathur

European Conference on Solid State Chemistry 2009, Muenster, 20-23 September 2009.

4. Formation and Structure Evolution of Tin Oxide One-dimensional Heterostructures (Poster)

**J. Pan**, R. Fiz, T. Fischer, R. Müller, H. Shen, S. Mathur

3<sup>rd</sup> International Workshop on Smart Materials & Structures, Kiel, 19-21 August 2009.

5. Controlled Synthesis and Growth Mechanism Study of Tin Oxide Nanowire Arrays (Poster)

**J. Pan**, J. Altmayer, J. D. Wei, N. Donia, U. Werner, H. Shen, S. Mathur

MSE08 - Materials Science and Engineering, Nürnberg, 1-4 September 2008.

## **AWARDS AND HONORS:**

1. Best Poster Prize, Sommer Fest of Department of Chemistry, University of Cologne (2010)

2. Chinese Government Award for Outstanding Self-Financed Students Abroad (2009)
3. Best Poster Prize, Conference of 3<sup>rd</sup> International Workshop on Smart Materials & Structures (2009)
4. Best Poster Prize, Conference of Materials Science and Engineering 2008, Nürnberg (2008)
5. Central South University Present Graduate Registration Scholarship (2003-2005)
6. Excellent Graduate Student, Central South University (2001-2003)
7. Excellent Graduate Student Leader, Central South University (2001-2003)
8. Excellent Society Practice Advanced Student, Central South University (2001)
9. Competition of "Start an Enterprise for Youth" in Hunan province, Third Prize (2001)
10. Central South University Scholarship (1999-2001)





潘 军

荣获二〇〇九年度国家优秀自费留学生  
奖学金，特颁证嘉奖，以资鼓励。

**CHINA SCHOLARSHIP COUNCIL**

Presents the

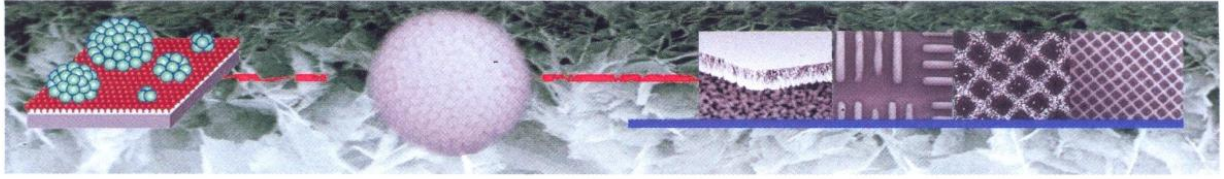
**2009 Chinese Government Award  
for Outstanding Self-financed  
Students Abroad**

to

*Pan Jun*

---

Dr. Liu Jinghui  
Secretary-General  
China Scholarship Council



---

3<sup>rd</sup> International Workshop on Smart Materials & Structures

August 19-21, 2009, Kiel, Germany

# Best Poster Award

To

**Jun Pan,**

Raquel Fiz, Thomas Fischer, Ralf Müller,  
Hao Shen and Sanjay Mathur

---

For the best contribution in the field of Smart Materials & Structures entitled

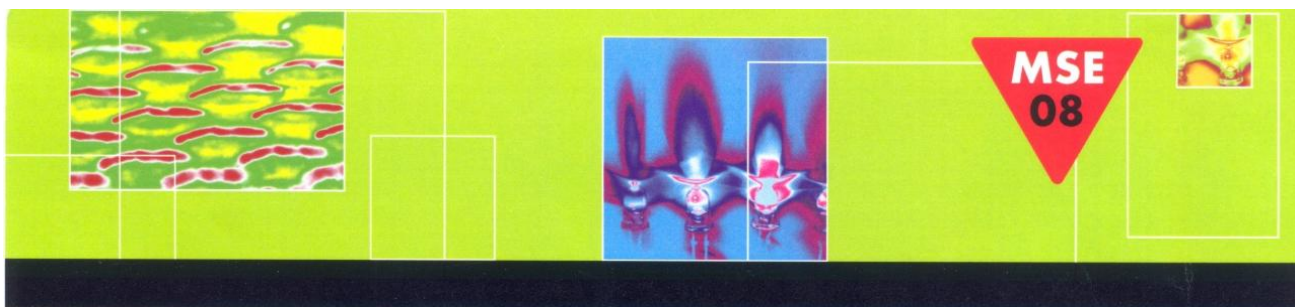
**Formation and structure evolution of tin  
oxide nanowire based heterostructures**

The Workshop Chairs

Prof. Dr. Mohammed Es-Souni  
Institute for Materials and Surface  
Technology  
University of Applied Sciences Kiel  
Germany

Prof. Dr. Sanjay Mathur  
Institute of Inorganic and Materials  
Chemistry, University of Cologne  
GERMANY

Prof. Dr. Horst-Günter Rubahn  
NanoSYD, Mads Clausen Institute  
University of Southern Denmark  
DENMARK



# Materials Science and Engineering

1 - 4 September 2008, Nürnberg, Germany

 WILEY-VCH

Poster Prize

---

awarded to

**Jun Pan**

**Leibniz-Institut für Neue Materialien gGmbH,  
Saarbrücken, Germany**

for the best poster

**Controlled Synthesis and Growth Mechanism Study  
of Tin Oxide Nanowire Arrays**

presented at MSE 2008, Congress and Exhibition  
on Advanced Materials and Processes



---

Dr. Jörn Ritterbusch  
Wiley-VCH Verlag GmbH & Co.KGAA